FRIEDRICH-ALEXANDER
UNIVERSITÄT
ERLANGEN-NÜRNBERG

Naturwissenschaftliche Fakultät
Friedrich-Alexander-Universität
Erlangen-Nürnberg

ERLANGEN CENTRE
FOR ASTROPARTICLE
PHYSICS

Monte Carlo Simulation of Cyclotron Lines in Strong Magnetic Fields

Theory and Application

Der Naturwissenschaftlichen Fakultät
der Friedrich-Alexander-Universität
Erlangen-Nürnberg

zur

Erlangung des Doktorgrades Dr. rer. nat.

vorgelegt von

Fritz-Walter Matthias Schwarm

aus Nürnberg

Als Dissertation genehmigt
von der Naturwissenschaftlichen Fakultät
der Friedrich-Alexander-Universität Erlangen-Nürnberg

Tag der mündlichen Prüfung: 03. Mai 2017

Vorsitzender des Promotionsorgans: Prof. Dr. Georg Kreimer

Gutachter: Prof. Dr. Jörn Wilms
Gutachter: Prof. Dr. Peter A. Becker

To my father

Abstract

Cyclotron resonance scattering features (CRSFs), or cyclotron lines, are observed as quasi-harmonically spaced absorption lines in the spectra of some accreting X-ray binaries. They exhibit the fundamental micro-physics in strong magnetic fields. Ironically, cyclotron lines can only be observed from a macro-physical point of view, that is, by astronomical observations. Neutron star binary systems provide us with the laboratories necessary to study the behavior of matter in the vicinity of fields of a strength close to the critical magnetic field strength, $B_{\mathrm{crit}} = 44.14 \times 10^{12}\,\mathrm{G}$, the realm of which is far from being approached by earth based experiments. The interaction of X-ray photons with quantized plasma electrons in terms of resonant cyclotron scattering in such systems is studied in this thesis from a theoretical point of view. The complex scattering cross sections are discussed as well as the numerical methods required to develop a Monte Carlo model for the generation of synthetic cyclotron lines. The development of such a model represents the core of this work. Its application to measured spectra of accreting X-ray binaries and the combination with state of the art models for relativistic light bending and radiative processes in the accretion columns of such sources constitute the outcome of this thesis. These results allow for drawing conclusions about the characteristics of the line forming region, such as its magnetic field strength, temperature, velocity, optical depth, and geometry, among others, on firm physical ground.

Ausführliche deutsche Zusammenfassung

Monte-Carlo-Simulation von Zyklotronlinien in starken Magnetfeldern

— Theorie und Anwendung —

Zyklotronlinien (cyclotron resonance scattering features, CRSFs) werden als beinahe äquidistante Absorptionslinien in den Spektren einiger akkretierender Röntgendoppelsterne beobachtet. Sie enthüllen die fundamentale Mikrophysik in starken Magnetfeldern, lassen sich aber ironischerweise nur in makrophysikalischen, nämlich astronomischen, Systemen beobachten. Doppelsternsysteme mit einem Neutronenstern dienen uns als die zur Erforschung des Verhaltens von Materie in Magnetfeldern nahe der kritischen Magnetfeldstärke, $B_{\mathrm{crit}} = 44.14 \times 10^{12}\,\mathrm{G}$, notwendigen Laboratorien fernab der Magnetfelder die in erdgebundenen Experimenten erreicht werden können. In dieser Arbeit wird die Wechselwirkung von Photonen im Röntgenbereich mit quantisierten Plasmaelektronen durch resonante Zyklotronstreuungsprozesse vom theoretischen Standpunkt aus untersucht.

Die Röntgendoppelsterne, die Zyklotronlinien formen, bestehen aus einem Neutronenstern der, auf verschiedene Arten abhängig von der jeweiligen Konfiguration des Doppelsternsystems, Materie von einem optischen Begleiter akkretiert. So kann im Falle eines Begleitsterns, der seine Roche-Grenze überschreitet, Materie über den Lagrange-Punkt L_1 vom Begleiter zum Neutronenstern übertragen werden. Ein anderes mögliches Szenario ist die Windakkretion bei der über den stellaren Wind des Begleitsterns abgegebene Masse durch das Gravitationspotential des Neutronensterns — meist über eine zwischengeschaltete Akkretionsscheibe — eingesammelt wird. Be-Akkretion findet im Perihel der exzentrischen Umlaufbahn eines Neutronensterns um einen massiven OB-Stern statt.

Die akkretierte Materie wird vom Magnetfeld des Neutronensterns zu Akkretionssäulen kanalisiert, welche an den Polen auf der Neutronensternoberfläche enden. Das starke in diesen Akkretionssäulen vorherrschende Magnetfeld führt zu einer Quantisierung der Elektronenimpulse des akkretierenden Plasmas senkrecht zur Magnetfeldachse. Gleichzeitig werden durch Schwarzkörper-, Synchrotron- und Bremsstrahlung in der Säule beziehungsweise auf der Neutronensternoberfläche Photonen erzeugt, welche mit den akkretierenden quantisierten Elektronen wechselwirken. Der dominierende Wechselwirkungsprozess unter den gegebenen Voraussetzungen ist die Zyklotronstreuung. Aufgrund der Quantisierung der Elektronenimpulse weist diese Form der Wechselwirkung ein hochgradig resonantes Verhalten auf: Photonen, die mit der richtigen Energie und unter dem richtigen Winkel auf ein Elektron treffen, um dieses in ein höheres Energieniveau anzuregen, werden mit sehr großer Wahrscheinlichkeit wechselwirken, wohingegen Photonen, welche die Resonanzbedingung nicht erfüllen, beinahe ungehindert entkommen. Der Anregung eines Elektrons in einen höherenergetischen Zustand folgt eine sukzessiven Abregung desselben bis der Grundzustand wieder erreicht ist. Die Energiebilanz wird in Form neu erzeugter Photonen ausgeglichen. Die Streuwinkel und die Winkel, unter denen neu erzeugte Photonen emittiert werden, ergeben sich, in Ab-

hängigkeit einer Vielzahl von Parametern, jeweils aus den komplexen differenziellen Wechselwirkungsquerschnitten beziehungsweise Zerfallsraten und machen eine korrekte analytische Berechnung der aus der Akkretionssäule entkommenden Strahlung unmöglich. Die Vielfalt an möglichen geometrischen Formen der Säule erschwert außerdem analytische Abschätzungen. Um die stark winkel- und energieabhängigen Profile der Zyklotronlinien physikalisch selbstkonsistent zu modellieren, bedarf es daher eines Monte-Carlo-Codes, der die physikalischen Prozesse der Interaktion quantisierter Elektronen mit Photonen für ein gegebenes Set von Parametern simuliert.

Die komplexen Wirkungsquerschnitte und die numerischen Methoden, die den Weg zu einem Monte-Carlo-Modell zur Erzeugung synthetischer Zyklotronlinien ebnen, werden erläutert. Die Entwicklung eines solchen Modells stellt den Kern dieser Arbeit dar. Seine Anwendung auf gemessene Spektren beispielhafter akkretierender Röntgendoppelsterne und die Kombination mit Modellen zur relativistischen Krümmung von Licht und Strahlungsprozessen in den Akkretionssäulen dieser Quellen stellen weitere Resultate dieser Dissertation dar. Dies ermöglicht es, auf Basis physikalischer Prinzipien Rückschlüsse auf die Charakteristika der Linien formenden Region, wie die darin vorherrschende Magnetfeldstärke, Temperatur, Geschwindigkeit, optische Tiefe und ihre Geometrie, zu ziehen.

CONTENTS

1 INTRODUCTION

Cyclotron resonance scattering features (CRSFs, or cyclotron lines) are spectral features formed by the interaction of photons with electrons in very strong magnetic fields of the order of some 10^{12} G. As the name suggests, they are formed by cyclotron scattering, that is, the possibly inelastic scattering of an X-ray photon off a quasi-free electron. Simply speaking, this process corresponds to Compton scattering in strong B-fields. Both the photon and the electron outlive the interaction. The discrete energy state occupied by the electron is called Landau level. It defines the quantized electron momentum perpendicular to the direction of the magnetic field and may change in the course of the interplay. The electron momentum parallel to the magnetic field axis is continuously distributed and reflects the temperature of the electrons. If an electron has been excited to a higher Landau level, it will de-excite to lower levels until it reaches the ground state. This is called cyclotron emission because of the photon emitted in the course of each transition. The opposite mechanism of exciting an electron to a higher Landau level by completely absorbing a photon is called cyclotron absorption. These processes will be studied in this thesis in the context of accreting neutron star binaries and will be investigated from a theoretical point of view. The corresponding cross sections and cyclotron line shapes are highly sensitive to many parameters of the medium in which they are formed. Such parameters are, for example, the density, the plasma geometry, the temperature, the plasma velocity, and of course the magnetic field strength. These properties make CRSFs good tracers of the actual physics and the environmental conditions close to the neutron star in an accreting X-ray pulsar. Furthermore, the strongly angular dependent line profiles allow

for inferences on the viewing angle with respect to the magnetic field axis.

Accreting neutron star binaries consist of a neutron star and an optical companion (see, e.g., Pringle & Rees, 1972; Davidson & Ostriker, 1973; Lamb et al., 1973; Brown, 1995; Bildsten et al., 1997; van der Klis, 2000). Both objects are moving around their common center of mass while matter flows from the optical companion onto the neutron star (Davidson, 1973). The accreting neutron stars considered here exhibit magnetic fields of the order of some 10^{12} G in the vicinity of their surface (e.g., Taam & van den Heuvel, 1986; van den Heuvel & Bitzaraki, 1995; Bildsten et al., 1997; Lattimer & Prakash, 2004). B-fields that close to the critical field strength $B_{\rm crit}$ (see Eq. 4.1) currently can not be produced in experimental setups (Lai, 2001; Blandford, 2005; Yamada et al., 2010; Takeyama et al., 2010; Fujioka et al., 2013). In the laboratory one generally distinguishes between pulsed and continuous B-fields. The former can be further divided in destructive and non-destructive groups depending on whether the magnetic coil survives the experiment. The highest magnetic field ever generated was of pulsed, destructive nature: fields exceeding 600 Tesla (6×10^6 G) have been generated by the Institute for Solid State Physics of the University of Tokyo's International MegaGauss Science Laboratory (Matsuda et al., 2002). The world record for the highest magnetic field of 730 Tesla has been established by Takeyama et al. (2010) in the MegaGauss laboratory as well. Continuous fields up to 45 Tesla can be generated in the MagLab in Florida (Hannahs & Palm, 2010). These fields are still more than ten orders of magnitude below the critical field strength. Astronomical systems therefore provide us with the only known laboratory for the study of interactions between electrons and photons in the vicinity of fields close to the critical field strength. This can be used to test the quantum-electro-dynamic theory of electrons in such strong fields experimentally. Furthermore, cyclotron lines provide a unique possibility for directly measuring the magnetic field of the line forming region — the part of the accretion column where the CRSFs are formed — of neutron stars. Their complex shapes (Nishimura, 2008; Fürst et al., 2015) contain much more information than only the strength of the magnetic field at the line forming region, as will be shown in this thesis. But only using a sophisticated physical model can this fundamental information about accreting X-ray pulsars be extracted from the measured cyclotron line profiles.

Figure 1.1 displays simulated cyclotron line shapes for different magnetic field strengths. They come in multiple harmonics differing in depth and width. The fundamental line, that is, the lowest-energy feature, is the most complex one. It often shows line wings — an increased flux before and after the fundamental line — in simulations (Isenberg et al., 1998b; Araya & Harding, 1999; Schönherr et al., 2007b; Schönherr, 2007; Nishimura, 2008). These line wings result from a combination of an inelastic scattering process and the subsequent de-excitation of the interacting electron via cyclotron emission (Nishimura, 1994). However, line wings have not been observed in the X-ray spectra of neutron stars. In general the observed spectra look less complicated than the ones from CRSF simulations (see, e.g., Fürst et al., 2013). This important issue will be resolved for the first time in this thesis, as discussed in Chapter 6. In other aspects, theory and experiment are in agreement. The fundamental line, for instance, is often found to be shallower than the first harmonic (Fürst et al., 2014).

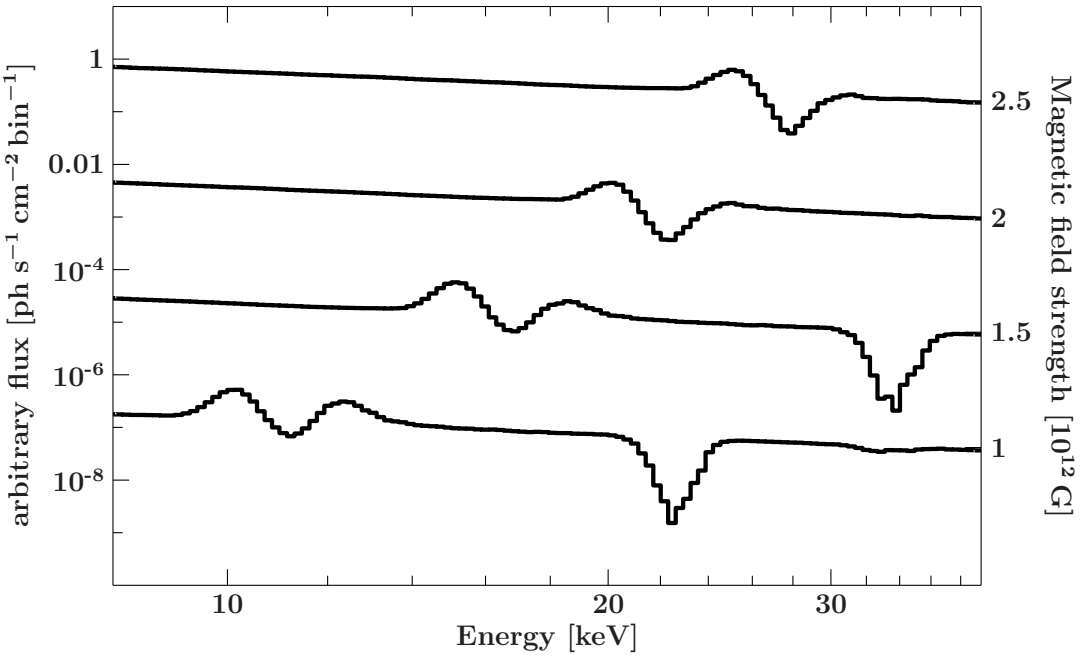

Figure 1.1.: Synthetic cyclotron lines for several magnetic fields strengths. The line energy depends on the B-field which is increasing from the bottom to the top. The line shape is determined by the complex scattering process. In general multiple harmonics can be observed.

This thesis aims at bringing together the observational side with a newly developed simulation suite for the generation of synthetic cyclotron lines for the purpose of improving the understanding of accreting X-ray pulsars. The need for a completely new simulation suite, developed from scratch, arose from the amount of newly available physical models for the accretion column structure and radiation properties (e.g., Becker & Wolff, 2007; Postnov et al., 2015a) in contrast to the scarcity of CRSF models. A new CRSF code, flexible beyond the realm of earlier implementations, was mandatory for a combination of these models with a physical CRSF model. However, its results should be combinable with any model for the continuum. This is necessary because observers still mostly resort to empirical models for the continuum since the overall spectral shape of cyclotron line sources can not always be described with the comparably new physical continuum models. Therefore the new software developed in the course of this thesis features a highly configurable CRSF Monte Carlo (MC) simulation the results of which are transferable to a — also newly developed — XSPEC (Arnaud, 1996) model. This enables the scientific community to utilize it as a fit model in a familiar way. Furthermore, it can be used for basic studies about the parameters influencing the formation of CRSFs. The simulation suite, `CycloSim`, and the associated XSPEC model, `cyclofs`, constitute a self-consistent approach of unprecedented accuracy and flexibility toward the modeling of cyclotron line profiles. Additionally, the correctness of the software is verified by comparing the simulation results and intermediate data products to the often approximative ones obtained by previous works for their comparably simple physical setups. Thus the software

is verified for setups for which previous works offer contrastable results, extends the complexity of possible setups, and provides the flexibility to be "hybridized" with arbitrary models for the continuum radiation. Its combination with physical models for the accretion column ought to give insight into the physics of the neutron star accretion column's last mile.

1.1. Outline

The remainder of this thesis is structured as follows. The astrophysical background is described in Chapter 2 in order to illustrate the greater field of research and showcase the neutron star "laboratory". The classification and the properties of accreting X-ray binaries are discussed, starting with the "big picture". Each Section is narrowing down the focus toward the surface of the neutron star, close to which the region where the cyclotron line is formed is assumed to be located. An introduction to the different ways of large-scale accretion of matter from the optical companion to the neutron star is followed by a short digression on the near-scale accretion, which is collimated by the magnetic field of the neutron star. Then, the region close to the neutron star is examined. This zone is crucial for the formation of CRSFs: the physical processes within the accretion column and at the surface of the neutron star, such as, for example, blackbody radiation, bremsstrahlung, or synchroton radiation, produce the (continuum) seed photons. These seed photons are altered by the cyclotron interactions, which are the dominant process in the strong magnetic field in the vicinity of the neutron star. The Chapter closes with observational evidence for cyclotron lines from accreting X-ray binaries. The early misinterpretation of cyclotron lines originally motivated theoretical studies such as the one performed here. Today, the improved X-ray telescopes render the analysis of the exact shapes of cyclotron lines possible for the first time, opening up new possibilities for their theoretical interpretation. A physical model is necessary for connecting the observed cyclotron line spectra with the physical parameters of the line forming region of accreting X-ray binaries. This constitutes another of the main scientific motivations for this work.

In Chapter 3 the processes responsible for the formation of cyclotron lines are discussed, together with the overall physical conditions under which they occur. Cyclotron emission, absorption, and scattering, are described in detail individually, and an overview of the various derivations of the corresponding cross sections is given. The advantages and drawbacks of the available computational formalisms are discussed in light of their implementation into a generalized MC simulation. Various data products developed in the course of and used throughout this thesis are compared to other works. This elaboration is important considering that they form the basis of the simulation code. The scattering cross sections have to be averaged over the relativistic electron parallel momentum distribution to compute the photon mean-free path. This averaging involves a numerical integration for which an adaptive Simpson scheme is utilized. The method is described and the resulting averaged cross sections are compared to literature.

The simulation itself is described in detail in Chapter 4. Information is given about the

exact procedure for the generation of synthetic cyclotron lines. Such lines are produced and compared to previous works for the purpose of verification. The complexity of the general, non-approximative, implementation results in long calculation times. Decreasing them was mandatory to make full use of the newly gained generality, that is, the ability to calculate multiple physical setups on a realistic number of CPUs. This goal led to the development of a mean free path (MFP) interpolation scheme. Tables storing the averaged scattering cross sections are calculated and can be used in the simulation to interpolate the mean free photon-path. The interpolation scheme used for making the calculations computationally manageable is laid out as well as the table structure, the necessary computational effort, and the interpolation accuracy. Furthermore, the simulation is employed to generate tables storing the response of a medium to mono-energetic photon injection. These tables are discussed together with the associated model and a comparison to the results of previous works is performed.

With a flexible simulation code in hand, the parameters typically influencing the CRSF line shapes can be studied in detail. This is done in Chapter 5. Contrary to observations, MC simulations allow for an investigation of the influence of changes of individual parameters on the line properties. Common patterns such as an increase in line depth or width by an increasing optical depth or a decreasing angle to the magnetic field axis, respectively, are investigated. This kind of deeper understanding about the influence of distinct parameters is necessary to make good decisions during the fitting of synthetic CRSF spectra to observational data.

The actual application of the fitting model to spectra of astrophysical objects is performed in Chapter 6. The model is fitted to observational data, combined with physical continuum models, used for the testing of a theoretical model, and combined with a physical continuum and a light-bending model in parallel for a study of the angular dependencies of cyclotron lines with and without the allowance for bulk velocity. The latter gives an idea of the interface to the light-bending code from Falkner et al. (2013). This combination with a relativistic light bending model allows for the self-consistent simulation of observed cyclotron lines and is employed by Falkner et al. (2017) in combination with the input continuum from Postnov et al. (2015a).

Many more astrophysical applications can be envisioned. Some examples are given in Chapter 7 after summarizing the results of this thesis.

Additional multimedia content and useful information about implementation related details can be found in the Appendices. Appendix A provides details about the electronic version of this thesis and the additional movie. This movie visualizes the MC simulation process using the photon tracing capabilities of the simulation code. A new C library, the `RCL`, has been developed by the author to reduce code repetition in the simulation suite and for providing an interface to various low level data products directly. Its modules are briefly described in Appendix B. Appendix C describes the usage of the developed software suite. It contains detailed instructions on how the mean free path interpolation tables can be calculated, how simulations can be run, and how Green's function tables can be generated from the simulation results.

2

BACKGROUND

Experiments involving the firing of α-particles from a Polonium source onto atomic nuclei (Bothe & Fränz, 1927; Bothe & Becker, 1930a,b,c) led to questions about the possible existence of a new form of radiation. Bothe & Becker (1930b) found that the new form of radiation must originate from the nuclei of the atoms hit by the α-particles. An interpretation in terms of γ-radiation was found to be problematic because it violates the conservation of energy and momentum (Curie & Joliot, 1932; Bothe, 1933). Furthermore, Curie & Joliot (1932) found that rays emitted by Lithium have a penetrating power, in lead, less than that of the γ-rays of Polonium. Instead, they were much more readily absorbed by paraffin than by lead. These results confirmed the interpretation of Chadwick (1932) that this radiation actually consists of a new kind of chargeless particles of nearly the same mass as protons, the neutrons. Only shortly after, Baade & Zwicky (1934a,b) — in the course of studying and introducing the term supernova — carried the theory of neutrons into the realm of astrophysics by proposing a star consisting of neutrons, a "neutron star", as a possible remnant of a distinct type of nova. Even earlier, Chandrasekhar (1931) calculated the maximum mass of an ideal white dwarf (see also Chandrasekhar, 1935a,b) and Landau (1932) conjectured that "the laws of ordinary quantum mechanics break down [...] when the density of matter becomes so great that atomic nuclei come in close contact, forming one gigantic nucleus.". Yakovlev et al. (2013) show that this interpretation might have taken place one year before Chadwick's successful experimental

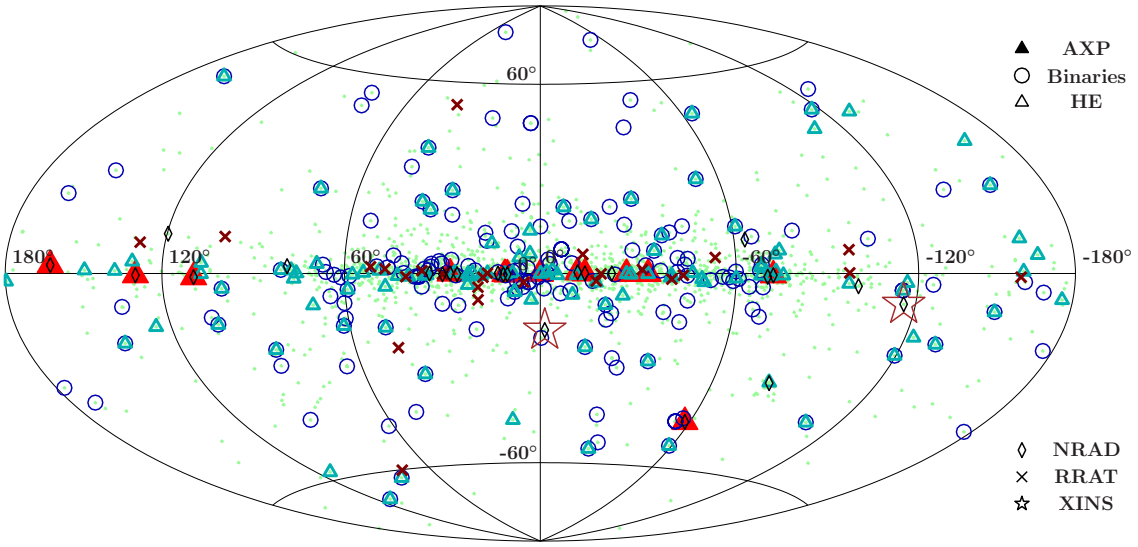

Figure 2.1.: Positions of various pulsars in galactic coordinates, using the Hammer-Aitoff equal-area projection (see, e.g., Taylor et al., 1993, for a comparison). The data are from the ATNF Pulsar Catalogue (Australia Telescope National Facility, 2005; Manchester et al., 2005).

confirmation of the existence of neutrons[1]. Landau (1932) postulated that a body with a mass greater than 1.5 $M_\odot$ is necessary for the formation of such a core (see also Landau, 1938). Oppenheimer & Volkoff (1939) and Oppenheimer & Snyder (1939) performed theoretical calculations on the mass of these — at this time purely hypothetical — objects as well. They derived a mass of ∼1.4 $M_\odot$. This value is still in use today for all kinds of calculations (e.g., Steiner et al., 2013; Bauswein et al., 2013; Oertel et al., 2015, and also this work). Recent works on constraining the neutron star mass mostly propose a slightly higher value (see, e.g., Akmal et al., 1998; Casares et al., 1998; Thorsett & Chakrabarty, 1999; Demorest et al., 2010; Lattimer, 2012; Antoniadis et al., 2013).

However, it took some time until observational evidence for the existence of neutron stars was found. Using radio measurements at a center frequency of 81.5 MHz with 1 MHz bandwidth, J. C. Bell found a source emitting ∼0.3 s pulses with a period of about 1.337 s (Bell & Hewish, 1967; Hewish et al., 1968). These signals originated from objects within the galaxy. The remarkable precision of the measured pulsations gave, after excluding the possibility of man — or even alien civilization — made origins (Drake et al., 1968), the first observational hints toward the existence of neutron stars. The source was named CP 1919[2] and its pulse structure was studied in detail by Drake (1968). A follow up survey performed by Pilkington et al. (1968) for the purpose of finding similar objects in the sky resulted in the detection of three additional pulsed sources. Drake & Craft

[1] Landau submitted his paper "On the Theory of stars" on 7 January 1932, that is more than one month before Chadwick's announcement of the discovery of the neutron but the last line of the paper says "February 1931, Zurich" (Yakovlev et al., 2013).

[2] The source was named CP 1919 in the beginning. Different additional suffixes have been used later. The source names given below generally refer to the source name given in the associated reference.

(1968b) compared the pulse shapes of all four pulsed radio sources: CP 0834, CP 0950, CP 1133, and CP 1919. They exhibited varying pulse periods of approximately 1.274 s, 0.253 s, 1.188 s, and 1.337 s, respectively. Drake & Craft (1968a) found a second periodic pulsation of the order of 10 ms in the observations of AP 2015+28 and CP 1919+22. They associated this second class of pulsations with the energy source of the pulses. The class 1 pulsations "contain a mechanism which either modulates or generates the radio emission excited basically by the class 2 energy source" (Drake & Craft, 1968a).

Gold (1968) argued that an intense gravitational field is mandatory for these sources to explain the concentration of energy deduced from the very high emission per unit emitting volume in combination with an emitting region not much larger than the distance light travels in the few milliseconds that represent the lengths of the individual pulses. As discussed by Hoyle & Narlikar (1968), the small period of 0.253 s measured for the source CP 0950+08 is close to the break up limit of 0.2 s for white dwarfs (Thorne & Ipser, 1968a,b). Together with considerations about the pulse shape and the combination of the pulsars' precise timing in conjunction with the enormous variation in amplitudes, this makes the explanation as white dwarfs implausible. Therefore the alternative interpretation of these measurements as emission from neutron stars, which were predicted theoretically before (Wheeler, 1966; Pacini, 1967; Pacini & Salpeter, 1968), marked the beginning of pulsar astronomy.

Figure 2.1 shows the positions of 2052 pulsars from the ATNF Pulsar Catalogue (Australia Telescope National Facility, 2005; Manchester et al., 2005) using a Hammer-Aitoff equal area projection (Snyder, 1987). Only pulsars with measured spin periods have been selected. They are mainly classified depending on their emission characteristics (see Australia Telescope National Facility, 2005, for details about the classification). Some pulsars are contained in multiple groups.

Neutron stars are remnants of massive stars (Prakash et al., 1997; Postnov & Yungelson, 2014), but still have a mass that is low enough to not collapse into a black hole (Truran & Cameron, 1971). They are assumed to trace the galactic plane, meaning that they are born in the spiral arms (Faucher-Giguère & Kaspi, 2006) where most stars are born and spend their lives with a slightly higher concentration close to the galactic center (Yusifov & Küçük, 2004a). Yusifov & Küçük (2004b) find the maximum galactocentric distribution of pulsars to be located at 3.2±0.4 kpc and the scale-length of this distribution to be 3.8±0.4 kpc.

As more and more pulsars were discovered, astronomers became fond of some sort of visualization scheme. It should allow for the grouping of pulsars into distinct classes, maybe even showing their evolution, similar to classification schemes for stars. In optical astronomy, Rosenberg (1910) introduced a diagram showing the apparent magnitude of stars in the Pleiades (M45) with respect to a measure for the relative strength of the calcium K line with respect to the hydrogen H_δ and H_ζ lines. This measure, effectively comparing the temperature of the stars, constitutes an *accurate reagent* for the progressive evolution of the spectral types of the stars. Effectively showing the luminosity over temperature, it has been used extensively by, and named after, Hertzsprung (1911) and Russell (1914) and

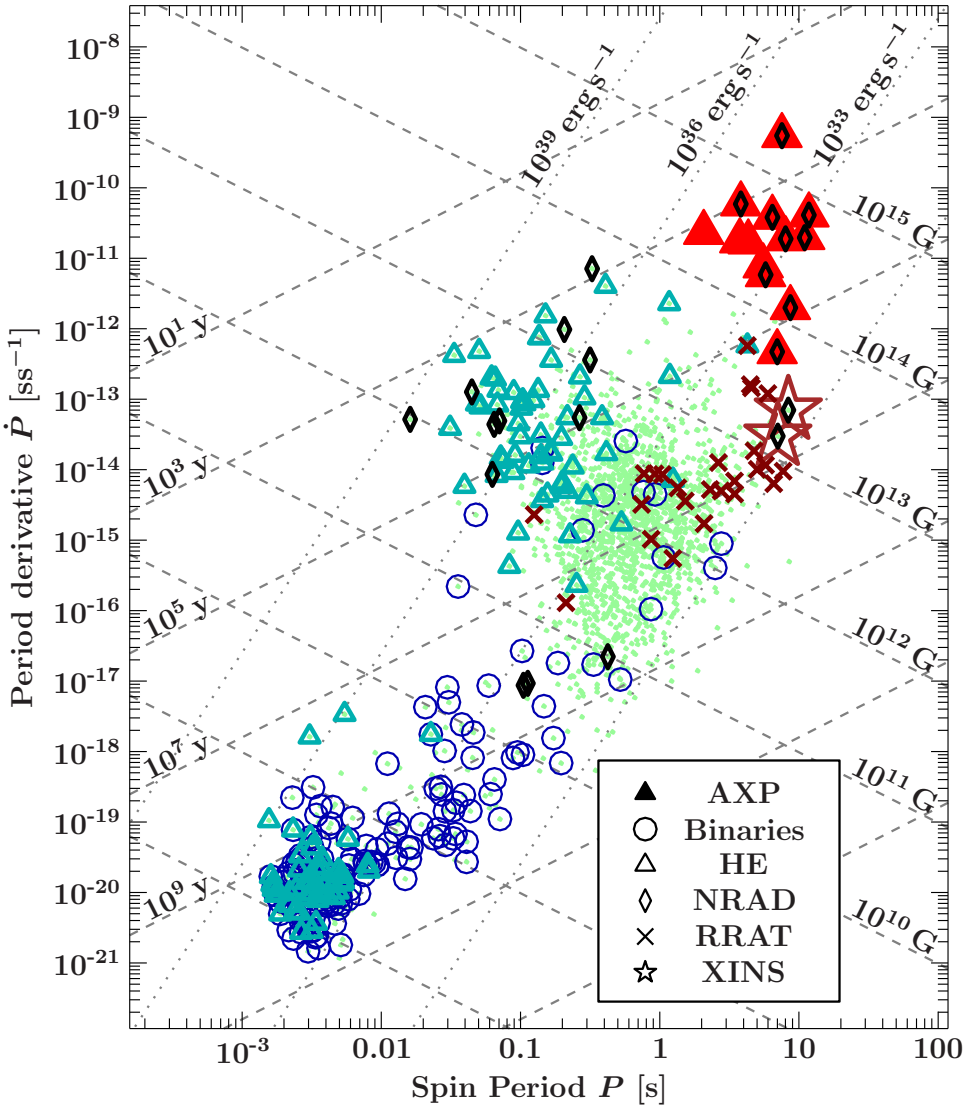

Figure 2.2.: $P\dot{P}$ diagram showing the period derivative with respect to the pulse period. The data are from the ATNF Pulsar Catalogue (Australia Telescope National Facility, 2005; Manchester et al., 2005).

is still used today for depicting the spectral evolution of stars in the optical. Neutron stars are one possible outcome of stellar evolution but can hardly be integrated in this type of diagram since their photometric temperature is difficult to determine. They would populate the very bottom of the Hertzsprung-Russell diagram, presumably at the left side, similar to where white dwarfs — another kind of stellar remnant — reside. Such a picture is difficult to justify, though, as they are just not well comparable in the optical. Furthermore, some neutron stars tend to cool more rapidly than others due to complex physical processes, such as superfluidity in the stellar interior, surface envelopes of light elements, neutrino emission processes, and, of course, the influence of the strong surface magnetic fields (see, e.g., Pethick, 1992; Yakovlev & Pethick, 2004; Page et al., 2004, 2006; Heinke & Ho, 2010;

Shternin et al., 2011). Considering their most prominent property, which actually revealed their presence in the first place, namely their pulsating nature, it seems almost obvious to classify them by their timing behavior. This is done in the $P\dot{P}$ (read "P-Pdot") diagram (see Fig. 2.2), which shows the change in pulse period, that is, the period derivative (i.e., spin down rate) with respect to the pulse period itself. In this type of diagram different types of neutron stars, such as radio pulsars, X-ray pulsars, supernova remnants, magnetars, and transient types of pulsars tend to group in, partially overlapping, regions. Furthermore, straight lines of different adapted slopes confine distinct regimes of age, luminosity, and magnetic field strength. Therefore the magnetic field can be roughly estimated by a pulsar's position in the $P\dot{P}$ diagram. This suggests a connection between the pulse period and magnetic field evolution. Many scenarios leading to an evolution of the magnetic field strength are imaginable, such as Ohmic decay, Hall drift, crustal effects, or screening of the field (see, e.g., Konar & Bhattacharya, 1997, 1999a,b; Goldreich & Reisenegger, 1992; Pons & Geppert, 2007; Sang & Chanmugam, 1987; Cumming et al., 2004; Haensel et al., 1990; Jones, 1988; Urpin & Muslimov, 1992; Hollerbach & Rüdiger, 2002, 2004; Geppert & Rheinhardt, 2002).

However, the estimates from the $P\dot{P}$ diagram should be taken with caution. They are based on some simple approximations, which are briefly described in the following (Rybicki & Lightman, 1979; Condon, 2016): By measuring the pulse period P and its time derivative $\dot{P}$, the rate at which the rotational energy is decreasing can be estimated as

$$\frac{dE_{\mathrm{rot}}}{dt} = -4\pi^2 I \dot{P} P^3 \tag{2.1}$$

where I is the neutron star's moment of inertia. It is approximately given by

$$I = \frac{2}{5} M R^2 \approx 10^{45}\,\mathrm{g\,cm^2} \tag{2.2}$$

for a canonical neutron star of mass $M = 1.4\,M_\odot$ and radius $R = 10\,\mathrm{km}$. It agrees surprisingly well with more sophisticated calculations. Worley et al. (2008), for example, derived values of $1.30–1.63 \times 10^{45}\,\mathrm{g\,cm^2}$ from nuclear constraints for a component of one particular neutron star system.

By assuming that the pulsar is loosing rotational kinetic energy solely due to magnetic dipole radiation a lower limit for the magnetic field can be estimated:

$$B > 3.2 \times 10^{19} \sqrt{\frac{P\dot{P}}{\mathrm{s}}}\,\mathrm{G} \tag{2.3}$$

Under the assumptions that the product $P\dot{P}$, or B from the considerations above, is constant and that the pulsar's initial period was much shorter than the current one, the characteristic age of a pulsar can be defined as

$$\tau \equiv \frac{P}{2\dot{P}} \tag{2.4}$$

These approximations are depicted as straight lines the $P\dot{P}$ diagram shown in Fig. 2.2. It shows the same sample of pulsars as Fig. 2.1 from the ATNF Pulsar Catalogue (Australia Telescope National Facility, 2005; Manchester et al., 2005).

The estimate of the magnetic field strength from the period and its time derivative shows — as proposed by theoretical considerations of Gold (1968) — that neutron stars have very strong magnetic fields. The origin of this magnetic field lies in the conservation of the magnetic flux of the progenitor star during the final collapse (see, e.g., Canuto et al., 1970; Ferrario & Wickramasinghe, 2006; Reisenegger, 2007; Peng & Tong, 2007; Schwarm, 2010). Ostriker & Gunn (1969) illustrate this quantitatively by giving the example of a star of radius 10^6 km and a magnetic field on the surface of 10^2 G evolving into a neutron star with radius 10 km and a surface field of 10^{12} G (see also Gunn & Ostriker, 1970; Sturrock, 1971). The possibility for much weaker fields on the order of $\lesssim 10^{10}$ G (Goldreich & Reisenegger, 1992), as well as, for much stronger fields of 10^{14}–10^{15} G (Duncan & Thompson, 1992; Woods & Thompson, 2006), has been discussed. This suggests some form of magnetic field evolution. Young neutron stars may start their life with a strong magnetic field, inherited from the progenitor star by magnetic flux conservation, and decaying over time. Goldreich & Reisenegger (1992) specifically discuss three mechanisms that may lead to a loss of magnetic field, such as, Ohmic decay, possibly enhanced by the Hall drift effect, and ambipolar diffusion. Harding & Lai (2006) favor the accretion process as an effect which might be able to explain the large reduction on a timescale of 10^9 yr. It should not be left unmentioned here that the theory of magnetic flux conservation as the dominant origin for the high B-fields of neutron stars has been challenged in favor of theories postulating a dynamo driven origin of the field (Akiyama et al., 2003; Thompson & Duncan, 1993; Blandford, 2005; Ferrario & Wickramasinghe, 2008; Kholtygin et al., 2011).

2.1. Accreting X-ray Binaries

The leap from radio to X-ray observations revealed a special group of neutron stars. Contrary to isolated neutron stars, they have a companion star that donates matter to the neutron star. Therefore two characteristic periods are observable: the spin period gives rise to short pulsations similar to the ones observed from radio pulsars. The orbital period is caused by the movement of the stars around their common center of mass. Figure 2.3 shows an example for observational evidence of the former. An example for the long term variability of an accreting X-ray binary is shown in Fig. 2.4.

On June 18, 1962 the Geiger counters on board of an Aerobee rocket measured a “considerable flux of radiation [...] that has been identified as consisting of soft x rays” (Giacconi et al., 1962). The experiment was originally intended for studying fluorescence of X-rays

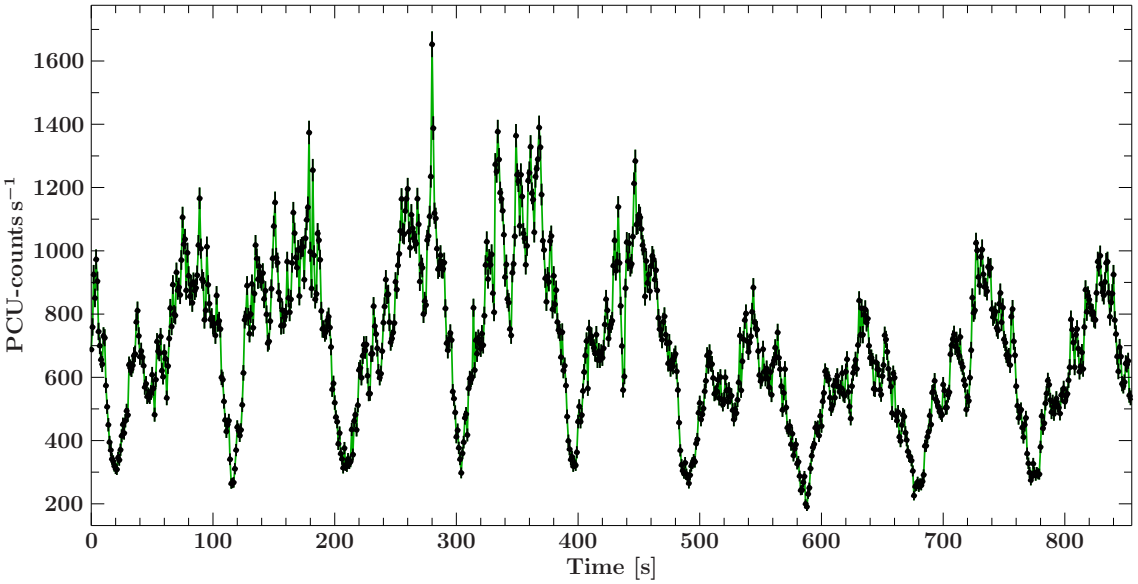

Figure 2.3.: X-ray pulsations from the accreting X-ray binary source GRO J1008−57 measured with *RXTE*-PCA (3–60 keV). The plot is based on a script from Kühnel (2016, priv. comm.).

produced on the lunar surface by X-rays from the sun. It revealed soft X-rays with energies in the detector range of 1.6–6.2 keV from a source presumably without the solar system. The source discovered was Sco X-1. It was found at the same position using experiments with a better spatial resolution (Bowyer et al., 1964; Giacconi et al., 1964). Giacconi et al. (1965) found that the spectrum of this source is not consistent with blackbody radiation. Later, Giacconi et al. (1971) found evidence for periodic pulsations in the X-ray emission from Cen X-3 in *UHURU* data. Schreier et al. (1972) found that the regular changes in intensity between two distinct levels with a period of 2 days goes in hand with continuous variations of the short pulsations — of 4.8 s — within the same cycle. Since this behavior is suggestive of a physical connection between these two periods (see also Corbet, 1986), Schreier et al. (1972) proposed the interpretation of Cen X-3 as a binary system consisting of a compact object and a massive companion star. This view was established further as a similar behavior, but with a 1.7 day cycle in conjunction with 1.24 s pulsations, was found by Tananbaum et al. (1972) in X-ray observations of Her X-1. It was the second system to fit into this new group of X-ray sources, the accreting X-ray binaries. Her X-1 mainly differs from Cen X-3 by its additional 35-day cycle. There were many attempts to explain the origin of this periodicity. Tananbaum et al. (1972) proposed several mechanisms to account for the large fraction of time — 27 out of 36 days — in which the source is in its off-state, contrary to the 9-day interval in which the pulsations are observable: the system could, for instance, be a three-body system with a highly eccentric orbit. Alternatively, the compact object might be embedded in the atmosphere of a pulsating central star, such that the X-rays from the compact object are absorbed by the atmosphere whenever the extension of the latter is sufficient. Another explanation is the break of the accretion flow due to instabilities at the Roche lobe. The geometrically constrained visibility of

strongly beamed radiation from the pulsar might be another possible explanation. Petterson (1977a) explained the 35-day cycle with a tilted accretion disk, using multiple model components: an optically thick accretion disk, an Alfvèn shell, a hot optically thin corona, and a time-varying accretion stream. The model has been discarded by Truemper et al. (1986), who confirmed the 1.24 s pulse periodicity using *EXOSAT*. Bai (1981) elaborate on reasons for this additional periodicity as well. Staubert et al. (2006) studied the long term behavior of Her X-1 (1971 – 2005) and found that the 35-day cycle and the 1.24 s pulse period both vary in a highly correlated way (see also Staubert, 1997; Staubert et al., 2000). Middleditch & Nelson (1976) found that optical pulsations, near to, but not generally identical to, the 1.24 s pulse period are present for particular values of the binary and 35-day phases. Similarly, Gerend & Boynton (1976) found that the optical light curve of Her X-1 and its optical companion HZ Herculis varies in a systematic fashion over the 35-day cycle. The characteristics of the optical and X-ray emission from Her X-1 and its companion can be explained by a tilted-twisted precessing accretion disk (Katz, 1973; Shakura et al., 1999; Scott et al., 2000; Leahy, 2002). Occultations of the line of sight by such a disk influence the measured flux (Gerend & Boynton, 1976). The tilt might result from an instability of the response of the disk to the illumination by the central source and will cause the precessing of the disk (Wijers & Pringle, 1999). This radiation induced warping can form a precessing reasonably stable disk in binary X-ray sources (Pringle, 1996; Maloney et al., 1996). The 35-day cycle of Her X-1 and the peculiar behavior of other individual sources will not be discussed here in further detail since it is only marginally relevant for the science of CRSF formation, which takes place much closer to the neutron star. Instead it serves the purpose of demonstrating the complexity arising in the modeling of accreting neutron star binaries. For more recent works and an in depth discussion on this matter the work of Staubert et al. (2009, 2013, 2014, and references therein) is highly recommended. In the following, only general properties of all accreting X-ray binaries are investigated for providing the astrophysical background and terminology for the scientific interpretations in the following sections.

The X-rays emission of accreting X-ray binaries is mainly powered by the gravitational energy released during the accretion of matter from the companion star (Lamb et al., 1973). A mass accretion rate of $10^{-9}\ M_{\odot}\mathrm{yr}^{-1}$ is required to obtain an X-ray luminosity of $10^{37}\ \mathrm{ergs\,s}^{-1}$ from the gravitational infall onto the surface of a 1 $M_{\odot}$ neutron star (Davidson & Ostriker, 1973). Due to the conservation of angular momentum the matter can not fall directly onto the neutron star. Instead, the geometry of the binary system and the properties of the donator star lead to diverse accretion mechanisms.

Accretion-powered X-ray pulsars appear to come in three different classes (Blair & Candy, 1985): those with a massive OB — and therefore comparably young — star as companion are assumed to accrete largely via Roche-lobe overflow or wind accretion. In the first scenario the companion star "fills" its Roche-lobe (see, e.g., Postnov & Yungelson, 2014) and starts losing mass via the gravitational saddle point region in between the two components (Savonije, 1979). In the second case, stellar winds drive the matter toward the compact object if the companion is sufficiently massive to have such a strong stellar wind

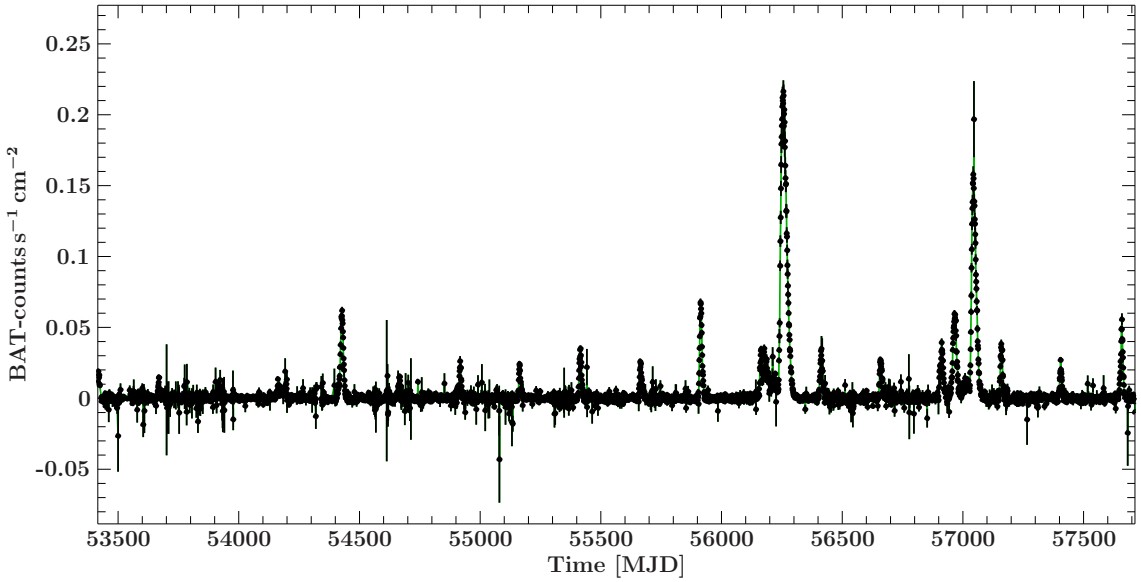

Figure 2.4.: Long term variability of GRO J1008−57 as measured with *Swift*-BAT (Krimm et al., 2013). Periastron passages of the neutron star lead to accretion and regular X-ray outbursts (Kühnel et al., 2013). The plot is based on a script from Kühnel (2016).

(Davidson & Ostriker, 1973). Figures 2.5 and 2.6 illustrate this qualitatively[3]. Sources typically associated with wind accretion are GX 301−2 or Vela X-1, while Cen X-3, SMC X-1, or LMC X-4, with their high luminosities are associated with Roche-lobe overflow (Nagase, 1989). They form the group of high mass X-ray binaries (HMXBs), named after their companion star's high mass. The third type of X-ray binaries in this class is also associated with wind accretion according to Nagase (1989): the Be-X-ray binaries, which have a Be-star companion and are mostly of transient nature. Typical examples are 4U 0115+63, A 0535+26, and GX 304−1. Figure 2.4 shows the long term *Swift*/BAT light curve of GRO J1008−57, which is another example of this group. Coe et al. (1994) found its optical counterpart to be a Be-star. Levine & Corbet (2006) derived the orbital period to be 248.9±0.5 d from data of the All-sky Monitor (ASM) on board of the *Rossi X-ray Timing Explorer (RXTE)*. Kühnel et al. (2013) improved the orbital period and the time of periastron passage by analyzing all *RXTE* observations available at that time in addition to data from *Swift* and *Suzaku* and found GRO J1008−57 to be an "(almost) predictable transient X-ray binary" (Kühnel et al., 2013). As the transient behavior of these sources caused by their excentric orbit distinguishes them from the previously mentioned sources a third distinct accretion channel is illustrated in Fig. 2.7. The outbursts are typically occurring during the periastron passages where the density may be enhanced due to the presence of an equatorial Be-disk. GX 304−1 is of this type (Mason et al., 1978; Parkes et al., 1980; Priedhorsky & Terrell, 1983; Pietsch et al., 1986; Postnov et al., 2015b). Finally, there is the group of low mass X-ray binaries (LMXBs), mainly accreting via Roche-lobe overflow, often with an intercalated disk. The probably most famous representative is Her X-1. It is

[3]None of the figures showing the accretion mechanisms are to scale. They merely serve the purpose of illustration.

also the first source in which a cyclotron line has been detected as described in Section 2.3.

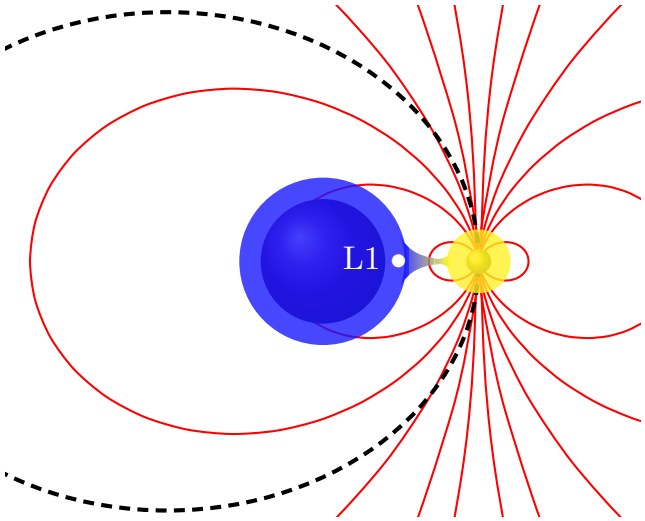

Figure 2.5.: Illustration of the Roche lobe overflow accretion mechanism. Matter is transferred to the neutron star via the Lagrange point L1.

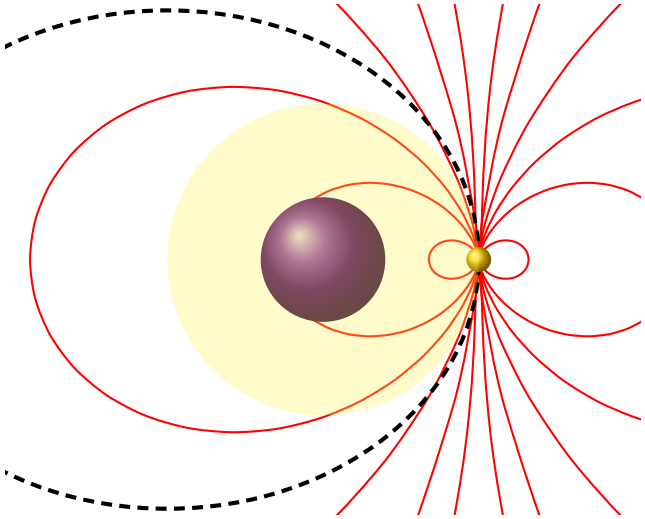

Figure 2.6.: Illustration of the wind accretion mechanism. The stellar wind of the companion star provides matter to the neutron star. Close to the neutron star the matter will couple to the magnetic field, depicted here as a simple dipole field.

Contrary to the case of isolated neutron stars, the spin period of a neutron star in a binary system is affected by the accretion flow from the companion star onto the compact object (Ghosh & Lamb, 1979). Therefore another type of classification scheme (see Section 2 for a scheme using the pulse period and its derivative) becomes useful for the classification of accreting X-ray binaries: the Corbet diagram (see, e.g., Fig. 2.8) shows the rotational

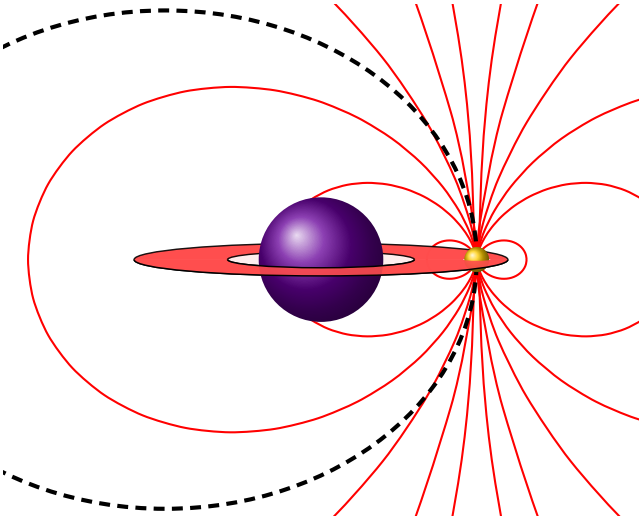

Figure 2.7.: Illustration of a Be accretion scenario. The neutron star accretes matter from the optical star's disk while crossing it.

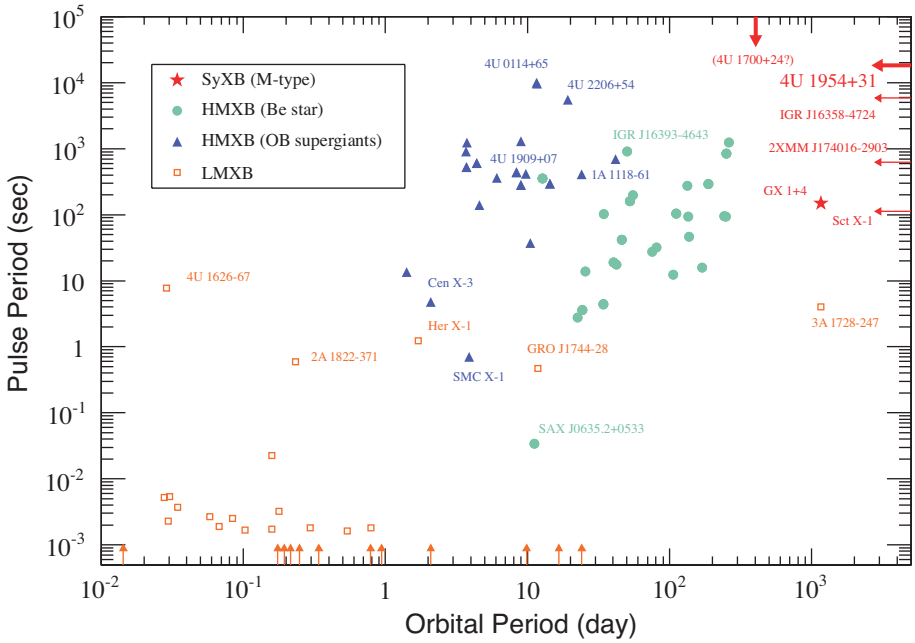

Figure 2.8.: Corbet diagram showing the rotational period of neutron stars in a binary system with respect to the orbital period of the binary system (Enoto et al., 2014).

(pulse) period of a neutron star with respect to the orbital period of the binary system formed by the neutron star and its companion (Corbet, 1984, 1985). Corbet (1986) divided the HMXBs into three classes: binaries with a Be companion, which show a correlation between the spin and the orbital period (see also Townsend et al., 2011, for a study about the correlation between the orbital period and the eccentricity of the binary system), binaries with a supergiant companion, which populate the upper left corner of the Corbet diagram, and a third class of binary systems with a supergiant or main-sequence companion star,

which possibly fills its Roche lobe, and relatively short pulse periods. The Corbet diagram in Fig. 2.8 shows several classes of X-ray binaries using this scheme. The relatively new class of symbiotic X-ray binaries (SyXBs) consists of binaries with an X-ray bright neutron star and an M-type giant companion (Enoto et al., 2014). These sources share properties of LMXBs and HMXBs in that the mass of the companion would classify them as LMXBs but the spectral and timing behavior, especially its very large orbital period compared to common LMXBs, contradicts such an interpretation. They are not further discussed here as most symbiotic X-ray binaries are assumed to have a white dwarf instead of a neutron star as compact component (Chakrabarty & Roche, 1997).

As the accreting matter is approaching the neutron star an accretion disk may form, depending on the details of the magnetospheric structure (Lamb et al., 1973; Pringle, 1981). It does not have to be flat but might be twisted instead (Petterson, 1977b,c). Petterson (1977a) proposed such a twisted disk model for Her X-1. The matter is then transferred from the disk, along the magnetic field lines, toward the poles of the neutron star. For a fast rotating star the accretion might not be continuous but result in some rapid but regular periodic effect (Pringle & Rees, 1972). Pringle & Rees (1972) further find that if accretion is taking place and a disk is formed the matter falling in from the disk speeds up the stellar rotation. This has been confirmed by Istomin & Haensel (2013) for disk accretion under the influence of a rotating magnetic field.

2.2. Accretion Column

As the accreting matter further approaches the rotating neutron star the influence of the magnetic field becomes larger.

2.2.1. Magnetospheric Accretion

The surface within which the ionized gas is pulled around by the star's magnetic field is called Alfvén surface (Ridpath, 2004) named after the Nobel Price winner Hannes Alfvén who studied the magneto-hydrodynamics of magnetized plasma (see, e.g., Alfvén, 1963, 1967). Strictly speaking, the Alfvén surface (see also Mészáros, 1992, Chap. 7.2) is defined as the surface where the Alfvén speed equals the advection velocity (Guilet et al., 2011). Within this surface the magnetic field tries to bring the gas into co-rotation with the star (Campbell, 1997). But as Ghosh et al. (1977) pointed out, the matter inside the Alfvén surface does not generally co-rotate with the star but rather moves along field lines in the frame co-rotating with the star. These flows might actually rotate in a sense opposite that of the net angular momentum flux toward the star. The Alfvén surface is generally understood as the boundary at which the magnetic field of the neutron star first dominates the flow of matter toward the star and can not lie outside of the radius where the pressure in the magnetosphere balances the pressure of the infalling matter (Lamb, 1975). Davidson

& Ostriker (1973) provide an estimate of such a magnetospheric radius of a neutron star

$$R_m \approx \left(\frac{B_0^2 R_0^6}{4 S_{\rm accr} c \sqrt{R_G}} \right)^{2/7} \tag{2.5}$$

with radius R_0 and surface magnetic field B_0 from the equilibrium of the magnetic pressure $B_m^2/8\pi$, with $B_m = B_0 R_0^3/R_m^3$, and the ram-pressure

$$\rho v_{\rm infall}^2 \approx S_{\rm accr} c \sqrt{R_G}/2\pi R_m^{5/2} \ , \tag{2.6}$$

where $R_G = G m_X/c^2$ is the gravitational radius:

Lamb et al. (1973) estimate its radius to be ~1000 km for typical neutron star parameters by equating the energy density of the magnetic field with the kinetic energy density of the accreting matter. They argue that this is, apart from a factor of order unity, equivalent to equating the pressure of the stellar field to the pressure of the accreting matter including both ram pressure and thermal pressure. The expression for the Alfvén radius resulting from their approach becomes

$$r_{\rm A} \approx 2.6 \times 10^8 \mu_{30}^{4/7} \left(\frac{M}{M_\odot} \right)^{1/7} L_{37}^{-2/7} R_6^{-2/7} \, {\rm cm} \ , \tag{2.7}$$

where μ_{30} is the magnetic momentum of the neutron star in units of $10^{30}\,{\rm G\,cm^3}$, and L_{37} and R_6 are its luminosity in $10^{37}\,{\rm erg\,s^{-1}}$ and radius in 10^6 cm, respectively. For the case of a rapidly spinning neutron star they provide an alternative approximation based on the rotational energy density instead of the magnetic energy density. The Alfvén radius then becomes

$$r'_A \approx 2.6 \times 10^8 \mu_{30}^{4/13} P^{4/13} \left(\frac{M}{M_\odot} \right)^{3/13} L_{37}^{-2/13} R_6^{-2/13} \, {\rm cm} \ , \tag{2.8}$$

with the rotational period P.

Inside the Alfvén surface the matter is more and more coupling to the field lines and is funneled toward the poles of the neutron star, forming two accretion columns, one at each magnetic pole (Davidson, 1973). The matter is then stopped at the neutron star surface, producing hot spots, which are heated by the kinetic energy released by the impact of the matter on the neutron star surface. The abrupt halt results in bremsstrahlung emission, which, together with the thermal blackbody radiation, produces X-ray photons. Davidson & Ostriker (1973) proposed a model where the in-falling material is stopped by the radiation pressure from the thermal mound before hitting the surface. Basko & Sunyaev (1975), who studied the radiative transfer in a strong magnetic field of compact objects as well, find that the light pressure may exceed the gravitational acceleration by two orders of magnitude if the pulsar luminosity approaches the local Eddington rate at the neutron star (see also Staubert et al., 2007), $L_x \sim 10^{37}\,{\rm ergs^{-1}}$. This limiting luminosity was further investigated by Basko & Sunyaev (1976) for two different accretion scenarios, the hollow column, and the filled column scenario.

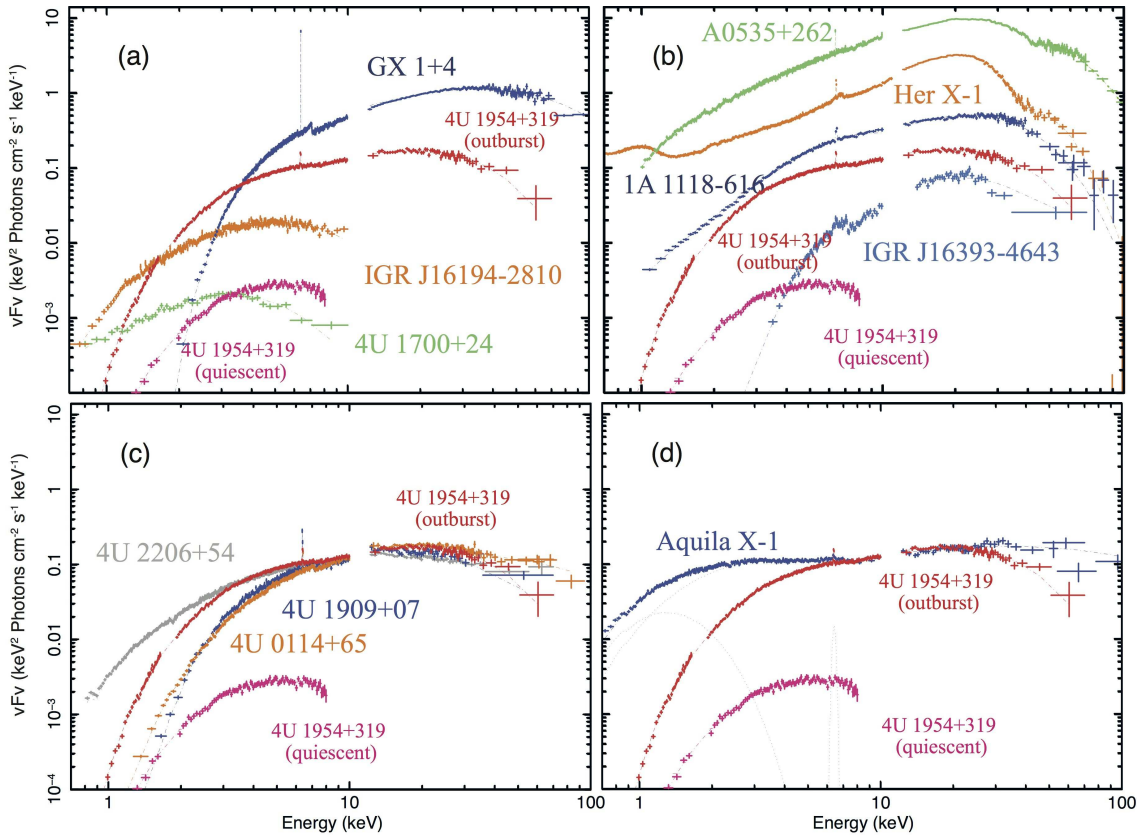

Figure 2.9.: Figure from Enoto et al. (2014) showing X-ray continua of four different categories of neutron star binaries: (a) symbiotic X-ray binaries, (b) CRSF sources, (c) long period pulsars, and (d) the LMXB Aquila X-1 (Sakurai et al., 2012) in the low/hard state. Two spectra of the symbiotic X-ray binary 4U 1954+319 are shown in all panels: one in quiescence and one measured during an outburst.

2.2.2. Empirical Continuum Modeling

Multiple processes are generating and altering the spectral shape of the X-ray continuum radiation in an accretion column and at the hot spot on the neutron star surface. Figure 2.9 shows spectra of several neutron star binaries. They exhibit different slopes and features — such as differently pronounced iron emission lines — but have a high energy cut off in common, meaning that the flux decreases above some cut off energy. At medium energies the spectral shape can often be described by a powerlaw. No physical model covering the parameter ranges of accreting X-ray pulsars has been found so far. For this reason mostly empirical models are used for the data analysis of accreting X-ray binaries. These include:

Power law (POWER LAW)

$$F(E) = AE^{-\Gamma} \tag{2.9}$$

Power law with high energy cut off (HIGHECUT)

$$F(E) = AE^{-\Gamma} \begin{cases} 1 & (E \leq E_{\text{cut}}) \\ e^{-(E-E_{\text{cut}})/E_{\text{fold}}} & (E > E_{\text{cut}}) \end{cases} \tag{2.10}$$

Power law with high energy exponential cut off (CUTOFFPL)

$$F(E) = KE^{-\Gamma} e^{-E/\beta} \tag{2.11}$$

Fermi-Dirac cut off powerlaw (FDCUT)

$$F(E) = AE^{-\Gamma} \frac{1}{1 + e^{-(E-E_{\text{cut}})/E_{\text{fold}}}} \tag{2.12}$$

Negativ-Positive power law Exponential (NPEX)

$$F(E) = A(E^{-\Gamma_1} + BE^{+\Gamma_2}) e^{-E/E_{\text{fold}}} \tag{2.13}$$

All of the above empirical models have some kind of photon index Γ responsible for the slope of the continuum. The cut off energy E_{cut} marks the points where the spectrum is bent down. A high energy cut off is observed in many accreting X-ray binaries (see, e.g., Pravdo et al., 1978; White et al., 1983; Kreykenbohm et al., 1999; Reig & Roche, 1999; Chakrabarty et al., 2014; Jaisawal & Naik, 2016; Breed et al., 2016). The folding energy describes the curvature of this down bending of the spectrum. Although there is no physical justification for using these functions, they tend to fit many observed continua very well. One has to be careful, though, with interpreting the results as unique solutions. For instance, the NPEX model introduced by Mihara (1995), consisting of two exponentials, gave rise to some criticism in the past: its usage lead to a perceived anti-correlation between the fundamental cyclotron line energy and the luminosity (Mihara et al., 2004; Tsygankov et al., 2007). Müller et al. (2013) show that the origin of this anti-correlation is the unphysical interplay of parameters of the cyclotron line with the NPEX continuum model. Such problems further motivate the investigation of physical models for the X-ray continuum from accreting neutron star binaries.

2.2.3. Physical Continuum Modeling

Becker & Wolff (2005a) presented the first *ab initio* calculation of the X-ray spectrum associated with the physical accretion scenario suggested by Davidson (1973), in which the accreting gas passes through a radiative, radiation-dominated shock before settling on the surface of the star (Becker & Wolff, 2005b). A shock builds as soon as the radiation flux in the column becomes super-Eddington, meaning that the X-ray luminosity (Becker

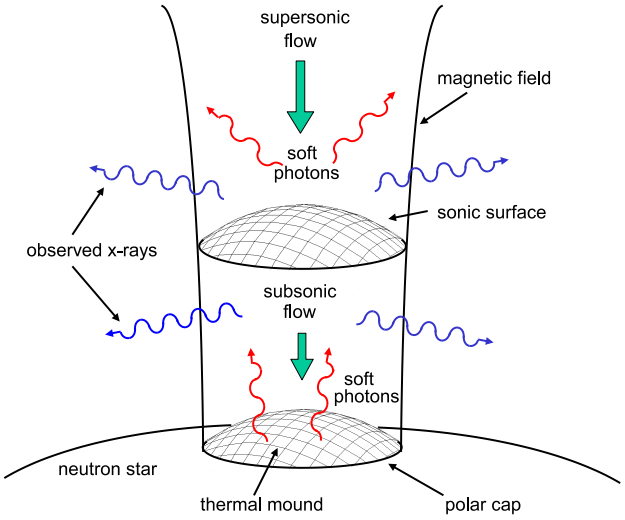

Figure 2.10.: Column model from Becker & Wolff (2007, Fig. 1 therein). Matter is falling onto the polar cap of a neutron star. Seed photons are produced within the column via bremsstrahlung and cyclotron emission. The thermal mound emits additional blackbody seed photons.

& Wolff, 2007)

$$L_X = \frac{GM_*\dot{M}}{R_*} \tag{2.14}$$

becomes comparable to the critical luminosity (Becker, 1998; Basko & Sunyaev, 1976; Becker & Wolff, 2007)

$$L_{\rm crit} \equiv \frac{2.72 \times 10^{37}\sigma_{\rm T}}{\sqrt{\sigma_{\parallel}\sigma_{\perp}}} \frac{M_*}{M_\odot} \frac{r_0}{R_*} \,{\rm ergs\,s^{-1}} \,, \tag{2.15}$$

with mass accretion rate $\dot{M}$, polar cap radius r_0, stellar mass M_*, stellar radius R_*, gravitational constant G, and the scattering cross sections $\sigma_{\parallel}$ and $\sigma_{\perp}$, parallel and perpendicular to the magnetic field axis, respectively. In the case of pure Thomson scattering both cross sections equal the Thomson scattering cross section $\sigma_{\rm T}$, that is, $\sigma_{\parallel} = \sigma_{\perp} = \sigma_{\rm T}$. Becker & Wolff (2005a) show that such an accretion column with a blackbody source at its base is able to reproduce the power-law spectra observed in low-luminosity accreting X-ray binaries such as X Persei. The spectral shape essentially results from the Comptonization of thermal radiation originating from the hot spot on the neutron star surface due to the bulk motion of the downfalling plasma (bulk Comptonization). Additional seed photons are produced within the accretion column by cyclotron radiation and bremsstrahlung. The model has the following physical parameters: the column radius r_0, the temperature at the top of the thermal mound T_0, and the accretion rate $\dot{M}$, provided that the stellar mass and radius are given. Becker & Wolff (2007) generalize this physical continuum model by introducing thermal Comptonization to enable the modeling of spectra with an exponential high energy cut off and a flat shape at lower energies. Such a shape cannot be modeled using the pure bulk Comptonization model but has been observed in bright sources such

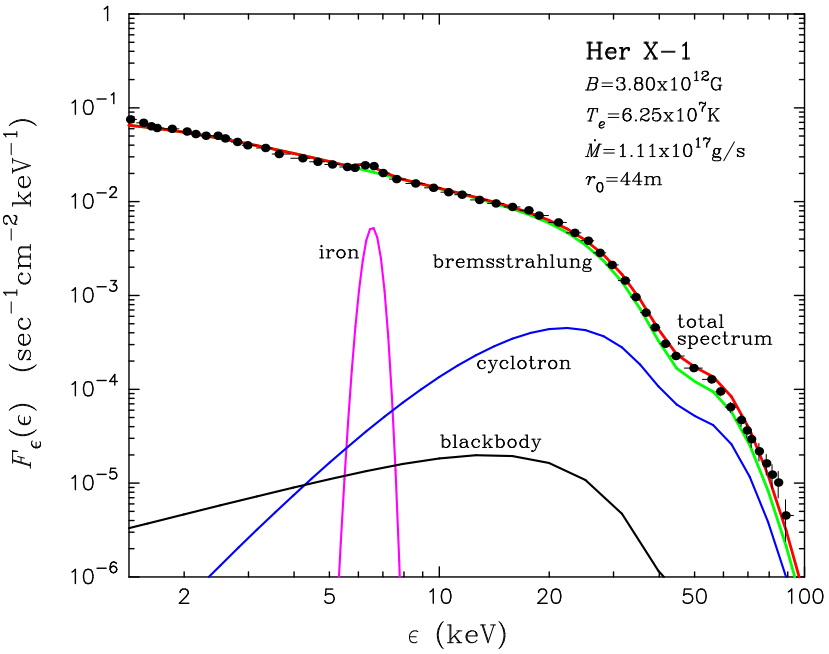

Figure 2.11.: Figure from Becker & Wolff (2007, Fig. 6 therein): The total spectrum and the individual components due to Comptonized bremsstrahlung radiation, Comptonized cyclotron emission, Comptonized blackbody radiation, and the iron emission line feature.

as Her X-1 and Cen X-3 (White et al., 1983). It is based on several physical seed photon components, mainly blackbody, cyclotron radiation, and bremsstrahlung. The general picture is the same as the one described before (see, e.g., Davidson & Ostriker, 1973; Basko & Sunyaev, 1975, 1976) and is illustrated in Fig. 2.10. The down-falling plasma is stopped by the radiation pressure limiting the maximum luminosity. The thermal Comptonization is included in the model by incorporating the full Kompaneets operator (Kompaneets, 1957) into the transport equation. The resulting Green's functions are convolved with seed photons, generated throughout the column by bremsstrahlung and cyclotron radiation, and backbody emission at the surface of the thermal mound. The model has been technically revised and applied to Her X-1 by Wolff et al. (2016). Ferrigno et al. (2009), Farinelli et al. (2012), and Farinelli et al. (2016) offer the alternative implementations of the BW07 model `beckerwolf`, `compmag`, and `xscompmag`, respectively. The physical setting is the same, but the implementation differs in numerical methods. See Hemphill et al. (2017) for a comparison to the recent implementation by Wolff et al. (2016). Figure 2.11 shows the total spectrum for a set of parameters for Her X-1. It is strongly dominated by the bremsstrahlung component. The same parameters are used in Section 6.3 for the combination of this physical continuum model with the physical cyclotron line shape model developed in the course of this thesis. Apart from using the total column integrated spectrum, that is, using the currently available XSPEC model implementations, this comparison makes use of a preliminary height dependent implementation based on tabulated model spectra provided by Becker (2014).

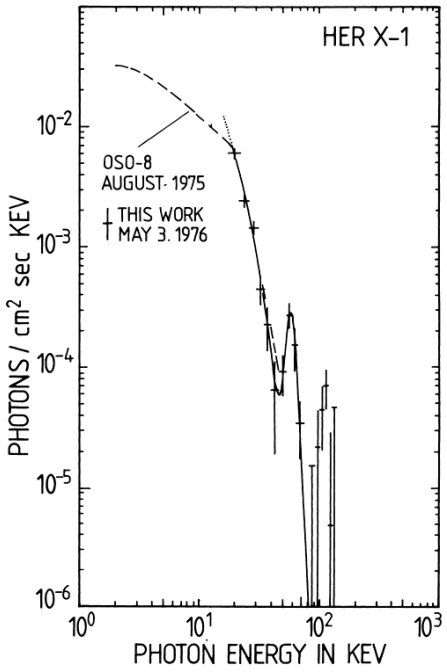

Figure 2.12.: First cyclotron line ever measured. The figure from Truemper et al. (1978) shows the X-ray spectrum from Her X-1 with its famous cyclotron line.

2.3. Cyclotron Lines

Cyclotron lines were first discovered by Truemper et al. (1978) in the X-ray spectrum of Her X-1 (see Fig. 2.12). It has been unclear in the beginning whether the observed feature is an emission line at 52 keV or an absorption line at 38 keV (Voges et al., 1982). The discovery was received by the scientific community with large interest. Daugherty & Ventura (1977) studied the structure of cyclotron lines and their higher harmonics. Focusing on the emission process they discussed the probability for populations of electrons above the ground state. The influence of the plasma temperature has been studied as well and has been found to be of large influence. Bonazzola et al. (1979) calculated theoretical spectra suitable to roughly resemble the spectra of the observed cyclotron line in Her X-1. They also discussed the CRSF process as an origin for the cooling of electrons. In a similar manner, Wasserman & Salpeter (1980) studied the radiative transfer of cyclotron line photons through optically thick atmospheres. Bonazzola et al. (1979) deduced a maximum temperature of 50 keV from the line width of the cyclotron feature which was at this time generally believed to be an emission line (Mészáros & Ventura, 1978). They inferred that the cyclotron line could not be generated by thermal excitation. In their study of alternatives they show that combined absorption and emission, namely resonant scattering, dominates the radiation transfer responsible for the formation of cyclotron lines. Also, Bonazzola et al. (1979) provide a simple cyclotron spectral fit model. They obtained a good fit to the measured Her X-1 spectrum with a cyclotron energy of $\hbar\omega_B = 33.2\,\mathrm{keV}$, corresponding to a magnetic field of $B = 2.83 \times 10^{12}\,\mathrm{G}$. Melrose & Zhelezniakov (1981) found that

the cyclotron line in Her X-1 — still interpreted as an emission line — is compatible with thermal emission from a hot spot with a temperature of $T \approx 25\,\mathrm{keV}$. Later it was shown that the line is in absorption instead (Nagel, 1980; Wasserman & Salpeter, 1980). Nagel (1981) studied the cyclotron line in Her X-1 using non-relativistic, polarization-, angle-, and energy-depend cross sections as an input for their transfer equation. They used Feautrier's method (Mihalas, 1978) and their results further strengthened the interpretation of the cyclotron line in Her X-1 as an absorption line.

Other source types have been considered as CRSF sources as well. Harding & Preece (1989) consider the possibility of measuring cyclotron lines in gamma ray burst spectra. Such a possibility has been further studied, for instance, by Alexander et al. (1989). Magnetars have an even larger magnetic field than accreting X-ray binaries and might also exhibit CRSFs (Fernández & Thompson, 2007; Nobili et al., 2008a,b). This work is about neutron star binaries only, but most results can easily be transferred to other types of objects with strong magnetic fields.

A possible variation of the cyclotron line energy with the orbital and the pulse phase has been a subject of discussion from the very beginning of CRSF research. Voges et al. (1982) show sinusoidal fits to the combined spectra from *HEAO 1*/A-4 and the MPI/AIT balloon-detector observations of Her X-1 with respect to the 1.238 s spin phase. Klochkov et al. (2008) found the relative amplitude of the cyclotron line centroid energy of the same source measured by *INTEGRAL* to vary by 25%. They state that a simple change of the height of the line forming region — and therefore a change in magnetic field strength and line energy — requires a variation by 1.1 km under the assumption of a dipole magnetic field and a neutron star radius of 10 km. Staubert et al. (2007) analyzed *RXTE* data for the variability of the CRSF under the aspect of different accretion regimes. They find a positive correlation of the cyclotron line energy with the maximum flux of the respective 35-day cycle. Focusing on the accretion column dynamics, Becker et al. (2012) investigate the positive and negative correlations between luminosity and CRSF energy with their model for a height-, and — due to the equilibrium between radiation- and ram-pressure — luminosity-dependent line forming region. It explains the observed variation in cyclotron line energies by changing heights of the CRSF line forming region within the accretion column. A completely different view on CRSF formation and its correlation with luminosity was proposed by Poutanen et al. (2013). They conjecture that the cyclotron lines are formed in an atmosphere layered around the neutron star instead of the accretion column. In their model continuum radiation from the accretion column, beamed down due to the bulk velocity of the falling plasma, is reflected by this atmosphere, which is imprinting the CRSFs. The correlation of luminosity and CRSF energy is explained by a variation of the illuminated fraction of the stellar surface. This scenario will be discussed in Section 6.5 and tested using the simulation developed in the course of this thesis.

Cyclotron lines have now moved even more to the focus of observers' attention because X-ray telescope can resolve CRSF shapes for the first time. The increased sensitivity of X-ray telescopes also leads to a growth of the number of known CRSF sources, currently 21. Furthermore, the polarization depend treatment of CRSFs becomes more important because X-ray polarization measurements are becoming technically realizable. This underlines the

importance of models for the line formation as the one laid out in this thesis.

3
Theory of Cyclotron Processes

In the following, the cyclotron processes in strong magnetic fields on the order of 10^{12} G are discussed together with the corresponding cross sections used for their implementation in the MC simulation code. The terminology and assumptions used in later Chapters are also introduced, and an overview is given over the various code versions and individual works related to the calculation of data products for the MC simulation of cyclotron lines.

Electrons in strong magnetic fields, approaching the critical field strength, $B_{\mathrm{crit}} = 44.14 \times 10^{12}$ G, occupy Landau levels, that is, their momenta perpendicular to the B-field are quantized (Canuto & Ventura, 1977). Their momenta parallel to the field, however, can take any value and their distribution can be interpreted as the plasma temperature of the medium (Harding & Daugherty, 1991, and references therein). The higher the temperature becomes the more electrons have a large momentum parallel to the B-field axis (Schwarm et al., 2017b). As laid out, for example, by Canuto & Ventura (1977), cyclotron lines come in multiples (see, e.g., Fig. 1.1). The feature at the lowest energy is called the fundamental line. The higher lines are called harmonics. The fundamental line originates from the transition of electrons from the ground state to the first excited Landau level. Its multiples result from transitions to higher Landau levels. There is no upper limit for the number of lines but their depths decrease toward higher energies. At the same time the effective area of currently available X-ray telescopes is significantly reduced at high energies (see, e.g., Madsen et al., 2015). 4U 0115+63 is the record holder in terms of the number of CRSFs observed. Five lines have been detected in its spectrum (Heindl et al., 2000). The excited electron subsequently migrates back to the ground state under the emission of *spawned*

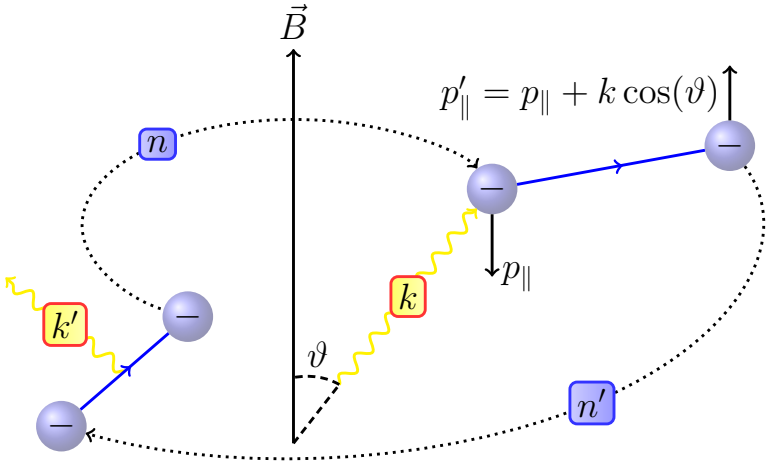

Figure 3.1.: Schematic illustration of the absorption of a photon with energy k, and angle ϑ to the magnetic field axis, by an electron in Landau level n with initial parallel momentum $p_\parallel$. The electron is excited to Landau level n' in the process. A resonant photon of energy k' is spawned during the ensuing de-excitation process.

photons conducting the previously deposited energy. This process is illustrated in Fig. 3.1.

3.1. Assumptions and Notation

Various other processes take place in the cyclotron line forming region of accreting X-ray pulsars. As the photon energy approaches the electron rest mass, for example, pair production starts to play a non-negligible role. This work focuses on cyclotron processes. Other processes in strong magnetic fields have been studied and compared quantitatively by Sina (1996) and are disregarded in this thesis apart from mentioning their possible influence in cases where the assumption of cyclotron scattering as the dominant process is questionable. This assumption is readily justified by the parameter ranges considered here: the low optical depth below $\sim 10^{-2}\,\tau_\mathrm{T}$, where τ_T is the Thomson optical depth, the magnetic field regime $0.01 \lesssim B/B_\mathrm{crit} \lesssim 0.12$, and the photon energies $\omega \ll m_\mathrm{e}c^2$ (Wang et al., 1988; Sina, 1996; Isenberg et al., 1998a,b; Araya & Harding, 1999). Even in the regime of pure cyclotron scattering various assumptions have to be made in order to implement the process in terms of a computer simulation. In the following the general notation used throughout this work is introduced and the most important universal assumptions are discussed. Minor assumptions of less constraining nature and relevance for only segregated parts of this work will be discussed in the corresponding Sections.

Optical depths are generally given in units of the Thomson scattering optical depth τ_T. Similarly, cross sections are given in units of the Thomson scattering cross section σ_T. For a given electron column density N_e, which is constant within a column of length l, the optical depth becomes $\tau = \sigma_T N_\mathrm{e} l$ (Schwarm, 2010).

Apart from its Landau level n, an electron in a strong magnetic field of strength B is specified by its momentum parallel to the magnetic field p, its spin, and its rest energy. The total energy of an electron in a magnetic field is given by (Harding & Daugherty, 1991)

$$E_n = \sqrt{m_\mathrm{e}^2 + p^2 + 2nBm_\mathrm{e}^2}\,, \tag{3.1}$$

where m_e is the electron rest mass. Canonical units are used throughout this thesis if not indicated otherwise, meaning that the Planck constant h and the speed of light c satisfy $h = c = 1$, the magnetic field, B, is given in units of the critical magnetic field strength B_crit, the electron mass is given by the electron energy in the rest frame of the electron, $m_\mathrm{e} \approx 511\,\mathrm{keV}$, the electron momentum is given in units of $\mathrm{keV}/c = \mathrm{keV}$. The electron spin is specified by its sign, $s_\mathrm{e} \equiv \pm 1$, and is mostly referred to as "spin up" or "spin down" for positive and negative spin values, respectively. In the ground state the electron can have spin down only (Harding & Daugherty, 1991; Araya & Harding, 1999). The excited Landau levels allow for spin up as well.

This notation is the one usually used in theoretical works on CRSF physics and therefore facilitates comparisons to other works. It is kept as consistent as possible with the works from Sina (1996), Harding & Daugherty (1991), Isenberg et al. (1998b), Araya & Harding (1999) and Schönherr (2007), which had a great influence on this work. Explicit physical units will be used in some cases for providing the reader with an explicit form of the most important equations for the application to observations and data analysis, where SI and/or CGS units are more commonly used. They are easily recognizable by the appearances of c or h. The parameters resulting from fits to observational data are consequently given in explicit units as well: the magnetic field strength is given in units of 10^{12} Gauss, as this is the order of magnitude of the magnetic fields of accreting X-ray binaries exhibiting cyclotron lines and allows for an easy calculation of the expected line energy of the n-th cyclotron line by the, so called, "12-B-12 rule" (Schwarm, 2010; Schönherr et al., 2007b; Schönherr, 2007; Schwarm et al., 2017b):

$$\omega_n \approx n \times 12\, B_{12}\,\mathrm{keV} \tag{3.2}$$

The photons are specified by their energy ω, sometimes referred to by the scalar variable k, while the vector $\vec{k}$ denotes the wave vector, their angle to the magnetic field axis ϑ, and the polarization mode, which can be either $\parallel$ or $\perp$. Due to the cylinder symmetric geometries and field configurations assumed in this work, and the corresponding symmetry of the cyclotron processes, the angle ϑ to the magnetic field axis is the only angle playing a role here. It is mostly specified by its cosine

$$\mu = \cos\vartheta = \vec{k} \cdot \vec{B}\,. \tag{3.3}$$

The bulk flow velocity v is the net velocity of the plasma falling onto the neutron star. Additionally, electrons have a thermal momentum parallel to the field. These velocities make it important to be aware of the frame of reference at hand. Most of the terms in

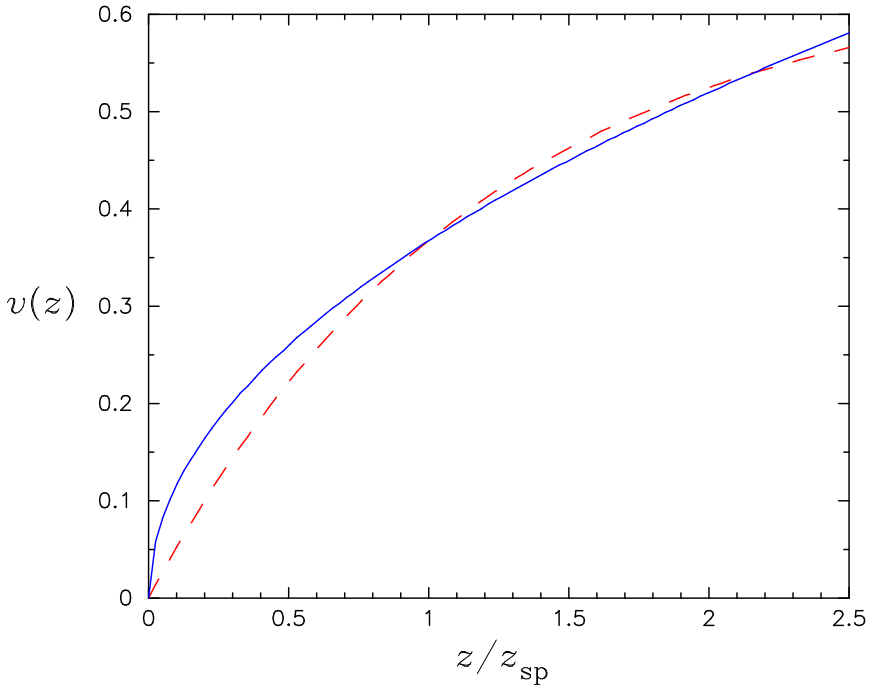

Figure 3.2.: Velocity of the accreting matter in units of c with respect to the height above the surface of the neutron star in units of the height of the sonic point (Becker & Wolff, 2007, Fig. 2 therein). The approximate and exact velocity profiles are shown as solid and dashed line, respectively.

this work refer to the corresponding identities in the rest frame of the line forming region. This frame of reference coincides with the rest frame of the neutron star if the line is forming in the accretion mounds. The mounds are the heaps formed at the polar regions right above the surface where the accreted matter is piled up (see, e.g., Mukherjee & Bhattacharya, 2012). This applies to other hot spot models as well as long as the matter at the hot spot is assumed to have a vanishing (or at least non-relativistic) bulk velocity. Such hot spots are forming on the neutron star's magnetic poles where the matter is abruptly stopped by the collision with the surface. The bremsstrahlung and blackbody radiation resulting from the impact are therefore generated in the rest frame of the neutron star as well. On the contrary, recent models explaining the correlation between the CRSF energy and the observed luminosity (Becker et al., 2012), which depends on the rate of mass accretion onto the neutron star, assume that the height of the line forming region is changing significantly. Therefore, in these models the line forming region is placed above the surface in a domain where the bulk velocity can not be neglected. Figure 3.2 illustrates this: it shows the approximate velocity profile assumed for the model by Becker & Wolff (2007) and the exact profile from the analytic expression for a radiation dominated pulsar accretion column derived by Becker (1998, Eq. 4.18) and Basko & Sunyaev (1976). The input continuum used for CRSF simulations under these conditions should be calculated within the rest frame of the plasma as well. If, however, a continuum model describing the radiation in the rest frame of the accretion column is to be used together with a line

forming region at the surface, as is the case, for instance, for the reflection model from Poutanen et al. (2013), then the seed photons have to be boosted into the rest frame of the line forming region before injecting them into an CRSF simulation code. In general the users of a physical CRSF model, such as the one presented in this work, must always ask the question "In which frame of reference is the seed radiation produced?" and "in what connection does it stand with the region where the cyclotron lines are formed?". The third relevant frame of reference is the one actually observed by X-ray telescopes. It is rotated, due to the neutron star's spin, orbital period, and light bent due to the neutron star's mass and relative velocity. All cross sections and decay rates are calculated in yet another reference frame, that is, the electron rest frame. It coincides with the rest frame of the line forming regions for electrons with zero parallel momentum.

For the simulations and theoretical considerations a homogeneous magnetic field is assumed across the whole simulated volume. The large scale considerations motivate the assumption of a neutron star with a dipole magnetic field. This is reasonable as a first order approximation but gives rise to criticism especially close to the surface of the neutron star: first of all multipole magnetic fields anchored in the star might have a strong influence on the field structure (see, e.g., Krolik, 1991; Mastrano et al., 2013; Pétri, 2015). Even if a pure dipole field can be assumed, the field at the polar caps might by buried and therefore deformed by the accreting matter (e.g., Payne & Melatos, 2004; Mukherjee & Bhattacharya, 2012). It might even form buoyant magnetic bubbles (Payne & Melatos, 2007). Payne et al. (2008) point out that "magnetic mountains" forming at the polar caps are in general offset from the spin axis and may generate detectable gravitational waves. Oscillations and magnetic field instabilities (e.g., Lander & Jones, 2011), and for higher magnetic fields, such as the ones observed from magnetars (see, e.g., Duncan & Thompson, 1992), even deformations of the equatorial radius of the star (e.g., Mallick & Schramm, 2014) and complex field structures such as twisted magnetic field lines (e.g., Thompson et al., 2002; Thompson, 2008) may become relevant.

In this work polarization is included up to the point of the MC simulation of the radiative transfer. Pure vacuum polarization modes (Adler, 1971; Shabad, 1975; Sina, 1996), $e_{\parallel}$ and $e_{\perp}$, are used for the description of the photon polarization. These modes define the linear states of photon polarization parallel and perpendicular to the plane formed by the wave vector $\vec{k}$ and the direction of the magnetic field $\vec{B}$. The simulation discussed in Chapter 4 uses cross sections that are averaged over polarization modes in order to limit the parameter space of simulations to a manageable amount. The calculations of the cross sections and decay rates described in the following have been implemented in a generalized way, though. They offer the possibility to retrieve polarization dependent results. Therefore the inclusion of polarization into the MC simulation is a mere problem of CPU time and disk space. This is discussed in detail in Section 4.10, which also provides details on the parameter regimes in which the pure vacuum modes are a reasonable choice.

The functions necessary for the calculation of the data products described in the following are available as part of the `cyclo` module of the Remeis-C-Library (Schwarm, 2016, RCL). This library has been developed in the course of this thesis in order to reduce code repetition and to make the numerous helper functions developed for the usage in the MC

simulation code available. An overview over its functionality can be found in Appendix B.

3.2. Cross Section Calculation

The number of derivations of the cross sections for the cyclotron interactions emission, absorption, and scattering are numerous. They vary in complexity depending on the assumptions and approximations made in each particular derivation. Some have a rather limited scope of application, while others pay for their generalization with a devastating increase in intricacy. An overview over related work shall be given in the following Sections together with the description of the corresponding process. Before coming to the fully relativistic QED cross sections, simpler derivations shall be described first to provide the reader with some historic background and the necessary terminology. Many explanations have been given by Canuto & Ventura (1977) where an introduction to the general physics of electrons in strong magnetic fields can be found. A short summary has been provided by Schwarm (2010).

Compton scattering is the process of photons being in-elastically scattered off free charged particles. In the low-energy limit, this process is described by Thomson scattering. An introduction to Compton scattering and to other astrophysical radiation processes is given, for instance, by Rybicki & Lightman (1979). Canuto et al. (1971) derived the Thomson cross section for scattering in strong magnetic fields, meaning that they generalized the Thomson scattering process to the realm of strong B-fields. The resulting equations are definitively not trivial but appear wonderfully simple compared to the set of equations necessary to calculate the fully relativistic cross sections using physically meaningful operators and wave functions. Polarization becomes important in the scattering cross section calculations in the vicinity of strong magnetic fields because of the coupling of the electron spin to the magnetic field and the different possible photon modes. Ventura et al. (1979) explicitly show the effects of vacuum polarization on the CRSF cross sections. Alexander et al. (1989) found that polarization may become important in the generation of synthetic cyclotron line spectra. See Section 4.10 for a more detailed view on this topic.

The calculations of the individual cross sections will be described roughly. It is assumed that the reader is familiar with the QED S-matrix expansion scheme. It has been introduced by Dyson (1949) as a direct derivation of the method from Feynman (1949) from a simple expression for the S-matrix (Wick, 1950) and contains the complete information about all collision processes in a form suitable for extracting the transition amplitude for a specific process to any order of perturbation theory (Mandl & Shaw, 1984, Introduction to Chapter 6, the exact form is given by Eq. 6.23):

$$S = \sum_{n=0}^{\infty} \frac{(-i)^n}{n!} \int \dots \int d^4x_1 d^4x_2 \dots d^4x_n T\{\mathcal{H}_1(x_1)\mathcal{H}_1(x_2)\dots\mathcal{H}_1(x_n)\} \tag{3.4}$$

The integrations are over all space-time and $T\{\dots\}$ specifies the time ordered product of the Hamiltonian densities $\mathcal{H}_1(x) = -eN\bar{\psi}(x)A(x)\psi(x)$, with electron and photon wave

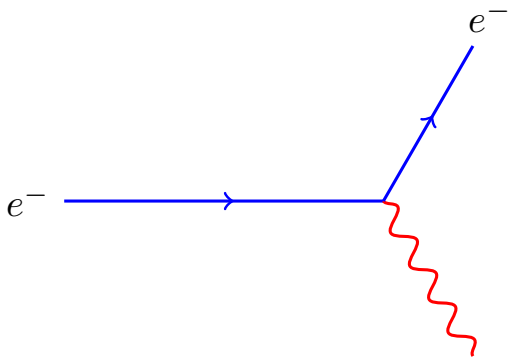

Figure 3.3.: Feynman diagram for cyclotron emission. A photon (curved line) is emitted by an electron (solid line) during the electron's de-excitation to a lower Landau level.

functions ψ and A, respectively. The amplitude for a transition from initial state $|i\rangle$ to final state $|f\rangle$ is then given by $S_{fi} \equiv \langle f| S |i\rangle$. The isolation of the non-vanishing terms from Eq. 3.4, containing the absorption operators to destroy the particles present in $|i\rangle$ and the creation operators to emit the particles present in $|f\rangle$ (Mandl & Shaw, 1984), is the main problem to solve for calculating the probability amplitude explicitly. This process can be generalized by applying selection rules, the so called Feynman rules, to the corresponding Feynman diagrams, which are on a par with the desired terms.

For a detailed introduction to the physics of interactions in QED see, e.g., Mandl & Shaw (1984). In some cases the equations can not be given *in extenso* without obscuring the overall picture or obstructing the text flow. References to publications containing a complete form will be given in these cases.

3.3. Emission

Cyclotron emission is the process of an electron emitting a photon during its de-excitation to a lower Landau level. Figure 3.3 shows the corresponding Feynman diagram. The electron initially occupies a higher energetic state to which it might have been excited by, for example, collisions with other particles or by absorbing a resonant photon via the cyclotron absorption process (see Section 3.4).

The radiated frequency for transitions from the first excited state to the ground state is $\omega = \gamma^2 \omega_\mathrm{B}$, with the parallel Lorentz factor γ of the electron and $\omega_\mathrm{B} = eB/m_\mathrm{e}$. It surpasses the kinetic energy of the electron when $B > \frac{\gamma-1}{\gamma^2}\frac{m_\mathrm{e}^2}{e}$ (Sina, 1996). The excited state has a finite lifetime and will de-excite to a lower Landau level on rather short timescales. Araya & Harding (1999) pointed out that neglecting a collisional excited population of electrons in favor of the assumption that all electrons are in the ground state is readily justified at (continuum) optical depths below $3 \cdot 10^{-3}\tau_\mathrm{T}$. The reason is the much higher

cyclotron de-excitation rate compared with the collisional excitation rate. This means that excited electrons can be neglected while simulating the scattering process. Nevertheless, photons will be generated by cyclotron emission from electrons which have been excited by such collision excitations. These photons have to be considered as seed photons for the simulation. Therefore the inclusion of a *cyclotron emission* component in models of the seed continuum does not imply a double inclusion of cyclotron emission. In fact it is necessary if the cyclotron emission due to collisional excitation is meant to be taken into account. An example is the seed continuum from Becker & Wolff (2007), which does include a cyclotron emission component and will be used in Section 6.3 to model physically motivated spectra for Her X-1. Bonazzola et al. (1979) provide an approximation for the collisional excitation rate and discussed the probability for collisional de-excitation to the ground state in detail.

Herold et al. (1982) derived the fully relativistic quantum mechanical decay rate for cyclotron emission using the electron wave functions from Sokolov et al. (1968, ST). These wave functions are physically more meaningful than the ones from Johnson & Lippmann (1949, JL) for reasons that will be discussed in Section 3.5. The decay rates from Herold et al. (1982) are the best possible choice one can make for continuative calculations. Figure 3.4 shows that their decay rates agree with the ones used in this work, which are either calculated using a direct implementation of the rates from Herold et al. (1982) or by an interface to the code from Sina (1996). The different technical implementations have been found to be usable interchangeably. Their validity is verified by the comparison to Herold et al. (1982).

The final expression derived by Sina (1996, Eq. 2.15 therein) for the cyclotron emission rate from Landau level n_i and electron spin s_i to final Landau level n_f and electron spin s_f is given by

$$\frac{d\Gamma}{d\Omega} = \frac{\alpha\omega}{2\pi} \frac{|D_{u,u}^{n_\mathrm{f},n_\mathrm{i},s_\mathrm{f},s_\mathrm{i}}(k)|^2}{1 - \beta_\mathrm{f} \cos\vartheta} \,, \tag{3.5}$$

where $\beta_\mathrm{f} = p_\mathrm{f}/E_\mathrm{f}$ is the parallel velocity of the final electron with energy E_f (see Eq. 3.1) and final parallel momentum p_f. The vertex functions $D_{T_n,T_m}^{\mathrm{n,m,sn,sm}}(k)$ contain the polarization dependence and are given in Section 3.5. Sina (1996) notes that the momentum perpendicular to the field is not constrained. The magnetic field rather can "absorb or emit" momentum perpendicular to it. The kinematic equations corresponding to the cyclotron emission process are, for example, given by Araya & Harding (1999):

$$p_\mathrm{f} = p_\mathrm{i} - \omega\cos\vartheta \tag{3.6}$$

$$E_\mathrm{f} = E_\mathrm{i} - \omega \tag{3.7}$$

The energy of the emitted photon then becomes (Sina, 1996, Eq. 2.18 therein)

$$\omega = \frac{(E_\mathrm{i} - p_\mathrm{i}\cos\vartheta) - \sqrt{(E_\mathrm{i} - p_\mathrm{i}\cos\vartheta)^2 - 2eB\sin^2\vartheta(n_\mathrm{i} - n_\mathrm{f})}}{\sin^2\vartheta} \,, \tag{3.8}$$

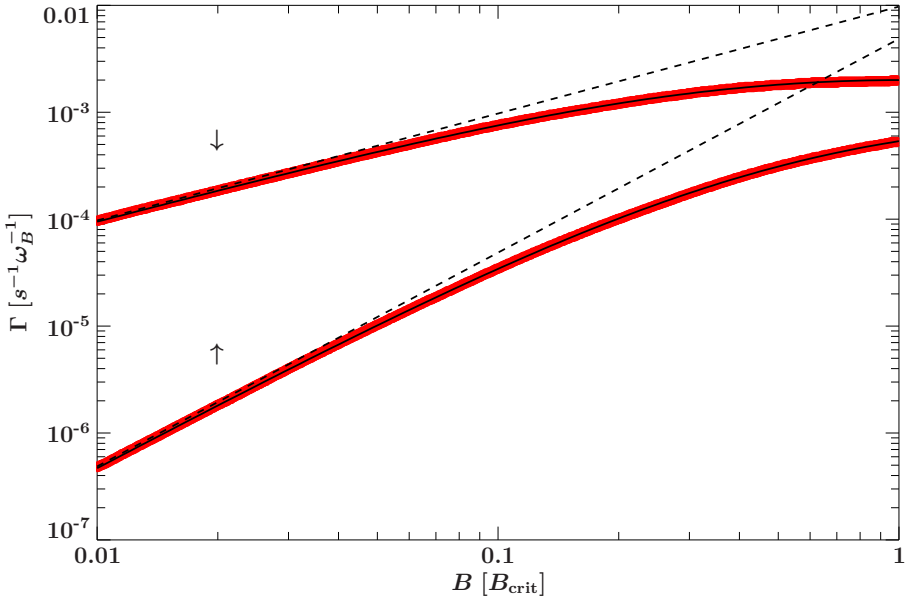

Figure 3.4.: Comparison of the total transition rates used in this work with the ones from Herold et al. (1982, Fig. 2 therein) for the transition from the first excited Landau level to the ground state and different initial spin orientations indicated by the arrows. The dashed lines show the non-relativistic approximations (Eqs. 3.9 – 3.11). All possible polarization states are summed.

which already implies the resonance energy for cyclotron absorption in the electron rest frame ($p = 0, E = m$) given by Eq. 3.12 in Section 3.4.

Herold et al. (1982) provide formulae for the non-relativistic case as well:

$$\Gamma_{-}^{N\to N-1} = \frac{4}{3}\alpha m (B/B_{\rm crit})^2 N\,, \tag{3.9}$$

$$\Gamma_{+}^{N\to N-1} = \frac{4}{3}\alpha m (B/B_{\rm crit})^2 (N-1), \quad \forall N > 1\,, \tag{3.10}$$

$$\Gamma_{+}^{1\to 0} = \frac{2}{3}\alpha m (B/B_{\rm crit})^3\,. \tag{3.11}$$

Similar formulae and a general discussion about transitions between neighboring Landau levels can be found in the work by Latal (1986). This paper also contains a quantitative comparison between the transition probabilities to the next lower Landau level and even lower ones. Latal (1986) finds that the rates for a transition to neighboring Landau levels is higher by orders of magnitude. Therefore, during the de-excitation process, only very few photons are generated at the energies of the higher harmonics. In other words, the spawned photons mostly have energies around the fundamental cyclotron resonance energy. Thus, in contrast the higher harmonics, the fundamental line is expected to be of very complex shape due to the majority of photons spawned in the vicinity of the first CRSF energy by electron transitions between neighboring Landau levels. Table 3.1 shows this quantitatively for a magnetic field of 0.01 $B_{\rm crit}$. The rates are averaged over initial and final

Table 3.1.: Cyclotron decay rates for a magnetic field $B = 0.01\,B_{\rm crit}$, averaged over initial and final electron spins and summed over all possible polarization modes, in units of $\omega_{\rm B}$. The rates are given for transitions from the initial Landau level $n_{\rm i} \leq 7$ (first column) to all final Landau levels $n_{\rm f}$ for which $n_{\rm f} < n_{\rm i}$ (first row).

n	0	1	2	3	4	5	6
1	9.5105×10^{-5}						
2	4.3373×10^{-6}	2.7476×10^{-4}					
3	3.4759×10^{-7}	1.6204×10^{-5}	4.4162×10^{-4}				
4	3.8978×10^{-8}	1.5758×10^{-6}	3.4150×10^{-5}	5.9677×10^{-4}			
5	5.5378×10^{-9}	2.0607×10^{-7}	4.0164×10^{-6}	5.6969×10^{-5}	7.4119×10^{-4}		
6	9.4284×10^{-10}	3.3226×10^{-8}	6.0813×10^{-7}	7.8554×10^{-6}	8.3657×10^{-5}	8.7576×10^{-4}	
7	1.8561×10^{-10}	6.2939×10^{-9}	1.1044×10^{-7}	1.3507×10^{-6}	1.3175×10^{-5}	1.1338×10^{-4}	1.0013×10^{-3}

Table 3.2.: Same as Table 3.1 but for a magnetic field of $B = 0.1\,B_{\rm crit}$.

n	0	1	2	3	4	5	6
1	7.8708×10^{-4}						
2	2.4432×10^{-4}	1.7366×10^{-3}					
3	1.1313×10^{-4}	5.8499×10^{-4}	2.2486×10^{-3}				
4	6.3951×10^{-5}	2.8415×10^{-4}	8.6338×10^{-4}	2.5362×10^{-3}			
5	4.0800×10^{-5}	1.6579×10^{-4}	4.4945×10^{-4}	1.0698×10^{-3}	2.6992×10^{-3}		
6	2.8234×10^{-5}	1.0818×10^{-4}	2.7355×10^{-4}	5.8940×10^{-4}	1.2188×10^{-3}	2.7889×10^{-3}	
7	2.0710×10^{-5}	7.6123×10^{-5}	1.8357×10^{-4}	3.7232×10^{-4}	7.0200×10^{-4}	1.3252×10^{-3}	2.8336×10^{-3}

spin and summed over final polarization. Table 3.2 shows the same but for a magnetic field of $0.1\,B_{\rm crit}$. In the later case, the ratio between the rate for a transition from Landau level $n_{\rm i} = 2$ to Landau level $n_{\rm f} = 1$, that is, $\overline{\Gamma}_{21} \approx 1.74 \times 10^{-3}$, and the corresponding transition to the ground state, $\overline{\Gamma}_{20} \approx 2.44 \times 10^{-4}$, becomes $\overline{\Gamma}_{21}/\overline{\Gamma}_{20} \approx 7.11$. This value is in agreement with the corresponding calculation by Latal (1986, Table 5 therein). The ratio is becoming smaller for larger fields. The values from the first row of Table 1 from the paper by Latal (1986), which partially overlap with the Tables 3.1 and 3.2, are identical to the ones computed by Herold et al. (1982) despite the "seemingly different form of the respective general expressions" (Latal, 1986). The calculation of the emission rate used in this thesis is therefore in agreement with Latal (1986) as well.

Tables 3.3 and 3.4 show only the decay rates for final spin down and initial spins down and up, respectively. The sum of the first columns of these Tables results in the first column of Table 3.2. This only applies to the first column, that is, transitions to the ground state because transitions to higher Landau levels might result in positive final spins.

Finally, Tables 3.5 and 3.6 show the polarization dependent rates for a magnetic field $B = 0.1\,B_{\rm crit}$, initial electron spin down, and final electron spin down. This is the same configuration as in Table 3.3, which is identical to the sum of these Tables.

The calculation of the total emission rate involves an integration over all possible final angles to the magnetic field axis. An adaptive Simpson method (see Section 4.7.1 for details about this method) is used for the numerical integration. The successive splitting of the integration interval with this method allows the code to store the partial integrals together with the corresponding angular grid points. The resulting distribution is visualized

Table 3.3.: Cyclotron emission rates for a magnetic field $B = 0.1\,B_{\rm crit}$, initial electron spin down, and final electron spin down (i.e., no spin flip), summed over all possible polarization modes, in units of $\omega_{\rm B}$.

n	0	1	2	3	4	5	6
1	7.5279×10^{-4}						
2	2.2540×10^{-4}	1.1179×10^{-3}					
3	1.0128×10^{-4}	4.1290×10^{-4}	1.3076×10^{-3}				
4	5.5809×10^{-5}	2.0917×10^{-4}	5.4587×10^{-4}	1.4084×10^{-3}			
5	3.4825×10^{-5}	1.2455×10^{-4}	2.9892×10^{-4}	6.3711×10^{-4}	1.4604×10^{-3}		
6	2.3635×10^{-5}	8.2032×10^{-5}	1.8785×10^{-4}	3.6841×10^{-4}	6.9921×10^{-4}	1.4841×10^{-3}	
7	1.7039×10^{-5}	5.7917×10^{-5}	1.2870×10^{-4}	2.4085×10^{-4}	4.2087×10^{-4}	7.4121×10^{-4}	1.4909×10^{-3}

Table 3.4.: Same as Table 3.3 but for an initial electron spin up, that is, for the case of a spin-flip transition.

n	0	1	2	3	4	5	6
1	3.4289×10^{-5}						
2	1.8916×10^{-5}	2.0056×10^{-5}					
3	1.1847×10^{-5}	1.8691×10^{-5}	1.2756×10^{-5}				
4	8.1424×10^{-6}	1.5136×10^{-5}	1.5412×10^{-5}	8.6279×10^{-6}			
5	5.9751×10^{-6}	1.2169×10^{-5}	1.4605×10^{-5}	1.2225×10^{-5}	6.1167×10^{-6}		
6	4.5994×10^{-6}	9.9330×10^{-6}	1.3060×10^{-5}	1.2892×10^{-5}	9.6621×10^{-6}	4.5003×10^{-6}	
7	3.6708×10^{-6}	8.2602×10^{-6}	1.1515×10^{-5}	1.2452×10^{-5}	1.1010×10^{-5}	7.6937×10^{-6}	3.4119×10^{-6}

as polar diagrams in order to compare the cyclotron emission patterns — not only the total angle integrated decay rate — to the ones shown by Sina (1996). Figure 3.5 shows the emission patterns for a transition from the first excited level with initial spin up (left) and down (right) to the ground state at the critical magnetic field strength. They agree with the corresponding figures by Sina (1996, Figs. 2.6 and 2.7 therein). Note that the coordinate system has been rotated by 90° for aligning the emission patterns with the magnetic field axis. The orientation of the B-field axis is therefore along the y-axis like in the visualizations of the discussion of the MC process (see, e.g., Fig. 4.2). The emission patterns nicely illustrate the correlation between the initial electron spin and the polarization mode of the emitted photon. The solid line shows perpendicular mode cyclotron emission and the dashed line shows parallel mode emission. The absolute numbers of the different initial spin configurations differ but the emission patterns look the same only with switched polarization modes. "For initial electron spin up the parallel mode is dipolar and the perpendicular mode has quadruple distribution. The remarkable

Table 3.5.: Same as Table 3.3 but for final polarization mode $\perp$.

n	0	1	2	3	4	5	6
1	5.6272×10^{-4}						
2	1.8646×10^{-4}	8.2233×10^{-4}					
3	8.7735×10^{-5}	3.3537×10^{-4}	9.5011×10^{-4}				
4	4.9632×10^{-5}	1.7809×10^{-4}	4.3677×10^{-4}	1.0134×10^{-3}			
5	3.1503×10^{-5}	1.0903×10^{-4}	2.5077×10^{-4}	5.0346×10^{-4}	1.0426×10^{-3}		
6	2.1637×10^{-5}	7.3146×10^{-5}	1.6218×10^{-4}	3.0516×10^{-4}	5.4673×10^{-4}	1.0526×10^{-3}	
7	1.5737×10^{-5}	5.2327×10^{-5}	1.1328×10^{-4}	2.0540×10^{-4}	3.4478×10^{-4}	5.7437×10^{-4}	1.0516×10^{-3}

Table 3.6.: Same as Table 3.3 but for final polarization mode ||.

n	0	1	2	3	4	5	6
1	1.9007×10^{-4}						
2	3.8941×10^{-5}	2.9554×10^{-4}					
3	1.3550×10^{-5}	7.7525×10^{-5}	3.5747×10^{-4}				
4	6.1772×10^{-6}	3.1083×10^{-5}	1.0909×10^{-4}	3.9495×10^{-4}			
5	3.3225×10^{-6}	1.5519×10^{-5}	4.8150×10^{-5}	1.3366×10^{-4}	4.1779×10^{-4}		
6	1.9980×10^{-6}	8.8860×10^{-6}	2.5675×10^{-5}	6.3253×10^{-5}	1.5248×10^{-4}	4.3148×10^{-4}	
7	1.3017×10^{-6}	5.5902×10^{-6}	1.5414×10^{-5}	3.5453×10^{-5}	7.6094×10^{-5}	1.6684×10^{-4}	4.3922×10^{-4}

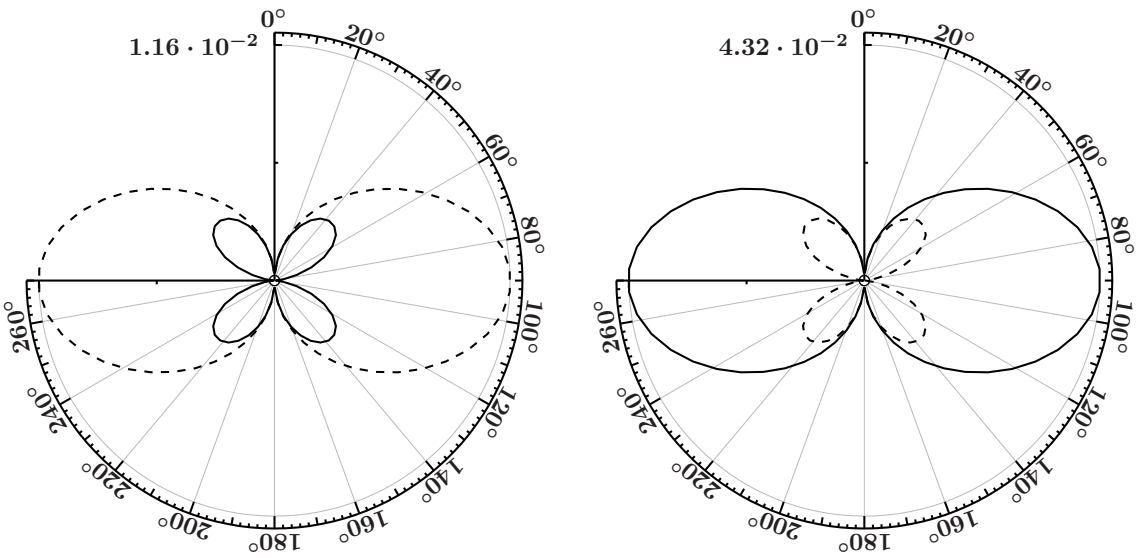

Figure 3.5.: Cyclotron emission patterns for a transition from the first excited Landau level to the ground state (spin down). The case of initial electron spin up is shown on the left side. The right side shows the transition from an electron with initial spin down. Emission producing a perpendicular mode photon is shown as a solid line. The dashed line shows parallel mode emission. The magnetic field was chosen to be $B = B_{\rm crit}$ to allow for a comparison to Sina (1996, Figs. 2.6 and 2.7 therein). The direction of the magnetic field is chosen to point upwards, i.e., the labels correspond to the emission angle with respect to the magnetic field axis.

feature of these distributions is that the role of mode is exactly reversed when an electron with initial spin down is considered." (Sina, 1996).

Figure 3.6 shows the same emission patterns but for a transition from the third excited state to the ground state. As discussed before, this transition is suppressed in favor of transitions to neighboring Landau levels, $n_{\rm f} = 2$ in this case. The figure shows that it also features compressed emission patterns.

Figure 3.7 shows the same emission patterns as Fig. 3.6 but summed over all possible final Landau levels and electron spins. A mixing of dipole and quadrupole moments is observed, especially in the case of initial electron spin down. This is caused by the mixing of favored polarization states due to the summation of final electron states. Figure 3.8 shows the corresponding patterns for transitions from $n_{\rm i} = 3$ to the neighboring Landau level $n_{\rm f} = 2$

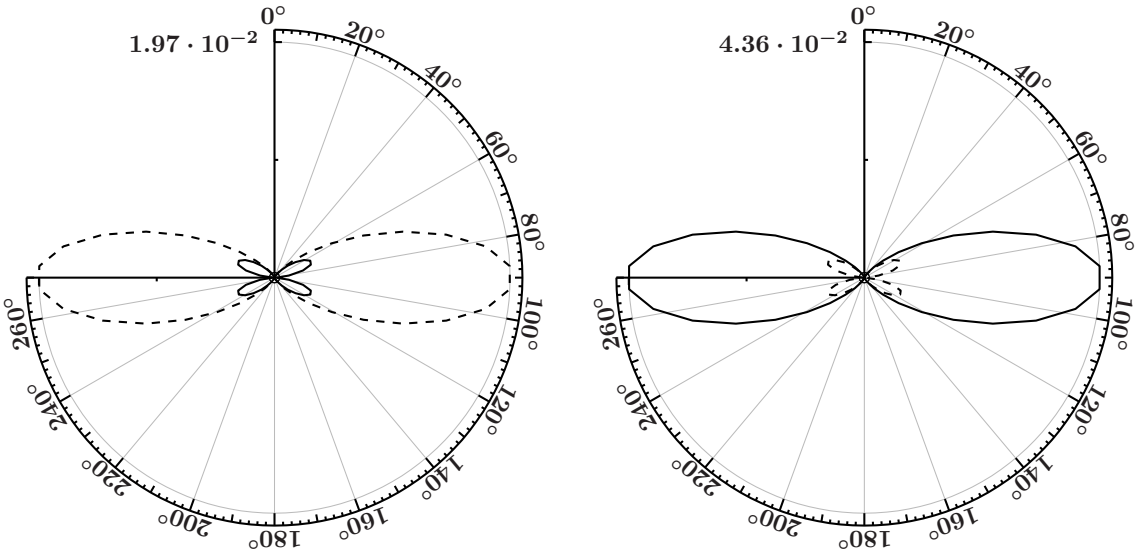

Figure 3.6.: Same as Fig. 3.5 but with initial Landau level $n_\mathrm{i} = 3$.

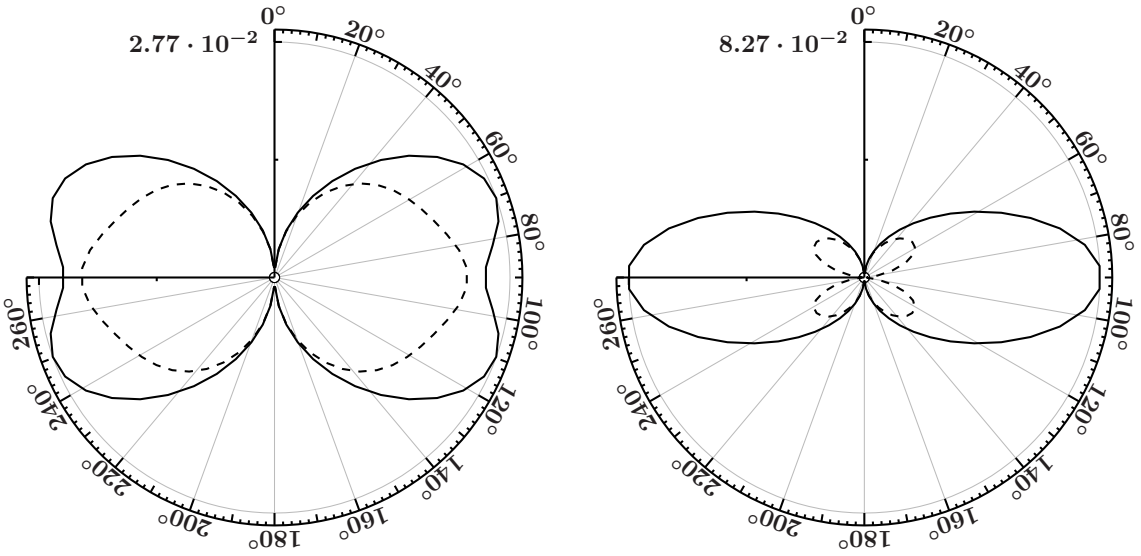

Figure 3.7.: Same as Fig. 3.6 but summed over all possible final Landau levels and electron spins.

only.

Figure 3.9 shows the emission patterns for a transition from Landau level $n_\mathrm{i} = 5$ to $n_\mathrm{f} = 4$, only considering final electron spin down. It resembles Figures 2.9 and 2.11 from Sina (1996).

The dipole component predominates the emission patterns in all cases. The corresponding direction of highest emission, in the neutron star's frame of reference, depends on the initial electron momentum parallel to the magnetic field axis, which is assumed to be zero here. The beaming of cyclotron angular patterns due to a non-zero electron parallel momentum will be discussed in more detail in Sections 5.6 and 6.4.

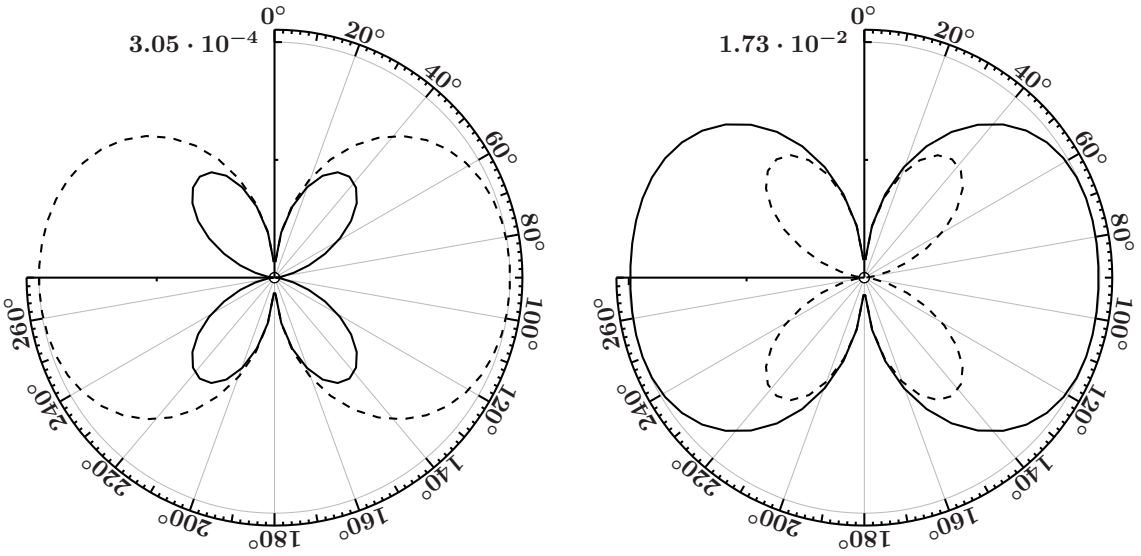

Figure 3.8.: Same as Fig. 3.7 but for a transition to the neighboring Landau level $n_f = 2$ only.

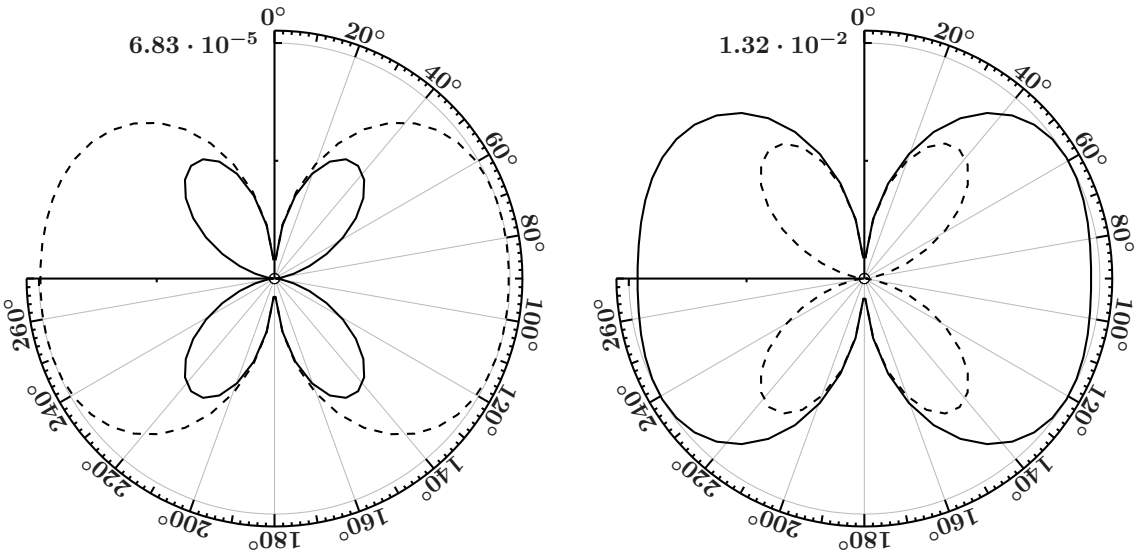

Figure 3.9.: Same as Fig. 3.7 but for the transition from Landau level $n_i = 5$ to $n_f = 4$ with final spin down. Same as Figures 2.9 and 2.11 from Sina (1996).

3.4. Absorption

The cyclotron absorption process excites an electron to a higher Landau level by absorbing a photon. The Feynman diagram for this process is shown in Fig. 3.10. The photon is destroyed in the process and its energy and parallel momentum are transferred to the electron. The photon must be resonant in the comoving frame of the gyrating electron,

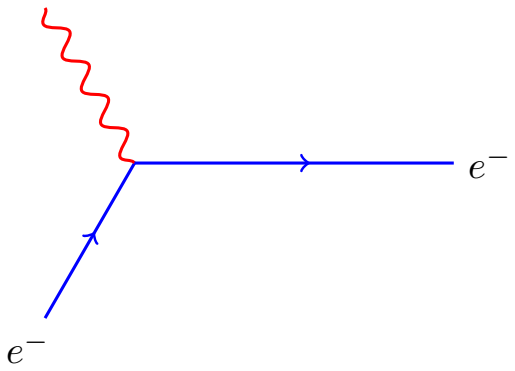

Figure 3.10.: Feynman diagram for cyclotron absorption. A photon is absorbed by an electron, which is excited to a higher Landau level in the process. The photon transfers its energy and parallel momentum to the electron and vanishes.

meaning that, its energy must equal the resonance energy (Harding & Daugherty, 1991)

$$\omega_n = m_\mathrm{e} \frac{\sqrt{1 + 2nB \sin^2 \vartheta} - 1}{\sin^2 \vartheta} \,. \tag{3.12}$$

The excited electron will successively de-excite to the ground state and emit spawned photons in the course of each transition (see Section 3.3).

The cross section for this process was derived by Daugherty & Ventura (1978) using the electron wave functions from Johnson & Lippmann (1949). They also elaborate on the differences between cyclotron absorption and scattering, take into account polarization modes, and discuss the lifetimes of the first excited state. These lifetimes correspond to the cyclotron emission rates examined before (see Section 3.3).

Harding & Daugherty (1991) derived fully relativistic cyclotron absorption cross sections using the JL wave functions for the derivation of the cross sections but utilized the wave functions from Sokolov et al. (1968) for the calculation of the cyclotron emission rates, which are used within the cross sections. Harding & Daugherty (1991) state that this can be done since the ST wave functions are eigenfunctions of the same spin operator as the wave functions from Johnson & Lippmann (1949). Sina (1996) derived the absorption cross sections using the ST wave functions throughout. The following expression results for an electron initially in the ground state (Sina, 1996, Eq. 2.23):

$$\sigma = 2\pi \frac{\alpha}{\omega} \frac{|H_{u,\mu}^{n_\mathrm{f},n_\mathrm{i},s_\mathrm{f},s_\mathrm{i}}(k)|^2}{1 - \beta_\mathrm{i} \cos \vartheta_\mathrm{i}} \frac{\Gamma_\mathrm{f}}{(E_\mathrm{i} + \omega - E_\mathrm{f})^2 + \Gamma_\mathrm{f}^2/4} \tag{3.13}$$

The nomenclature is the same as for the cyclotron emission rate in Section 3.3. The vertex functions $H_{T_n,T_m}^{n,m,sn,sm}(k)$ are given in Section 3.5. In this form the energy width due to the finite lifetime of the final electron state is incorporated by a Lorentzian the width of which is given by the corresponding cyclotron emission rate Γ_f.

The RCL implements the absorption cross sections given by Harding & Daugherty (1991) as well. They agree very well with the ones from Sina (1996) despite the usage of JL wave functions in the latter derivation. The ST wave functions should be preferred for the calculation of the scattering cross sections, though, as described in Section 3.5. The interface to the Sina (1996) implementation is faster, which is why it has been preferred to the RCL implementation for some of the following calculations. The latter is more accurate though due to the usage of an adaptive Simpson numerical integration scheme (see Section 4.7.1) contrary to Gaussian quadrature integration. Both versions have been compared for some points and have been found to not deviate by more than the plotted line width for the corresponding test points.

Figure 3.11 shows the cyclotron absorption cross section for transitions from the ground state with electron spin down, summed over possible final states, for a magnetic field of $B = 0.1\, B_{\mathrm{crit}}$. The x-axis shows the corresponding energy of the absorbed photon. The calculations from Harding & Daugherty (1991), which are shown as black dots, show that the implementation developed in the course of this thesis using the derivation from Sina (1996) is in agreement with their work. This is expected since the usage of JL or ST electron wave functions should matter only in the polarization dependent case. An initial electron momentum of $p = 0$ is assumed here, like in the work of Harding & Daugherty (1991).

The cross sections are a superposition of all possible transitions, which are the (physically) possible combinations of the final electron Landau level and spin. This is illustrated in Figure 3.12, which shows only the transition from the ground state, necessarily with spin down, to final Landau level $n_{\mathrm{f}} = 2$, but still summed over final electron spins. This transition constitutes the major part of the total cross section for energies around $\approx \omega_2$. Its shape is mainly a Lorentzian with a width due to the time-, and therefore energy-, uncertainty caused by the cyclotron emission rates.

3.5. Scattering

In contrast to the absorption process, the cyclotron scattering process preserves the scattering photon. Inelastic scattering with an excitation of the interacting electron to a higher Landau level can occur if it is energetically possible: if the energy of the interacting photon exceeds the energy difference to a higher Landau level in the rest frame of the electron a transition might take place. Figure 3.13 shows the Feynman diagrams for the cyclotron scattering process. The absorption (left) or emission (right) of a photon by an incoming electron results in the emission or absorption of a photon, respectively. These processes are indistinguishable and therefore both have been considered in the calculation of the cross section for this process.

I refrain from completely listing all derivations of the cyclotron scattering cross sections in strong magnetic fields, as they are numerous and their subtle differences are often crucial. Wang et al. (1988) provides a good starting point on that matter by listing different

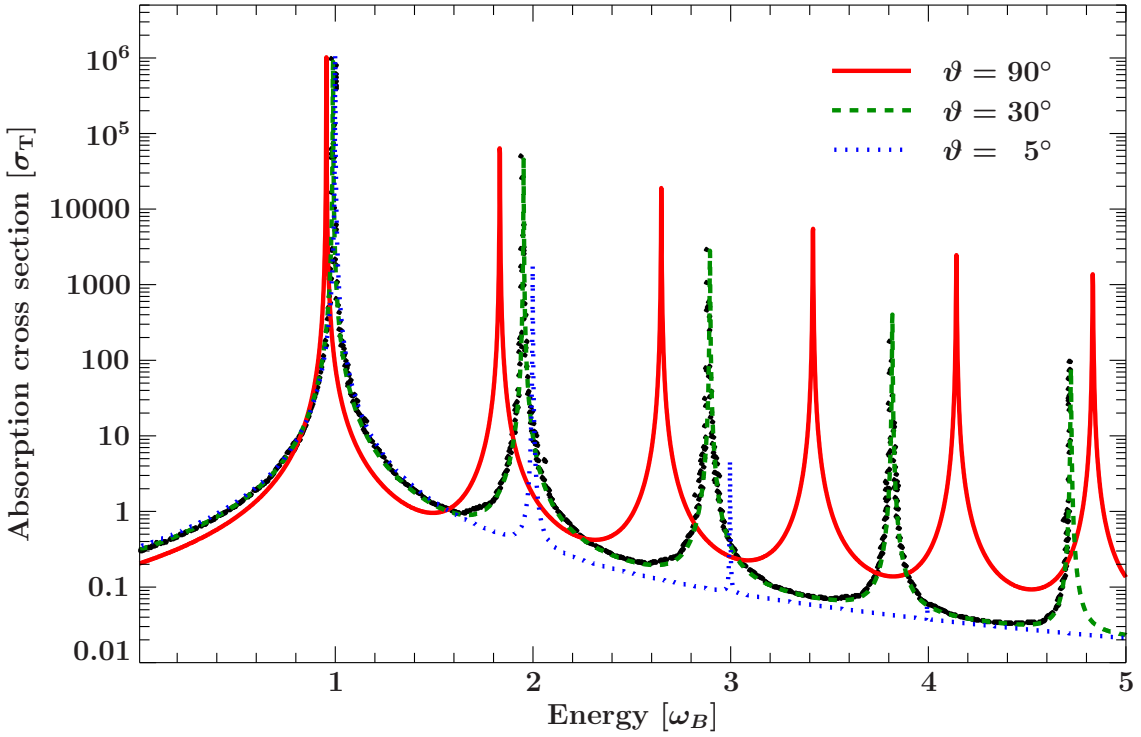

Figure 3.11.: Absorption cross section for a magnetic field of $B = 0.1\,B_{\rm crit}$ with respect to the photon energy in units of the resonance energy $\omega_{\rm B}$. Three angles of the incoming photon with respect to the B-field axis, $\vartheta = 90°, 30°, 5°$, are shown as solid, dashed, and dotted (blue) lines, respectively. The black points show the absorption cross section calculated by Harding & Daugherty (1991, dashed line in their Fig. 1) for an incoming angle of 30°.

cyclotron line modeling approaches with their most important characteristics. Here only some are discussed to point out important differences. Canuto et al. (1971) derived the Thomson cross section for scattering in strong magnetic fields. Ventura (1979) extends the work by Canuto et al. (1971) beyond the cold plasma limit. The same formalism was used by Nagel (1981) for studying the effects of Comptonization in a strongly magnetized plasma. A comparison between non-relativistic and relativistic Thomson cross sections in strong magnetic fields has been performed by Herold (1979). The classical Thomson cross section has been addressed by Börner & Meszaros (1979) as well. They specifically discuss the polarization dependence of the cross sections in a fully ionized plasma. For the assumptions laid out before (see Section 3), the best choice is certainly to use the cross section derivation by Sina (1996), which is the first one using a fully relativistic, polarization depend treatment and the electron wave functions from Sokolov et al. (1968) together with pure vacuum polarization states. This derivation is utilized in this work but using an own implementation based on the original code from Sina (1996). The code has been restructured to minimize code repetition and increase readability. It has been generalized, such that previously hard-coded variables, like the numerical integration boundaries and methods, or the maximum number of Landau levels taken into account,

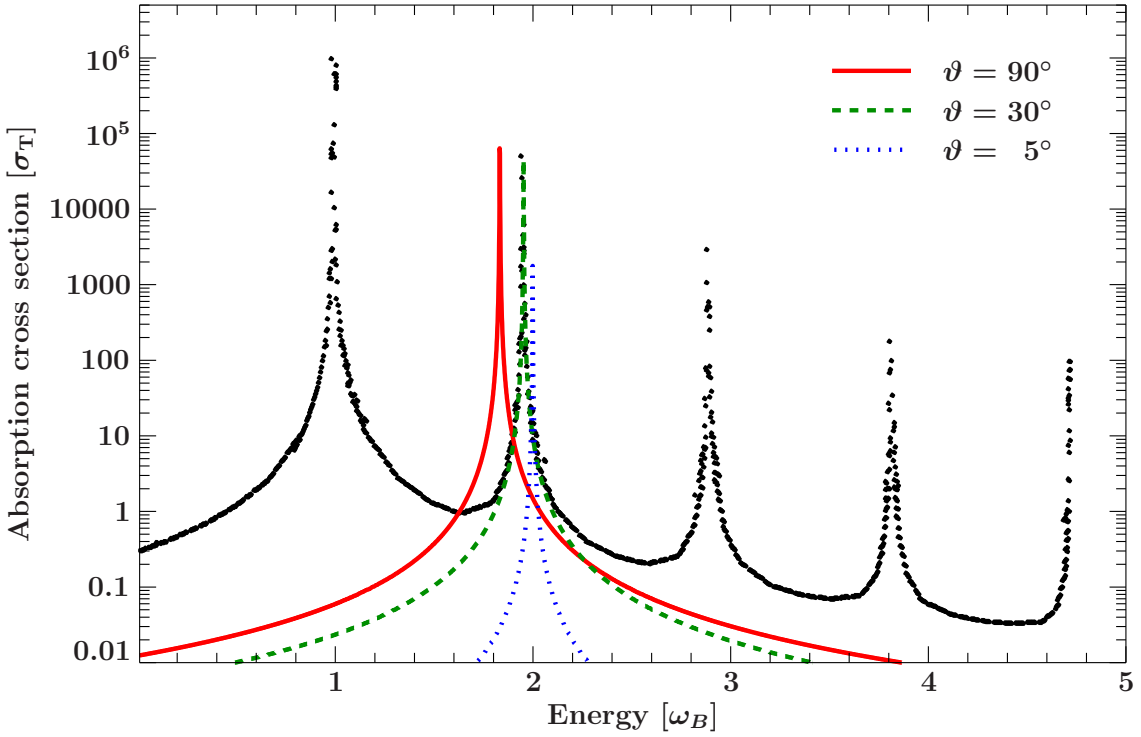

Figure 3.12.: Same as Fig. 3.11 but for excitations to the second excited Landau level, $n_f = 2$, only. The same data from Harding & Daugherty (1991) as in the previous plot is shown for reference.

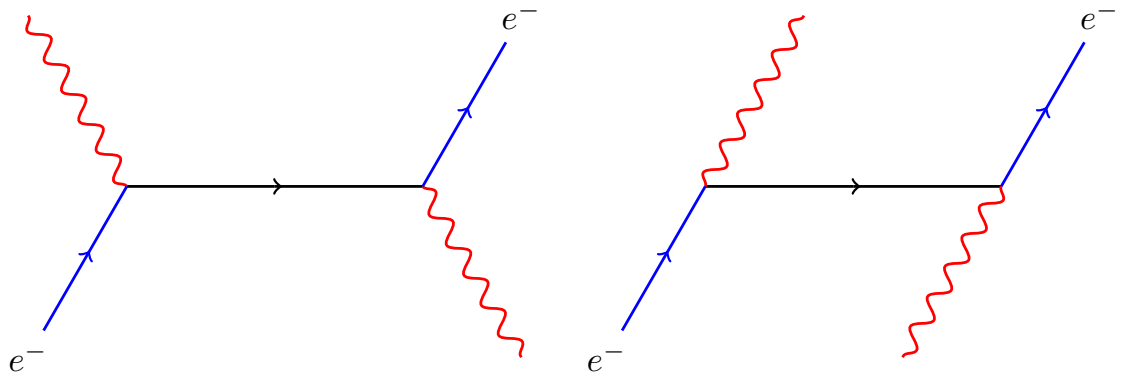

Figure 3.13.: Feynman diagrams for cyclotron scattering. A photon is either absorbed and re-emitted by an electron (left) or the interacting electron emits a photon before absorbing the initiating photon (right).

can be changed dynamically. It has also been extended to arbitrary temperatures by including an adaptive Simpson integration scheme for averaging the cross sections over the thermal electron momentum distribution. Improved error handling and the addition of warning messages result in a more robust implementation as needed for the time consuming interpolation table calculations. Unit tests ensure that the resulting cross sections are in

agreement with the ones calculated by the original code. The resulting cross sections are also in agreement with other works as discussed at the end of this Chapter.

The fully relativistic differential Compton cross section derived by Sina (1996) makes use of the Breit-Wigner broadening approximation (Breit & Wigner, 1936; Breit, 1938; Wigner, 1946) and the ST electron wave functions, which are consistent with the perturbation theoretic order of the calculation. As discussed before, Sina (1996) also derived the relativistic emission- and absorption cross sections and the cross sections for other processes in strong magnetic fields, like (two photon) pair production and annihilation, muon production, Møller scattering, Bhabha scattering, and trident production. A derivation of the cyclotron cross sections using electron wave functions from Johnson & Lippmann (1949) has been presented by Daugherty & Ventura (1978). Harding & Daugherty (1991) used the JL wave functions in combination with a derivation of the cyclotron emission rate using the ST wave functions. These differences are important because Graziani (1993) showed that the decay rates derived using the ST formalism obey the expected time dilation relation $\Gamma_{\mathrm{Lab}} = \gamma^{-1}\Gamma_{\mathrm{Rest}}$ in contrast to the JL states. Baring et al. (2005) performed a similar analysis by comparing their derivations of cyclotron decay rates using the JL and ST wave functions. A whole section (Baring et al., 2005, Section 3.2) is dedicated to the discussion of the Lorentz boost characteristics of the decay rates calculated using the two variants. The numerical behavior of the cyclotron scattering cross sections has been studied by Gonthier et al. (2000). They derived analytic approximations for the differential and total cross sections for the special case of $\vartheta = 0°$ and study the influence of a super critical magnetic field. Gonthier et al. (2014) derive the CRSF scattering cross sections using both the JL and ST electron wave functions. The derivation with the later is based on the work of Sina (1996). They restrict themselves on the $\vartheta = 0°$ case of photons initially propagating along the field and show that the JL wave functions lead to an overestimation of the cross sections right within the first resonance. In the following the approach from Sina (1996) is reproduced: the relativistic transition rates needed for the cross section calculation, and later for the sampling of the final Landau level into which an initially excited electron decays, have been discussed in Section 3.3 and agree with the ones from Herold et al. (1982). The scattering matrix elements corresponding to the Feynman diagram shown in Figure 3.13 are given by

$$S_{\mathrm{fi}}^{A} = -e^2 \int [\bar{\Psi}_{\mathrm{f}}(x')\gamma_\mu A_{\mathrm{f}}^{\mu}(x')G(x'-x)\gamma_\nu A_{\mathrm{i}}^{\nu}(x)\Psi_{\mathrm{i}}(x)]d^4x d^4x' \tag{3.14}$$

$$S_{\mathrm{fi}}^{B} = -e^2 \int [\bar{\Psi}_{\mathrm{f}}(x')\gamma_\mu A_{\mathrm{i}}^{\mu}(x')G(x'-x)\gamma_\nu A_{\mathrm{f}}^{\nu}(x)\Psi_{\mathrm{i}}(x)]d^4x d^4x' \tag{3.15}$$

where Ψ is the wave function of the electron and A_{i}^{μ}, and A_{f}^{μ}, are the wave functions for the incoming and outgoing photon respectively,

$$A_{\mathrm{i}}^{\mu} = \frac{\epsilon^{\mu}}{\sqrt{2\omega L^3}} e^{ik_\nu x^\nu} \tag{3.16}$$

$$A_{\mathrm{f}}^{\mu} = \frac{\epsilon^{\mu}}{\sqrt{2\omega L^3}} e^{-ik_{\nu}x^{\nu}} \tag{3.17}$$

and

$$\begin{aligned} G(x'-x) = \int \sum_{n=0}^{\infty} \sum_{m=1}^{2} [-i\theta(t'-t) u_n^m(x') \bar{u}_n^m(x) e^{-iE_n(t'-t)} + \\ i\theta(t-t') v_n^m(x') \bar{v}_n^m(x) e^{iE_n(t'-t)}] \frac{Lda_n}{2\pi\lambda^2} \frac{Ldp_n}{2\pi} \end{aligned} \tag{3.18}$$

with intermediate state electron energy

$$E_{nk} = \sqrt{m_{\mathrm{e}}^2 + p_{nk} + 2n_n B} \tag{3.19}$$

where k refers to the diagram, and is either A, or B. The momentum of the intermediate electron is either

$$p_{nA} = p_{\mathrm{i}} + \omega_{\mathrm{i}} \cos\theta_{\mathrm{i}} \tag{3.20}$$

or

$$p_{nB} = p_{\mathrm{i}} - \omega_{\mathrm{f}} \cos\theta_{\mathrm{f}} \tag{3.21}$$

This leads to the differential Compton scattering cross section (Sina, 1996, eqs. 3.15, 3.16, 3.24, D.50, D.52, p. 39–41 and in Appendix D),

$$\begin{aligned} \frac{d\sigma}{d\Omega_{\mathrm{f}}} =& \frac{\alpha^2}{(1-\beta_{\mathrm{i}}\cos\theta_{\mathrm{i}})(1-\beta_{\mathrm{f}}\cos\theta_{\mathrm{f}})} \frac{\omega_{\mathrm{f}}}{\omega_{\mathrm{i}}} \\ & \sum_{n=0}^{\infty} [|Z_{c1}(n)|^2 + |Z_{c2}(m)|^2 + \\ & \sum_{m=0}^{\infty} [Z_{c1}(n)^* Z_{c2}(m) + Z_{c1}(n) Z_{c2}(m)^*] J_{m+n-n_{\mathrm{i}}-n_{\mathrm{f}}}(\lambda^2 k_{\perp \mathrm{i}} k_{\perp \mathrm{f}})] \end{aligned} \tag{3.22}$$

with

$$Z_{c1}(n) = \sum_{sn} [\frac{D_{u,\mu}^{\mathrm{f,n,sf,sn}}(k_{\mathrm{f}}) H_{u,\mu}^{\mathrm{n,i,sn,si}}(k_{\mathrm{i}})}{\omega_{\mathrm{i}} + E_{\mathrm{i}} - (E_{n1} - i\Gamma_n/2)} + \frac{D_{u,\nu}^{\mathrm{f,n,sf,sn}}(k_{\mathrm{f}}) H_{\nu,\mu}^{\mathrm{n,i,sn,si}}(k_{\mathrm{i}})}{\omega_{\mathrm{i}} + E_{\mathrm{i}} + (E_{n1} - i\Gamma_n/2)}] \tag{3.23}$$

$$Z_{c2}(n) = \sum_{sn} [\frac{H_{u,\mu}^{\mathrm{f,n,sf,sn}}(k_{\mathrm{i}}) D_{u,\mu}^{\mathrm{n,i,sn,si}}(k_{\mathrm{f}})}{\omega_{\mathrm{i}} + E_{\mathrm{i}} - (E_{n1} - i\Gamma_n/2)} + \frac{H_{u,\nu}^{\mathrm{f,n,sf,sn}}(k_{\mathrm{i}}) D_{\nu,\mu}^{\mathrm{n,i,sn,si}}(k_{\mathrm{f}})}{\omega_{\mathrm{i}} + E_{\mathrm{i}} + (E_{n1} - i\Gamma_n/2)}] \tag{3.24}$$

$$
\begin{aligned}
H^{\mathrm{n,m,sn,sm}}_{T_n,T_m}(k) = [\epsilon_0[&(C_{1,n}C_{1,m} + C_{3,n}C_{3,m})\Lambda_{m-1,n-1}(k)+ \\
&(C_{2,n}C_{2,m} + C_{4,n}C_{4,m})\Lambda_{m,n}(k)]+ \\
\epsilon_-&(C_{1,n}C_{4,m} + C_{3,n}C_{2,m})e^{i\phi}\Lambda_{m,n-1}(k)+ \\
\epsilon_+&(C_{2,n}C_{3,m} + C_{4,n}C_{1,m})e^{-i\phi}\Lambda_{m-1,n}(k)+ \\
\epsilon_z[&(C_{1,n}C_{3,m} + C_{3,n}C_{1,m})\Lambda_{m-1,n-1}(k)- \\
&(C_{2,n}C_{4,m} + C_{4,n}C_{2,m})\Lambda_{m,n}(k)]]
\end{aligned}
\tag{3.25}
$$

$$
\begin{aligned}
D^{\mathrm{n,m,sn,sm}}_{T_n,T_m}(k) = [\epsilon_0[&(C_{1,n}C_{1,m} + C_{3,n}C_{3,m})\Lambda_{n-1,m-1}(k)+ \\
&(C_{2,n}C_{2,m} + C_{4,n}C_{4,m})\Lambda_{n,m}(k)]+ \\
\epsilon_-&(C_{1,n}C_{4,m} + C_{3,n}C_{2,m})e^{i\phi}\Lambda_{n-1,m}(k)+ \\
\epsilon_+&(C_{2,n}C_{3,m} + C_{4,n}C_{1,m})e^{-i\phi}\Lambda_{n,m-1}(k)+ \\
\epsilon_z[&(C_{1,n}C_{3,m} + C_{3,n}C_{1,m})\Lambda_{n-1,m-1}(k)- \\
&(C_{2,n}C_{4,m} + C_{4,n}C_{2,m})\Lambda_{n,m}(k)]]
\end{aligned}
\tag{3.26}
$$

$$\Lambda_{0,0}(x) = e^{-x/2} \tag{3.27}$$

$$\Lambda_{0,j}(x) = \sqrt{x/j}\Lambda_{0,j-1}(x) \tag{3.28}$$

$$\Lambda_{l,j}(x) = \frac{(l-1+j-x)\Lambda_{l-1,j-1}(x) - \sqrt{(l-1)(j-1)}\Lambda_{l-2,j-2}(x)}{\sqrt{lj}} \tag{3.29}$$

$$x = \frac{\lambda^2 k^2}{2} \tag{3.30}$$

$$\Lambda_{l,m}(k) = (-1)^{l+m}\Lambda_{m,l}(k) \tag{3.31}$$

$$\Lambda_{l,m}(0) = \delta_{l,m} \tag{3.32}$$

The photon normal modes from Shabad (1975) are used,

$$\epsilon^{(0)}_\mu = \frac{1}{\sqrt{k_\perp^2 + k_3^2 - k_0^2)}}(-k_0, k_1, k_2, k_3)^T \tag{3.33}$$

$$\epsilon^{(1)}_\mu = \frac{1}{\sqrt{k_1^2 + k_2^2}}(0, -k_2, k_1, 0)^T \tag{3.34}$$

$$\epsilon^{(2)}_\mu = \frac{1}{\sqrt{k_0^2 - k_3^2}}(k_3, 0, 0, -k_0)^T \tag{3.35}$$

$$\epsilon^{(3)}_\mu = \frac{1}{\sqrt{k_\perp^2(k_0^2 - k_3^2)(k_0^2 - k_\perp^2 - k_3^2)}}(-k_0 k_\perp^2, (k_0^2 - k_3^2)k_1, (k_0^2 - k_3^2)k_2, k_\perp^2 k_3)^T \tag{3.36}$$

The constants C_i cited by Sokolov et al. (1968) and Sina (1996) are given by

$$C_1 = \frac{1}{2\sqrt{2}} B_3 (A_3 + A_4) \tag{3.37}$$

$$C_2 = \frac{1}{2\sqrt{2}} B_4 (A_4 - A_3) \tag{3.38}$$

$$C_3 = \frac{1}{2\sqrt{2}} B_3 (A_3 - A_4) \tag{3.39}$$

$$C_4 = \frac{1}{2\sqrt{2}} B_4 (A_3 + A_4) \tag{3.40}$$

$$A_3 = \sqrt{1 + p_z/\epsilon} \tag{3.41}$$

$$A_4 = \frac{\epsilon\tau}{E} \sqrt{1 - p_z/\epsilon} \tag{3.42}$$

$$B_3 = \sqrt{1 + \tau m_\mathrm{e}/\epsilon_\perp} \tag{3.43}$$

$$B_4 = \sqrt{1 - \tau m_\mathrm{e}/\epsilon_\perp} \tag{3.44}$$

where $\tau = 1$ for spin parallel and $\tau = -1$ for spin anti parallel to the magnetic field axis.

The cross sections are sharply peaked functions. Figure 3.14 shows the cross sections for transitions from the Landau ground state with initial spin down summed over possible final Landau states and electron spins. Fifteen Landau levels have been taken into account, though much less Landau levels are required to obtain an accurate cross section value for photons with energies in the regime shown here. The reason is that the state summed cross sections at energies $\approx \omega_{n_\mathrm{f}}$ are dominated by the transitions to Landau level n_f. The same has been observed in the case of the absorption cross sections (see Fig. 3.11).

Figure 3.15 shows the scattering cross sections for the case of an excitation of the interacting electron to Landau level $n_\mathrm{f} = 2$. In contrast to Fig. 3.12 the resonant behavior occurs at resonance energies ω_n with $n > 2$ contrary to the single resonance at ω_2 in the case of absorption. The reason that the cross section is suppressed at this point in the case of scattering is that the definition of scattering requires the photon to outlive the interaction, meaning that, it must have some energy left after the scattering process and therefore it must have an energy above the excitation threshold. The figure therefore must not be interpreted physically but is merely shown here to highlight this particular behavior of the scattering process. In the real world such a restriction of the possible outcome of the final electron Landau level will never occur. The question of the resonant behavior at higher Landau levels with energies $\omega_{n>2}$ remains. Equation 3.22 contains one sum over the final electron Landau levels and another one for the summation of the possible intermediate Landau levels. These intermediate levels are the states the virtual electrons (straight horizontal lines in Fig. 3.13) may reside in. Figure 3.16 shows the same scattering cross section but with the intermediate level artificially restricted to $n_\mathrm{v} = 3$. In this case the resonant behavior occurs only at the ω_3 resonance. The higher resonances are triggered by transitions with intermediate Landau level $n_\mathrm{v} > 3$ accordingly.

Looking at the Feynman diagrams for cyclotron emission, absorption, and scattering

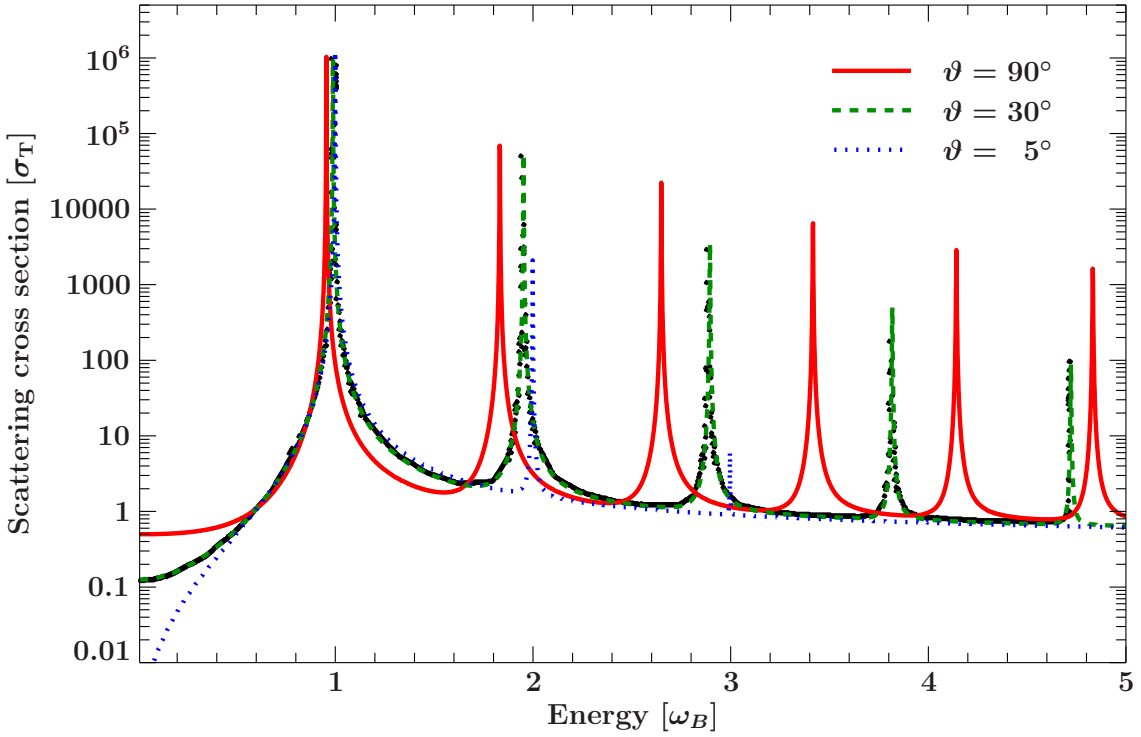

Figure 3.14.: Cyclotron scattering cross sections for a magnetic field of $B = 0.1\,B_{\rm crit}$ with respect to the photon energy in units of the resonance energy $\omega_{\rm B}$. Three angles of the incoming photon with respect to the B-field axis, $\vartheta = 90°, 30°, 5°$, are shown as solid, dashed, and dotted (blue) lines, respectively. The black points show the scattering cross sections calculated by Harding & Daugherty (1991, solid line in Fig. 1 in there) for an incoming angle of 30°.

(Figs. 3.3, 3.10, and 3.13), another question arises: is it necessary to include CRSF absorption and emission into the MC process, or is it already included in the scattering cross section? An answer is given, for example, by Daugherty & Ventura (1978, Fig. 2 therein): when the kinematic conditions (Eqs. 4.4 and 4.3) are satisfied, the left side of diagram 3.13 becomes equivalent to the sequential pair of the diagrams shown in Figs. 3.3 and 3.10, for which the virtual state approaches the mass shell of a real electron. This does generally not have to be the case because the kinematic conditions do not have to be fulfilled for virtual particles, or, as Harding & Preece (1989) puts it: the physical difference between these two treatments is that in the cyclotron absorption-emission picture, energy and momentum must be conserved at two steps because the intermediate state is a real state, while the virtual intermediate state in the scattering picture does not require strict energy-momentum conservation at each vertex. This results in an added intrinsic width and asymmetric resonance features for the scattering treatment.

It is only logical to make sure that the implementation used here is able to reproduce the cross sections from the original work. For this purpose, Fig. 3.17 shows the cross sections for all possible transitions between the vacuum polarization modes, as calculated with the new implementation, compared to the ones from Sina (1996). Their agreement shows

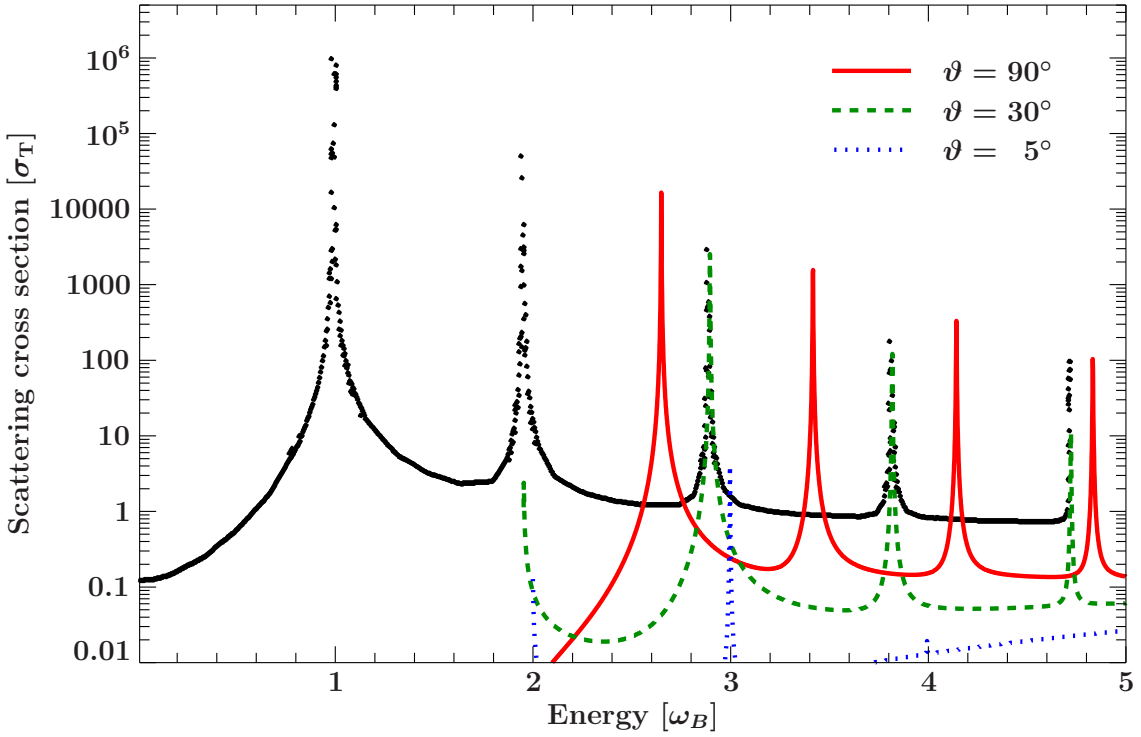

Figure 3.15.: Same as Fig. 3.14 but for excitations to the second excited Landau level, $n_f = 2$, only. The same data from Harding & Daugherty (1991) as in the previous plot are shown for reference.

B [B_{crit}]	0.01	0.12
T [keV]	3.00	15.00
μ	0.00	1.00
n_i	0	15

Table 3.7.: Table showing the valid parameter ranges for which cross sections can be obtained with the implementation of the derivation by Sina (1996) developed in the course of this work. These include the tested ranges only, the functions probably have a much wider domain of validity.

that the restructured code produces the same results. Advantages of the numerical and structural code tuning are the more robust functions, reliably evaluating the cyclotron scattering cross section in a large parameter regime, which is shown in Table 3.7.

In the following the cross sections will be further validated by comparing them to other works. Differences to other implementations will be discussed as well.

Canuto et al. (1971) derived simple approximations for the magnetic Thomson cross section the cases $\vartheta = 0$ and $\vartheta = \pi/2$, corresponding to photons perpendicular and parallel to the magnetic field, respectively. These approximations provide an easily viable way for roughly verifying the order of magnitude of more complex calculations. They agree surprisingly well with the correct cross sections at low energies below the first cyclotron resonance. Such a comparison has been performed by Gonthier et al. (2000) and is also shown in Fig. 3.18, which additionally shows the compact approximation found by Gonthier et al. (2000) for the scattering cross section in the case of photons moving parallel

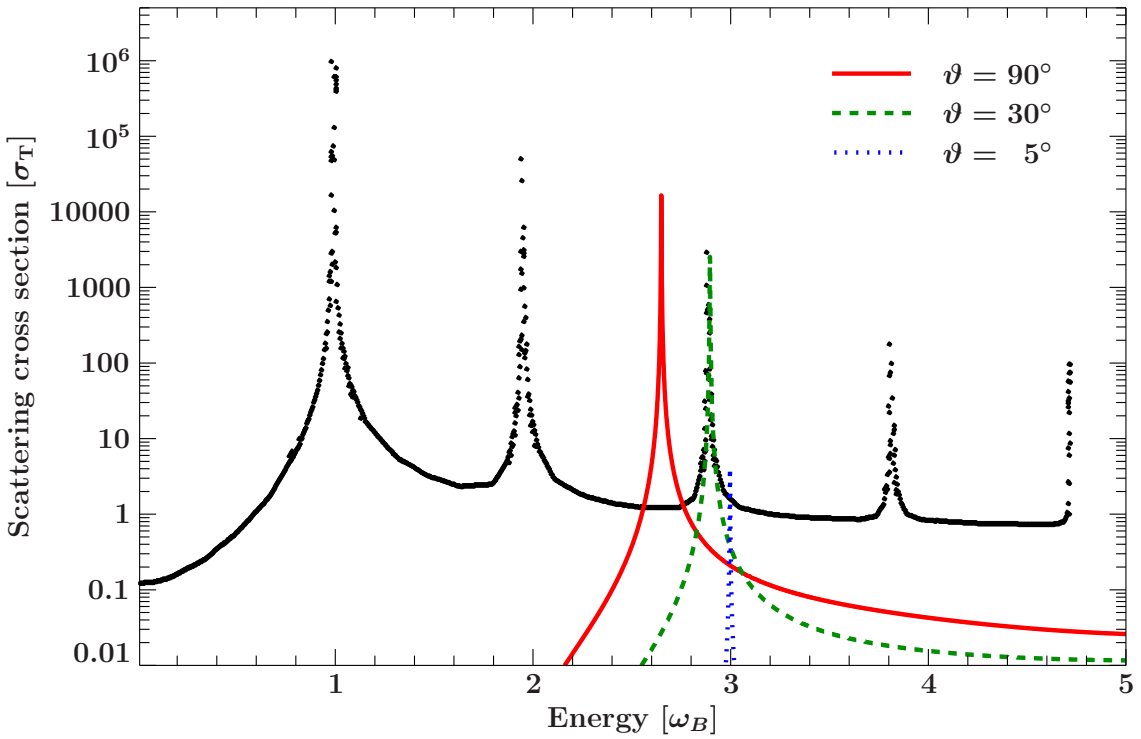

Figure 3.16.: Same as Fig. 3.15 but taking into account only transitions via the intermediate Landau level $n_\nu = 3$.

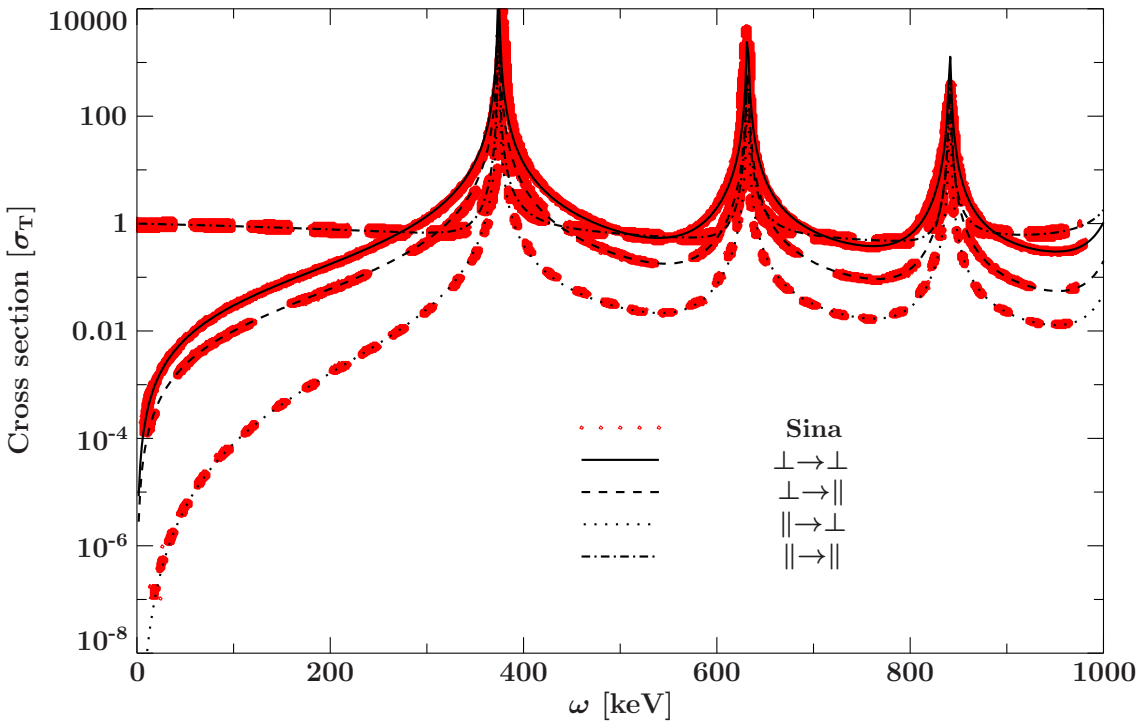

Figure 3.17.: Comparison to Sina (1996) showing all different polarization modes.

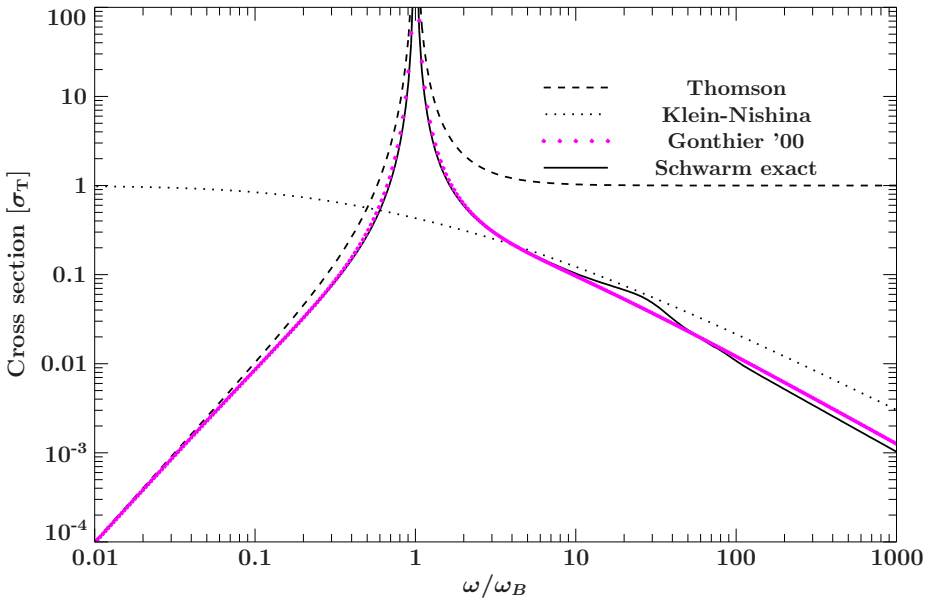

Figure 3.18.: Comparison to the approximation from Gonthier et al. (2000) (color points). The solid line shows the ST-based cross sections from this thesis. The dashed line shows the magnetic Thomson cross section from Canuto et al. (1971). The Klein & Nishina (1929) cross sections are shown as a dotted line. See text for an explanation of the feature at $\omega/\omega_B \approx 10$.

to the magnetic field axis, that is, $\vartheta = 0°$. Note that there is a typo in Eq. 7 from Gonthier et al. (2000). The correct formula for the magnetic Thomson cross section in the $\vartheta = 0°$ case is

$$\sigma_T = \frac{x^2}{2}(1/(x-B)^2 + 1/(x+B)^2)\,, \tag{3.45}$$

with $x = k/m_e c^2$. The Klein & Nishina (1929) equation is used for a comparison at higher energies where it seems to asymptotically converge toward the real cross sections. The approximation from Gonthier et al. (2000) fits the non-approximative cross sections from this work surprisingly well. Unfortunately, such an approximation is only available for the $\vartheta = 0°$ case and only one cyclotron resonance is taken into account, which impedes its use in MC simulations of cyclotron lines. The bump at $\sim 20\,\omega/\omega_B$ results from the maximum number of 15 Landau levels considered here for the cross section calculation. The number of Landau levels can easily be increased, but the summation over more than 15 Landau levels is quite pointless for the application in MC simulations because it increases the calculation time and the observable energy regime is far below ω_{15}. Even if this energy regime will be made accessible by future X-ray missions the observation of high order cyclotron lines is questionable since their depths decrease with the order of the resonance. Also, for an intermediate magnetic field strength of $\sim 0.067\, B_{\rm crit}$[1] the energy of the 15th Landau level equals the rest energy of an electron and cyclotron scattering may loose the role of being the dominant process (see, e.g., Sina, 1996).

[1] Intermediate in terms of the field strengths considered in this work.

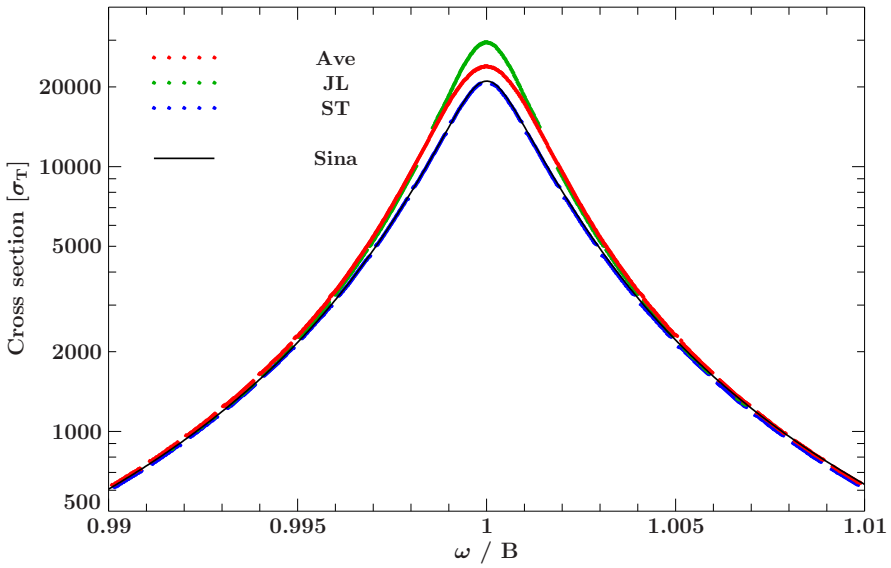

Figure 3.19.: Comparison to Gonthier et al. (2014, Fig. 5, right) within the first cyclotron resonance. The topmost (green), lowermost (blue), and middle (red) lines show the scattering cross sections derived by Gonthier et al. (2014) using the electron wave functions from Johnson & Lippmann (1949), Sokolov et al. (1968, ST), and an average of both, respectively. The black solid line shows the cross sections used in this work, which use the ST wave functions as well and therefore coincide with the corresponding calculations from Gonthier et al. (2014).

The usage of the JL wave functions (see, e.g., Daugherty & Harding, 1986) leads to deviations within the resonance compared to cross sections derived using the ST formalism (Gonthier et al., 2014). For validating the cross sections used in this work by yet another independent derivation and in order to err on the side of caution regarding the usage of the physically more meaningful ST wave functions, Fig. 3.19 shows a comparison to the work from Gonthier et al. (2014, Fig. 5 therein). They used the same formalism as Sina (1996), but restricted themselves on the $\vartheta = 0°$ case and derive the scattering cross sections using both the JL and the ST wave functions. The figure compares the cross sections right within the first resonance. The JL wave functions overestimate the cross sections within the resonance compared to the ST wave functions. The cross sections used in this work are in agreement with the ST version of Gonthier et al. (2014), as expected.

Mushtukov et al. (2016) generalized the approach from Gonthier et al. (2014) for arbitrary angles. Therefore their cross sections are indirectly based on the work by Sina (1996) as well and should agree to the ones used in this work. The deviations are significant, though (Fig 3.20). They are especially pronounced for the || mode cross sections (O) in the $\vartheta = 90°$ case (right side). The cross sections from Mushtukov et al. (2016) drop slightly below the Thomson cross section (lower plot on the right side), rise almost vertically, and decline much slower after the first cyclotron resonance than the ones used in this work. The drop below σ_T and the asymmetric shape are unexpected and difficult to justify physically. In the case of an angle of $\vartheta = 60°$ to the magnetic field axis, the thermally averaged

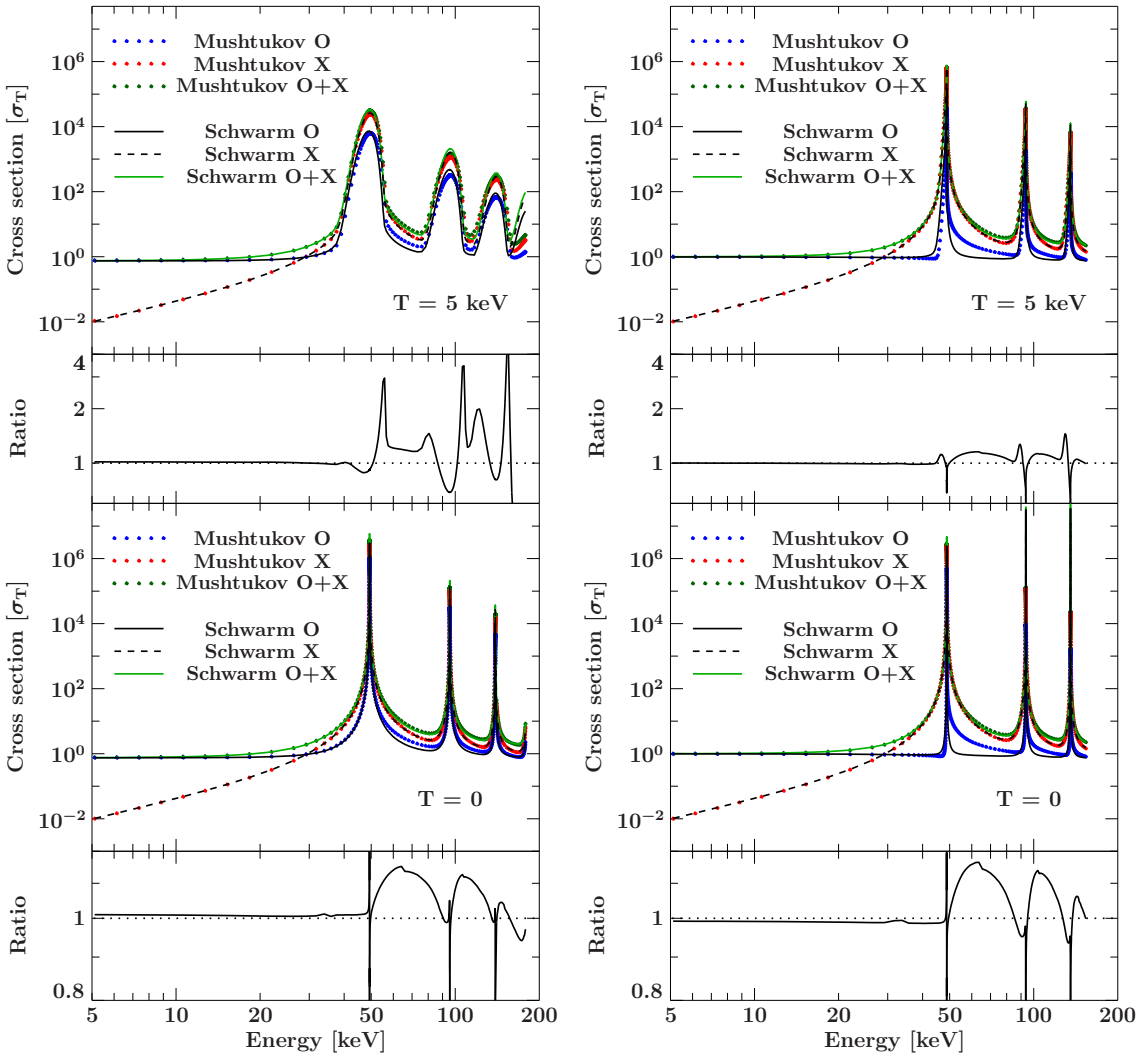

Figure 3.20.: Comparison of the ∥-mode (O) and ⊥-mode (X) cross sections from this work to the ones from Mushtukov et al. (2015) for an angle of 60° on the left side and for an angle of 90° to the magnetic field axis on the right side. The somewhat misleading O/X nomenclature has been used here in compliance with the notation by Mushtukov et al. (2015). The smaller panes show the difference between the different O-mode cross sections on a linear scale. The top plots show thermally averaged cross sections for a temperature $T = 5\,\mathrm{keV}$.

cross sections (left side of Fig. 3.20) show that the calculations from Mushtukov et al. (2016) overestimate the cross sections between the cyclotron resonances and underestimate them within the resonances. Unfortunately, the reason for this deviation has not been identified yet (Mushtukov, 2016a, priv. comm.). The process of thermally averaging will be discussed in detail in the next Section, parts of which are following, partially in verbatim, the corresponding Sections from Schwarm et al. (2017b).

3.6. Thermally Averaged Cross Sections

For the Monte Carlo simulation of cyclotron lines, which will be discussed in detail in the next Chapter, the path length of a photon must be sampled. This requires the knowledge of the photon mean free path, which essentially corresponds to the thermally averaged scattering cross section. More specifically, the mean free path of a photon in a CRSF medium is the inverse of the sum over the cross sections of all possible CRSF related interactions between the photon and its possible scattering partners, which throughout this work are assumed to be only electrons (see Eq. 3.48 below). This calculation not only involves a summation over all possible final Landau levels and spin states of the electrons, but also a summation over all possible intermediate states. Furthermore, the electrons have a temperature dependent continuous momentum distribution parallel to the magnetic field axis. It leads to Lorentz boosting of the scattering photons in the electrons' rest frames and gives rise to an integration over possible initial electron parallel momenta. Finally, the cross sections are summed over final polarization states and averaged over the initial ones for a polarization averaged mean free path.

The calculation of the mean free path therefore relies on the integration of the scattering cross section σ over a range of electron momenta p, effectively averaging the cross section over the parallel electron temperature (Daugherty & Harding, 1986),

$$\langle \sigma(\omega,\mu) \rangle_{f_\mathrm{e}} = \int_{-\infty}^{+\infty} \mathrm{d}p\, f_\mathrm{e}(p,T)(1-\mu\beta)\sigma_\mathrm{rf}(\omega_\mathrm{rf},\mu_\mathrm{rf}) \,, \tag{3.46}$$

where $\mu = \cos\vartheta$, ϑ is the angle between the photon's direction and the magnetic field axis, ω is the photon energy, and $\beta = v/c$. The subscript "rf" refers to values in the rest frame of the electron. These parameters in the electron rest frame are the reason that an analytic integration is impossible: the photon energy and momentum are relativistically coupled to the electron momenta. $f_\mathrm{e}(p,T)$ is the electron parallel momentum distribution. Here a one-dimensional relativistic Maxwellian with temperature T is used (see Fig. 3.21),

$$f_\mathrm{e}(p,T) \propto \exp\left(-\frac{1}{k_\mathrm{B}T}\left(\sqrt{m_e^2c^4+p^2c^2}-m_ec^2\right)\right) \tag{3.47}$$

The mean free path, λ, is then given by (Araya & Harding, 1999)

$$\lambda(\omega,\mu) = 1/\langle \sigma(\omega,\mu) \rangle_{f_\mathrm{e}} \,. \tag{3.48}$$

The numerical evaluation of Eq. 3.46 is closely related to the evaluation of the probability distribution of the electron momentum (Araya & Harding, 1999),

$$F(p) \propto \int_{-\infty}^{p} \mathrm{d}p'\, f_\mathrm{e}(p',T)(1-\mu\beta)\sigma_\mathrm{rf}(\omega_\mathrm{rf},\mu_\mathrm{rf}) \,, \tag{3.49}$$

which is required in Monte Carlo simulations for finding the momentum of the photon's

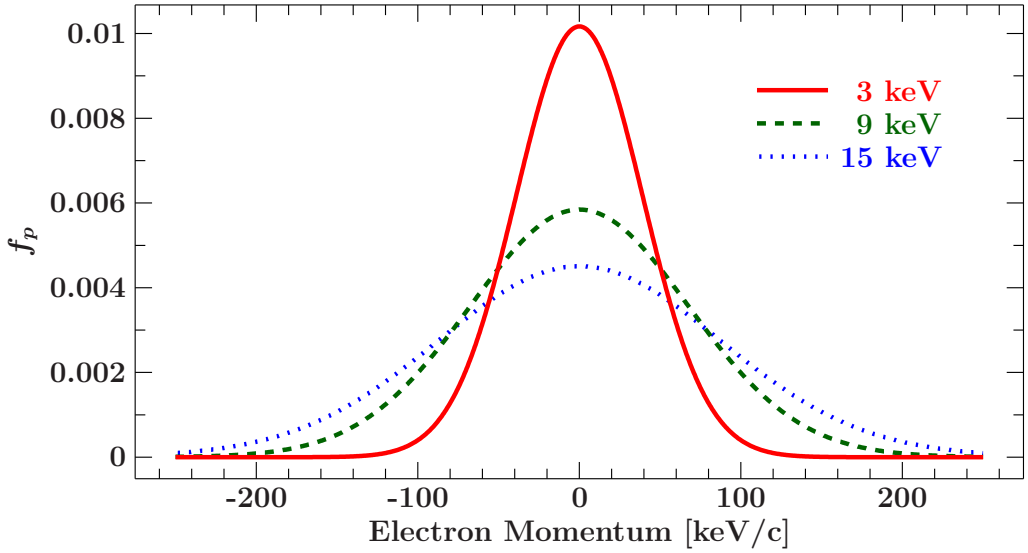

Figure 3.21.: Electron momentum distribution for different temperatures normalized to unity.

scattering partner. The total inverse mean free path, calculated by Eq. 3.46, accounts for all possible electron momenta and is used to normalize $F(p)$ to unity. By searching for the momentum p for which $F(p) = \mathrm{Rn}$, with a random number $0 \leq \mathrm{Rn} \leq 1$, the parallel momentum of the scattering electron can be sampled.

Figure 3.22 shows another example for the scattering cross section σ for transitions from the Landau ground state with initial spin down to a final state with spin down summed over the first five possible final Landau levels. A slight shift of the position of the resonances to higher energies occurs for smaller angles of the photon to the magnetic field. The cross sections' sharply peaked shapes make them difficult to be integrated numerically.

In order to calculate $F(p)$ for a given magnetic field, temperature, photon energy, and angle, an adaptive Simpson integrator (McKeeman, 1962) is used. The thermal momentum distribution $f_\mathrm{e}(p,T)$ becomes very small for large absolute values of the electron momentum. Therefore the numerical integration limits were set to $\sim \pm m_\mathrm{e}c^2$. They cover a range much larger than the expected momentum range of the electrons. This way the $45k_\mathrm{B}T$ boundaries used by, for example, Araya & Harding (1999) are also covered for the temperature range of 3–15 keV. In the adaptive approach the integration interval is successively split into smaller intervals. The integrals of these intervals are approximated by integrating a suitable third order polynomial. The larger momentum range used compared to earlier works leads to only marginally increased computing time due to the adaptive nature of the integration method.

The splitting of the integration intervals has to be stopped when a suitable convergence criterion is fulfilled. Lyness (1969) shows that in fifth order approximation the maximum error of the integrator can be estimated as

$$\epsilon = \frac{1}{15} \sum_i F_{a_i}^{c_i} - \left(F_{a_i}^{b_i} + F_{b_i}^{c_i}\right), \tag{3.50}$$

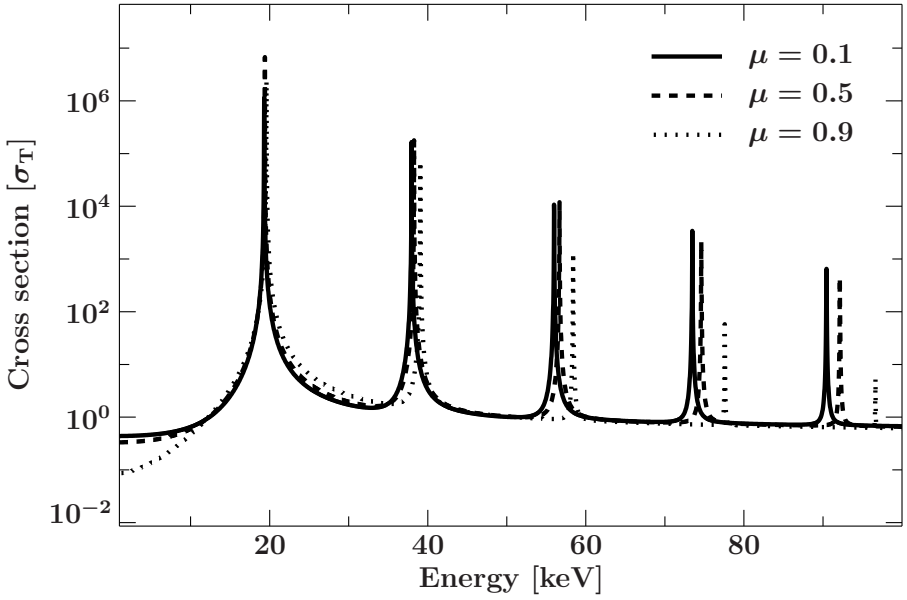

Figure 3.22.: Scattering cross section as a function of rest frame energy for exciting an electron in initial Landau level $n_i = 0$ with spin down to level n_f with $n_i \leq n_f \leq 6$ and final spin down within a magnetic field of strength $B = 0.0385\ B_{crit}$, resulting in a fundamental cyclotron resonance at ∼20 keV. The solid, dashed, and dotted lines show cross sections for $\mu = \cos\vartheta = 0.1, 0.5, 0.9$, corresponding to angles between the path of the incoming photon and the B-field direction of 84.°2, 60°, and 26.°8, respectively. Figure from Schwarm et al. (2017b).

where $F_{a_i}^{c_i}$ and $(F_{a_i}^{b_i} + F_{b_i}^{c_i})$ are the numerical estimates for the integrals over the interval $[a_i, c_i]$ before and after bisecting the interval. A relative maximum error of $1/15$ is chosen as a convenient compromise between accuracy, calculation time, and table size. The error is halved in each recursion step to ensure that the total error estimate remains below the chosen maximum error for the total interval.

The revised implementation of the code developed by Sina (1996) is employed for the calculation of the scattering cross sections as described above. The original code has been used in the MC simulation from Araya (1997). This MC simulation has been employed by Schönherr (2007) to calculate the Green's functions necessary for their CRSF fitting model. The thermally averaged cross sections used in the Araya (1997) code differ from the ones calculated by Harding & Daugherty (1991) as discussed by Schwarm et al. (2012). Schwarm (2010) verified that the origin of this difference lays in the integration of the cross section code into the MC simulation rather than the cross section calculation itself. The revised implementation of the Sina (1996) code successfully reproduces the profiles from Harding & Daugherty (1991). Harding & Daugherty (1991) compare the cyclotron absorption and scattering cross sections against the background of using the absorption cross section as an approximation for the more complex scattering cross section. They show thermally averaged cyclotron cross sections for different angles, temperatures, and magnetic fields. Figure 3.23 from Schwarm et al. (2012) shows a direct comparison of the

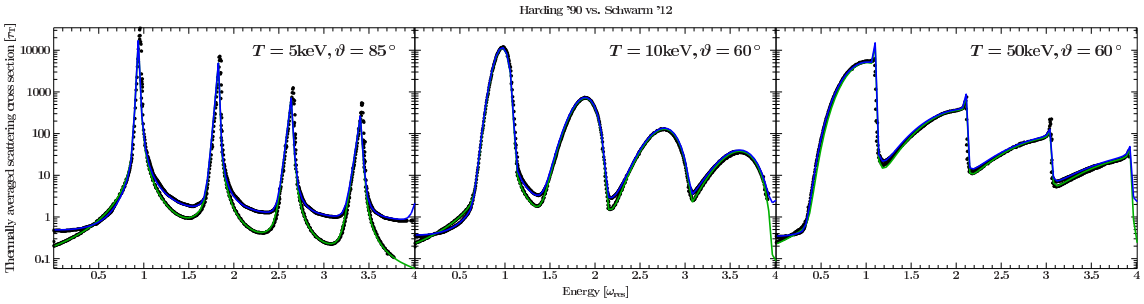

Figure 3.23.: Figure from Schwarm et al. (2012): comparison of the cross sections used in this work (solid lines) to the ones from Harding & Daugherty (1991, black points). The upper line (blue) shows the scattering cross sections. The lower one (green) shows the absorption cross sections. Both are shown for different combinations of the electron parallel temperature and the photon angle to the magnetic field axis as indicated in the plots.

thermally averaged cross sections for cyclotron scattering and absorption used in this work to the ones from Harding & Daugherty (1991). Both variants agree very well despite that they are based on different electron wave functions. Harding & Daugherty (1991) used the JL electron wave functions. The cross section from Schwarm et al. (2012) are based on the ST wave functions and agree with the ones used in this work aside from technical changes in the implementation. The diverging usage of the JL and ST wave functions does not seem to have any influence on the thermally and, even more important, spin and polarization averaged cross sections. This result stands in direct contrast to the finding of Mushtukov et al. (2016). They explicitly state that "a small difference [to Harding & Daugherty (1991)] in the [averaged] cross section at the resonance exists because the Sokolov-Ternov wave-function are used [...] instead of the Johnson-Lippmann wave functions" (Mushtukov et al., 2016). The reference given by Mushtukov et al. (2016) for the existence of a principle deviation in the CRSF cross sections between the usage of JL and ST wave functions is the work by Gonthier et al. (2014). It was found to agree with this work. Figure 3.19 shows a direct comparison to the crucial figure from Gonthier et al. (2014). The cross sections used in this thesis agree with the cross sections derived by Gonthier et al. (2014) using the ST electron wave functions for the special case of $\vartheta = 0°$. The difference between the usage of JL and ST wave functions does not lead to a significant deviation in the averaged cross sections as seen in Fig. 3.23. It seems therefore that the thermally averaged cross sections derived by Mushtukov et al. (2016) do not agree with the ones derived by Harding & Daugherty (1991) due to an another reason and not because of the different electron wave functions used by Harding & Daugherty (1991). Furthermore, it should be noted here that the left side of Fig. 2 from Mushtukov et al. (2015) does not show the polarization dependent thermally averaged cross sections for an angle of 60°, as indicated in the figure, but for an angle of 45° instead (Mushtukov, 2016b, priv. comm.). The notation used by Mushtukov et al. (2015) and Mushtukov et al. (2016) is not optimal since they actually use the same polarization modes as the ones used by Araya & Harding (1999), that is, pure vacuum polarization modes (see, e.g., Adler, 1971; Shabad, 1975), at least for their Fig. 2 (Mushtukov, 2016c, priv. comm.). Their modes should therefore better be referred

to as “parallel”, $\parallel$, and “perpendicular”, $\perp$, instead of “ordinary”, O, and “extra-ordinary”, X. One has to say, though, that there seems to be no strict convention and some works even provide both notations for the pure vacuum states at the same time (see, e.g., Nobili et al., 2008b). The general unexpected deviations between the non-averaged cross sections derived by Mushtukov et al. (2016) and the ones derived by Sina (1996) have already been discussed in Section 3.5 above.

4

SIMULATION

With the discussion of the cyclotron emission, absorption, and scattering processes the basis for the Monte Carlo simulation has been established. The simulation itself, `CycloSim`, will be described in this Chapter, following, partially in verbatim, the works by Schwarm et al. (2017a) and Schwarm et al. (2017b).

Simulations of CRSFs have been performed by various groups in the past. They can be divided into three classes: Monte Carlo (e.g., Wang et al., 1988, 1989; Araya & Harding, 1996, 1999; Schönherr et al., 2007b; Nobili et al., 2008a,b), Feautrier (e.g., Meszaros & Nagel, 1985; Alexander et al., 1989; Nishimura, 2008), and (semi-)analytic methods (e.g., Wang et al., 1993). Wang et al. (1988) provide an overview over the methods used in earlier works. Isenberg et al. (1998b) discuss the features of the fundamental approaches and use multiple methods for the generation of synthetic cyclotron lines in various parameter regimes. For optical depths of the order of 10^{-4}–10^{-3} τ_{T} Monte Carlo simulations are the suitable method (Isenberg et al., 1998b). Nobili et al. (2008a) and Nobili et al. (2008b) performed non-relativistic and relativistic MC simulations of cyclotron line spectra. The later work contains useful analytic expressions for the differential cross sections for the special case of transitions to the ground state and from the second excited level to the first excited Landau level. It should also be mentioned that Fernández & Thompson (2007) performed MC simulations of cyclotron lines in the realm of magnetars. From all of the calculations mentioned above only Schönherr et al. (2007b) provided a method for direct comparison between data and observations with the corresponding large grids of parameters. Also, mostly approximative forms of the complex cyclotron scattering

cross sections are used and often other simplifications are made such as the limitation to transitions involving only one or a few of the first Landau levels.

Araya & Harding (1996) performed a first comparison of simulated MC line shapes to data from the X-ray pulsar A 0535+26. The simulated cyclotron lines are too deep, though, because of a problem[1] with the implementation of the thermally averaged cross sections into the MC code (Schwarm, 2010; Schwarm et al., 2012, 2017b). Isenberg et al. (1998a) show MC simulated spectra of synthetic cyclotron lines for different system properties. In the second paper of their series (Isenberg et al., 1998b) the effects of geometry are studied by comparing synthetic spectra for slab and cylinder geometry. They discuss the Compton temperature, which is used as an equilibrium temperature, and specifically differentiate the cases of small, moderate, and large optical depths of the line forming medium. A comparison of the resulting spectra for moderate optical depths to this work is performed below. In a similar manner, but using their own MC code, Araya & Harding (1999) study the effect of optical depth and geometry, as well. The whole MC process is discussed in detail and coincides with the method used in this work with a completely independent, newly developed simulation code, which will be described in this Chapter. Schönherr et al. (2007b) turned the MC code from Araya & Harding (1999) into a fitting model: by convolving precalculated Green's functions, which are describing the response of a CRSF medium to monoenergetic photon injection, with arbitrary input continua, Schönherr et al. (2007b) disentangled the time consuming MC simulations from the choice of input continuum. This approach allowed for the development of a code which can be used to compare MC simulated spectra to observational data using standard X-ray astronomical data analysis packages such as XSPEC (Arnaud, 1996) or ISIS (Houck & Denicola, 2000).

A disadvantage of the earlier calculations, however, is that they are limited to very simple predefined geometries. In addition, while the general properties of the line behavior are correct, unfortunately the error in the integration of the scattering cross section code by Sina (1996, see Schwarm 2010 and Schwarm et al. 2012 for details) mentioned above remained. The same approach of tabulating the response of the simulated medium to the injection of monoenergetic photons is used in this work. A newly developed code is used for the generation of and interpolation from the precalculated Green's function tables, though. It features multiple interpolation methods and arbitrary parameters as needed for the desired cyclotron MC simulation generalization. Furthermore, the method has been generalized to allow for arbitrary data products to be stored and interpolated from such tables. The code has been made available in terms of the `table` module contained in the RCL (see Appendix B for details). Schönherr et al. (2007a) used their model to fit *INTEGRAL* data of the January 2005 outburst of V0332+53. An application of the new simulation and modeling codes presented here to *NuSTAR* data of the same source is shown in Section 6.1.

Building on these previous results and experiences a new simulation tool has been developed to calculate synthetic line profiles for arbitrarily complex cylindrical symmetric

[1] The code developed by Araya & Harding (1996) had been altered (without any kind of version control system) by at least 3 more people by the time I received it. It had been a very useful tool for comparison after replacing the mean free path calculation/interpolation with the scheme described in Section 4.7.1.

geometries. This generalization naturally requires a big computational effort which must be met with new strategies. The mean free path (MFP) tables used for the interpolation of the thermally averaged scattering cross sections play a key role in this task. They have been described in detail by Schwarm et al. (2017b, see also Section 4.7.1). In the following, the description and application of the full MC scattering code will be provided. It has been written with the prime goal of imprinting cyclotron lines on the continuum emission of astronomical X-ray sources and includes a working fit model. The XSPEC model code and the Green's tables necessary to generate synthetic cyclotron lines spectra are available online[2] together with instructions on how to use them. The discussion of more sophisticated physical scenarios and application to observational data will be performed in Chapter 6. Here, some examples of selected synthetic spectra are shown for illustration and for comparison to other works. First of all, the physical setup and the Monte Carlo approach will be described before discussing how these simulations can be sped up. The various classical accretion geometries will be explained as well. They are used later on and also in Chapter 6 to validate our results with the ones from earlier works.

4.1. Physical Setup

Here, the interactions of photons with electrons in strong magnetic fields via the cyclotron scattering process are considered. Other particles, such as protons, which might form "proton cyclotron lines" (Ibrahim et al., 2002, 2003) in the spectra at energies below the electron cyclotron lines, are neglected. There are several other processes altering the properties and paths of X-ray photons in the vicinity of magnetic fields near the critical field strength,

$$B_{\mathrm{crit}} = \frac{m_{\mathrm{e}}^2 c^3}{e\hbar} = 4.413 \times 10^{13}\,\mathrm{G}\,. \tag{4.1}$$

Photon splitting, which describes the process of splitting one photon into two photons, dominates over Compton scattering for very high magnetic field strengths and densities (Adler, 1971). Pair production becomes possible if the photon energy exceeds $2m_{\mathrm{e}}c^2$ (Daugherty & Harding, 1983). Apart from photon-electron interactions, Sina (1996) also analyzed the properties of Møller and Bhabha scattering where electrons are scattered off electrons or positrons, respectively. In the regime of interest, cyclotron scattering is the dominant process and therefore all other possible interactions are neglected, as discussed in Chapter 3.

As shown by Schwarm (2010) and Schwarm et al. (2017b, see also Chapter 3) the momenta of the CRSF forming electrons perpendicular to the direction of the B-field are quantized to discrete values corresponding to the Landau energy levels, $E_n \sim n \cdot 12\,\mathrm{keV} \cdot B/10^{12}\,\mathrm{G}$ (Canuto & Ventura, 1977). The electrons can move freely parallel to the field lines. Inelastic scattering of photons off these electrons leads to the formation of CRSFs which appear as absorption-like lines at the fundamental Landau energy E_1 and its integer multiples

[2] http://www.sternwarte.uni-erlangen.de/research/cyclo

(Gnedin & Sunyaev, 1974; Canuto & Ventura, 1977; Araya & Harding, 1996; Araya, 1997; Schönherr et al., 2007b; Schönherr, 2007, and references therein).

The cyclotron scattering cross section strongly depends on the scattering angle of the incident photons with respect to the magnetic field and the photon energy (Canuto et al., 1971; Canuto & Ventura, 1977; Ventura, 1979; Mészáros & Ventura, 1979). The angle $\vartheta_{\rm in}$ is measured with respect to the magnetic field axis and mostly specified by its cosine, $\mu_{\rm in} = \cos\vartheta_{\rm in}$. In the rest frame of an electron, the photons' energies and propagation angles are Lorentz boosted due to the electrons' motion parallel to the B-field axis. The inclusion of relativistic effects therefore makes accurate analytic approximations difficult (Canuto et al., 1971) because a photon's energy and angle are relativistically coupled in the electron rest frame.

Cyclotron absorption and emission processes as well as resonant scattering (see Chapter 3) generate highly complex line shapes. In contrast to Compton scattering, which does not absorb or create photons, the number of photons that contribute to the spectrum is not conserved (Bonazzola et al., 1979). A photon can be "quasi-absorbed" by an electron if it has the right energy and angle to excite the electron to a higher Landau level. Almost immediately, the electron will emit "spawned" photons during its successive de-excitation to the ground state. Since de-excitation preferentially takes place to the next lower Landau level (Latal, 1986), the majority of spawned photons will have energies corresponding to the energy difference between neighboring Landau levels. This is close to the fundamental energy E_1 regardless of the initial Landau level of the electron. The transition process continues until the ground state is reached, effectively increasing the number of photons within the medium. Especially for high optical depths such multi-photon processes become important (Alexander & Meszaros, 1991a,b). Therefore complex computational methods are necessary to determine the exact shape of cyclotron resonance features.

4.2. Monte Carlo Simulation

The advantage of a Monte Carlo simulation is that its photon tracing approach allows for the simulation of the radiative transfer in very complex setups of the scattering medium. In general, in a MC simulation a seed photon is generated at a place where the primary photons originate. The photon is assigned an energy, position, and direction. A random number is then drawn from an exponential distribution, which depends on the photon mean free path. This random number is the optical depth that the photon will travel. Precalculated mean free path tables are used to speed this step up.

The scattering geometry is realized in the simulation by describing the medium with a list of cylinders with arbitrary dimensions. They may be combined to model all kinds of cylindrically symmetric shapes of accretion columns. The geometry of each cylinder is parameterized by its inner — to allow for hollow cylinders — and outer radii and the distances of its bottom and top to the neutron star surface. The physical properties inside

are given by its homogeneous density[3], magnetic field, electron temperature, and velocity toward the neutron star. Multiple cylinders can be stacked on top of, or inside of each other in order to properly simulate parameter gradients. Simple one-cylinder geometries are used for comparison of the simulation results to other works. These classical geometries are illustrated in Fig. 4.5 together with their implied seed emission patterns.

The seed photons in a simulation run result from the configured photon sources. Different emission patterns are available for each individual source: a point source emits photons isotropically from its static origin, a line source corresponds to photon emission from a line along part of the magnetic field axis, meaning that the height of each photon above the hypothetical neutron star is sampled individually. A plane source describes an emitting plane perpendicular to the B-field axis at a given height. Variants emitting only photons upwards — in the direction of the B-field axis — or downwards are available for the point and plane source types to provide a convenient way of preventing unprocessed photons from showing up in the resulting data. The implementation of photon spawning is straightforward: successive photon generation and propagation of the spawned photons from the coordinates of the de-exiting electron to the point where the spawned photons are interacting with or escaping the medium ensure self-consistent treatment. The most time-intensive parts of processing are parallelized using MPI (MPI Forum, 1994), decreasing the required CPU time efficiently as shown in Fig. 4.9. Because the available computing power has increased significantly since earlier approaches to this problem, additional features could be introduced to the simulation. This allows to specify the conditions to be simulated in a more flexible way. For example, more complex physical settings for the accretion column, including velocity gradients, B-field gradients, and an inhomogeneous density stratification.

4.3. Description of the Scattering Process

The core of the MC simulation is the propagation of individual photons through a given CRSF medium. This process is illustrated by Fig. 4.1. Seed photons, generated by the configured photon sources, must be processed as well as spawned photons. The latter are originating from the transition of an electron to a lower Landau level. The seed photons are injected into the simulation and photons spawned during their interactions are added to the current list of photons and processed the same way. Figure 4.2 shows a visualization of the initial injection phase. The photon source is a point source radiating only upwards. Escaped photons are collected and binned to spectra. The less dense lower half sphere, formed by photons moving downwards, is produced by back-scattered photons. Some resonant photons (yellowish) can be seen. Their seemingly random path with very small steps, compared to the slab dimensions, can be envisioned by having a look at the full

[3]The density is usually calculated from the optical depth into a given direction and the corresponding extension of the cylinder. For the classical “slab 1-0” and “slab 1-1” geometries the direction parallel to the B-field axis is chosen, while in the “cylinder” geometry the optical depth is defined perpendicular to this axis (see Fig. 4.5)

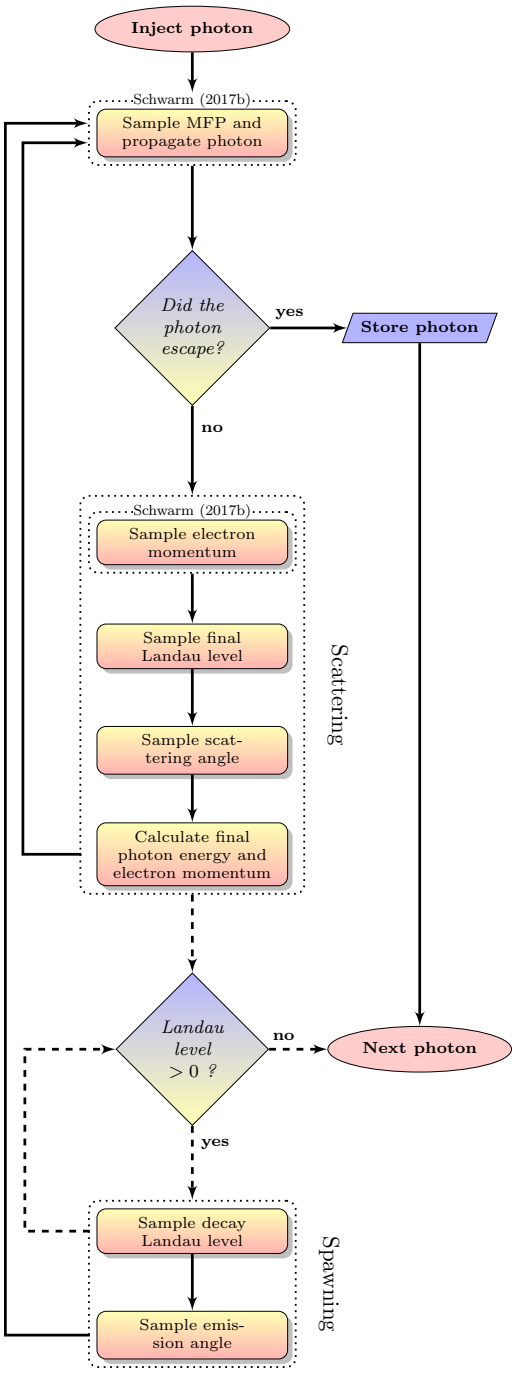

Figure 4.1.: Flowchart of the complete Monte Carlo process. The mean free path calculation and the electron momentum sampling block have been described detail by Schwarm et al. (2017b). Solid lines correspond to photon related steps, dashed lines show electron related processes. Diamond shapes depict decisions. Figure and caption from Schwarm et al. (2017a).

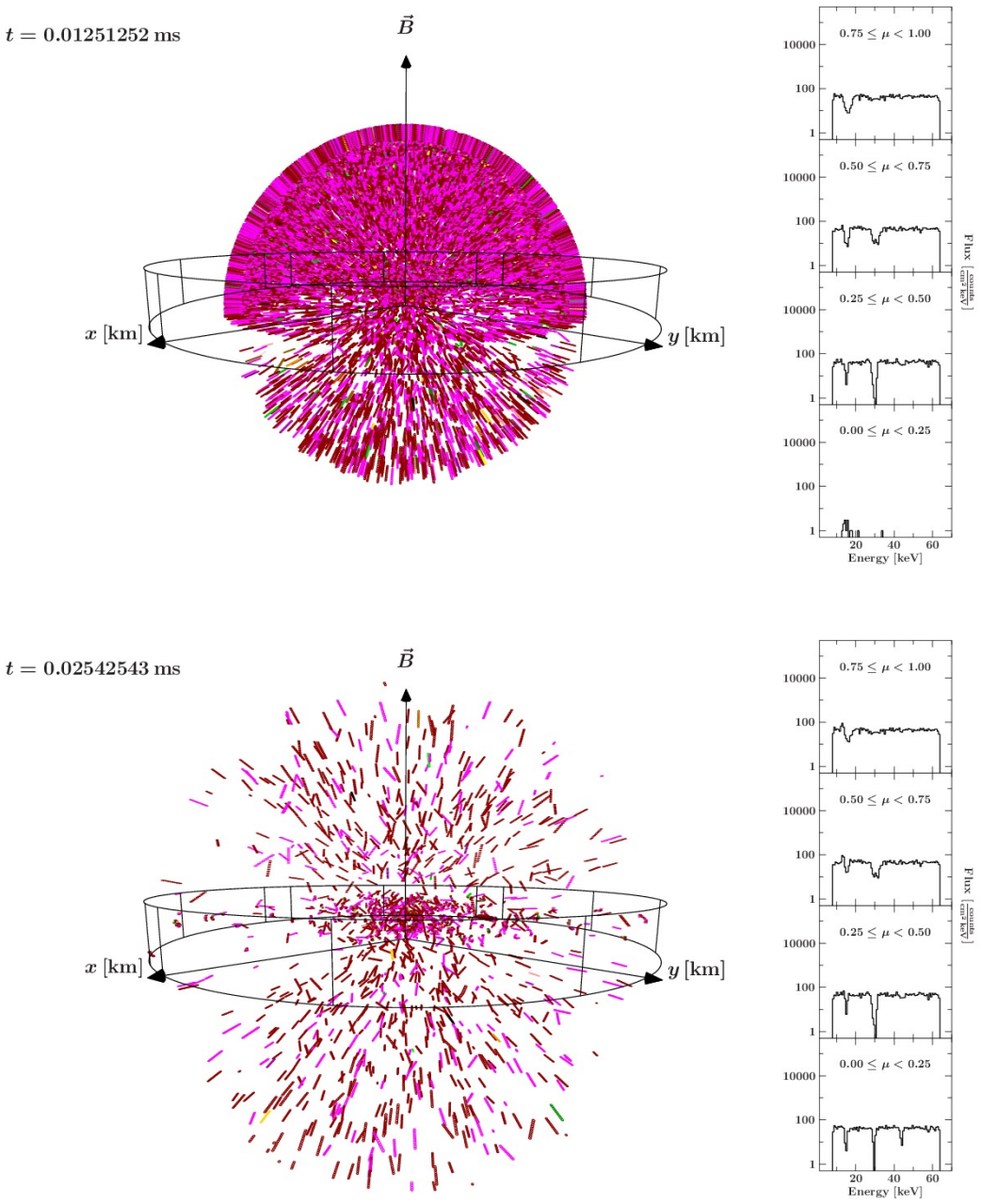

Figure 4.2.: Visualization of the simulation process. Seed photons are injected from an upwards directed point source at the center of the slab 1-0 bottom plane. The spectra on the right side are generated from photons escaping the slab in four angular regions. The top panel shows photons escaping roughly parallel to the B-field axis. This kind of emission is often referred to as pencil-beam emission. Fan-beam photons — escaping almost perpendicular to the magnetic field — are shown in the bottom panel. The two most prominent colors show photons above and below the resonance energy. The rare photons of other colors have energies very close to a cyclotron resonance and therefore a very high probability of being scattered.

movie (see Appendix A.2). The majority of photons are continuum photons sufficiently far away from the resonances to escape the slab unhindered. The pencil-beam-like spectra are built up first because the slab is extended much farther in the direction perpendicular to the magnetic field and therefore pencil-beam-like photons are escaping first due to geometrical reasons.

The choice of input continuum is essential for the simulation of synthetic cyclotron lines. This seed photon spectrum is reprocessed via cyclotron scattering and for harder input continuua more spawned photons are produced because more excitations to higher Landau levels take place. The formation of the accretion column and the related continuum radiation is by no means trivial and continuum photons are produced by various physical processes. In order to allow for all kinds of continuum models, the dependence of the cyclotron line model on the input continuum has been shifted to the post-simulation phase by using the Green's function mechanism described by Schönherr et al. (2007b): photons are injected for multiple energies separately and the escaping photons are binned to spectra for multiple viewing angles. The resulting spectra are normalized to the input flux in each angular bin. This yields the Green's functions, which are normalized to unity. For input energies away from the resonance energy, where the medium is optically thin, the resulting Green's functions look like δ-functions. For resonant input photons, on the other hand, non-zero probabilities for final photon energies around the fundamental cyclotron line are observed. Figure 4.3 shows Green's functions with respect to the output energy for three different input energies. Input energies below, at, and above the resonance energy are shown. The δ-function-like peak is suppressed in the case of a resonant input energy in favor of strong photon spawning (dashed line) around the resonance energy. This illustrates the origin of the line wings observed in synthetic CRSF spectra (see, e.g., Isenberg et al., 1998b; Araya & Harding, 1999; Schönherr et al., 2007b, and this work). The spectrum for arbitrary input continua can be calculated by convolving the Green's functions with the input continuum (Schönherr, 2007),

$$F_{\mathrm{out}}(E_0) = \int F_{\mathrm{in}}(E) G(E \rightarrow E_0) dE \tag{4.2}$$

where F_{in} and F_{out} are the input and output spectrum, respectively, and $G(E \rightarrow E_0)$ is the probability for a redistribution of input flux from energy E to energy E_0 (i.e., the Green's function). This way the choice of input continuum is deferred to the time of model evaluation. The Green's function approach has one drawback though: the influence of CRSF processes on the dynamic accretion column parameters, such as the electron temperature and the radiation pressure, is ignored. Therefore the affect of cyclotron scattering on the input continuum is neglected. The simulation does, however, store some simulation data products, such as the energy transferred from the interacting photons to the medium that can be used for estimating the error made by this assumption. For the optical depths considered in this work, a significant contribution to the overall energy balance was not recognized. At least not to an extent that would justify the vastly increased complexity of an iterative approach.

Each photon is propagated according to its current path length, which is sampled from

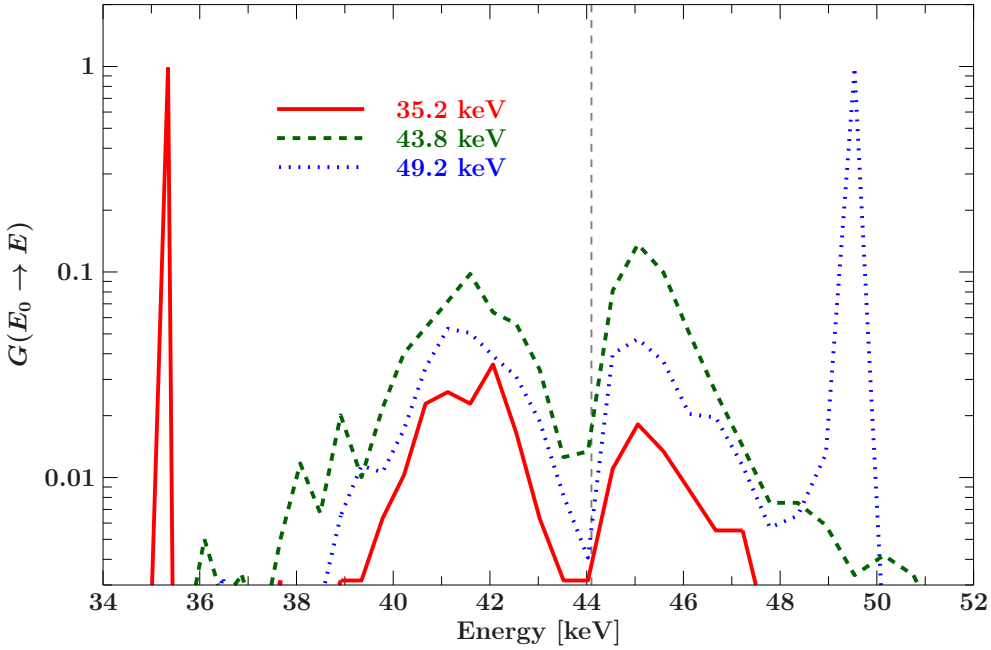

Figure 4.3.: Green's functions for input energies below (red solid line), at (green dashed line), and above (blue dotted line) the resonance energy (35.2, 43.8, and 49.2 keV, respectively). The vertical dashed line marks the position of the resonance energy (see Eq. 3.12): from the magnetic field $B = 0.09\, B_{\rm crit}$ and the cosine of the viewing angle $\mu = 0.063$ follows a resonance energy $E_{\rm res} \approx 44.1$ keV. The Green's functions have been calculated for a cylinder geometry and a temperature of $T = 6$ keV.

the mean free path tables provided by Schwarm et al. (2017b). The photon is stored to a file in FITS format if it escapes the medium and the simulation starts with the next seed photon. Otherwise the momentum of the interacting electron is sampled, again using precalculated tables. The electrons are assumed to be in the ground state and the excitation of electrons through other processes than resonant cyclotron scattering is neglected. This is justified by the comparably small time scales of the electron decay compared to the collisional excitation rate (Bonazzola et al., 1979; Latal, 1986; Arons et al., 1987; Araya, 1997; Isenberg et al., 1998b). The electrons can be excited to higher Landau levels in the course of resonant cyclotron scattering, though. The final Landau level for each interaction is sampled by comparing the scattering cross sections for all possible final levels below the maximum Landau level $n_{\rm f,max}$, which has been set to 5 for the simulations performed here[4], in compliance with the number of Landau levels taken into account for the MFP table calculations. In a similar manner, the scattering angle is sampled by assigning a random number to the cumulative angular distribution gained by integrating the cross section over all possible final photon angles. The kinematic calculations can be carried out

[4]The maximum number of Landau levels used in the simulation is read from a configuration file. This file provides multiple other settings as well, such as the maximum electron momentum taken into account and the maximum number of recursive steps for numerical integrations. All parameters, apart from physical constants such as, e.g., the electron mass, can be modified this way for each simulation run individually.

once the initial properties of the interacting electron and photon have been sampled, from the conservation of energy and momentum (Araya & Harding, 1999)

$$\omega_\mathrm{i} + E_\mathrm{i} = \omega_\mathrm{f} + E_\mathrm{f} \tag{4.3}$$

$$\omega_\mathrm{i}\mu_\mathrm{i} + p_\mathrm{i} = \omega_\mathrm{f}\mu_\mathrm{f} + p_\mathrm{f} \tag{4.4}$$

gaining the final electron momentum (Sina, 1996)

$$p_\mathrm{f} = p_\mathrm{i} + \omega_\mathrm{i}\mu_\mathrm{i} - \omega_\mathrm{f}\mu_\mathrm{f}\,, \tag{4.5}$$

with initial and final identities marked with the subscripts i and f, respectively. The final energy is given by the solutions from the standard quadratic equation

$$\omega_\mathrm{f} = \frac{-b \pm \sqrt{b^2 - 4ac}}{2a} \tag{4.6}$$

with coefficients (Araya & Harding, 1999)

$$a = 1 - \mu_\mathrm{f}^2 \tag{4.7}$$

$$b = -2[\omega_\mathrm{i}(1 - \mu_\mathrm{i}\mu_\mathrm{f}) + E_\mathrm{i} - p_\mathrm{i}\mu_\mathrm{f}] \tag{4.8}$$

$$c = \omega_\mathrm{i}^2(1 - \mu_\mathrm{i}^2) + 2\omega_\mathrm{i}(E_\mathrm{i} - p_\mathrm{i}\mu_\mathrm{i}) + 2B(n_\mathrm{i} - n_\mathrm{f})m_\mathrm{e} \tag{4.9}$$

and

$$E_\mathrm{i} = m_\mathrm{e}\sqrt{1 + 2n_\mathrm{i}B + p_\mathrm{i}^2/m_\mathrm{e}^2} \tag{4.10}$$

These relations only hold if possible dispersion effects due to the magnetic field are ignored and only the solution of Eq. 4.6 with the minus sign is physically meaningful (Sina, 1996).

The photon altered by the scattering process is now further propagated, starting again with the mean free path interpolation. The electron will produce spawned photons during its de-excitation to the ground state if it was excited to a higher Landau level during the scattering process. The maximum possible number of spawned photons depends on the Landau level the electron is excited to. It is mainly determined by the energy of the initial photon in the electron rest frame. The intermediate Landau levels occupied by the electron during this process are sampled by making use of the corresponding cyclotron decay rates. De-excitation preferentially takes place to the next lower Landau level and produces a photon with an energy corresponding to the energy difference of the involved Landau levels. A detailed quantitative analysis of the corresponding decay rates can be found in Section 3.3. Although the spacing of the cyclotron resonances is slightly anharmonic, these photons have energies very close to the fundamental energy in the electron's rest frame. For Landau levels above the first excited state an electron emits multiple photons during its successive de-excitation to the next lower level until the ground state is reached. The angles of the emitted photons with respect to the magnetic field axis are sampled according to the angle dependent decay rates. All spawned photons are further propagated in the same way like the seed photons until they leave the medium. The spawned photons have to be boosted to the neutron star frame before they are further processed, since the

electron that re-emits a photon has some velocity component parallel to the direction of the magnetic field due to the electrons' thermal momentum distribution. The simulation code features the possibility to configure an additional velocity component of the simulated medium. This leads to an additional boosting factor for all photons entering the medium and can be used to simulate the bulk velocity of the accreting matter. An overview over the relevant frames of references is given in Section 3. In the simulation code an ordinary one-dimensional Lorentz transformation is used to boost the photons' four vectors to another frame of reference. Alternatively, the parameters of each photon essential for the cyclotron interactions, namely its energy k and angle $\mu = \cos\vartheta$, may simply be boosted into another frame of reference using (Araya & Harding, 1999, Eq. 37)

$$k' = k\gamma(1 - \beta\mu) \quad \text{and} \tag{4.11}$$

$$\mu' = \frac{\mu - \beta}{1 - \beta\mu} \,, \tag{4.12}$$

with the dimensionless velocity $\beta = v/c$ and the Lorentz factor $\gamma = \left(1 - \beta^2\right)^{-1/2}$. The light bending code from Falkner et al. (2017) is utilized in Section 6.4 (see also Schönherr et al., 2014) to transform simulated spectra from the rest frame of the neutron star into the frame of reference of an observer. This transformation allows for a comparison of simulated phase dependent CRSF spectra with measured ones and is necessary for the calculation of phase dependent cyclotron line spectra and emission patterns from a cylindrically symmetric accretion column throughout which a flow with relativistic velocities is expected (see, e.g., Becker & Wolff, 2007). The overall boosting of spawned photons, together with the slightly an-harmonic spacing of the Landau levels, is responsible for the formation of line wings around the fundamental cyclotron line. This apparent excess of photons occurs at energies slightly above or below the first resonance E_1.

4.4. Electron Momentum Sampling

In the following the connection between cyclotron resonances and the corresponding behavior of the sampled electron parallel momenta is illustrated, following, mostly in verbatim, the work by Schwarm et al. (2017b). The electrons' momenta perpendicular to the magnetic field are quantized. The momenta parallel to the B-field are distributed according to Eq. 3.47. The integration of the product of this distribution with the corresponding scattering cross sections leads to the cumulative distribution function (Eq. 3.49). During the MC simulation the scattering electron's parallel momentum is drawn from this distribution. The influence of this sampling process on the cyclotron line shape is illustrated in Fig. 4.4. It shows the momenta drawn during a simulation with respect to the scattering photons' energies. Scattering events involving photons incoming at angles of ~90°, 79°, 60°, 37°, and 1° to the magnetic field (from top to bottom) are shown. The setup of the calculation is the same as in Isenberg et al. (1998b) with a magnetic field $B = 0.0385\, B_{\mathrm{crit}}$, electron parallel temperature $k_{\mathrm{B}}T = 5\,\mathrm{keV}$, and a bottom-illuminated slab geometry of the line-

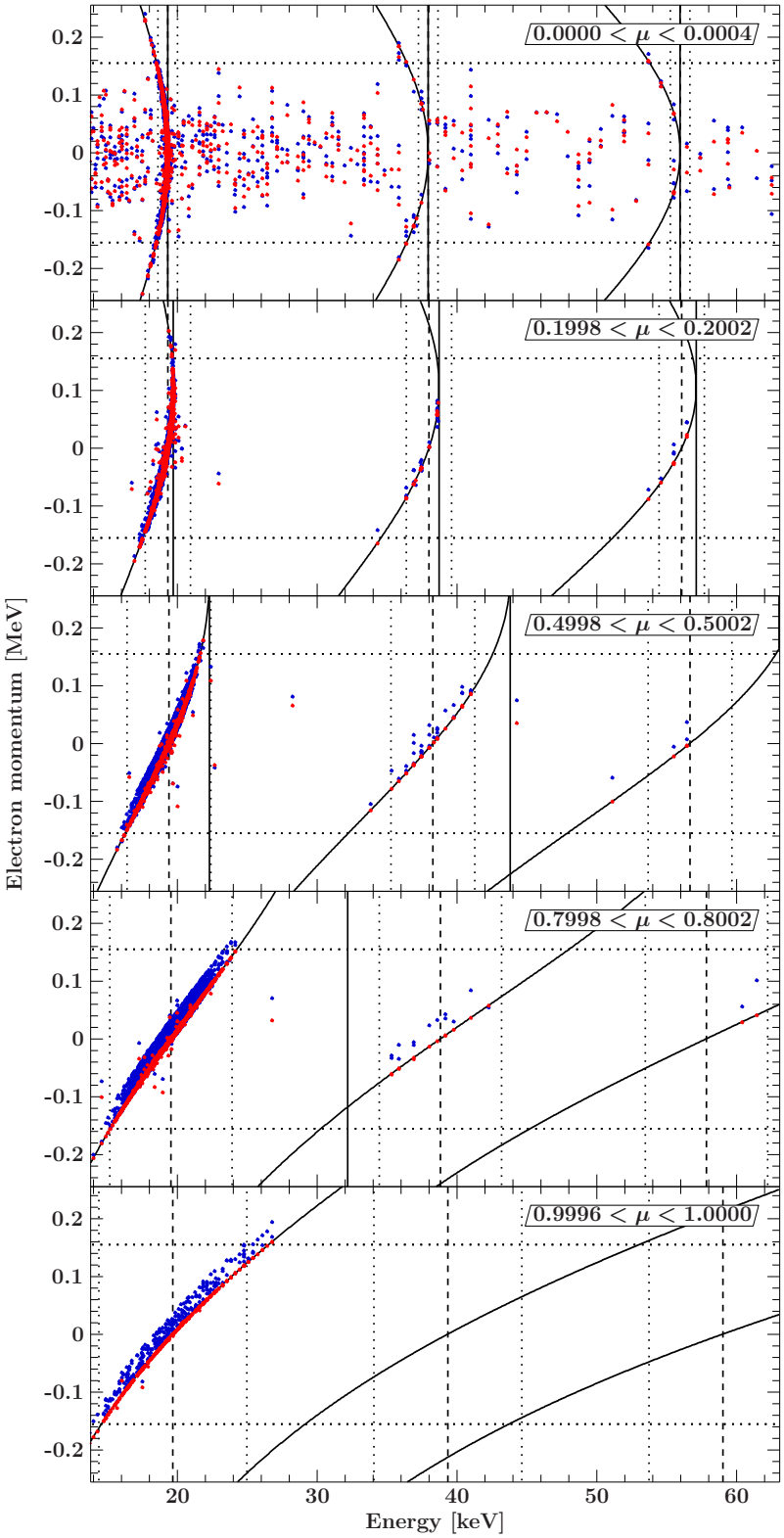

Figure 4.4.: Sampled electron parallel momenta for one MC run. Each point represents one scattered photon by its energy on the x-axis and the corresponding electron's momentum before (red) and after (blue) the scattering process on the y-axis (Schwarm et al., 2017b). See text for full description.

forming region. Vertical dashed lines show the cyclotron line energy, which is slightly shifted to higher energies for smaller angles to the magnetic field, because of the angular dependence of the resonance energy. This shift is often neglected by observers in favor of using the simplified 12-B-12 rule. Solid vertical lines mark the position of the cut-off energy beyond which no resonant scattering is possible. Dotted horizontal lines enclose the electron momentum range in which 99% of the electrons are located (assuming a relativistic Maxwellian, Eq. 3.47). Solid curved lines show the possible solutions for resonant scattering. The vertical dotted lines indicate the Doppler width of the cyclotron lines (see Eq. 4.15). The probability for photons to scatter off an electron with the right momentum to make the photon fulfill the resonance condition in the electron's rest frame is much higher. Therefore the events shown in Fig. 4.4 track the resonance condition (see, e.g., Daugherty & Ventura, 1978; Harding & Daugherty, 1991)

$$\sqrt{p^2c^2 + m_\mathrm{e}^2c^4} = pc\cos\vartheta + n\frac{B}{B_\mathrm{crit}}\frac{m_\mathrm{e}^2c^4}{\omega} - \frac{\omega}{2}\sin^2\vartheta\,. \tag{4.13}$$

Harding & Daugherty (1991) already discussed the solutions to this equation. They have to be found numerically and are often being referred to as zero line width solutions. They are shown as curved lines in Fig. 4.4. The resonance condition can only be fulfilled for photon energies below the cut-off energy[5],

$$\omega_\mathrm{cut}(n) = \frac{\sqrt{1 + 2nB/B_\mathrm{crit}} - 1}{\sin\vartheta} m_\mathrm{e}c^2\,. \tag{4.14}$$

The vertical solid lines in Fig. 4.4 mark the corresponding positions of the cut-off energies. No interaction involving the excitation of an electron to Landau level n occurs beyond that energy. In the following the zero line width solutions are described in energy-momentum space and physically motivated regimes are provided in which these solutions are expected to be fulfilled, that is, energy and momentum limits. Using this visualization, Schwarm et al. (2017b) showed, for the first time, simulated MC scattering events in the context of these zero line width solutions (and their limits) with the aim to establish an understanding of the complex cyclotron scattering process. Furthermore, this representation is used as a consistency check for the MC simulation. Schwarm (2010) performed a similar check using the MC code of Araya (1997) without the physically motivated limits in energy and momentum space. Only photons moving upwards or almost perpendicular to the column axis are shown. Therefore no decrease in electron momentum occurs. Numerically calculated solutions of Eq. 4.13 are shown in Fig. 4.4 as black solid curves. Vertical solid lines mark the positions of the cut-off energies corresponding to the three cyclotron resonances shown. Positive and negative electron momenta are possible to fulfill the resonance condition for photons with incoming angles almost perpendicular to the magnetic field axis and energies below the cut-off energy. At the cut-off energy a unique solution is possible for electrons with zero parallel momentum. For smaller angles to the magnetic field axis the momentum solutions deform, following the cut-off energy

[5]Despite the name this cut off energy has nothing to do with the cut off energy known from empirical continuum models.

which is shifting to higher energies. The sampled events are bound to a limited region of the energy-momentum space. The cyclotron resonance widths provide boundaries on the energy axes, since only photons whose momentum averaged mean free path is small enough for scattering to take place will appear in the figure. As an estimate, the full Doppler width for thermal cyclotron line broadening (Meszaros & Nagel, 1985),

$$\frac{\Delta E}{E} = \sqrt{8 \ln 2 \, \frac{k_\mathrm{B} T}{m_\mathrm{e} c^2}} \cos \vartheta \tag{4.15}$$

is used.

The electron momentum space is limited by the width of the relativistic Maxwellian momentum distribution. Its definition is used in Eq. 3.47 to calculate the momentum range in which 99% of the initial electrons reside. Therefore, the plasma temperature is the main parameter responsible for a limited spreading of scattering events in energy-momentum space (Mészáros, 1978). The boundaries of the energy-momentum space available for scattering events are shown in Fig. 4.4 as dotted vertical and horizontal lines respectively. Finally, the dashed lines in Fig. 4.4 show the cyclotron line energies where $n(\omega, \mu)$ is integer (see Eq. 4.18). For photons moving perpendicular to the B-field this line overlaps with the cut-off energy. Comparing the red points in Fig. 4.4, which mark the initial parallel momentum, with the blue points, which correspond to the electron momentum after the scattering process, shows that the electrons gain parallel momentum in the (projected) direction of the incoming photon. For angles perpendicular to the magnetic field axis there is no continuous momentum transfer. For photons incoming at smaller angles to the magnetic field axis parallel momentum is transferred. Figure 4.4 shows only photons moving upwards. The electron momenta for scattering processes with a parallel component are therefore shifted to higher positive momenta. The number of scattering events declines for very small photon angles to the magnetic field direction, from ~4000 scattering events in the top panel to ~300 events in the bottom panel. The reason for this is twofold: first, the almost zero photon momentum component perpendicular to the field leads to a decrease of resonant cyclotron scattering events and second, repeated cyclotron scattering favors a redistribution of the interacting photons toward larger angles to the B-field, especially for photon energies close to the cyclotron energy. A detailed description of the classical CRSF geometries is provided in Section 4.5 below. Now it becomes possible to verify that scattering events are of resonant nature (i.e., they involve an excitation of an electron), the resonant scattering events coincide with the zero line width solutions, and the final electron momentum is increasing with decreasing scattering angle. The points which are off the zero line width solutions mark elastic scattering processes not involving any electron excitations. They occur mainly close to $\vartheta \approx 90°$ where resonant scattering is suppressed because the photons have to have exactly the right energy to excite an electron. Photons with a smaller angle to the magnetic field axis, on the other hand, can transfer excessive energy to the electron's momentum parallel to the field. Therefore the red and blue points of the resonant scattering events are almost congruent in the top panel of Fig. 4.4, while the gap between them increases with increasing $\mu = \cos \vartheta$. The data show that our physically

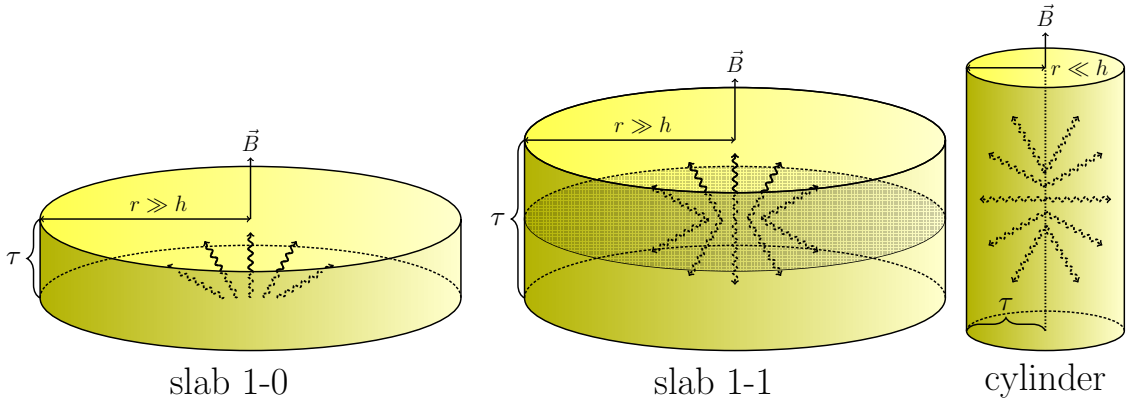

Figure 4.5.: Accretion column geometries used in earlier cyclotron calculations. The slab 1-0 geometry is a bottom illuminated slab. The slab 1-1 geometry corresponds to a slab illuminated by a seed photon plane in the middle of the slab. In cylinder geometry the seed photons are injected isotropically from a line in the center of the cylinder. Spectra emerging from the cylinder geometry are characterized by the optical depth in the radial direction, while the total optical depth along the vertical axis is used to define the scale of slab geometries. Figure and caption from Schwarm et al. (2017a).

motivated limits provide accurate boundaries for the majority of scattering events and further justifies the usage of Eq. 4.15 as an approximation for the CRSF line width.

4.5. Classical Geometries

The cyclotron line shape is strongly influenced by the geometry of the medium in which the cyclotron line is formed. In the following the classical geometries used by earlier works are introduced. Figure 4.5 depicts these classical geometries. They differ in radius, height, and the position and type of the seed photon source. Slab geometries mimic a thin scattering volume of infinite radius. This is approximated in the numerical simulations by setting the radius to a value very large compared to the height of the medium. A factor of 1000 between the radius and the height has been found empirically to be a good choice. The output spectrum does not change significantly for a larger extension in radial direction, that is, only a few specific photons, if any, travel that far perpendicular to the B-field axis without escaping through the bottom or top of the slab. The height of the slab is specified in terms of the Thomson optical depth. The density in the slab can therefore be calculated in the simulation from the slab extension and its optical depth. For slab geometries the optical depth parallel to the magnetic field is used to describe the medium, because the slab radius is infinite or at least much larger than its height. Using optical depths as parameters here is only logical since a usage of extension lengths and densities would contain redundant information. This can be envisioned as a very long, extended but thin medium, which forms exactly the same cyclotron lines as observed from a medium with higher density but accordingly smaller extension. Using the notation of Isenberg

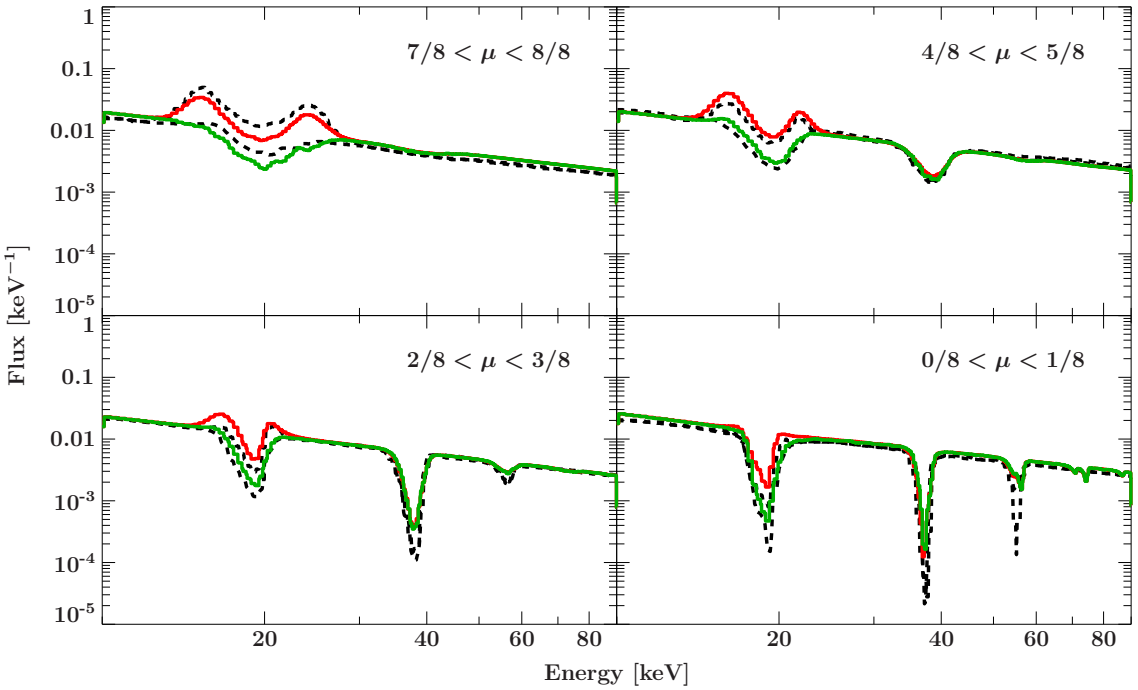

Figure 4.6.: Comparison of Schwarm et al. (2017a, solid lines) to Isenberg et al. (1998b, their Fig. 7; dashed lines). To allow for a comparison between both works, the Green's table spectra were averaged over the output angle ranges used by Isenberg et al. (1998b). Red lines denote the slab 1-1 geometry, green lines the slab 1-0 geometry. Temperatures of 7 keV and 8 keV have been used for the slab 1-0 and slab 1-1 geometries, respectively. Figure and parts of the caption from Schwarm et al. (2017a).

et al. (1998b), in a slab 1-0 geometry the medium is solely illuminated from the bottom, while in slab 1-1 geometry a source plane in the middle produces seed photons within the medium. In cylinder geometry the medium's radius is much smaller than its height. Therefore, the optical depth perpendicular to the B-field axis, that is, the cylinder radius in units of optical depths is used as a parameter to describe the medium instead. Here, the seed photons are also produced within the column but only along the cylinder's axis. In this work spectra for slab 1-0 and slab 1-1 geometry are shown in Fig. 4.6. Figure 6.5 in Section 6.3, for instance, shows spectra for cylinder geometry. The CRSF shape is, in general, highly sensitive to the simulated geometry. The formation of line wings, for example, is especially pronounced in slab 1-1 geometry for viewing angles almost parallel to the magnetic field, which can be seen in Fig. 4.6.

4.6. Code Verification

In order to validate the general simulation, Fig. 4.6 compares spectra obtained using the approach described here with earlier calculations by Isenberg et al. (1998b) for two different accretion column geometries. Four different angular regimes are shown. The upper left plot

shows the simulated spectra for a viewing angle almost parallel to the magnetic field axis. The lower right plot shows spectra for viewing angles almost perpendicular to the B-field axis. The corresponding angle bins are defined in terms of the cosine of the viewing angle $\mu = \cos\vartheta$. The calculations agree well: the line width decreases with increasing viewing angle to the B-field axis. The depth of the line decreases with decreasing viewing angle. Indications for a third harmonic line can be seen in spectra emerging perpendicular to the direction of the magnetic field. For viewing angles parallel to the magnetic field axis only a complex fundamental line is observed. The strong line wings become less pronounced for input continua with a high energy cut off, as less photons are spawned from the higher harmonics (Isenberg et al., 1998b; Araya, 1997; Schönherr et al., 2007b; Schönherr, 2007, and references therein). Previous works based on the numerically calculated cyclotron cross sections by Sina (1996), such as Araya (1997) and Schönherr et al. (2007b), do not show such a good agreement with the spectra from Isenberg et al. (1998b). Some slight deviations remain in the line wings. These are formed by spawned photons. In the spectra from Isenberg et al. (1998b) a larger number of spawned photons escape at small angles to the magnetic field axis. These extra photons appear at larger angles in the `CycloSim` simulation. The reason for this disagreement is probably a different angular redistribution scheme or the approximation of the total scattering cross section used by Isenberg et al. (1998b, Eq. 11 therein) for modeling the resonant scattering at harmonics above the first one. Isenberg et al. (1998b) use this approximation (see also Daugherty & Ventura, 1977; Fenimore et al., 1988), which is strictly valid only near line center, for resonant scattering involving the excitations of higher harmonics. They resort to a numerical integration over the scattering angle of the more correct form given in their Eq. 10 (see also Canuto et al., 1971; Herold, 1979; Ventura, 1979; Wasserman & Salpeter, 1980; Harding & Daugherty, 1991; Graziani, 1993) for transitions involving only the ground state and the first excited state.

The discussion of cyclotron resonant scattering as a cooling process for the electrons in the accretion column is beyond the scope of this work. Nevertheless, some reasoning for the two different temperatures used in the comparison will be given briefly: the electron temperature depends on the photon interactions, which in turn depend on the electron temperature. In the regime where cyclotron resonant scattering is the dominant cooling process, a convenient choice for an equilibrium temperature is the temperature at which the energy transfer is zero. The point of equilibrium depends on the geometry. Figure 4.6 therefore assumes temperatures of 7 keV and 8 keV for the slab 1-0 and slab 1-1 geometries, respectively, following Isenberg et al. (1998b). These temperatures correspond to the Compton temperature where the energy transfer is minimal. Lamb et al. (1990) used this technique to show that the ratio of this equilibrium temperature to the magnetic field is fairly constant if the temperature is determined solely due to cyclotron resonant scattering.

Figure 4.7 from Schwarm et al. (2012) shows a comparison of the `CycloSim` simulation from this work with the results from the simulation code developed by Araya & Harding (1999, see Fig. 4 therein). The cyclotron lines from the latter code are deeper because of the erroneous implementation of the thermally averaged scattering cross sections resulting in larger mean free paths and therefore deeper cyclotron lines. This is discussed in more

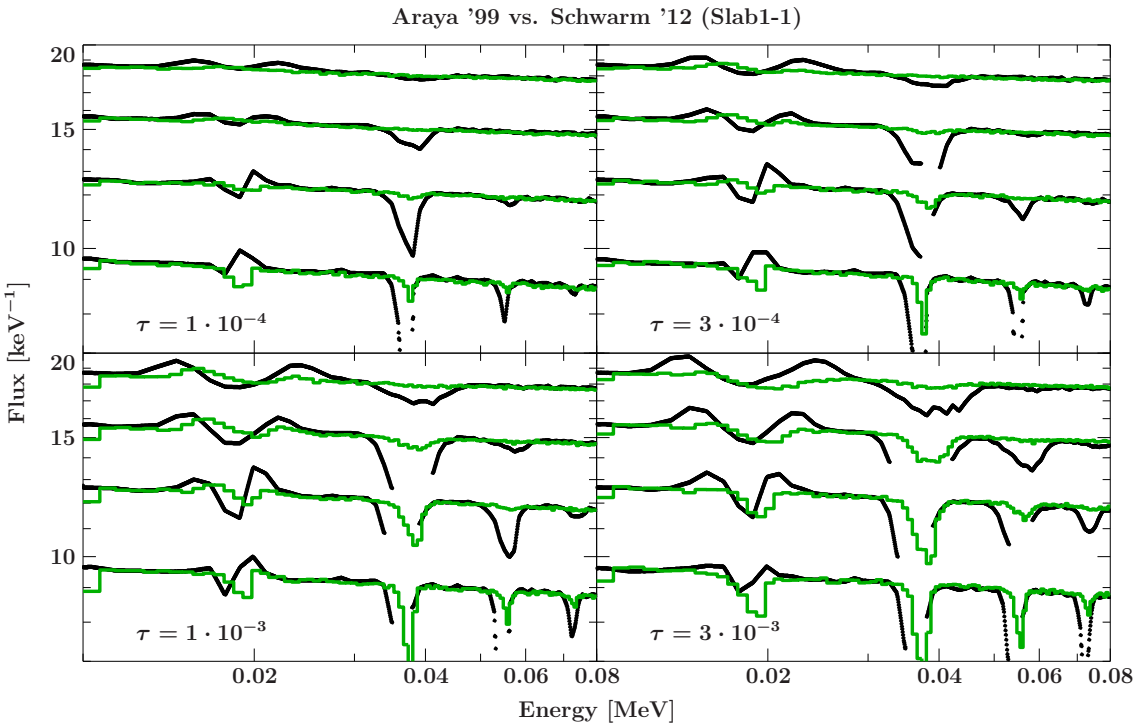

Figure 4.7.: Comparison to Araya & Harding (1999). Plot from Schwarm et al. (2012).

detail in Section 3.5. Apart from this obvious quantitative difference, the spectra show very similar qualitative behavior: the line depth is increasing with optical depth, the line widths correlate with the viewing angle to the magnetic field, and both simulations show the presence of emission wings around the fundamental CRSF energy. The line wings are much less pronounced in the `CycloSim` simulation developed in the course of this thesis, in agreement with expectations from observations. Also the improved energy resolution is clearly visible and the harmonics are resolved all the way down to the line center. The gaps in the Araya & Harding (1999) spectra, on the other hand, result from the limited number of scattering processes after which photons are thrown away.

The comparison to Schönherr et al. (2007b) shows similar characteristics: Schönherr et al. (2007b) used the code from Araya & Harding (1999) and are therefore affected by the erroneous implementation of the thermally averaged cross sections as well. Figure 4.8 shows a comparison between the XSPEC model from Schönherr et al. (2007b), namely `cyclomc`, and the new XSPEC model from Schwarm et al. (2017a), `cyclofs`, which clearly shows the differences in line depths.

4.7. Optimization

The absolute MC simulation time is reduced by using MPI to distribute the work among multiple processors. Figure 4.9 shows that the simulation code is parallelized efficiently.

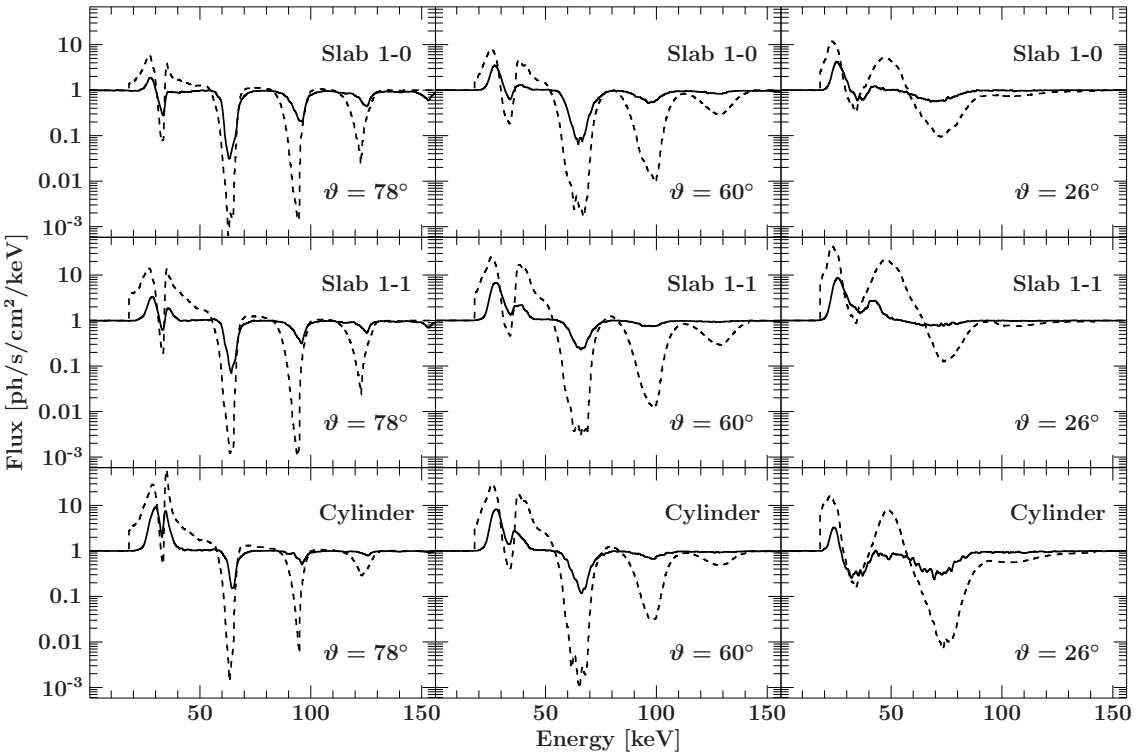

Figure 4.8.: Comparison to Schönherr et al. (2007b): the dashed lines show spectra calculated with the XSPEC model `cyclomc`. The solid lines show the new model `cyclofs`. Viewing angles of 78°, 60°, and 26° to the magnetic field axis are shown in the panels from left to right. The comparison is performed for all classical geometries, that is, slab 1-0, slab 1-1, and cylinder from the top to the bottom.

The tests have been performed on different computer systems. Using ~8 CPUs for each simulation provides a convenient compromise between simulation time and efficiency.

A significant fraction of the computing time for the simulations of cyclotron lines is spent on the calculation of the mean free path for each individual photon before scattering, since it involves a complex numerical integration over the product of the scattering cross section and the (thermal) velocity distribution of the scattering electrons as described in Section 3.5. Schwarm et al. (2017b) separated this core issue from the larger simulation code to allow for an efficient simulation of any complex X-ray pulsar geometry based on precalculated tables of the mean free path. This table interpolation scheme will be laid out in the following.

4.7.1. Mean Free Path Tables

Using the code developed in the course of this thesis, interpolation tables have been calculated, which can be used in CRSF simulations to sample the mean free path of the scattering photon and the momentum of the scattering electron. The tables also contain all the information required for sampling the scattering electron's final spin. The adaptive

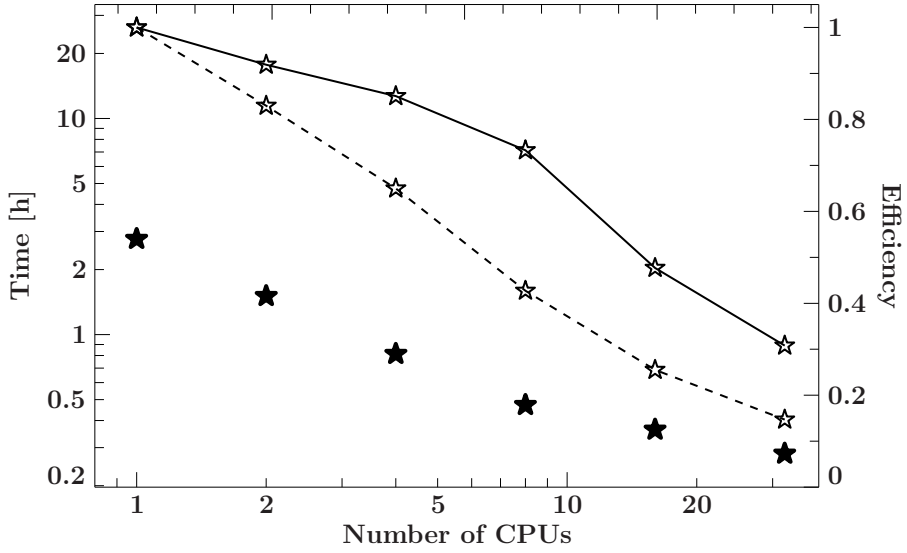

Figure 4.9.: Absolute CPU time (filled symbols) on the left axis and multi-core efficiency (lines) on the right axis for the simulation of synthetic spectra. The efficiency is calculated as $\eta = t_1/(nt_n)$, where t_n is the execution time on n CPUs. The simulation speed tests have been performed on an AMD Opteron 2.2 GHz system (dashed line) as well as on an Intel Xeon 2690 2.6 GHz system (solid line and filled symbols). The simulations have been performed for the same parameters as in Fig. 4.6 above, but with only 100 input photons per energy bin instead of 10000. Absolute CPU times will depend on the chosen parameter values. Figure and caption from Schwarm et al. (2017a).

Simpson integration scheme and a discussion of the numerical calculation of the mean free path related equations have been described in Section 3.5. The adaptive refinement of the energy and angle grids are described in the following with their application and physical implications, closely following, partially in verbatim, the work published by Schwarm et al. (2017b). The tables are not only used by the simulation to sample mean free photon paths but also for the sampling of the electron momenta. They are suited for mean free path calculations of MC simulations of the cyclotron scattering process for conditions expected in typical X-ray pulsar accretion columns ($0.01 \leq B/B_{\rm crit} \leq 0.12$, where $B_{\rm crit} = 4.413 \times 10^{13}$ G, and $3\,{\rm keV} \leq k_{\rm B}T \leq 15\,{\rm keV}$). The sampling of the tables is chosen such that the results have an estimated relative error of at most $1/15$ for all points in the grid. The tables are available online[6].

At the beginning of the simulation process, a photon with an initial energy is generated, as described above. Then the optical depth τ to be traveled by the photon is drawn from the exponential distribution $\exp(-\tau/\lambda)$, and converted into a geometric path length. This requires the calculation of the mean free path λ, that is, the inverse thermally averaged scattering cross section. The photon is then propagated over this distance and the scattering process is simulated, which requires the selection of an electron that has properties appropriate for this mean free path. The flow-chart of the full MC scattering process shown

[6] http://www.sternwarte.uni-erlangen.de/research/cyclo

in Fig. 4.1 illustrates this. Since the calculation of the geometric path and the scattering simulation are very time consuming, a tabular interpolation scheme has been developed for the mean free path and electron parallel momentum sampling to save computing time. It works on precalculated tables, which were obtained using an adaptive process refining the table until the interpolation error is smaller than a preset limit. Calculating the mean free path is only the first step in the MC sampling process, but replacing it by an interpolation scheme has a very large impact on the overall simulation time. The CRSFs can form at rather small optical depths due to the resonant nature of the cross sections. The small optical depths as considered here mean that most of the injected seed photons escape the CRSF medium immediately. Only 1–10% of the initial photons will interact with the medium via cyclotron scattering. Therefore the only evaluation necessary for the majority of photons is the one for their initial mean free path. The simulations show that interacting photons tend to scatter around the resonances in energy space until an electron with a parallel momentum that deviates sufficiently from the resonance condition is hit. Photons emitted by previously excited electrons during their transition to a lower Landau level are also generated close to the resonances. These spawned photons lead to a large number of resonant photons compared to continuum photons. This further motivates the usage of MFP interpolation tables since the calculation time tends to increase significantly near the resonances. For each interaction between photons and electrons, the parallel momentum of the electron must be sampled according to the corresponding thermal momentum distribution. For a given photon energy and angle, the electrons with momenta that cause the photon to be resonant in the electron rest frame have a much higher scattering probability. Therefore the cyclotron resonances manifest in parallel momentum resonances of the scattering electrons (see Section 4.4 above).

The mean free path tables store the total mean free paths as well as the probability distributions needed for sampling the electron momentum. Interpolating from these tables speeds up our simulation by a factor of ~60 compared to the case where all data needed during the simulation is calculated without resorting to interpolation tables. The difference between interpolation and calculation becomes even larger if the tables are used outside of the simulation simply to interpolate mean free paths for several energies without performing any other simulation steps. In this case interpolation is faster by a factor of ~2400 for input angles almost perpendicular to the magnetic field. An example for such an application would be the numerical simulation of the accretion column. While analytic approaches use comparably simple approximations for the scattering cross sections, numerical magnetohydrodynamic (MHD) simulations may actually resort to the MFP tables described here for increasing their accuracy. Many more applications can be envisioned, including the simulation of the influence of cyclotron scattering on the electrons, or the overall accretion geometry. In the following, the mean free path interpolation tables are discussed against the background of the MC simulation of cyclotron lines.

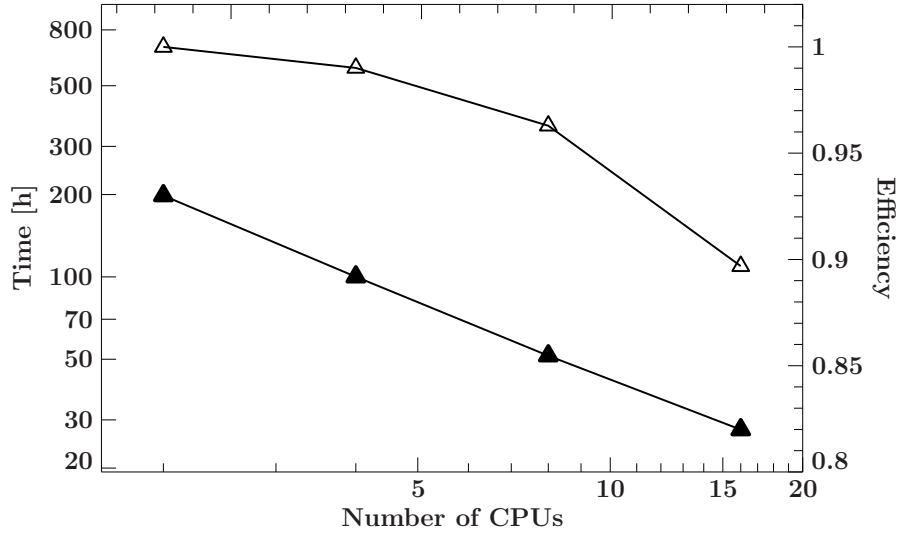

Figure 4.10.: Absolute CPU time (filled symbols) on the left axis and multi-core efficiency (open symbols) on the right axis for MFP table calculation. The efficiency is calculated as $\eta = t_1/(nt_n)$, where t_n is the execution time on n CPUs. $t_1 = 2t_2$ is assumed since performing the calculation on only one core is too time consuming. The MFP table calculations were performed on an AMD Opteron 2.2 GHz system. The execution times are for a magnetic field $B = 0.12B_{\text{crit}}$ and a temperature $k_{\text{B}}T = 3\,\text{keV}$ with a maximum error of 2/15. The CPU time scales with the table file size. Figure and caption from Schwarm et al. (2017b)

4.7.2. Optimizing Table Size: Adaptive Refinement

The adaptive nature of the cross section integration method described in Section 3.5 takes advantage of the fact that only few integration points are needed outside the resonances. These choices allow for a computationally manageable creation of mean free path tables on a time scale of 3000–30000 CPU hours on a typical work station with processor speed of 2–3 GHz, depending on the magnetic field, the temperature, and the error tolerance. These calculation times are achieved by utilizing a few dozen CPU cores[7] at the same time using MPI. Parallelization leads to a significant speed up by a factor of up to $0.8N_{\text{CPU}}$ with respect to earlier implementations, where N_{CPU} is the number of CPUs used. Figure 4.10 shows this speed up as a function of N_{CPU} in terms of the parallel computing efficiency. The efficiency is given by the total CPU time used for a mean free path table calculation divided by the CPU time needed on only one CPU.

4.7.3. Interpolation Techniques

For optimizing the table size of the tables the integrals are evaluated using an adaptive process where the energy and the angular grid points are iteratively refined until the mean

[7]For the sake of simplicity the terms “CPU” and “CPU core” are used equivalently.

free paths interpolated from the table do not deviate from the corresponding calculated ones by more than a given maximum deviation. After each calculation step of a new energy grid point, the result is compared to the value obtained by linear interpolation. The relative error of the interpolation is determined and used as a convergence criterion. A minimum recursion depth as well as maximal angle and energy differences prevent premature convergence.

In detail, the interpolation tables were refined adaptively by comparing the calculated profile σ_{calc} of a new point with the profile obtained by interpolation from the table σ_{interp}, without taking this newly calculated point into account. A linear interpolation scheme was used for refining the energy grid:

$$\langle\sigma\rangle_{\mathrm{interp}}(\mu,\omega) = \langle\sigma\rangle(\mu,\omega_1) + \frac{\langle\sigma\rangle(\mu,\omega_2) - \langle\sigma\rangle(\mu,\omega_1)}{\omega_2 - \omega_1}(\omega - \omega_1)\,. \tag{4.16}$$

The splitting of the energy intervals is stopped if

$$\frac{\langle\sigma\rangle_{\mathrm{interp}} - \langle\sigma\rangle_{\mathrm{calc}}}{\langle\sigma\rangle_{\mathrm{calc}}} \leq \epsilon\,, \tag{4.17}$$

where $\epsilon = 1/15$ has been found to be a good compromise between precision and calculation time. The same linear interpolation method can be used to interpolate profiles during Monte Carlo simulations. For an interpolation in μ and ω two linear interpolations have to be performed. First the inverse mean free path is interpolated for the surrounding angular grid points, each one on its own energy grid. Linear interpolation between these values with respect to the angle then gives the desired value.

For using the computed mean free path tables for the simulation of synthetic spectra with CRSFs, a physically motivated interpolation method was implemented as well. Instead of interpolating for the same energy on two different angular grid points, the energy is shifted to the corresponding energy of the angular point considered. This is done by calculating the order n of the energy in terms of the resonance condition for the desired angular value. This value is used to calculate the corresponding energies at the angular boundaries used for interpolation.

$$n(\omega,\mu) = \frac{\left(\omega \sin^2\vartheta / m_{\mathrm{e}}c^2 + 1\right)^2 - 1}{2B/B_{\mathrm{crit}} \sin^2\vartheta} \tag{4.18}$$

This interpolation scheme eliminates inaccuracies due to the shift of the resonance energy with ϑ, because interpolation is done at nearly constant "elevation" along the resonance ridges (Harding & Daugherty, 1991).

For testing the accuracy of the interpolation from the tables, the thermally averaged scattering cross section profiles (Eq. 3.46) have been calculated on a much finer grid than the tabulated one (~700–1800 energy grid points). Figure 4.11 visualizes the profile for a magnetic field of $B = 0.12\,B_{\mathrm{crit}}$, interpolated on a grid of 5000 energy grid points. The relative deviations from the calculated values do not exceed the relative maximum error of 1/15.

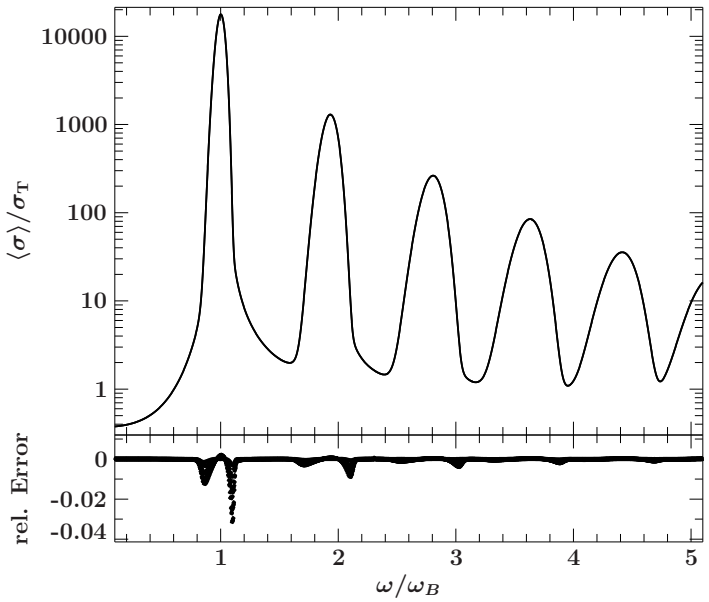

Figure 4.11.: Thermally averaged cyclotron scattering cross sections in units of the Thomson cross section σ_T interpolated for $B = 0.12\,B_{crit}$, $k_B T = 3\,\mathrm{keV}$, and angle $\vartheta = 60°$. The relative deviations to the calculated profiles, shown in the lower panel, are not exceeding the maximum error of 1/15 of the MFP table used for the interpolation. Figure and caption from Schwarm et al. (2017b)

The interpolated profiles for the parameter combinations for which tables are provided are plotted as a function of frequency and scattering angle for several B-fields and temperatures in Figs. 4.13 and 4.14.

The partial integrals, forming the cumulative distribution function (CDF) of the electron momentum, are stored in the FITS binary tables as well, allowing for efficient loading into a simulation. FITS tables can be opened and read by many processes in parallel, enabling the usage of parallel computation in simulations. Another advantage of the FITS format is the efficient caching provided by modern FITS libraries such as `cfitsio`[8], which minimize the bottleneck of disk reading operations. Although the whole size of such an interpolation table is of the order of 1–200 GB for the currently required accuracy, and thus will not completely fit into memory for most common computers, for a given setup the resonant nature of the scattering process means that the most frequently required mean free paths will be from a small fraction of the whole table only, which fits completely into memory and therefore reduces the number of disk reads dramatically.

4.7.4. Mean Free Path Table Structure

The naming convention of the mean free path tables was chosen as follows: all names start with `mfp_` followed by the table specific parameters, namely the magnetic field strength B

[8] `http://heasarc.nasa.gov/fitsio/fitsio.html`

Table 4.1.: List of FITS keywords.

Name	Description
B	Magnetic field [B_{crit}]
T	Electron temperature $k_{\mathrm{B}}T$ [MeV]
MU	Cosine of the incoming photon's angle to the magnetic field axis, $\mu = \cos\vartheta$
MAX_ERR	Maximum relative error in units of 1/15

and the temperature T. The magnetic field is in units of the critical magnetic field strength, with five digits. The temperature $k_{\mathrm{B}}T$ is given in units of MeV with five digits as well. For example, the first table in alphabetical order is named `mfp_B0.0100T0.0030.fits`.

Each mean free path table starts with an empty image HDU containing header keywords for the magnetic field strength B, the temperature T, and the relative maximum error as listed in Table 4.1. It is followed by a variable number of binary extensions any of which corresponds to one angular grid point. These binary extensions are ordered by increasing $\mu = \cos\vartheta$ and are described in detail in the following.

The value of μ is stored in the header keyword `MU`. Each row corresponds to one energy grid point, the value of which can be found in the first column. The second column contains the total thermally averaged scattering cross section summed over final electron spin states. The number of grid points used for the adaptive Simpson integration over the thermal electron momentum distribution (Eq. 3.46), can be found in the third column. The corresponding electron momentum grid points are stored in the fourth column as a variable length array of double numbers, followed by the spin averaged cumulative distribution function (CDF), the ensemble of partial integrals obtained from Eq. 3.49. The sixth column contains, again, the number of electron momentum grid points used for the integration of Eq. 3.46 taking into account only transitions with final electron spin down. Following the corresponding momentum grid points and cumulative distribution functions the pattern repeats once again for the case of final electron spin up.

The header keyword `MAX_ERR` contains the relative error of the table, ϵ, from Eq. 4.17, in units of 1/15. Table 4.2 visualizes the structure described here. The last six columns for the spin dependent cases are omitted for the sake of clarity.

4.7.5. Parameter Ranges

The tables are available online[9]. Tables are provided for the mean free path calculated for B-fields and temperatures covering the parameter ranges typical for accreting X-ray pulsars, namely $B = 0.01$, 0.03, 0.06, 0.09, and 0.12 B_{crit} and $k_{\mathrm{B}}T = 3$, 6, 9, 12, and 15 keV. Table 4.3 shows a list of the available tables and their uncompressed file size.

[9] `http://www.sternwarte.uni-erlangen.de/research/cyclo`

Table 4.2.: Description of the mean free path table structure for given values of $k_\mathrm{B}T$ and B/B_crit. The column pattern `# of grid points, Grid [MeV], CDF` is repeated two more times, omitted below for clarity, for the case of final electron spin down and final electron spin up, respectively. The first element of each `Grid` and `CDF` array is used for internal consistency checks. The user should only use the indices 1 to N_p. The dependency of N_p on angle and energy is not stated explicitly. N_μ, N_k, and N_p are typically of the order of a few hundred to thousand of points.

EXTENSION	MU	COLUMNS				
		Energy [MeV]	Cross section [σ_T]	# of grid points	Grid [MeV]	CDF
1	μ_1	k_1	$\langle\sigma(\mu_1,k_1)\rangle$	N_p	$[p_1,\ldots,p_{N_p}]$	$[F^{p_1}_{-m_\mathrm{e}c},\ldots,F^{p_{N_p}}_{-m_\mathrm{e}c}]$
		$\vdots$				
		k_{N_k}	$\langle\sigma(\mu_1,k_{N_k})\rangle$	N_p	$[p_1,\ldots,p_{N_p}]$	$[F^{p_1}_{-m_\mathrm{e}c},\ldots,F^{p_{N_p}}_{-m_\mathrm{e}c}]$
$\vdots$	$\vdots$	$\vdots\!\vdots$	$\vdots\!\vdots$	$\vdots\!\vdots$	$\vdots\!\vdots$	$\vdots\!\vdots$
N_μ	μ_{N_μ}	k_1	$\langle\sigma(\mu_{N_\mu},k_1)\rangle$	N_p	$[p_1,\ldots,p_{N_p}]$	$[F^{p_1}_{-m_\mathrm{e}c},\ldots,F^{p_{N_p}}_{-m_\mathrm{e}c}]$
		$\vdots$				
		k_{N_k}	$\langle\sigma(\mu_{N_\mu},k_{N_k})\rangle$	N_p	$[p_1,\ldots,p_{N_p}]$	$[F^{p_1}_{-m_\mathrm{e}c},\ldots,F^{p_{N_p}}_{-m_\mathrm{e}c}]$

Table 4.3.: Uncompressed file sizes for the parameter combinations made available in GB. Compression reduces the file size by approximately 50%.

$k_\mathrm{B}T$ [keV]	B/B_crit				
	0.01	0.03	0.06	0.09	0.12
3	44	16	10	7	11
6	89	29	16	11	16
9	148	42	23	16	22
12	198	61	32	20	26
15	238	74	35	24	32

As shown by Araya & Harding (1999), the low continuum optical depth and the small collisional excitation rate (Bonazzola et al., 1979; Langer, 1981) of a typical accretion column, combined with the high radiative cyclotron de-excitation rate (Latal, 1986), imply that all electrons can be assumed to reside initially in the ground state Landau level and have a relativistic thermal momentum distribution, which is unaffected by cyclotron resonant scattering. Therefore tables are provided for this case only. The full data set has an uncompressed size of approximately 2.7 Terabyte. Compressing the tables using `gzip` leads to a size reduced by roughly 50%.

The number of momentum grid points needed for convergence of the numerical integration of Eq. 3.46, correlates positively with the resulting inverse mean free path. Thus broader profiles and those with larger absolute values require more p-grid points. The number of energy grid points needed for accurate interpolation strongly depends on the complexity of the profile and therefore on the scattering angle. The sharply peaked profiles for angles $\sim 90^\circ$ to the magnetic field require many more angle grid points. The average number of

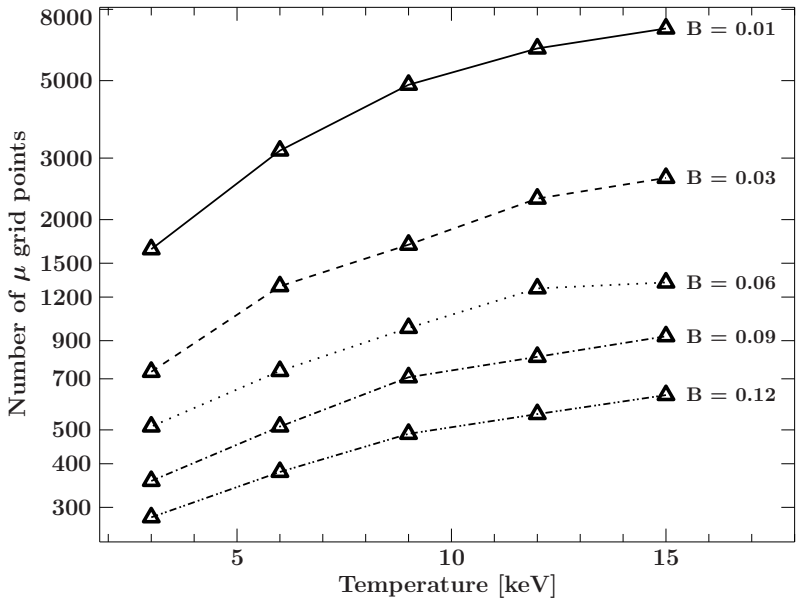

Figure 4.12.: Number of μ-grid points with respect to the electron temperature. Each line corresponds to one magnetic field strength (Schwarm et al., 2017b).

energy grid points for each table does not depend on the temperature, nor does it vary with the magnetic field strength for all but the highest field, $B = 0.12\,B_{\text{crit}}$. For this field the tables have twice as many energy grid points as the other tables. The number of angle grid points in each table is correlated with the temperature and the magnetic field strength. More μ-grid points are needed for higher temperatures since the broadening of the profiles toward larger μ increases with temperature. The negative correlation with magnetic field strength can be explained by the larger absolute values of the corresponding profiles. Figure 4.12 shows the number of μ-grid points, in the set of MFP tables presented here, as a function of the electron temperature and the magnetic field strength. The largest table was obtained for the lowest magnetic field strength and the highest temperature, and is 238 GB in size.

4.8. Green's Table Approach

Another important step is described in the following, which does not only speed up the generation of synthetic cyclotron line spectra for theoretical models: it makes the fitting of the results from the `CycloSim` simulation to observational data possible in the first place. Here, the corresponding part from the work by Schwarm et al. (2017a) is adapted, partially in verbatim.

Performing a time consuming simulation for each generation of a spectrum is impracticable in anticipation of the goal to fit simulated spectra to observational data. A large number of model evaluations is required where the shape of the emerging spectrum is simulated as a function of the input parameters. In addition to the magnetic field strength and the plasma

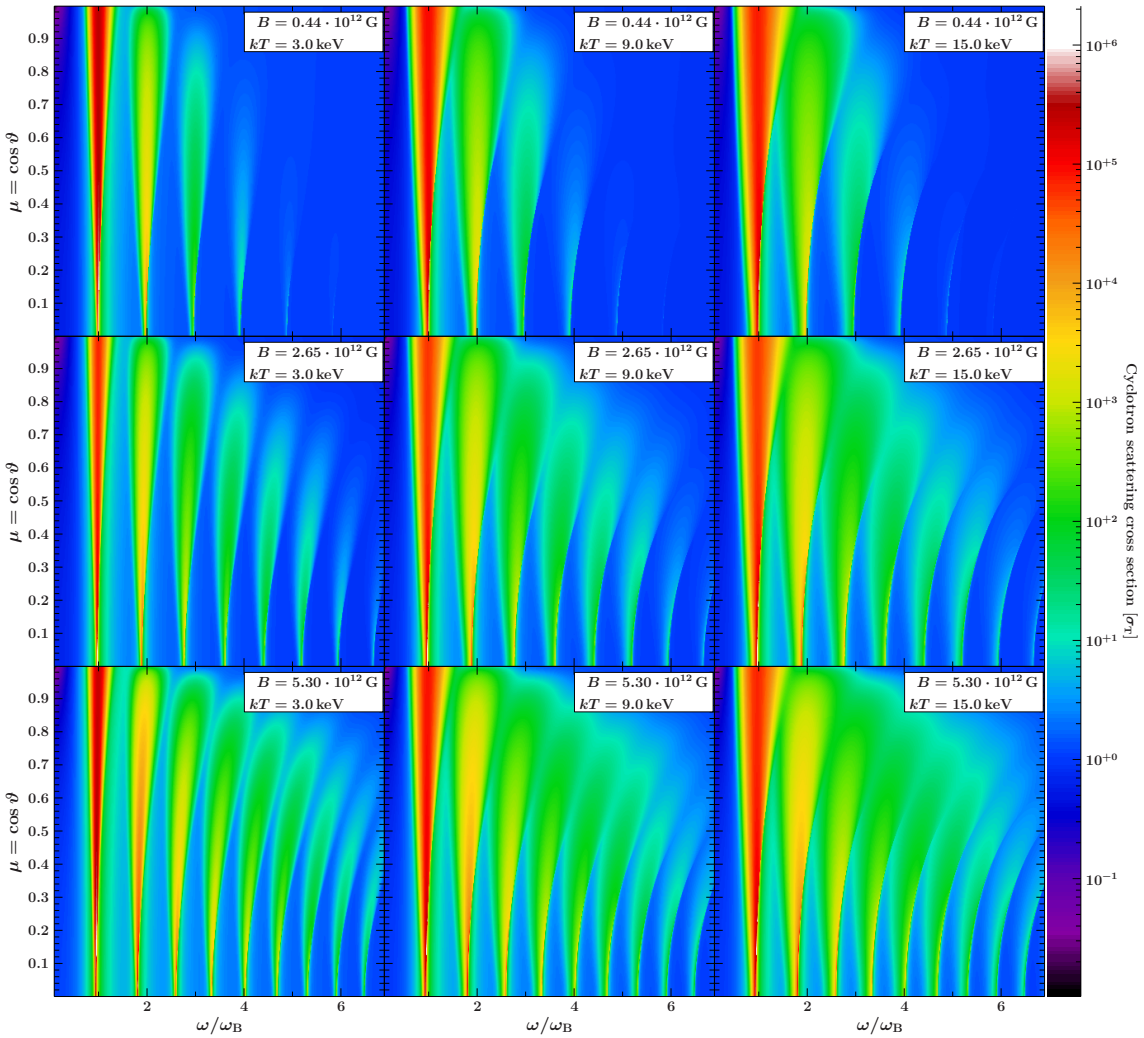

Figure 4.13.: Visualization of the adaptively calculated inverse mean free path values from the interpolation tables for $B = 0.01$, 0.06, and 0.12 B_{crit}. The colors correspond to the averaged scattering cross sections (Schwarm et al., 2017b).

temperature, the spectral shape of the incident photons is also variable. This significantly increases the computing time as potentially a huge parameter space needs to be covered. As it was shown previously (Schönherr et al., 2007b; Schönherr, 2007), the linear nature of the radiation transfer problem in accretion columns allows to avoid this large expense of computing time by calculating the Green's function of the radiative transfer problem. Photons are propagated through a medium with a given geometry, magnetic field strength, and temperature for a well sampled grid of mono-energetic seed photon energies. The photons escaping the medium are collected and binned to spectra for a grid of output angles. These emerging spectra, normalized to the seed photon flux in the corresponding angular bin, correspond to the Green's function of the radiative transfer problem. The emerging spectrum for an arbitrary seed photon spectrum, like a cutoff power law continuum or a continuum due to Comptonization in a radiative shock (Becker & Wolff, 2007), can then

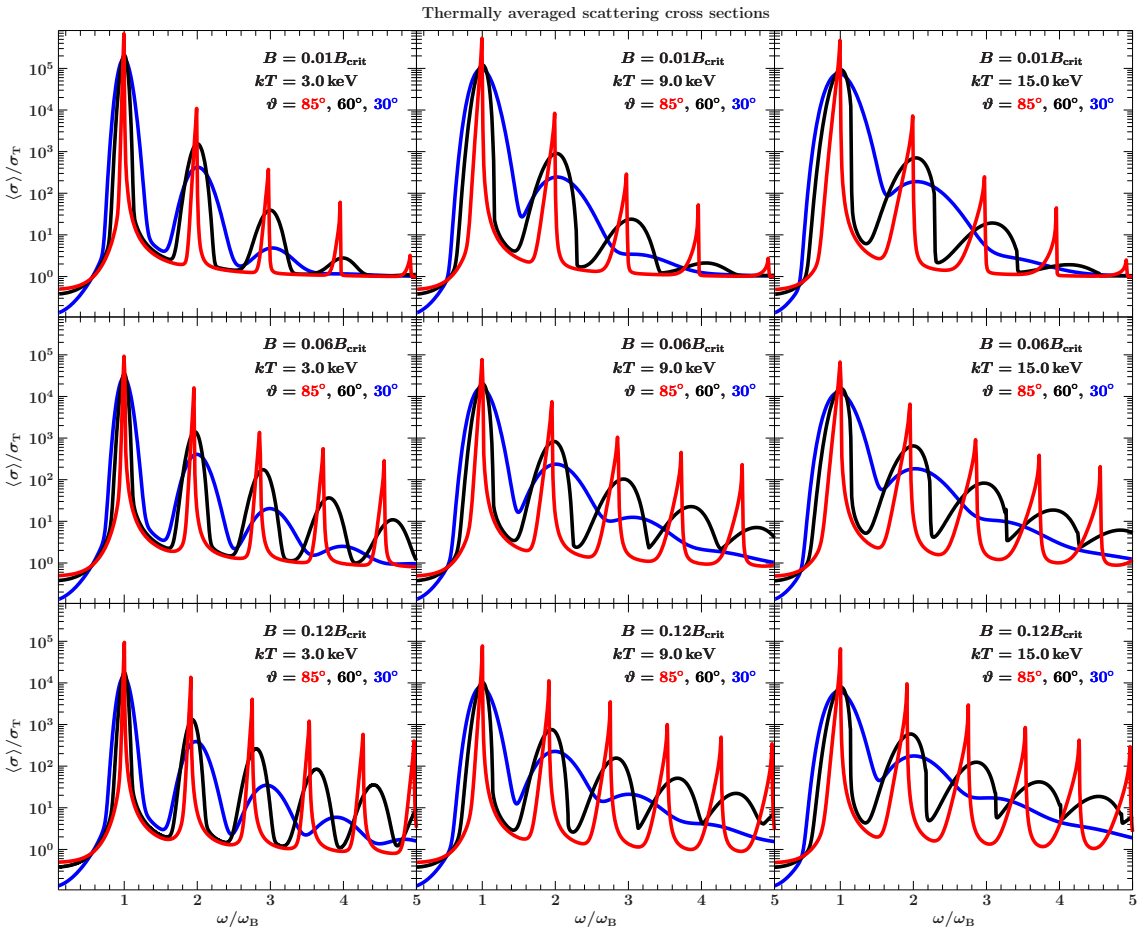

Figure 4.14.: Adaptively calculated averaged cyclotron resonance scattering cross sections. The colors correspond to different angles of the scattering photon with respect to the magnetic field (Schwarm et al., 2017b).

be obtained by convolving it with the Green's functions.

In general, this approach requires the interpolation of the Green's functions for the energies on which the seed photon continuum is defined. This step is necessary because these energies are typically defined by the response matrix of the detector with which the data were taken. The grids have been calculated with a logarithmic energy spacing. It is fine enough that linear interpolation is sufficient to re-grid the Green's functions in energy.

A second interpolation step in the magnetic field strength is required to obtain a Green's function for a B-field value not covered by the grid of precalculated values. Since the Green's functions are self-similar in E/B, they are interpolated for different B in this "energy shifted" system. In a similar way further interpolations in temperature, output angle, and optical depth are used to approximate the final spectrum for parameter combinations off the grid points.

Using MFP interpolation tables, the Green's functions can be calculated for a large parameter range and with a resolution better than the resolution of all currently flying X-ray

Table 4.4.: Parameter ranges covered by CRSF Green's function tables

Parameter	Minimum	Maximum
Magnetic field [$B_{\rm crit}$]	0.01	0.12
Electron temperature $k_{\rm B}T$ [keV]	3	15
Cosine of the viewing angle to B-field axis, $\mu = \cos\vartheta$	0.001	0.999
Optical depth [$\tau_{\rm T}$]	$1 \cdot 10^{-4}$	$3 \cdot 10^{-3}$

telescopes for the energy range where cyclotron lines are observed. This takes about 300 CPU hours for one geometry on rather coarse grained magnetic field and temperature grids. In principle the MFP table mechanism and the creation of Green's tables can be carried out for magnetic fields $0.01 < B/B_{\rm crit} \leq 0.12$ and temperatures $0\,{\rm keV} < T \leq 50\,{\rm keV}$, although for the testing of different geometries and other parameters Schwarm et al. (2017b) concentrated on an optimized subset to save CPU time. The Green's functions needed for the evaluation of model spectra for arbitrary parameters within the precalculated ranges are interpolated from these tables using the methods given in Section 4.9.1 below. It also describes the extrapolation beyond the covered parameter regime. However, this extrapolation should be taken with extreme caution.

4.9. `cyclofs` XSPEC Model

Schwarm et al. (2017a) published improved Green's function tables for the classical geometries, which can be used together with an XSPEC "local model", `cyclofs`, to imprint cyclotron lines to arbitrary input continua. Table 4.4 shows the parameter ranges covered by these tables. Each table corresponds to one geometry. The tables have been calculated using thermally and polarization averaged cross sections.

`cyclofs` convolves the given Green's table with the given input continuum. It can, in principle, extrapolate beyond the ranges provided in Table 4.4, but this should be used with care and currently triggers a warning message. The model and Green's function tables are available online[10]. The Green's function table utilized by the model can be selected for use by

- setting the environment variable *CYCLOFS_TABLE* to the table's location
- defining the table location as initialization string in the `model.dat` file

Table 4.5 lists all model parameters. At least one optical depth, the magnetic field, the temperature, and the angle or the angular range and the number of angular points must be set for a successful model evaluation. Setting both optical depths to zero effectively de-activates the model and can be used to evaluate the model spectrum without cyclotron lines.

[10] http://www.sternwarte.uni-erlangen.de/research/cyclo/

Table 4.5.: XSPEC model parameters.

Name	Description
tau_para	Parallel optical depth [τ_T]
tau_perp	Perpendicular optical depth [τ_T]
B	Magnetic field [10^{12} G]
T	Electron temperature $k_\mathrm{B}T$ [keV]
mu	Cosine of the viewing angle to the B-field axis, $\mu = \cos\vartheta$
mu_N	Number of mu-values to average over (0 for exact value of mu)
mu_min	Minimum value of mu for averaging
mu_max	Maximum value of mu for averaging

4.9.1. Interpolation of the Green's Functions

The model allows for an interpolation between parameter values in different ways[11]: a linear interpolation scheme is currently utilized for the interpolation of all parameters. Model spectra are also extrapolated, if the desired parameter combination is not covered by the Green's table. A linear scheme is used here as well. The model prints out a warning message if extrapolation is used. The extrapolation method used for the optical depth is slightly different from the others: for a given optical depth out of the table range, the model convolves its output iteratively with a suitable optical depth within the table range. This extrapolation-via-successive-convolution method turned out to be as accurate as linear extrapolation close to the boundaries but yields much better results than any other method for extrapolation over orders of magnitude. This is especially useful for studies in the regime of high optical depths where calculation time increases significantly. The accuracy of such an extrapolation over orders of magnitude is questionable, though, as it depends on the assumption of isotropic angular redistribution, which is normally not justified, as shown before by Schönherr et al. (2014). It is, nevertheless, very useful for studying the influence of increased line depth on the overall combined model flux and is therefore included as default behavior with a warning message.

4.9.2. Angular Averaging

The model is designed to calculate spectra for exactly one angle to the magnetic field axis, given by its cosine *mu*. It provides the possibility for averaging over the output angle, ϑ, to the B-field, by returning the mean value of *mu_N* spectra between *mu_min* and *mu_max* for each energy bin. If *mu_N* is set to 0, only one spectrum for the angle *mu* is calculated. If it is set 1, one spectrum right in the middle of the angular range specified by *mu_min*

[11] The parameter grids have been chosen such that the choice of the interpolation methods does not affect the resulting spectra much. Whenever the choice of method might be of crucial importance, e.g., if the distributed tables are altered by the user to contain less grid points, the header file of the version of the model code used should be consulted for the correspondingly used methods, since these might change in future revisions

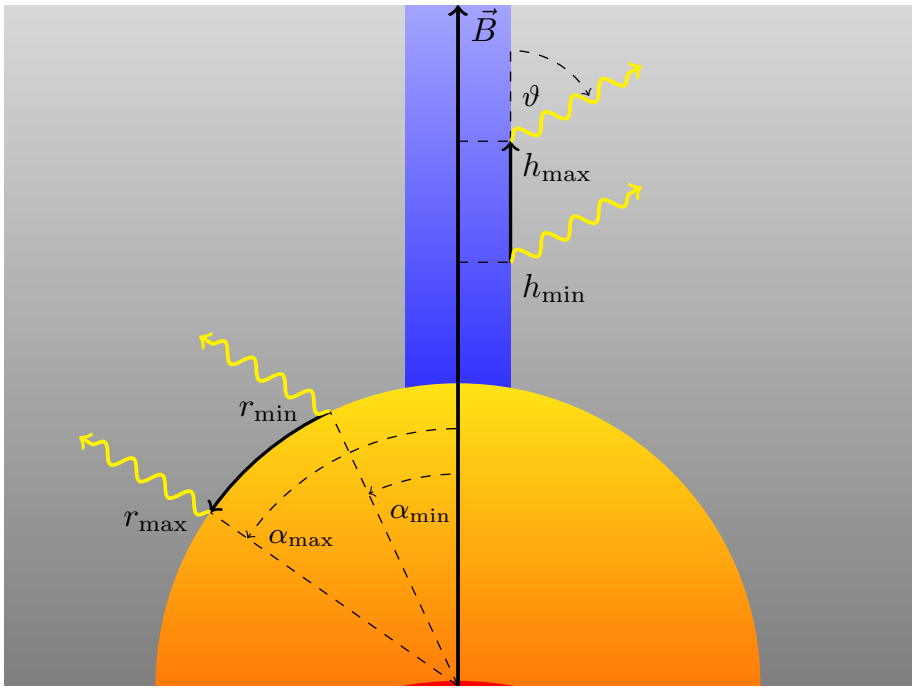

Figure 4.15.: Illustration of the geometric model parameters.

and *mu_max*, that is, for an angle $\mu = 0.5(\mu_{\min} + \mu_{\max})$, is returned. A *mu_N* value of 2 will result in a spectrum averaged from two points, namely *mu_min* and *mu_max*. For higher values, the additional points are equally spread over the angular range. Note that the parameter *mu* is not used at all if *mu_N* is larger than zero and should be frozen during fitting to avoid useless iterations. The same applies to the parameters *mu_min* and *mu_max* in the case of *mu_N* = 0.

4.9.3. Extension Models

Two extension models, namely `cyclocol` and `cyclocap`, have been developed to provide the user with a convenient way of estimating the influence of spatial magnetic field variations in a dipole field. `cyclocol` averages CRSF spectra from *h_N* heights between the provided minimum and maximum values, *h_min* and *h_max*, respectively. The heights are measured from the neutron star's surface and used for the calculation of the magnetic field strength at each point assuming a dipole field centered at the neutron

star. This requires the neutron star radius *r_ns*, which is provided as a fitting parameter, as well. The cyclotron lines are imprinted on the given continuum for the respective B-field strength and the resulting *h_N* spectra are summed and divided by the number of heights. This procedure may change the CRSF shape significantly and allows, in principle, for fitting the neutron star radius for a given accretion column setup with well known spatial boundaries of the emitting region. However, such results would be unrealistic due to the assumption of a simple dipole field (see Chapter 3) and the neglect of the height dependent magnitude of the total flux (see Section 6.3). The `cyclocol` model extension rather has been developed for estimating the height variations necessary to explain the observed line shape. It can be used to estimate the preferableness of a (cylinder symmetric) accretion column model over a (slab-like) hot spot model solely from the CRSF line shape. A similar extension is provided for the more slab-like geometries: the `cyclocap` model. It averages over a radial extension from *r_min* to *r_max* instead of an extension in height. This introduces a further approximation error as the dipole field orientation with respect to the surface is neglected, since large radial extensions of the CRSF forming region are not expected from most modeled accretion column and hot spot models anyway. Figure 4.15 shows a sketch of these geometric model parameters. The number of steps in both extensions correlates linearly with the calculation time for the model since *r_N*, or *h_N* in the case of the `cyclocol` model, spectra have to be calculated for each model evaluation[12]. Both models make use of the main model's model function for reduced code repetition, meaning that changes in the main model are reflected in the derived models without further programming work.

4.10. Polarization

The calculation described in this Chapter is averaging over polarization modes. However, all data products needed for the simulation, such as the scattering cross sections and electron decay rates, are provided in a polarization dependent way. Therefore polarization can be taken into account in the MC simulation code by accessing the polarization dependent low level data products. In detail this means that the mean free path tables described in Section 4.7.1 would have to be calculated for all possible photon polarization transitions: $\parallel\rightarrow\parallel$, $\parallel\rightarrow\perp$, $\perp\rightarrow\parallel$, and $\perp\rightarrow\perp$. This approach is necessary for achieving the same simulation times as in the polarization averaged case. It would not only increase the needed CPU time for the creation of the interpolation tables but also the overall size of these tables by a factor of four. This would result in a total size of ~5.6 TB if the tables are calculated on the same parameter grids. Absolute calculation times and file sizes of MFP tables can be found in Section 4.7.1. In order not to double the size of this thesis it has been forbore from discussing the possible cross section derivations for different choices of polarization modes, and their implications, in detail. Instead, the possible modes will shortly be introduced and an overview over the complexity of this topic is given in the

[12]The time needed for the calculation of the B-field strength at the individual points and the spectral averaging is small compared to the time needed for one evaluation of the basis model.

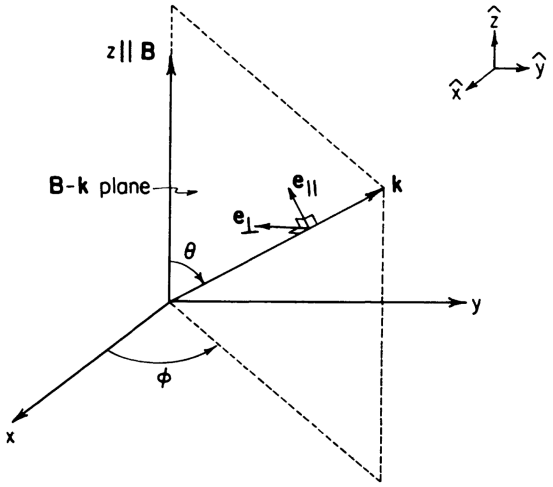

Figure 4.16.: Figure from Wang et al. (1988) illustrating the vacuum polarization mode parallel to the plane formed by the wave vector $\vec{k}$ and the magnetic field vector $\vec{B}$, $e_{\parallel}$, and the one perpendicular to that plane, $e_{\perp}$.

following.

In a strong magnetic field the vacuum becomes birefringent (Novick et al., 1977). In general one has to distinguish between two different formalisms of polarization modes: the magnetic vacuum normal modes, also referred to as (pure) vacuum modes, $e_{\parallel}$ and $e_{\perp}$ and the "(extra-)ordinary" plasma modes e_X and e_O. The former will be used in this thesis. They are linear polarization modes named after their orientation to the plane formed by the magnetic field axis and the photon propagation direction (Fig. 4.16). They are most applicable in the regime of high magnetic field strength and low densities (Wang et al., 1988) and have been used, for example, by Pravdo & Bussard (1981) for performing MC simulations of X-ray pulsar spectra including polarization mode changes, or by Sina (1996) for his derivation of the relativistic cyclotron scattering cross sections, as described in Section 3.5.

The plasma modes, on the other hand, are better suited in the domain of low B-fields and high densities (Wang et al., 1988), as, for example, for the calculation of the dynamical structure of the accretion column core. Becker & Wolff (2007) resort to this formalism in order to derive a physical accretion column model. Bonazzola et al. (1979) applied the plasma modes to this kind of radiative transfer problem as well. They focused on the hot spot and neglected the energy released inside the column. Successive works on this matter, all with their own approximations and features, such as the inclusion of spin flip transitions, angular redistribution, and electron recoil, to name just a few, mostly used the plasma modes as well (see Meszaros et al., 1980; Nagel, 1980, 1981; Wasserman & Salpeter, 1980; Yahel, 1979, 1980; Bussard et al., 1986). Others explicitly embraced the difference of the different polarization formalisms by applying both (Mészáros & Ventura, 1978; Meszaros & Nagel, 1985; Ventura et al., 1979; Wang et al., 1988). Figure 4.17 from Mészáros & Ventura (1978) shows such a comparison at the first cyclotron resonance

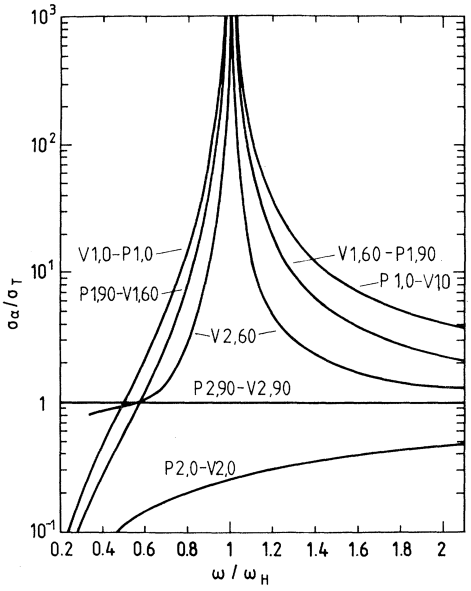

Figure 4.17.: Thomson cross section for scattering of photons off electrons in a strong magnetic field with (V) and without (P) vacuum polarization included (Mészáros & Ventura, 1978, Fig. 3 therein). Plasma polarization is included in both cases. The numbers 1 and 2 refer to the extraordinary and the ordinary plasma polarization modes, respectively. The numbers after the comma show the angle to the magnetic field in degrees. The magnetic field strength is $B = 0.1\, B_{\rm crit}$ and the electron number density is $n_{\rm e} = 10^{21}{\rm cm}^{-3}$.

for different angles to the magnetic field axis within a field of strength $B = 0.1\, B_{\rm crit}$. A summary table about the choices made about polarization modes and the different features included in various works is given by Wang et al. (1988).

Both polarization formulations are approximations to the general dielectric tensor in a magneto-plasma (Wang et al., 1988). These authors explicitly discuss the regimes in which each set of modes, used on its own, serves as a good approximation and provide a ratio for the relative importance of plasma and vacuum polarization:

$$\frac{w}{\delta} = 3 \times 10^{-6} \frac{n_{\rm e}}{10^{23}\ {\rm g\,cm}^{-3}} \left(\frac{B}{B_{\rm crit}} \right)^{-4} , \tag{4.19}$$

If $\delta \lesssim w$, the plasma dielectric tensor dominates over the vacuum dielectric tensor and the plasma modes may be used, while in the case of $w \ll \delta$ the vacuum modes should be used instead. The more complicated modes derived by Mészáros & Ventura (1979) and Pavlov et al. (1980) have to be used in cases where these regimes can not be clearly separated (Wang et al., 1988).

More recent works about the influence of vacuum polarization, the overall interrelationships and leverages of plasma and vacuum polarization, and comprehensive diagrams about their physical connections can be found in the works by Lai & Ho (2003a) and Lai & Ho (2003b).

Potekhin et al. (2004) discuss polarization with respect to neutron star atmospheres. An overview over the literature about explicit derivations of vacuum polarization tensors is given by Schubert (2000a). The second part of this series of papers (Schubert, 2000b) focuses on "string-inspired" techniques.

Last but not least, it should be noted that the description of the radiative transfer in terms of two polarization modes is valid only in the limit of Faraday depolarization, which might be violated: Soffel et al. (1983) found that mode ambiguities may occur at "mode collapse parameters". Such conditions are actually satisfied in hot magnetized plasmas close to the cyclotron frequency (Kirk, 1980; Kirk & Meszaros, 1980). Therefore — as a direct consequence of dissipative effects in wave propagation — it may become "unphysical" to require a unique designation of the polarization modes at all.

Mészáros & Ventura (1979) state that the entire radiative transfer of the regions near the magnetic poles of pulsars is dominated by the vacuum polarization and that an observation of the vacuum polarization effect appears most favorable in these systems. Experimental results in this direction might further constrain the parameter regime in which the cyclotron lines are formed and, for example, provide a way of distinguishing between the regimes of small and high optical depths (see, e.g., Pavlov et al., 1980) mentioned before. Now that polarimeters in the hard X-rays have become technically feasible and the first instrument of such kind, namely the *X-Calibur* telescope (Guo et al., 2011), has been launched successfully (Krawczynski, 2016), such experimental results are coming within reach.

Despite these arguments for the inclusion of polarization, the simulations in this work disregard polarization for various reasons. The increased amount of CPU time and disk space needed for calculating the MFP path tables renders it difficult, if not impossible, to obtain polarization depended simulation results in the time span of one thesis starting with the development of a simulation code from scratch. In order to remove this limitation, the code developed in the course of this thesis made arrangements for future integration of polarization: both, the MFP table code and the simulation code are "polarization-ready", meaning that polarization can be implemented without having to redevelop the complex adaptive calculation and simulation processes. In detail this would require the calculation of MFP tables for each polarization mode transition and the addition of polarization sampling to the simulation. The whole apparatus can then be used to gain polarization dependent results without having to deal with all the complex physical and technical details of cyclotron line simulations. The polarization dependent scattering cross sections needed for this extension are shown in Section 3.5. Furthermore, new observational results may have rendered this work unnecessary by this time. Wang et al. (1988) pointed out that polarization has less of an influence on the CRSF line formation if the magnetic vacuum polarization states, which are assumed to be the correct ones for the problem at hand for the reasons described above, are assumed. Araya & Harding (1999) explicitly relied on their findings: "the assumption that the deviations of the unpolarized from the polarized treatment are minimal renders the numerical code computationally manageable" (Araya & Harding, 1999). It might become apparent from future observations that polarization mostly affects the continuum, which is formed in the, optically thick, accretion column and therefore lies in the domain where the plasma polarization modes, or even more

complicated combined modes, must be used. Finally, the observational data available at the time of writing are of polarization averaged nature anyway. Insofar as the trade off between work load and results is concerned, the usage of the correct relativistic cross sections in combination with a self consistent sampling of all involved parameters, in contrast to previous approaches, thus outranks the inclusion of polarization.

5

VARIATION OF CYCLOTRON LINES WITH PARAMETERS

In the following an exemplary study of the influence of important parameters of the line forming region is performed by using the newly developed MC simulation described in Section 4. Synthetic cyclotron line spectra are shown for different parameter combinations, varying one parameter at a time. A constant flux, normalized to unity, is used as an input continuum to emphasize the changes of the line shape due to photon spawning. The resulting spectra are therefore not meant to be interpreted as realistic spectra expected from observations of accreting X-ray binaries but rather serve as artificial illustrations on physical grounds for the impact of parameter changes on cyclotron lines shapes. The most prominent deviation to the steep continua observed with X-ray telescopes is the exaggeration of the cyclotron line wings. They are resulting from the successive de-excitation of electrons that have been excited to higher Landau levels before. The higher the excited Landau level the more photons are generated. These spawned photons mostly have energies around the first resonance energy and therefore fill up the fundamental cyclotron line and lead to an excess of photons near to it. The reason for the slight deviations to the resonance energy lays in the emitting electrons' momenta parallel to the B-field axis, which lead to a boosting of the spawned photons with respect to the average electron momentum.

Several parameters are varied one after the other while keeping the others constant. The parameter order has been chosen to allow for a visible change in line shape as well as a

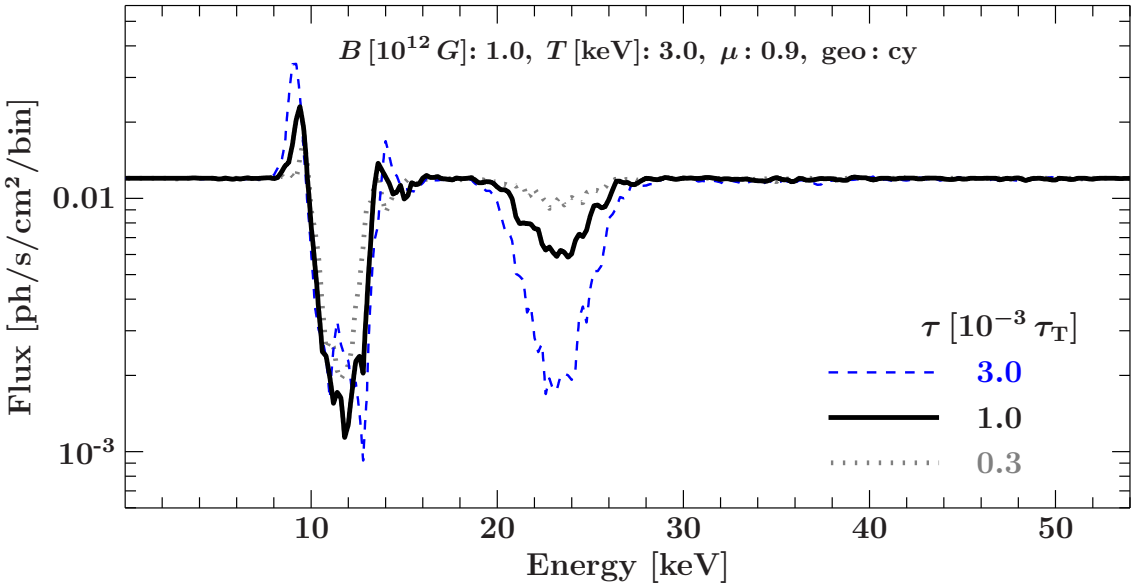

Figure 5.1.: A change in optical depth mainly affects the cyclotron line depth.

continuous transition from one parameter to the next. This representation helps theorists to compare competing simulations and observers to improve decisions during the process of fitting models to X-ray data.

5.1. Optical Depth

The optical depth, τ, is the parameter mainly responsible for the amount of scattering processes. It unifies information about density and extension. An elongated cylinder, for instance, might have the same optical depth, and therefore give rise to the same amount of CRSF interactions, as a shorter cylinder with a higher density. Using one parameter for the density and the length to store simulation results and as a model parameter circumvents the redundancy of information.

In the regime considered here, 1–30$\times10^{-4}$ τ_T, the most evident effect of a change in optical depth on the CRSF shape is its influence on the line depths. Figure 5.1 visualizes this for the case of a reduction of the optical depth by 1/3 in a cylinder geometry. Two optical depths are relevant for geometries described in this work: The optical depth perpendicular to the B-field axis, $\tau_\perp$, describes a geometry's "density-extent" in radial direction. The optical depth parallel to the field, $\tau_\parallel$, describes the medium's density along the magnetic field axis. $\tau_\perp$ is the relevant parameter for a cylinder geometry, which is infinitely extended along the field axis and therefore defined only by its radial optical depth. A slab geometry on the contrary is defined by the optical depth parallel the B-field axis.

As discussed in Section 4.10 the optical depth has a critical influence on the approximative polarization states used for the cross section calculation. It also limits the domain where

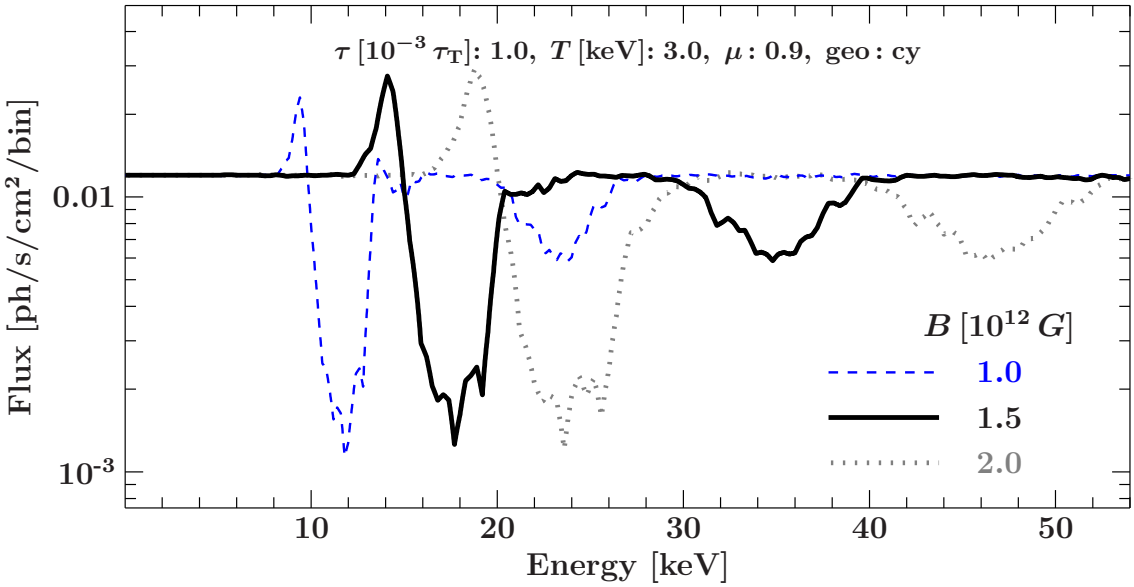

Figure 5.2.: Illustration of the influence of a change in magnetic field strength. The position of the cyclotron feature is shifted to higher energies for an increased magnetic field strength.

Monte Carlo simulation are the method of choice (see, e.g., Wang et al., 1988; Isenberg et al., 1998b) because the simulation time increases rapidly with increasing optical depth. Another assumption which relies on the optical depth regime mentioned above is the neglect of a collisionally excited population of electrons, which is well justified for the optical depths considered here (Araya & Harding, 1999).

5.2. Magnetic Field

The most obvious parameter for cyclotron lines is the magnetic field strength, B, the magnitude of which must be of the order of $\sim 10^{12}$ G for cyclotron lines to form at all. Figure 5.2 shows the influence of a change in the magnetic field strength. The energies of the Landau levels, and therefore the cyclotron line positions, correlate with the field strength and are therefore shifted. Another illustration of this behavior can be seen in Fig. 1.1 which shows multiple CRSF spectra for various field strengths. This correlation enables the direct measurement of the B-field of an accreting neutron star, though results must be interpreted carefully. One must take into account the gravitational redshift which depends on the distance to the neutron star. This z-shift is typically of the order of 0.3 for neutron star binaries (Schönherr et al., 2007b). Additionally, care has to be taken that the measured magnetic field strength is not necessarily the surface magnetic field of the neutron star but rather the magnetic field strength at the line forming region. Apart from the position of the cyclotron line, the magnetic field also has a more subtle influence on some other properties. The degree to which the classical cyclotron decay rate deviates from the relativistic calculation depends on the magnetic field strength, as shown in

Section 3.3. Herold et al. (1982) show that these deviations are by no means negligible for typical magnetic field strengths of cyclotron line sources. The error of the non-relativistic approximation is considerable even for magnetic fields of 0.1 $B_{\rm crit}$, where the deviations from the relativistic result lies between 29% and 42% depending on the spin orientation of the emitting electron (Herold et al., 1982). The absolute value of the scattering cross section decreases with increasing magnetic field strength, which can be seen in the cross section plots in Section 3.5 and especially in the thermally averaged ones in Section 3.6. This affects the spectral formation of CRSFs in complex ways because the decay rate is influencing not only the cyclotron scattering cross sections but also the emission of spawned photons from previously excited electrons.

The magnetic field also has a large influence on other scattering processes and their realms of operation. Wunner (1979) showed that one photon annihilation dominates over pair annihilation into two photons for fields above 0.24 $B_{\rm crit}$ (Sina, 1996). The two photon annihilation cross section reduces to 30% at the critical magnetic field strength. However, this is beyond the magnetic field domain considered in this work. Not only the surface magnetic field strength but also its overall shape, meaning its spatial distribution of strength and orientation alters the cyclotron line shapes. The magnetic field structure is often assumed to be a dipole for simplification. The evolution of multipole moments of higher order are possible due to thermal (Blandford et al., 1983) and crust plate tectonic (Ruderman, 1991a,b,c) effects. Nishimura (2005) discuss the influence of such non-dipole magnetic fields on the peak energies of cyclotron absorption lines.

The CRSF simulation of this work is able to simulate a magnetic field gradient by stacking multiple slabs with different magnetic fields on top of, or inside of each other. This results in an approximation of the magnetic field gradient, which can be refined arbitrarily by reducing the spatial dimension of these slabs in the direction of the field gradient, that is, increasing the number of slices.

Section 6.3 shows the more simple but versatile approach of implementing a magnetic field gradient by using Green's functions pre-calculated from single slab configurations with different magnetic fields. The same geometry is simulated for different B-fields and the model spectra at given positions are calculated by convolving the input continuum at each position with the Green's functions interpolated for the magnetic field at the corresponding position. This implies the neglect of interactions between slices with different B-fields, an assumption which is reasonable only if the change of the magnetic field is small on the length scales on which most photons escape the medium completely.

5.3. Electron Temperature

The electron temperature is the temperature associated with the movement of the plasma electrons parallel to the magnetic field (see, e.g., Isenberg et al., 1998b; Araya & Harding, 1999). Only their component parallel to the field matters because the electrons are quantized perpendicular to the field (Canuto et al., 1971). The parallel electron movement due to the

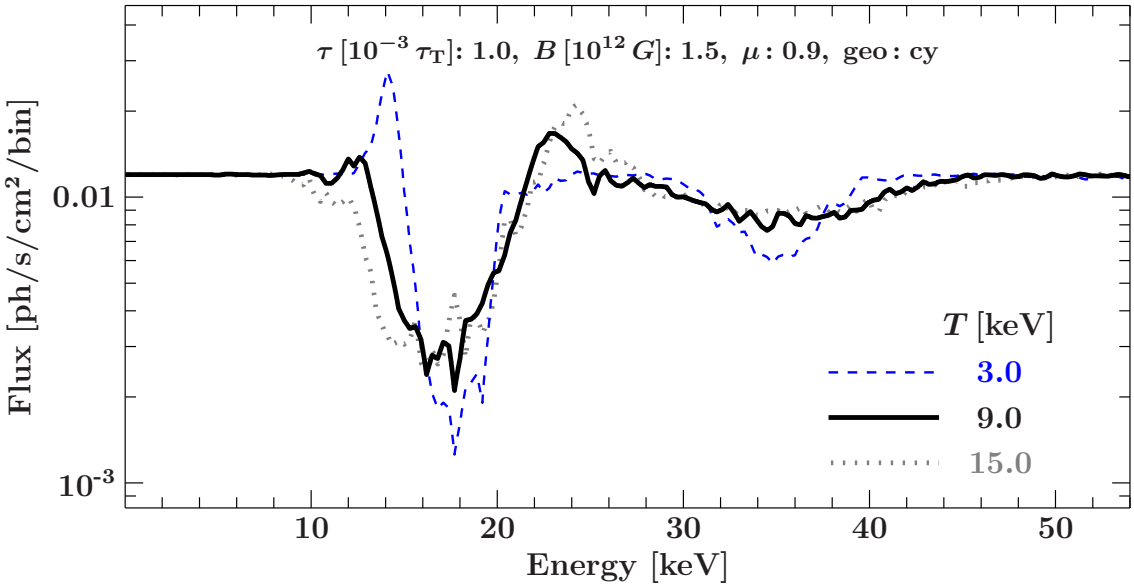

Figure 5.3.: Line broadening due to a change in electron temperature. A one dimensional relativistic Maxwell distribution (see Eq. 5.1) is assumed in the simulations. Only the electron momentum parallel to the magnetic field axis is continuously distributed. Therefore the broadening of the CRSFs due to the electron temperature is most notably for small angles to the B-field axis. This can be seen in the thermally averaged scattering cross sections from Schwarm et al. (2017b, Figs. B.1 and B.2 in the Appendix).

temperature overlays their bulk motion, that is, the falling of the accreted plasma onto the neutron star. The influence of this bulk motion will be described in detail in Section 5.6. An electron temperature distribution has to be assumed for the artificial sampling of electron parallel momenta. Popular choices are the usage of a one-dimensional version of the Maxwell velocity distribution (Maxwell, 1860a,b) and its relativistic counterpart (see, e.g., Harding & Daugherty, 1991; Araya, 1997; Isenberg et al., 1998b; Schönherr et al., 2007b; Schönherr, 2007; Schwarm et al., 2017b)

$$f(p) = N e^{-\frac{(E-m_e)}{k_B T}} , \tag{5.1}$$

where $k_B T$ is the electron temperature and $E = \sqrt{m_e^2 + p^2}$ in natural units. The normalization constant N is chosen such that $\int_{-\infty}^{+\infty} f(p)dp = 1$. Section 4.7.1 explains this in detail.

The cyclotron line width increases with increasing temperature due to an increased width of the corresponding thermally averaged cyclotron cross sections. The thermally averaged cross section profiles exhibit sharp peaks at the cut off energy for very high temperatures and large angles to the magnetic field since the temperature broadens their peaks only up to the cut off energy on the high energy side (Harding & Daugherty, 1991; Schwarm et al., 2017b). This broadening is evident even for very small μ as shown in Fig. 5.3.

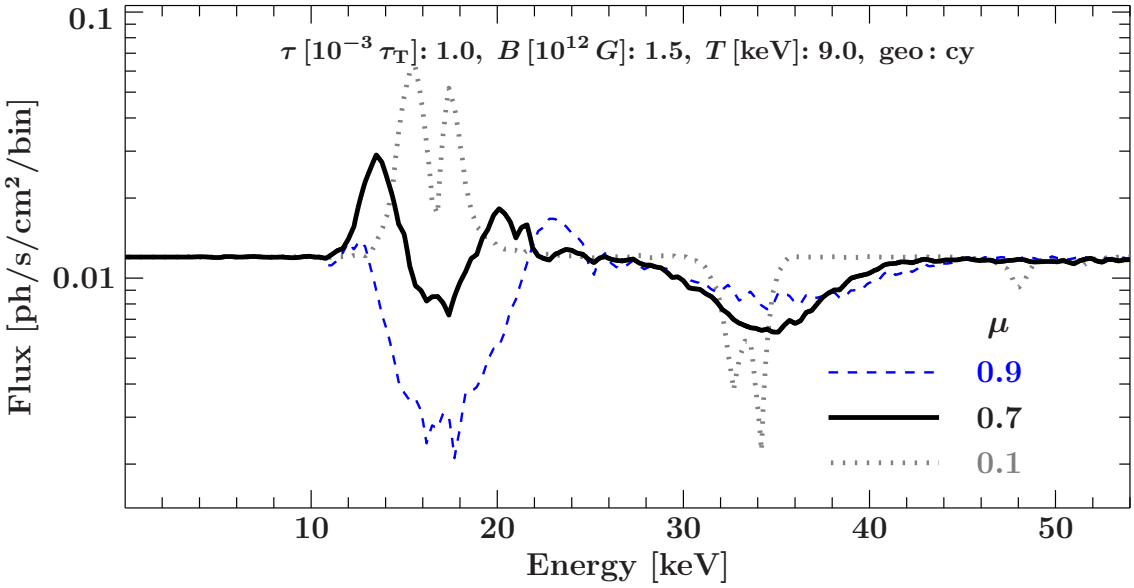

Figure 5.4.: Influence of a changing viewing angle to the magnetic field on the CRSF line shape.

5.4. Viewing Angle

The viewing angle, mostly defined by its cosine $\mu = \cos\vartheta$, is as important as the energy binning of the simulated spectra because they are relativistically coupled (see, e.g., Araya & Harding, 1999). This is due to the integration of the cross sections over a thermal electron momentum distribution, which determines the Lorentz-transformed properties of the interacting photons.

The influence of the viewing angle on CRSFs is illustrated in Fig. 5.4. In general, narrow and deep lines are expected for viewing angles perpendicular to the magnetic field axis. This is a direct consequence from the very narrow thermally averaged cross sections in this regime. Figures 4.13 and 4.14 illustrate this. The kinematic constraints limit the effective electron momentum range, which makes it difficult for the photons to find a suitable scattering partner if they are away from the resonances already. For smaller viewing angles to the magnetic field, meaning propagation parallel to the B-field axis, the photons can gain or loose momentum during the interaction resulting in wide shallow cyclotron lines. Opposite to the broadening due to an increased electron temperature (Section 5.3), the increase in line width goes along with a decrease in line depth. If phase averaged spectra are observed an angle mixing is expected to occur. This mixing can influence the line shape and is implemented in the CRSF model by averaging over a fixed number of angles in between angular boundaries. By fitting these boundaries an angular range can be obtained, which may allow for geometrical interpretations. In the case of phase dependent spectra the observed ranges are expected to be quite small depending on the timing resolution and the correct relativistic light bending becomes more important. In Section 6.4 a method is described in which the energy dependent angular dependencies can be utilized to possibly detect new cyclotron line sources.

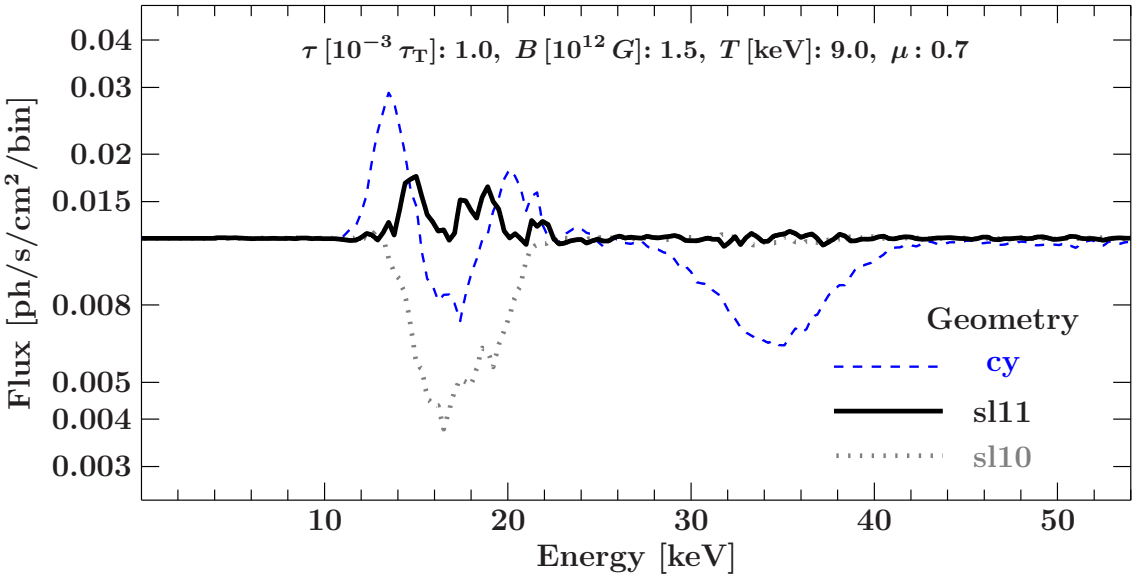

Figure 5.5.: Influence of the geometry. The CRSF line shape is highly dependent on the simulated geometry: cylinder, slab 1-0, and slab 1-1 geometries are shown here. For the present parameter combination the deepest fundamental line is observed for slab 1-0 geometry. The deepest harmonic occurs for cylinder geometry.

5.5. Geometry

The geometry largely influences the CRSF line shape. The difference between slab 1-0 and slab 1-1 geometry can be seen in Fig. 5.5. slab 1-1 geometry, where the seed photon source is embedded within the CRSF forming medium, exhibits more pronounced line wings. Both slab-type geometries are generally more probable for low luminosity sources, since a shock front above the neutron star surface, as expected in the case of higher luminosities, is more consist with an accretion column instead of a simple accretion mound hot spot. Cylinder type geometries, on the other hand, ought to be used whenever a fan-beam like emission pattern is more probable (Schönherr, 2007). In practice this means that the combination of physical continuum models assuming an accretion column, possibly with a shock front, such as the models by Becker & Wolff (2007) and Davidson (1973), should be combined with a cylinder symmetrical CRSF model. Continuum models with a limited extension in height (see, e.g., Pechenick et al., 1983; Ftaclas et al., 1986; Greenstein & Hartke, 1983; De Luca et al., 2005) are more consistent with a slab geometry. Mukherjee & Bhattacharya (2012), for example, modeled accretion mounds of heights of the order of some 10 m, which are optically thick parallel to the neutron star surface considering the hot spot radii of $\sim 10^5$ cm resulting from their MHD model. Zhelezniakov (1981) explicitly proposed a model containing components from both an accretion column and a hot spot. Such models require careful considerations for the combination with the CRSF model described here, especially about the position of the line forming region: if the cyclotron lines are forming within the accretion column, that is, in the rest frame of the accreting plasma, seed photons from a hot spot on the neutron star surface, which is in the rest frame

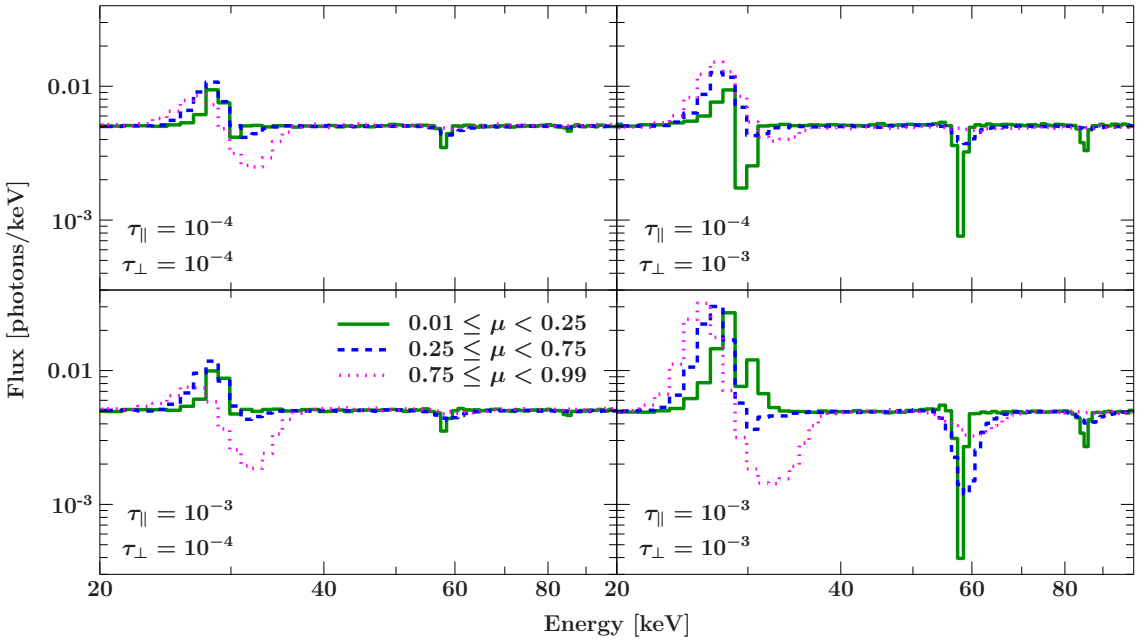

Figure 5.6.: Effects of a change from slab-like to cylinder-like geometries and vice versa.

of the neutron star, must be boosted into the frame of reference of the line forming region according to the downfalling plasma's bulk velocity.

Figure 5.6 further illustrates the spectral changes involved when going from a more slab-like geometry extended further in radial direction than in height, to a more cylinder-like geometry, which is more extended parallel to the magnetic field axis than perpendicular to it. Also, it shows the cases for a "cube-like" geometry with the same optical depth in radial direction and height.

5.6. Bulk Velocity

The accreted matter is falling toward the poles of the neutron star with relativistic velocities. Therefore the individual electron velocities parallel to the magnetic field are superposed by the bulk velocity. Figure 5.7 shows the influence of a constant bulk velocity on the CRSF spectra: the cyclotron line energies are shifted to lower energies for viewing angles to the magnetic field axis smaller than 90° because the interacting photons appear to have a higher energy in the restframe of the down-falling electron plasma. In the case of photons escaping toward the neutron star, in opposition to the B-field axis, the photons appear less energetic in the electrons' restframes, leading to a shift of the CRSFs toward higher energies.

Additionally, the different spawning behavior in these two angular regimes leads to extremely different shapes of the fundamental cyclotron line. The fundamental CRSF is an absorption line for medium angles ($\mu = 0.5$) along the B-field axis in contrast to a

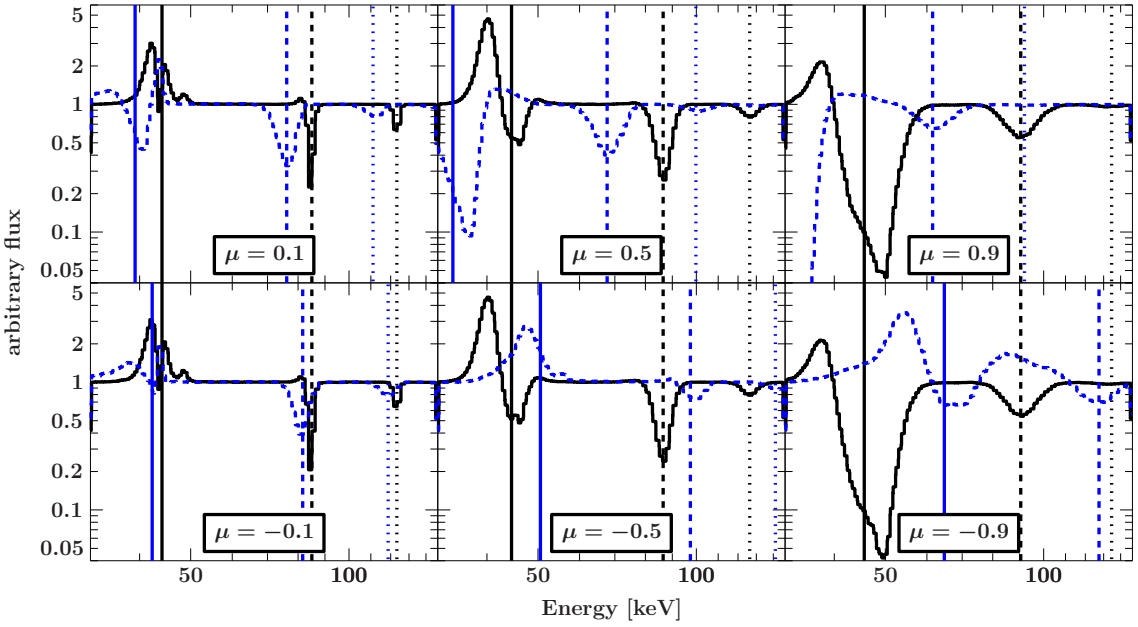

Figure 5.7.: For the illustration of the effect of bulk velocity a different set of parameters was chosen to demonstrate multiple effects: the figure from Schwarm et al. (2014) shows simulated CRSF spectra for cylinder geometry with a magnetic field of $B = 0.09\,B_{\mathrm{crit}}$ and temperature $k_{\mathrm{B}}T = 3\,\mathrm{keV}$ for different viewing angles $\mu = \cos\vartheta$. In the case of zero bulk velocity (black solid lines) the cyclotron lines for small angles to the B-field axis ($\mu = \pm 0.9$) appear in absorption. This symmetry is broken in the case of a bulk velocity of $v = -0.4c$ (blue dashed lines), which features emission-like lines for small angles anti-parallel to the B-field axis, i.e., photons escaping "downwards", into the direction of the neutron star. In contrast, the fundamental, absorption-like, line for small angles parallel to the field is shifted but not filled up with spawned photons if bulk velocity is assumed. This behavior originates from the angular redistribution due to cyclotron scattering in conjunction with the downward beamed spawning patterns. Figure 5.8 shows both. The overall shift in energy is expected since the scattering takes place in the electron rest frame which is Doppler shifted in energy by the additional velocity component.

cyclotron line in emission for a medium angle in the opposite direction of the B-field axis.

The shifting in energy interferes with a straight forward interpretation of shifted cyclotron lines as cyclotron lines from a line forming region differing only in the strength of the magnetic field. The angle dependent variation in emission/absorption-like behavior, on the other hand, complicates the interpretation of emission-like behavior due to very low optical depths (see Section 5.1) or due to the formation of CRSFs by reflection of radiation from the neutron star atmosphere (see Section 6.5), and absorption-like behavior due to large angles to the magnetic field axis.

Therefore bulk velocity should be taken into account for the combination of CRSF models with column models showing relativistic velocities of the accreted plasma. Whether or not a velocity gradient must be considered for CRSF simulations in X-ray binary accretion

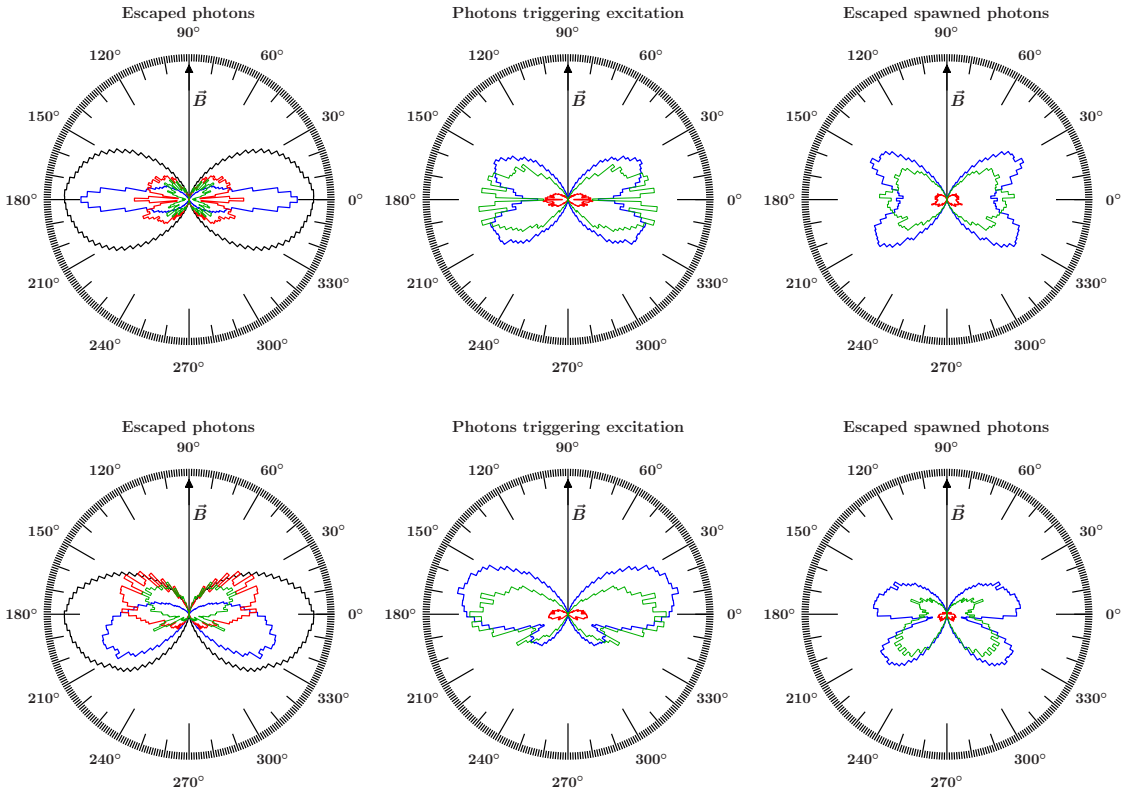

Figure 5.8.: Angular distribution of photons emerging from a static cylinder column (top) and from one with bulk velocity $v_{\text{bulk}} = -0.4\,c$ (bottom). From left to right: Continuum photons escaping unaltered, photons produced by spawning processes, and all emerging photons. The black lines correspond to arbitrary energies while the blue line corresponds to photons with an energy E for which $|E' - E'_{\text{res},0}| < 1\,\text{keV}$ showing photons effectively filling up the fundamental cyclotron line. The green and the red lines are the same as the blue line but for the higher resonances $n = 1$ (green) and $n = 2$ (red). In the case of bulk velocity photons spawned during decay processes are beamed downwards. Continuum photons tend to escape upwards due to the smaller variety of electron momenta in that direction. Figure and caption from Schwarm et al. (2014, Fig. 2).

columns depends on the magnitude of the change in bulk velocity within the, necessarily constrained, line forming region.

6

Astrophysical Application

In the following, the model developed in the course of this thesis will be applied to highly topical experimental data. This serves the purpose of verifying that the model lives up to the expectation of being capable of describing measured cyclotron line shapes. Also, its compatibility with modern astronomical data analysis tools, such as ISIS (Houck & Denicola, 2000) and XSPEC (Arnaud, 1996), is tested this way. Its ability to be used as a fitting model will be demonstrated by providing fitting results both from the author of this work and from a collaborator not involved in the development of the model code. It will be seen that theoretical features, such as the line wings around the fundamental cyclotron line, disappear, in agreement with the experimental data, as anticipated, for example, in Section 5 before. This is the first time that a detailed radiative transfer model including the correct scattering cross sections has been able to generate line profiles that agree with the observation data. A more detailed analysis is performed for another example source to highlight the models ability to converge to reasonable, and physically meaningful, parameter values including the calculation of errors. The combination with other models, in particular the combination with the light bending code from Falkner et al. (2017) and with the physical continuum model from Becker & Wolff (2007), demonstrates the CRSF model's versatile range of applications. For each point a different example source was chosen to show the catholicity with respect to different source types, as well. Also, the ongoing discussion of the position of the line forming region is illuminated from a CRSF modeling point of view.

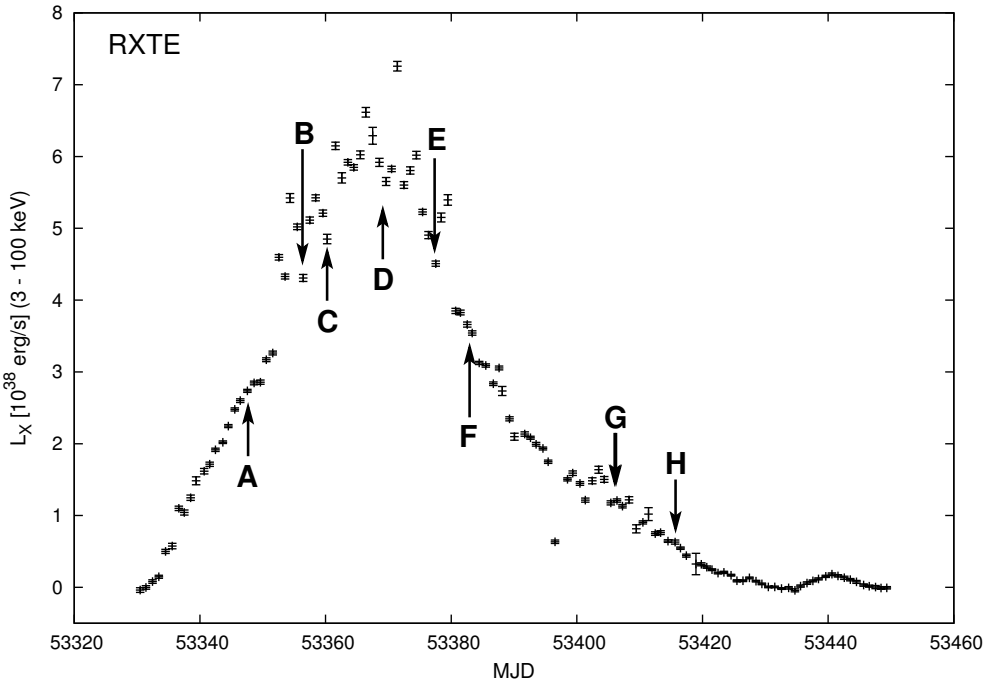

Figure 6.1.: V 0332+53 light curve during the 2004/2005 outburst observed with the All-Sky Monitor on *RXTE*. Figure from Sasaki et al. (2012, Fig. 4 therein).

6.1. Phase Resolved View on V 0332+53

V 0332+53 is a transient X-ray source with a pulse period of 4.37 s (Whitlock, 1989) and a 34 day orbit with an eccentricity of 0.31 (Stella et al., 1985). Analyzing the *Ginga* LAC spectra of its October 1989 outburst, Makishima et al. (1990) found that it features a cyclotron line. The spectra show hints for the first harmonic CRSF as well. A third cyclotron line and evidence for a non-Gaussian shaped fundamental line were found in the *RXTE*/HEXTE spectra of the December 2004 outburst by Coburn et al. (2005) and Pottschmidt et al. (2005). The presence of three lines was confirmed later by Kreykenbohm et al. (2005) using *INTEGRAL* data taken slightly after the peak of the outburst.

Sasaki et al. (2012) analyzed this outburst using the pulse-profile decomposition method described by Kraus et al. (1995) in order to improve the understanding of the geometry of the accretion onto the neutron star. They found that V 0332+53 operates in two distinct geometric regimes depending on the accretion rate. The emission can be interpreted as pencil-beam emission from the two modeled columns at the beginning and the end of the outburst. In contrast, a sideward beamed emission, that is, a fan-beam pattern (see their Fig. 15) is suggested by their model during the maximum of the outburst. They infer from this change in radiation pattern that an accretion column is formed in stages of high accretion. From a CRSF modeling point of view this can be interpreted as a change from slab 1-0 or slab 1-1 geometry to cylinder geometry during the outburst.

The complex physical setup described above requires a combination of the CRSF model

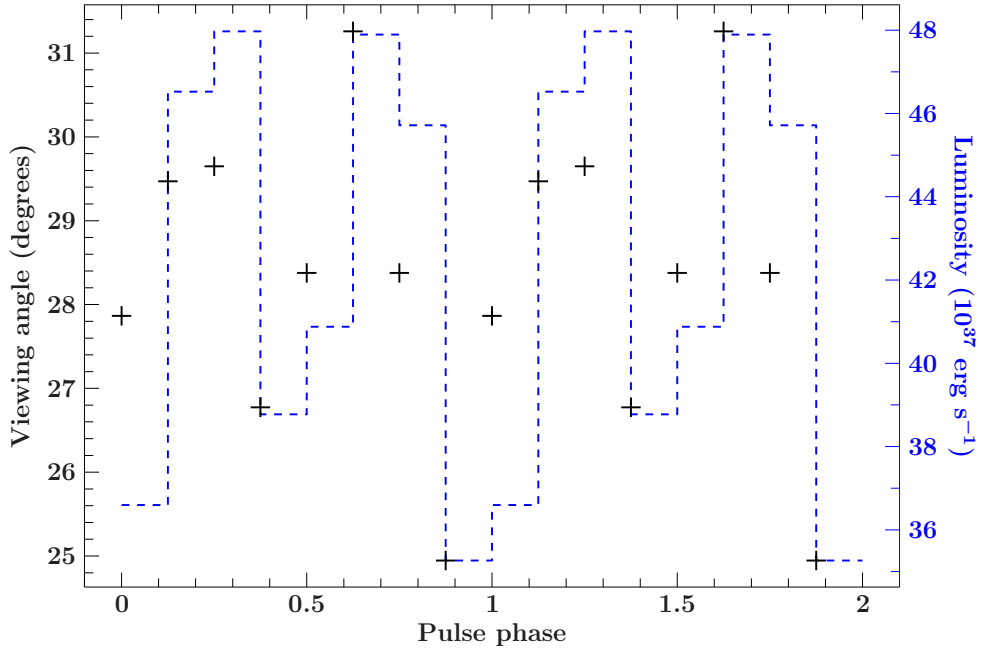

Figure 6.2.: Viewing angles (crosses) resulting from direct fits of the CRSF model to *RXTE* data of V 0332+53 with respect to the pulse phase. The axis on the right side shows the luminosity (dashed line), which is roughly tracked by the viewing angles. Figure courtesy of Hemphill (2016, priv. comm.).

with other sophisticated models in a self consistent way. The combination with a physically meaning full input continuum model is the subject of Section 6.3. The addition of a model for the geometric setup and light-bending effects will be discussed in Section 6.4. At this point, only an example for a very simple application of the CRSF model is given, by courtesy of Hemphill (2016), in order to demonstrate its technical feasibility to be directly fitted to data. The CRSF fitting model has been applied to the *RXTE* data right before the peak of the 2004/2005 outburst of V 0332+53, that is, IDs B and C in Fig. 6.1 (*RXTE* obsids 90089-11-03-* and 90089-11-04-*). A cylinder geometry table has been used due to the more likely fan-beam emission pattern during the outburst. The direct application of the CRSF fitting model implies that the cyclotron lines are formed in one column at one specific magnetic field strength, temperature, optical depth, and viewing angle. Figure 6.2 shows the resulting viewing angles with respect to the pulse phase. It varies only by $\sim 4^\circ$ (μ = 0.87–0.90) and seems to track the luminosity. Neither was the quality of the fit very good nor have errors been calculated, which, in combination with the very small fluctuations of the viewing angles, precludes any serious physical interpretation. Nevertheless, the application serves the purpose of demonstrating that the CRSF model is technically able to actually fit data and converge to parameter values within their given boundaries in a reasonable time. Furthermore the correlation of the viewing angle with the pulse phase proves that the model is capable of tracking the variations of multiple cyclotron line shapes simultaneously. The trend of a variation of the viewing angle with phase is theoretically expected as the neutron star is observed from different perspectives

during different pulse phases. The model parameters `mu_min`, `mu_max`, and `N_mu` in the CRSF model have been added in order to provide the user with a convenient way of averaging over a range of viewing angles. The spectrum is calculated for `N_mu` points in between, and including[1], `mu_min` and `mu_max`. The averaged spectrum is then build from the mean values of the calculated spectra for each energy bin. Such an averaging over the viewing angle is expected in phased averaged observations and leads to a smeared out cyclotron line profile, which is in better agreement with the CRSF line shapes observed. In Section 6.3 this technique is applied to a physical input continuum.

Additionally, the extension models `cyclocap` and `cyclocol` have been applied to the *NuSTAR* data of V 0332+53 (ObsID 80102002010). These fits are, again, not meant to be taken too serious as not much effort has been put in modeling the input continua in a physically meaningful way. This is especially evident in the input continuum for the case of cylinder geometry. Instead the focus was put on whether these models are able to model observed CRSF line shapes at all. This has by no means been obvious as the immense parameter range hinders theoretical considerations of this kind.

A slab-like model has been constructed, which is using the CRSF model developed in this work to superpose cyclotron lines generated at different points, and angles, in the slab. In contrast to the combination with a physical input continuum in Section 6.3, where a magnetic field gradient is included as a height variation, the varying magnetic fields here are generated by the radial dependencies of the magnetic field, which is assumed to be a dipole field, throughout the slab. Not only does the magnetic field vary depending on the distance to the center of the slab but so does the angle under which the slab is observed. This means that, though a slab limited by straight planes has been simulated using the CRSF MC simulation suite, the resulting Green's functions are interpreted as originating from a bent, spherical layer. Therefore the cosine of the angle to the magnetic field axis is calculated as $r/r_{\mathrm{NS}} - \mu$, where μ is the cosine of the angle to the magnetic field axis at the center of the slab[2]. The resulting best fit is shown in Fig. 6.3. Table 6.1 shows the corresponding parameters.

The resulting radius is very large and should not be interpreted as the radius of an accretion column but instead as the radiating polar cap of the neutron star, if interpreted at all. The reason for the large radius is that the smearing of the complex CRSF shapes as a reason for the broadening of the otherwise much more narrow single cyclotron lines depends on a rather large magnetic field gradient. Such a large gradient requires a large radial extension if a dipole field is assumed. An other example for a radial B-field gradient will be given in Section 6.5, where the work by Poutanen et al. (2013) is investigated, in which the correlation between the CRSF energy and the luminosity is explained by assuming a reflection on a variable fraction of the neutron star surface. Despite the mentioned concerns regard its physical interpretation, the results verify that the fitting models developed in the course of this work are able to describe cyclotron lines shapes measured in the X-ray

[1] If `N_mu` equals zero or one only one spectrum is calculated for the viewing angle given by `mu` or for the mean angle between the given boundaries, respectively.

[2] This shift in angle has been removed in later revisions as it does lead to additional systematic errors and hinders the physical interpretation. Its influence on the spectra shown here is only marginally.

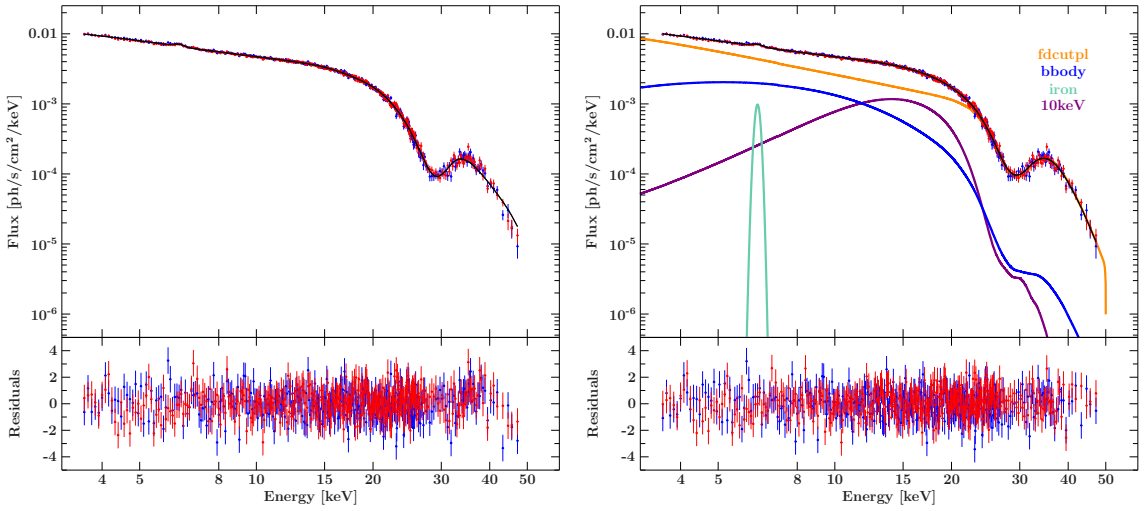

Figure 6.3.: Fits to NuSTAR data of V 0332+53. Left: Unfolded spectrum and `cyclocap` model for slab 1-0 geometry. Right: Same for cylinder geometry using the `cyclocol` model showing the individual continuum components, as well. The corresponding fit parameters are shown in Table 6.1.

spectra from accreting neutron star binaries.

In order to draw conclusions from the modeled CRSF shape, and for testing the model on other sources, a more rigorous application will be performed in the following on the example of the X-ray source Cep X-4.

6.2. Asymmetric Line Shape in Cep X-4

Cyclotron lines are mostly fitted using empirical absorption line models of primarily Gaussian shape. Vasco et al. (2013), for example, found a Gaussian absorption line to fit the cyclotron line observed in the X-ray spectra of Her X-1 well. Alternatively, a Lorentzian shaped line model is sometimes used in order to describe the line shape, which was found by Enoto et al. (2008) to describe the data better than a Gaussian absorption model. Fürst et al. (2013) found that both models describe the data equally well and that the overall shape of the line, at least in the case of Her X-1, the source investigated by all these works, is very symmetric.

The following Section, which is closely following, mostly in verbatim, the corresponding Section from Schwarm et al. (2017a), discusses the asymmetric line shape found by Fürst et al. (2015) in the source Cep X-4.

In order to demonstrate the applicability of the `cylofs` model to observed data, a comparison between empirically fitted line profiles with synthetic ones from the simulation described in Section 4 will be performed in the following. The results further motivate the necessity of a cyclotron line model based on firm physical grounds for the description of

Table 6.1.: Fits to NuSTAR data of V 0332+53. Left: Fit parameters for a slab 1-0 geometry using the CRSF model for simulating scattering on the neutron star's polar cap. Right: Fit parameters for a cylinder geometry. The corresponding spectra are shown in Fig. 6.3.

Parameter	Value	Unit	Parameter	Value	Unit
FPMB	1.01		FPMB	1.01	
N_H	0.1	10^{22}/cm^2	N_H	0.91	10^{22}/cm^2
Γ	1.88×10^{-2}		Γ	1.13	
E_{cut}	17.04	keV	E_{cut}	39.84	keV
E_{fold}	6.89	keV	E_{fold}	4.52	keV
$F_{3.5\,keV}^{10\,keV}$	0.24	keV/s/cm^2	$F_{3.5\,keV}^{10\,keV}$	0.22	keV/s/cm^2
kT	1.43	keV	kT	3.61	keV
$F_{3.5\,keV}^{10\,keV}$	6.67×10^{-2}	keV/s/cm^2	$F_{3.5\,keV}^{10\,keV}$	8.48×10^{-2}	keV/s/cm^2
A	1.62×10^{-3}	photons/s/cm^2	A	1.54×10^{-2}	photons/s/cm^2
E	17.79	keV	E	16.79	keV
σ	2.83	keV	σ	5.29	keV
τ	1.98×10^{-3}	τ_T	τ	2.88×10^{-4}	τ_T
B	3.36	B_{12}	B	3.33	B_{12}
T	7.13	keV	T	4.48	keV
μ	0.39		μ	0.9	
r_{ns}	10000	m	r_{ns}	10000	m
r	100	m	h	100	m
r_N	10		h_N	10	
r_{min}	1.73×10^3	m	h_{min}	1.29×10^2	m
r_{max}	3.15×10^3	m	h_{max}	7.71×10^2	m
Redshift	0.2		Redshift	0.2	
A	2.71×10^{-4}	photons/s/cm^2	A	2.45×10^{-4}	photons/s/cm^2
E	6.33	keV	E	6.32	keV
σ	0.11	keV	σ	0.1	keV
red. χ^2	1.09		red. χ^2	1.02	
d.o.f.	666		d.o.f.	667	

CRSF line profiles.

Cep X-4, also known as GS 2138+56, was discovered in 1972 June and July observations with the *OSO-7* X-ray telescope (Ulmer et al., 1973). It is an accreting HMXB with a pulse period of ~66 s as found in its 1988 outburst with *Ginga* (Makino & GINGA Team, 1988a,b) and later confirmed by Koyama et al. (1991). The optical counter part is a Be star (Roche et al., 1997) at a distance of 3.8 ± 0.6 kpc (Bonnet-Bidaud & Mouchet, 1998). Koyama et al. (1991) found that the addition of a cyclotron line at 31 keV improved the fit but they did not include it in their discussion for the sake of comparison to other cataloged X-ray pulsars. Mihara et al. (1991) proposed a cyclotron line at an energy of 30.5 ± 0.4 keV

and deduced a magnetic field of 2.6×10^{12} $(1 + z)$ G for the source. *RXTE*/PCA observed further outbursts in 1997 and 2002. McBride et al. (2007) performed a spectral and timing analysis of the latter outburst and found a cyclotron line at $30.7^{+1.8}_{-1.9}$ keV. *NuSTAR* (Harrison et al., 2013) observed Cep X-4 close to the maximum of the outburst and during its decline on 2014 June 18/19 and 2014 July 1/2, respectively (Fürst et al., 2015). The cyclotron line was measured at an energy of ∼30 keV in both observations. Fürst et al. (2015) found that its shape deviates from a simple Gaussian line profile (see also Jaisawal & Naik, 2015), which makes this observation a good candidate for an application of the physical CRSF model `cyclofs`.

Schwarm et al. (2017a) re-extracted the *NuSTAR* data from ObsID 80002016002 (2014 June 18/19, exposure time 40.5 ks) near the maximum of the outburst using the same settings and procedure as described by Fürst et al. (2015) but using the CalDB version 20160922 and the *NuSTAR* data analysis software (NuSTARDAS) version 1.6.0 as distributed with HEASOFT 6.19. The source and background spectra for focal plane module A and B (FPMA and FPMB) were extracted separately, using circular regions with radii of 120″. We use data in the 3.6–55 keV band and rebinned the data to a signal-to-noise (S/N) of 10 below 45 keV and a S/N of 5 above that.

Schwarm et al. (2017a) use the same empirical continuum model as Fürst et al. (2015), which was already found by McBride et al. (2007) to describe the continuum well, that is, a power-law with a Fermi-Dirac cutoff (Tanaka, 1986; Makishima & Mihara, 1992),

$$F(E) = AE^{-\Gamma} \frac{1}{1 + e^{-(E-E_{\mathrm{cut}})/E_{\mathrm{fold}}}}, \tag{6.1}$$

with normalization constant A, photon index Γ, cutoff energy E_{cut}, and folding energy E_{fold}.

An improved version of the `tbabs` model, namely `tbnew`[3], is used with abundances by Wilms et al. (2000) and cross sections by Verner et al. (1996) in order to account for photoelectric absorption of the continuum. A narrow iron Kα line has been used as in the analysis by Fürst et al. (2015). Their low energy black body was dismissed because it did not improve the fit. Also, contrary to the analysis by Fürst et al., but in agreement with the continuum model used by McBride et al. (2007), a "10 keV" feature has been added, that is, a Gaussian emission line that facilitates the modeling of the continuum in the ∼8–20 keV range, which has been applied before, for various sources and instruments (Mihara, 1995; Coburn et al., 2002). The width of this broad emission component is in agreement with but much better constrained than the corresponding component used by McBride et al. (2007). The centroid energy of 16.1/1.3 = 12.4 keV is below the value of 14.4 keV found by McBride et al. (2007). The additional factor of 1.3 is necessary for the comparison because of the gravitational redshift: in contrast to previous modeling approaches, the model by Schwarm et al. (2017a) includes a redshifting of all components but the iron line with a fixed redshift of $z = 0.3$ (see, e.g., Schönherr et al., 2007b). The XSPEC convolution model `zashift` is used for that purpose.

[3] `http://pulsar.sternwarte.uni-erlangen.de/wilms/research/tbabs/`

The luminosity of $1\text{–}6 \times 10^{36}\,\mathrm{erg\,s^{-1}}$ (Fürst et al., 2015) is low compared to other accreting X-ray pulsars exhibiting cyclotron lines (Fürst et al., 2015) and well below the theoretical limit where a shock in the accretion column is expected to form (Becker et al., 2012). This suggests the usage of a slab geometry for the `cyclofs` model, which is the only model used to fit the CRSF line profile, meaning that no other absorption line component has been used.

The complete fit model used is thus: $\mathtt{C_{FPMA}} \times$ `tbabs` $\times$ `(redshift(cyclofs(powerlaw` $\times$ `fdcut + gauss`$_{10\,\mathrm{keV}}$`)) + gauss`$_{\mathrm{iron}}$`)`, where $\mathtt{C_{FPMA}}$ is the cross-calibration of focal plane module FPMB relative to FPMA.

Starting with the parameters obtained from the fits by McBride et al. (2007) and Fürst et al. (2015), the physical CRSF model for a slab 1-0 geometry converged toward an acceptable fit with a reduced χ^2 of 1.17 for 862 degrees of freedom. The unfolded spectrum is shown in Fig. 6.4a together with the model for both detectors, FPMA and FPMB, and the corresponding residuals are shown in Fig. 6.4b. The best fit parameters can be found in Table 6.2, with uncertainties given at the 90% confidence level.

As discussed by Müller et al. (2013), the position of the cyclotron line can be affected by the continuum model. This complicates the comparison of the magnetic field strength to previous works. Koyama et al. (1991) noticed an absorption feature at ∼31 keV using a power-law plus exponential cutoff. Mihara et al. (1991) used a power-law times cyclotron scattering cutoff (Tanaka, 1986) to describe the continuum and found the feature to reside at 30.5 ± 0.4 keV. Using a model consisting of negative and positive power-laws with a common exponential cutoff (Mihara, 1995, NPEX), Makishima et al. (1999) detected the cyclotron line at 28.8 ± 0.4 keV. Jaisawal & Naik (2015) included a fundamental cyclotron line at 27.5 ± 0.4 keV, 27.7 ± 0.4 keV, or 29.6 ± 0.5 keV in their best-fit models for an NPEX, CompTT, or Fermi-Dirac plus blackbody continuum model, respectively, in their analysis of the *Suzaku* observation of Cep X-4 in 2014. The corresponding widths of the Gaussian absorption lines used for fitting the CRSFs differ from each other as well between the different continuum models. McBride et al. (2007) and Fürst et al. (2015), both using a Fermi-Dirac continuum model, found cyclotron lines at $30.7^{+1.8}_{-1.9}$ keV and $30.39^{+0.17}_{-0.14}$ keV (and $29.42^{+0.27}_{-0.24}$ keV during the decline of the 2014 outburst), respectively. The analyses of all these works differ by more than the continuum model: some use additional `gabs` model components to model the continuum and/or asymmetries in the fundamental line profile, different models are used to describe the line shape including Gaussian absorption lines and pseudo-Lorentzian profiles such as `cyclabs`, different instruments might be responsible for systematic deviations, and the physical behavior of the source itself, such as variations of the height of the line forming region with luminosity (see, e.g., Becker et al., 2012), might lead to different magnetic field strengths — and therefore differences of the measured cyclotron line energy — between observations. The range of the values from the previous works listed above, from ∼28 keV to ∼31 keV, and differences of ∼8% resulting from the application of different continuum models to the same observation further illustrate the incomparableness of cyclotron line energies resulting from differing analyses.

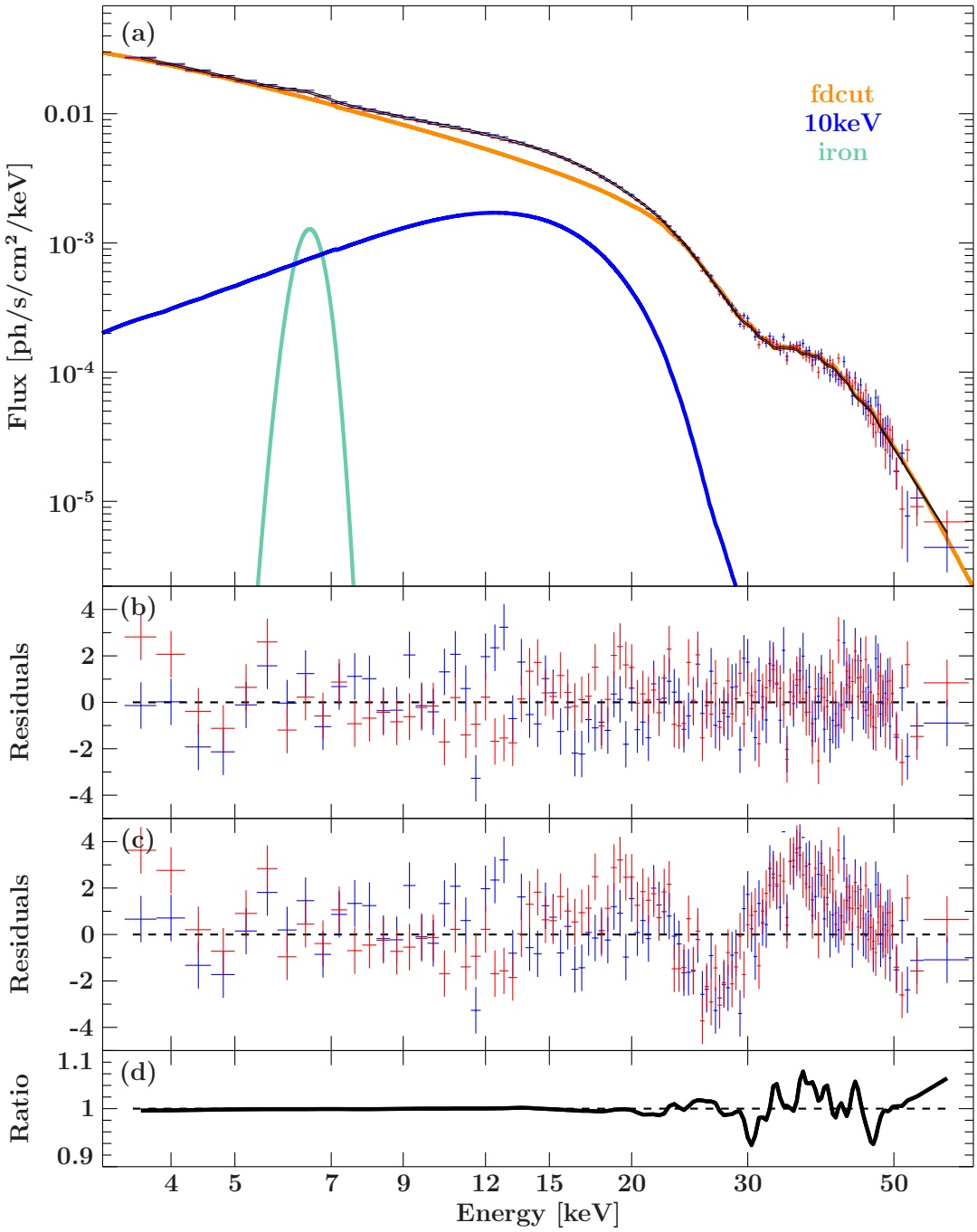

Figure 6.4.: (a) Unfolded spectrum, best-fit model, and individual continuum components for an observation (ObsID 80002016002) of Cep X-4. The data and residuals from *NuSTAR* FPMA and FPMB are shown in red and blue, respectively. (b) Residuals to the best-fit model. (c) Residuals to the best-fit model with a Gaussian absorption line centered at the cyclotron line position found by the best-fit model. Only the width and depth of the line have been fitted. (d) Ratio between the physical and the empirical model. In the empirical model, all line parameters were allowed to vary including the centroid energy. The data have been regrouped for improved clarity.

Table 6.2.: Best-fit parameters for the `cyclofs` model in combination with a Fermi-Dirac cutoff continuum model.

Parameter	Value	Unit
C_{FPMB}	1.0341 ± 0.0020	
N_H	$2.1^{+0.6}_{-0.5}$	10^{22} cm^{-2}
A_{cont}[a]	$0.230^{+0.036}_{-0.025}$	
Γ	$1.30^{+0.09}_{-0.07}$	
E_{cut}	$29.1^{+2.2}_{-1.9}$	keV
E_{fold}	$9.8^{+0.6}_{-0.4}$	keV
$A_{10\mathrm{keV}}$[a]	$0.025^{+0.009}_{-0.006}$	
$E_{10\,\mathrm{keV}}$	$16.1^{+0.5}_{-0.7}$	keV
$\sigma_{10\,\mathrm{keV}}$	$6.0^{+0.7}_{-0.6}$	keV
$\tau_{\parallel}$	$\left(2.59^{+0.16}_{-0.24}\right) \times 10^{-4}$	τ_{T}
B	$3.627^{+0.030}_{-0.031}$	10^{12} G
T[b]	$14.4^{+0.5}_{-0.9}$	keV
$\mu = \cos\vartheta$	$0.82^{+0.04}_{-0.05}$	
A_{iron}[a]	$\left(9.6^{+1.2}_{-1.0}\right) \times 10^{-4}$	
E_{iron}	$6.491^{+0.027}_{-0.028}$	keV
σ_{iron}	0.30 ± 0.05	keV
red. χ^2	1.17	
d.o.f.	862	

[a] In photons keV^{-1}s^{-1}cm^{-2} at 1 keV.
[b] The electron temperature in this fit is only slightly below the current upper boundary of 15 keV covered by the table. The corresponding upper error is therefore given at the 68% confidence level.

In order to compare the physical line model with an empirical model of the line shape on the basis of the same continuum, the `cyclofs` model has been replaced by a multiplicative absorption model, namely `gabs`, at the energy where such a simple absorption line would be expected for the best-fit magnetic field strength, that is, $E_{\mathrm{gabs}} = B_{\texttt{cyclofs}} \times 11.57\,\mathrm{keV} \approx 41.96^{+0.35}_{-0.36}\,\mathrm{keV}$ in the frame of the neutron star (i.e., before redshifting)[4]. Leaving this energy and all other parameters frozen while fitting the width and the depths of the empirical absorption line results in a reduced χ^2 of 1.57 for 876 degrees of freedom. The corresponding residuals are shown in Fig. 6.4c, which clearly illustrates that the centroid energy of the Gaussian absorption line model is off the cyclotron line. Only when all parameters of the `gabs` model are left free, can the profile of the cyclotron line

[4]Note that the physical cyclotron line model has been substituted in place, that is, the `gabs` model is still within the redshift model and therefore shifted to ~32.3 keV by `zashift`.

be represented by a Gaussian absorption line with a centroid energy of $40.01^{+0.15}_{-0.14}$ keV before redshift (red. χ^2 of 1.17 for 875 d.o.f.). The value of $E = 40.01\,\mathrm{keV}/(1+z) = 30.78^{+0.12}_{-0.11}$ keV after redshift reduction is almost consistent with the value found by Fürst et al. (2015) for the higher energetic Gaussian absorption line used to model the asymmetric line shape. The ratio of this model to the best-fit model using the physical CRSF model is shown in Fig. 6.4d. Evidently, the shapes of the line models differ significantly as expected.

The model for Cep X-4 presented here makes no claim of uniqueness. Instead many assumptions are made: other geometries might fit the spectrum equally well, neglecting bulk velocity becomes questionable if either the continuum or the cyclotron line are formed in a region of the accretion column with a significant velocity, and the usage of an empirical continuum with a "10 keV" feature (Mihara, 1995; Coburn et al., 2002, see, e.g.,) — the origin of which is unclear — is questionable *per se*, to name just a few. Furthermore, only one viewing angle to the magnetic field axis is taken into account, which is unrealistic considering that the data are averaged over pulse phase. The `cyclofs` model provides the possibility to average over multiple angles in order to overcome this inaccuracy albeit in an approximative way (see Section 4.9.2 for details). The width of the cyclotron line is strongly affected by the viewing angle and the temperature. Here, the width is mainly fitted by the angle to the magnetic field axis. Magnetic field, temperature, and velocity gradients are neglected, though they might largely influence the CRSF line width as well. Studies with more complex configurations of the CRSF medium are needed for estimating their influence quantitatively. Physical continuum models should be combined with the physical model for the CRSF line shape presented here. Their combined application to many observations of diverse sources covering a large parameter space of both continuum and line profile model parameters — some of these parameters might be tied together — might help to further constrain the highly degenerate parameter regime.

6.3. Physical Continuum for Her X-1

The following paragraph is adopted in verbatim from Schwarm et al. (2017a): Figure 6.5 shows synthetic cyclotron lines imprinted on the continuum from Becker & Wolff (2007, BW07) for the purpose of illustrating the influence of the continuum on the CRSFs and as an example for the cylinder geometry. The continuum parameters are the same ones as in the theoretical calculation from Becker & Wolff (2007) for Her X-1. This calculation agrees very well with the *BeppoSAX* data reported by dal Fiume et al. (1998). A spectral fit of a recent XSPEC implementation of the same continuum model to *NuSTAR* data of Her X-1 can be found in the work by Wolff et al. (2016). Figure 6.5 shows that the lines become deeper with increasing optical depth. The line width decreases with increasing viewing angle to the magnetic field, because of the smaller influence of Lorentz boosting in this regime. A cylinder geometry Green's table has been used for imprinting the cyclotron lines on the continuum. This approach leads to emission like behavior for very small optical depths and large angles to the magnetic field. Two higher harmonics can clearly be seen and are especially pronounced for large angles and relatively high optical depths

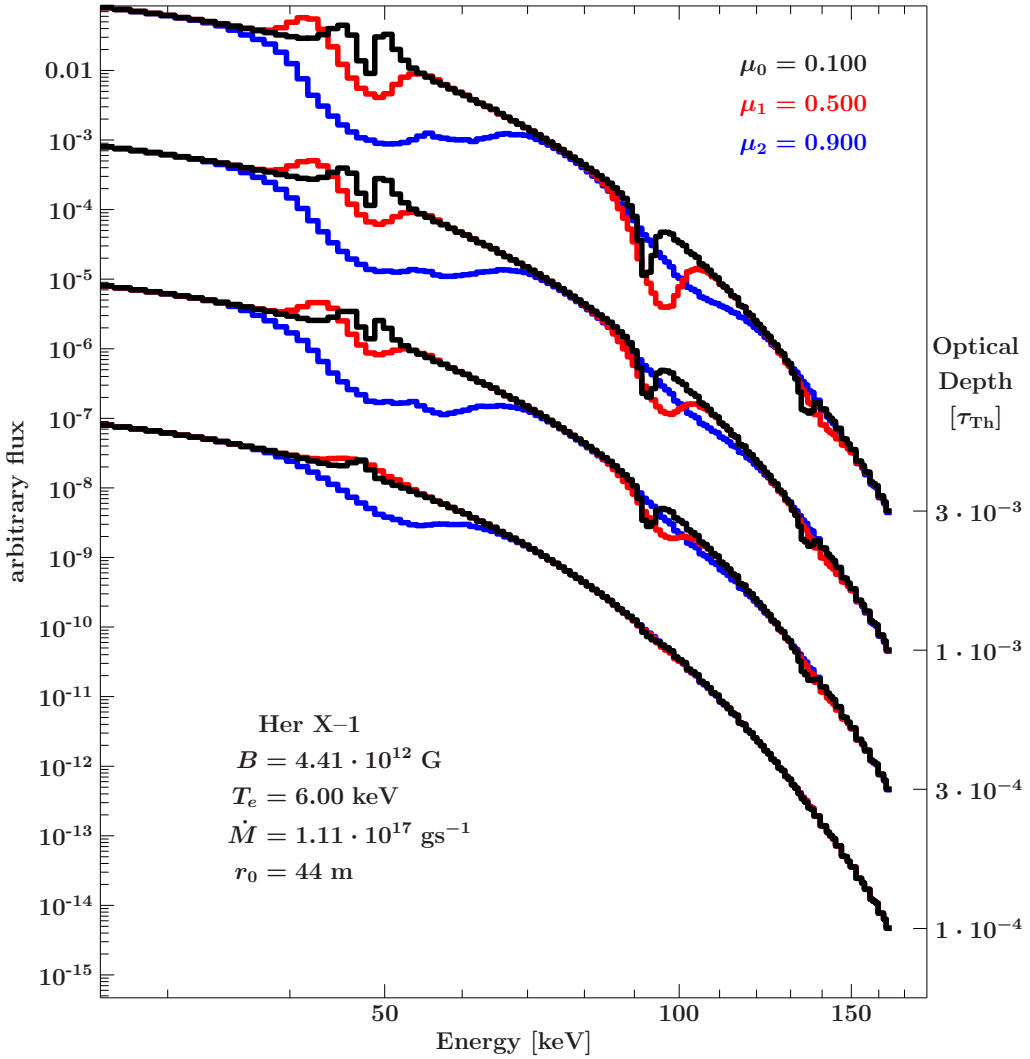

Figure 6.5.: Input continuum from Becker & Wolff (2007) with imprinted cyclotron lines for several angles to the magnetic field $\mu = \cos\vartheta$ and optical depths τ. The continuum input parameters are the same ones as in the spectrum from Becker & Wolff (2007, Fig. 6 therein) for Her X-1. The different colors show three angles to the magnetic field. The optical depth is increasing from the bottom to the top as shown by the right side axis. Figure and caption from Schwarm et al. (2017a).

of $\tau = 3 \times 10^{-3}\,\tau_{\mathrm{T}}$. These are theoretical spectra, which in contrast to observed spectra correspond to a line forming region with a constant magnetic field seen from a specific angle. Observations are expected to be smeared out due to an angle mixing with phase and an extended line forming region with a magnetic field gradient. Though the accurate handling of angle mixing requires the inclusion of relativistic effects (Schönherr et al., 2014), its influence on the CRSF line profiles, in the reference frame of the neutron star, can be roughly estimated by averaging over multiple viewing angles. Section 4.9.2 provides details on how this can be done easily with the `cyclofs` model.

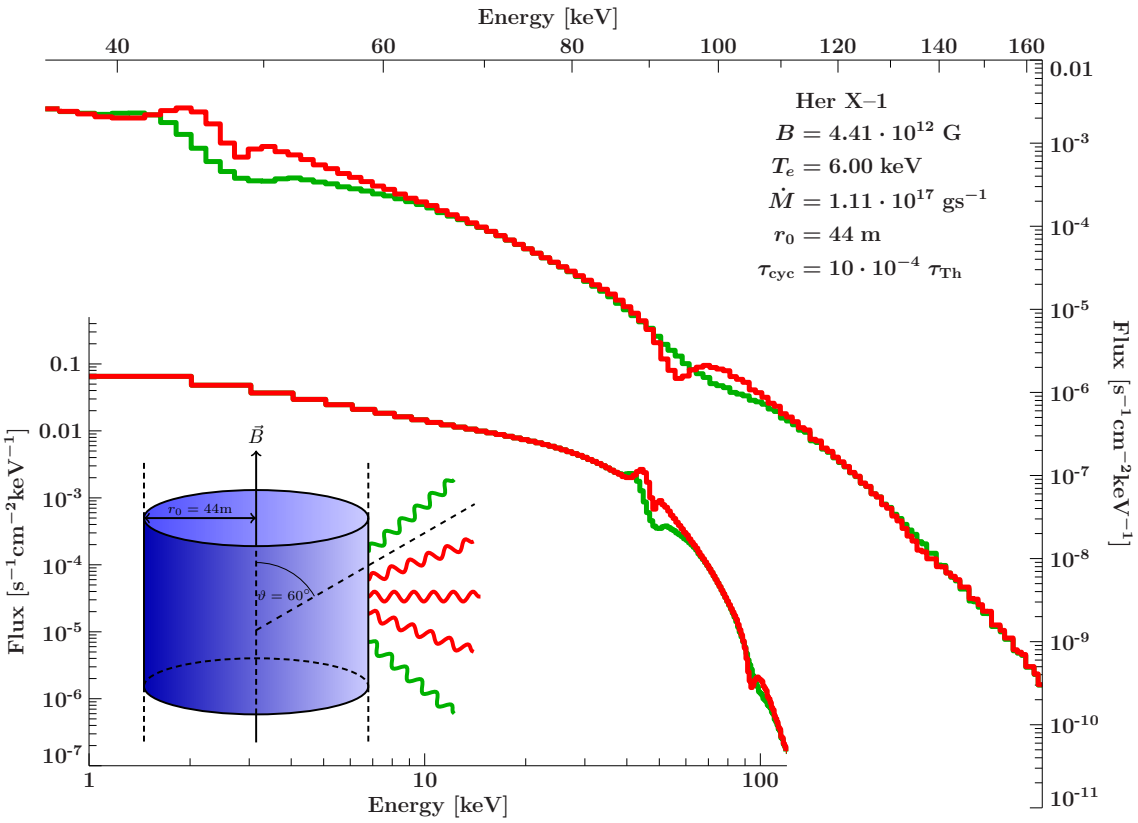

Figure 6.6.: Hybrid model combining Becker & Wolff (2007) and Schwarm et al. (2012). Spectra are averaged over two angular bins.

Figure 6.6 shows such angular averaged combination of the CRSF model with the continuum model. The synthetic spectra, calculated for the same set of parameters as for Fig. 6.5, are averaged in two angular ranges. This illustrates the expected effect of smearing out the sharp features in theoretical spectra. It is only a rough estimate for a realistic line shape, though.

Using height dependent data the cyclotron line model can be combined with the BW07 model in a physically better justified way: Peter Becker and Mike Wolff provided height dependent spectra of the Comptonized bremsstrahlung inside the column, that is, $\dot{N}_\epsilon$, as a function of energy and altitude (see Becker & Wolff, 2007, Eq. 70). The table contains the spectrum in units of photons/s/cm/erg for several energies in keV and heights in cm. They are converted to the RCL table format in order to allow for a convenient interpolation between the rather coarse grained grid points. The black dots in Fig. 6.7 show the energy grid points from the original data. The values in between are automatically interpolated by the RCL table methods[5]. Assuming a dipole magnetic field, a column according to the BW07 model is built and the resulting continuum — interpolated from the corresponding RCL table — is convolved with suitable CRSF Green's functions. The height determines

[5]Here the RCL is used for interpolation only, i.e., the spectra stored in the tables are interpolated/extrapolated for arbitrary parameter values but no convolution is performed.

the local magnetic field strength and therefore the cyclotron line energy. The BW07 model predicts a maximum flux at a certain height. Above that point the flux is decreasing, which makes the overall flux converge on integration over height. Figure 6.7 shows spectra for this hybrid model. The individual spectra for some specific heights are shown as well as the spectrum integrated over the whole column. Using an optical depth of the order of 10^{-3} is not sufficient for forming a CRSF as the one observed in Her X-1. The model rather shows that the combination of cyclotron lines from different heights smears out the column integrated spectrum. The reason is the dipole magnetic field assumed here together with the one to one correspondence of field strength and CRSF energy. A small dip still remains because the BW07 continuum has a specific region from which most of the flux is originating. This further motivates the assumption of the existence of a constrained line forming region but also implies that higher optical depths and/or the inclusion of other effects is needed to explain the comparably deep lines observed in the spectra from accreting X-ray pulsars. An excess in emission is observed in the case of viewing angles almost perpendicular to the magnetic field axis. It results from the strong line wings in this regime. Falkner et al. (2017) provide some details about the expectations of observing such behavior in actual data from accreting X-ray pulsars. Figure 6.8 illustrates that an increased optical depth has the expected influence on the spectra: the depth of the absorption dip increases due to the deeper cyclotron lines at individual heights. Work on a refinement of the grids on which the height dependent spectra are calculated toward a more continuous model is ongoing and might reveal further insight into the interplay between the accretion column continuum model and the cyclotron line shapes. From the study at hand it seems that the inclusion of other effects must be considered. Possible effects the omission of which hinders the forming of a deep cyclotron line here are, for example: the bulk velocity of the downfalling plasma, temperature and optical depths gradients in the CRSF sheath, a more complex geometry, or the presence of a second accretion column observed at another angle.

6.4. Phase Lags in 4U 0115+63

Cyclotron lines play an important role both in the energy space and in the time domain. Their strong angular dependence is crucial for the formation of the energy dependent pulse profiles due to the different observing angles under which an CRSF forming neutron star accretion column is seen over pulse phase. The angular mixing of two accretion columns is even more increased in complexity by general relativistic light bending, which must be taken into account in the vicinity of the neutron star. The Monte Carlo simulation presented in this thesis allowed for a first modeling attempt of these energy dependent pulse profiles taking into account a physical model for cyclotron resonant scattering features. It is described in this Chapter closely following the work of Schönherr et al. (2014).

The modeling of X-ray binary pulse profiles has been addressed by various authors in the past (e.g., Kraus et al., 1995; Kraus et al., 1996; Caballero et al., 2011; Sasaki et al., 2012). However, none of the previous modeling approaches have taken into account the angular

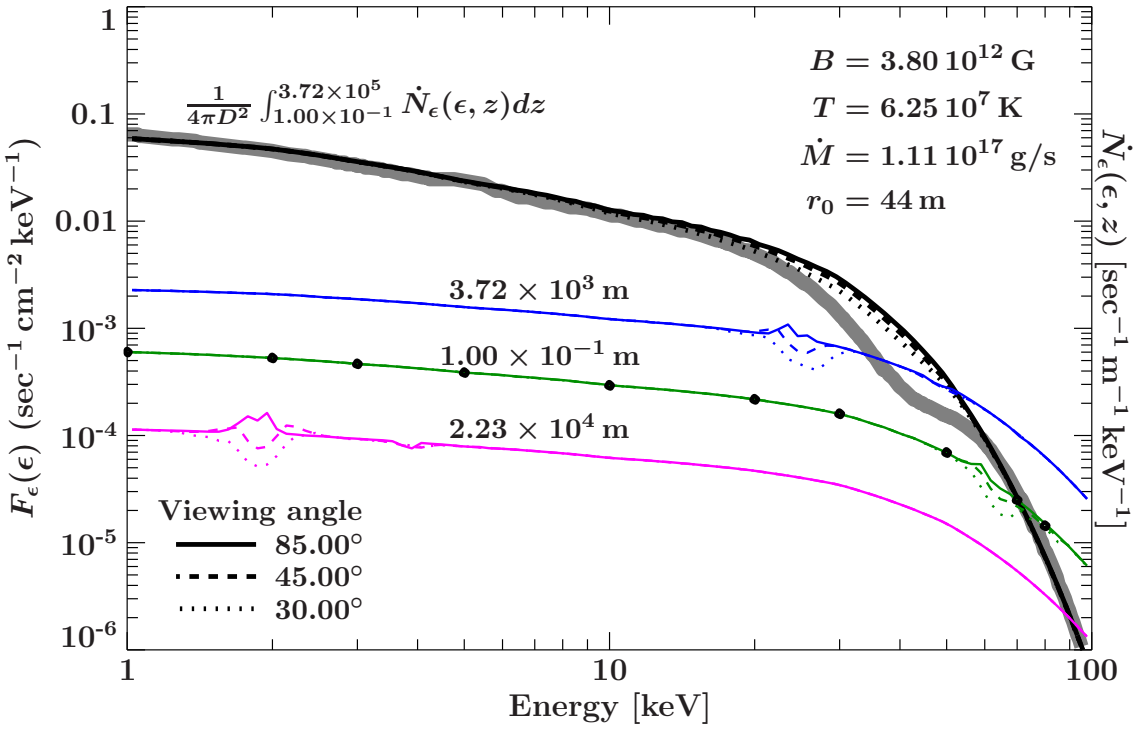

Figure 6.7.: Hybrid model combining a height dependent version of the model from Becker & Wolff (2007, BW07) with the cyclotron line model from Schwarm et al. (2017a). An optical depth of $\tau = 3 \times 10^{-4}\,\tau_{\mathrm{T}}$ has been assumed for the CRSF sheath around the optical thick accretion column core, which generates the continuum emission according to the BW07 model. The colored lines are example spectra at given heights in the column as indicated in the plot. The cyclotron lines depend on the magnetic field strength and are therefore shifted to lower energies for higher locations in the column. A dipole field is assumed. The flux of the individual spectra shows the height dependence of the total flux in the BW07 model quantitatively. The gray line shows the data from Becker & Wolff (2007). The black solid, dashed, and dotted lines show the total column integrated spectrum for viewing angles of 85°, 45°, and 30° to the magnetic field axis, respectively. The black points mark the tabulated energies from which the height dependent flux values are interpolated.

redistribution due to resonant cyclotron scattering. Using the simulation code, developed in the course of this thesis, energy dependent pulse profiles with an intrinsic radiation pattern have been simulated, for the first time on physical grounds, following earlier approaches (Mészáros & Riffert, 1988; Sturner & Dermer, 1994; Zheleznyakov & Litvinchuk, 1986; Soffel et al., 1985, and references therein).

From the observational side, neutron star binaries may exhibit highly energy dependent pulse profiles (Lutovinov & Tsygankov, 2009). The energy dependence is especially apparent around the energy of the cyclotron line since the resonant scattering leads to a complex angular redistribution of the interacting photons. Observations from Ferrigno et al. (2011) showed phase lags, that is, apparent delays of photons of specific energies

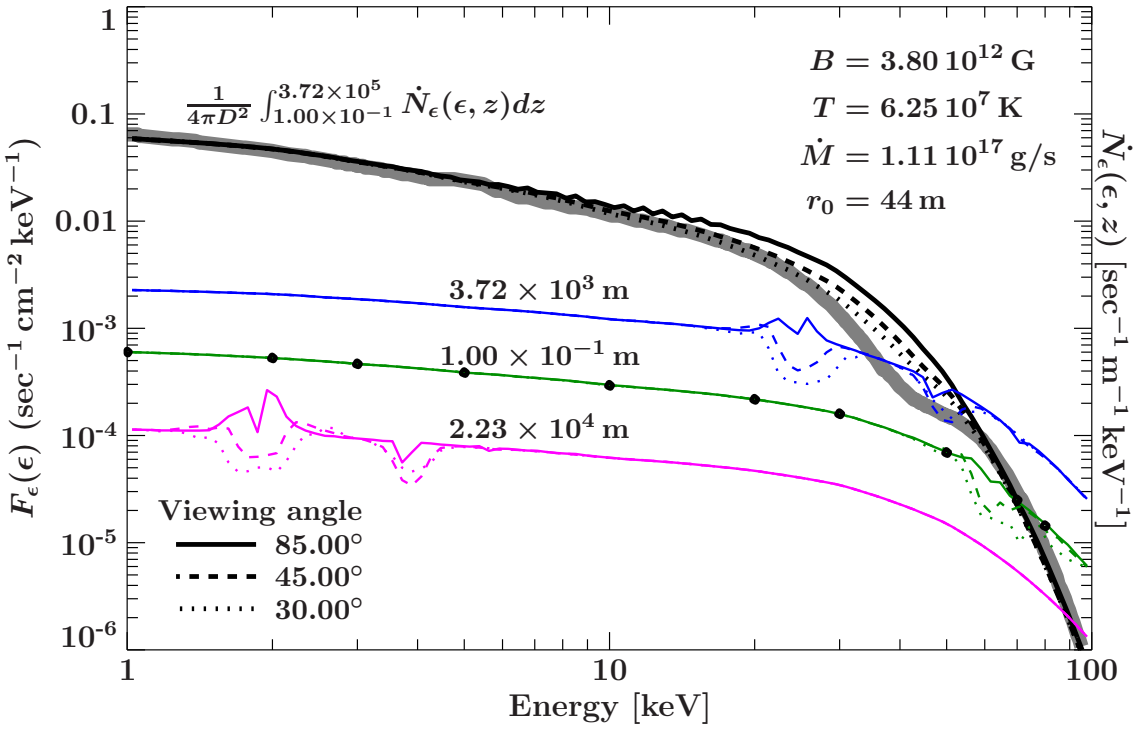

Figure 6.8.: Same as Fig. 6.7 but for an optical depths of $\tau = 3 \times 10^{-3}\ \tau_{\rm T}$.

with respect to photons of other energies, at the cyclotron line energy in spectra from 4U 0115+63. Around the CRSF energy the absorption dips are slightly shifted in phase. The reason for this behavior is the dependency of the CRSF emission pattern, and therefore the pulse profile, on the photon energy.

For a theoretical comparison, the observable emission has been generated as a function of spin phase, using the Monte Carlo simulation for cyclotron resonant scattering and a numerical ray-tracing routine accounting for general relativistic light-bending effects, for exemplary systems, which are described in the following. The neutron star ($M = 1.4\,M_\odot$, $R = 10$ km) with a magnetic field on the order of several 10^{12} G accretes matter onto two magnetic poles (see Fig. 6.9). In the assumed "fan beam scenario" only lateral emission from the walls of an elongated accretion column is observed. The line forming region, that is, the "efficient area of the accretion column to line formation" (Nishimura, 2008), at each pole is modeled by a simple, homogeneous, small cylindrical volume. Its location, radius, and height, the location of the accretion columns with respect to the spin axis of the neutron star, and the inclination of the system with respect to the observer are free model parameters. Any possible "pencil beam" radiation components are neglected. The intrinsic beam pattern at each pole is generated by convolving an X-ray input continuum from the inner column with Green's functions for cyclotron resonant scattering between electrons and X-ray photons in its outer layer. The magnetic fields of both poles' line forming regions are $B = 4 \times 10^{12}$ G, their parallel electron temperature is $k_{\rm B}T = 3$ keV, and the cyclotron scattering atmosphere has a Thomson optical depth $\tau = 10^{-3}\ \tau_{\rm T}$ perpendicular to the B-field axis (see, e.g., Schönherr et al., 2007b; Suchy et al., 2008). For the input

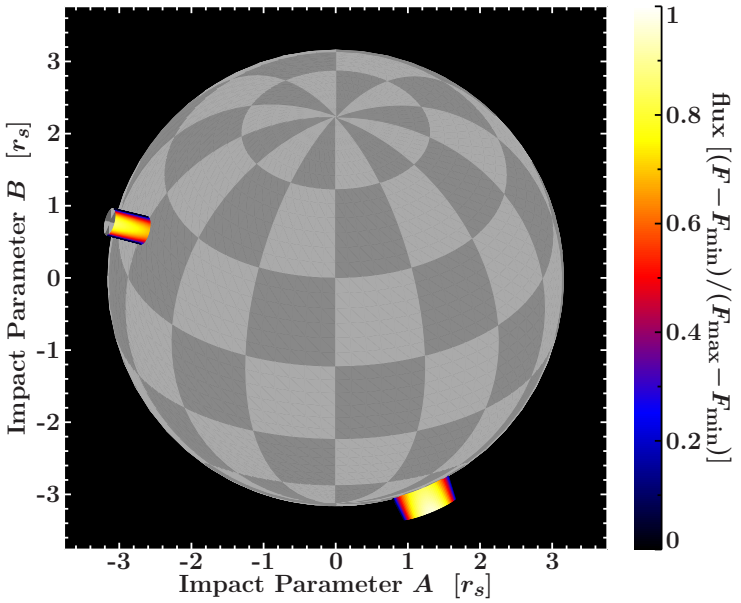

Figure 6.9.: Observer's view of a neutron star. The general relativistic light bending effects affect the visibility of the two accretion columns. Sky coordinates are parameterized through the impact parameters A and B, which correspond to the projected distance from the gravitational center in units of the Schwarzschild radius, $r_{\rm s}$ (Schönherr et al., 2014, Fig. 1 therein).

continuum an isotropic photon source with a power-law spectrum with photon index $\Gamma = 1$ is assumed. The qualitative behavior of the simulated phase lags is independent of the exact shape of the input continuum, though. In fact, the continuum is effectively removed in the visualizations in Figs. 6.11 and 6.12 by normalizing the flux in every energy bin such that its mean flux is zero.

The large-scale B-field structure of HMXBs and the magnetospheric coupling of the accretion flow are poorly constrained. Schönherr et al. (2014) investigated static volumes and a falling plasma with a bulk velocity of $0.4\,c$. A symmetric geometry and a geometry where the magnetic poles are displaced in longitude and latitude with respect to an antipodal setting have been tested. The latter has been shown to be one option to generate asymmetric pulse profiles that resemble observed ones best. Ferrigno et al. (2011) proposed a two-pole geometry with $i_1 = 74°$, $i_2 = 32°$ and a phase offset of 68° for an observation angle of $i_{\rm obs} = 60°$, as proposed by Sasaki et al. (2012), to explain the strong changes in the highly asymmetric and variable pulse profiles of the accreting X-ray pulsar 4U 0115+63. These parameters, as well as their laterally emitting columns of $r_1 = r_2 \sim 700\,\mathrm{m}$ and $h_1 = h_2 = 2\,\mathrm{km}$ have been adopted for the example of an asymmetric two-pole accretion column.

The cyclotron line spectra escaping from neutron star accretion columns not only strongly depend on the typical parameters of a static accretion column, like the magnetic field, temperature, geometry and the resulting output angle but are also strongly influenced by the bulk velocity of the column. The latter leads to additional Lorentz boosting, effectively

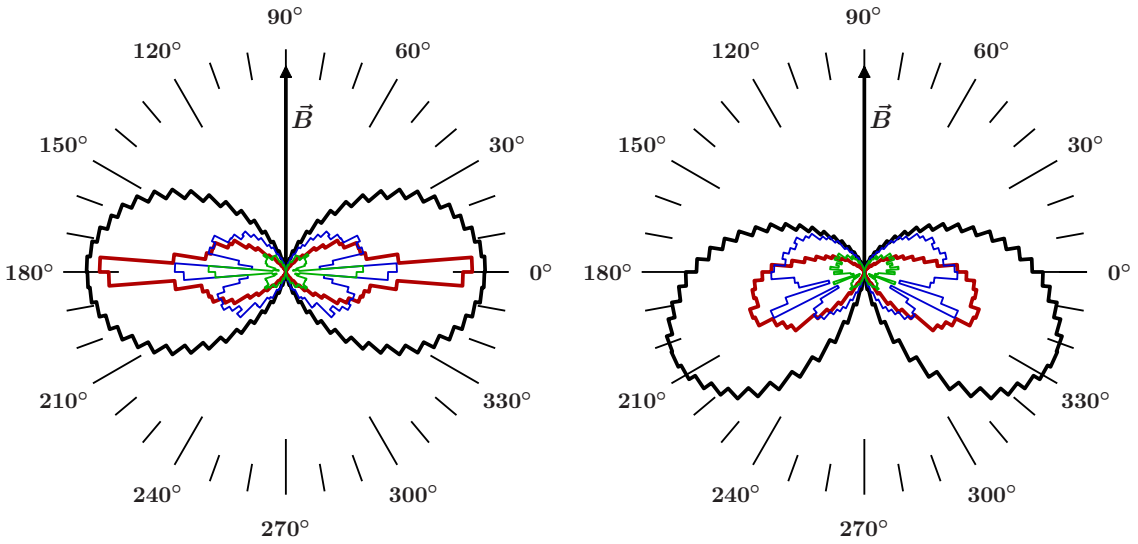

Figure 6.10.: Energy-resolved beam patterns after cyclotron scattering for a cylindrical geometry ("fan beam"). **Left:** case of a static plasma. **Right:** plasma with bulk velocity $v = 0.4\,c$. The black line shows the angular distribution of all photons. The red, green, and blue lines mark photons escaping at energies close to the cyclotron resonances for the respective angles (not to scale). The photons that escape at the fundamental resonance (red) have all undergone scattering. The photons escaping at the higher resonances are unaltered (see also Schwarm et al., 2013). Figure from Schönherr et al. (2014, Fig. 2 therein).

beaming the radiation downwards and therefore altering the angular distribution of the CRSF photons.

Figure 6.10 shows the angular dependent emission at three energy bands. The left side corresponds to the case of a static plasma, while on the right side the emission patterns are beamed downwards due to the bulk velocity of $0.4\,c$. These patterns can be interpreted as emission patterns from the walls of the accretion column. See Section 5.6 or Schwarm et al. (2013) for a more detailed discussion about the influence of bulk velocity on CRSF simulations. The patterns are further altered by relativistic light bending, which changes the angle observed at each phase. The corresponding geometric considerations and the light bending code from Falkner et al. (2013), which includes light bending, gravitational redshifting, and special relativistic effects due to the motion of the emitter, have been used here. The simulated spectra show that the pulse profile close to the CRSF resonances is shifted in phase. The flux in such an CRSF energy band changes before the continuum and is therefore delayed or ahead of the corresponding flux from a continuum band due to its different emission pattern. These phase lags can be illustrated with a phase lag map, like the one shown in Fig. 6.11, by plotting the phase dependent flux variations with respect to the energy. For the generation of the individual energy dependent pulse profiles, the flux emitted from each point of the surface of the walls of the cylindrical volume is obtained as a function of energy and angle with respect to the B-field axis. The additional light bending due to the neutron star mass is applied, and the resulting spectra are plotted with

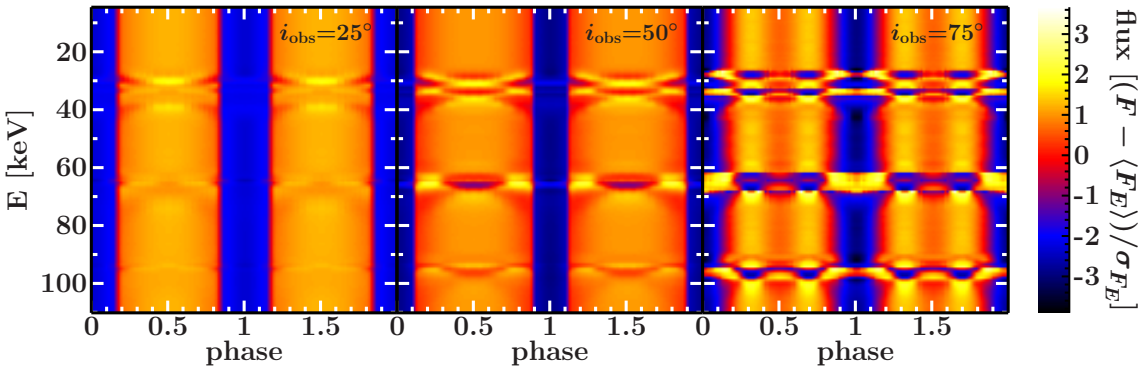

Figure 6.11.: Energy-dependent flux as a function of pulse phase for different observation angles $i_{obs} = 25°$, 50°, and 75° from left to right for the case of a static plasma, i.e., no bulk velocity is assumed. The pulse profiles are normalized such that for every energy bin the mean flux is zero and the corresponding standard deviation is unity (after Ferrigno et al., 2011) and are plotted twice for clarity. Figure from Schönherr et al. (2014, Fig. 3 therein).

respect to energy and phase.

The symmetric, antipodal geometry of two static accretion columns of radius $r_1 = r_2 = 1\,\mathrm{km}$ and height $h_1 = h_2 = 100\,\mathrm{m}$, which are displaced at an angle $i_1 = i_2 = 35°$ with respect to the spin axis of the neutron star results in the energy-dependent pulse profiles shown in Fig. 6.11 for different observing angles. Each figure represents pulse profiles at a given energy on each horizontal line. Vertical lines show the deviation of the X-ray spectrum from a normalizing continuum at a given pulse phase. For a system tilted by $i_{obs} = 25°$ to the line of sight with respect to the rotational axis, no significant phase-lags are seen. Instead one symmetric broad pulse is expected in observations over the entire energy range. The beaming of photons escaping at the cyclotron energies (see Fig. 6.10) leads to deviations of the pulse profiles around the corresponding, redshifted, energies (~32, 64, and 96 keV). This illustrates the necessity for taking into account the angular redistribution through cyclotron scattering.

Figure 6.12 shows the case of asymmetric located accretion columns for a static plasma and for a line forming plasma falling down to the neutron star with a bulk velocity of $v = 0.4\,c$. The bulk velocity leads to a wavy morphology similar to the observed one (see Figs. 3 and 5 of Ferrigno et al., 2011), in contrast to the rather symmetric profiles in the static case where only the neutron star surface introduces an asymmetry with respect to the overall radiation.

This method can be used as an indirect detection of CRSFs. By producing such maps from observational data and searching for the phase lags, cyclotron lines might be discovered in sources the spectrum of which alone inhibit a significant detection. Also, the understanding of characteristic trends in such simulations, as for example, reasons for the existence of asymmetries, and angular regimes where these asymmetries are enhanced or suppressed, allows for narrowing down a physically reasonable parameter space. This is necessary because of the high degree of freedom in theoretical predictions due to the large number of

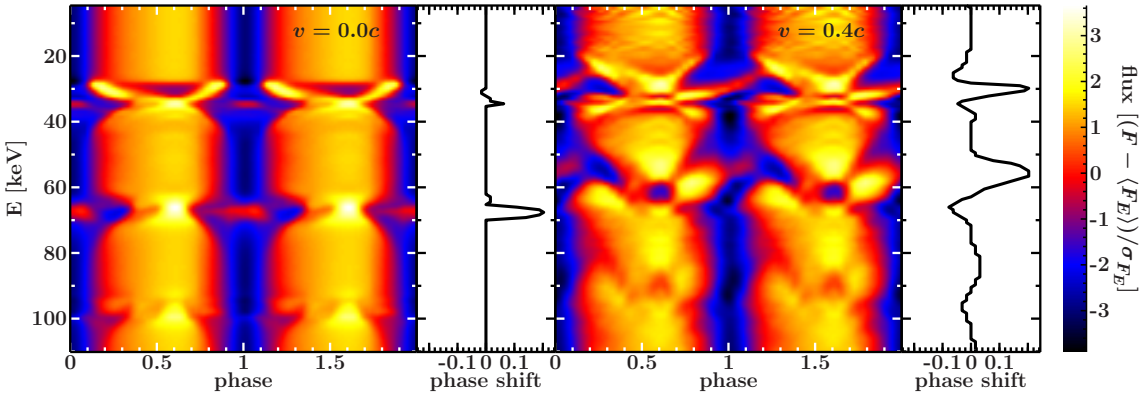

Figure 6.12.: Phase lag maps for the asymmetric geometry shown in Fig. 6.9. In the case of a static plasma a slight asymmetry caused by the non-antipodal positions of the accretion columns is apparent (left). The asymmetry is enhanced in the case of a bulk velocity of $v = 0.4\,c$ (right). The white panels show the energy-dependent phase shifts described in detail by Ferrigno et al. (2011). Figure from Schönherr et al. (2014, Fig. 4 therein).

model parameters.

Although only example configurations were studied in detail by Schönherr et al. (2014), the methods used have been developed to allow for maximum generality. Falkner et al. (2017) uses the same "pipeline" for generating artificial phase dependent spectra for the physically motivated input continuum from Postnov et al. (2015a). This eliminates the assumption of the empirical power-law continuum used here.

6.5. Challenging Paradigms

Poutanen et al. (2013) proposed a completely different view on the formation of CRSFs: the formation of cyclotron lines might take place in the thin atmosphere around the neutron star where down-beamed radiation from the accretion column is effectively reflected by cyclotron scattering. Models proposing the formation of CRSFs within, or at the boundary of, the accretion column, explain the variation of the cyclotron line energy with a change of the height of the line forming region due to radiation pressure. In contrast, the reflection model explains this variation of the cyclotron line energy by a change of the illuminated fraction of the neutron star. A smaller fraction of the neutron star surface is expected to be illuminated from the radiation emitted by the accretion column if the seed radiation is strongly downward beamed. This is expected in cases of an overall larger velocity of the plasma falling down on the neutron star. If, on the other hand, this bulk velocity is smaller, for example, due to an antagonistic radiation pressure or other dynamic properties of the accretion column, the opening angle of the resulting radiation pattern becomes larger and therefore the amount of the illuminated neutron star surface becomes larger and consequently the averaged magnetic field strength decreases, because of the radial

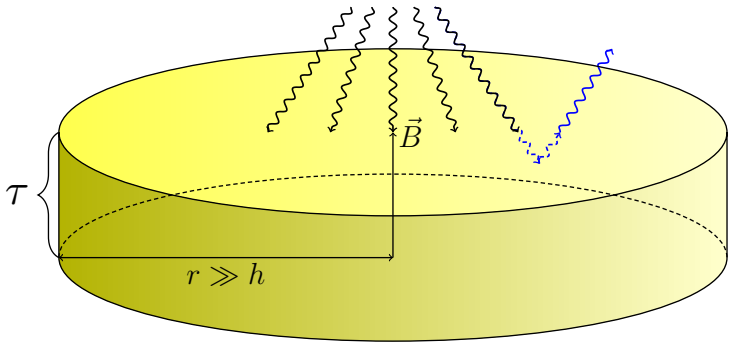

Figure 6.13.: Illustration of slab 0-1 geometry. The radially elongated medium is illuminated by a photon source centered above the cylinder symmetric slab. An example path of a photon, which is effectively reflected by the medium it intrudes into and interacts with, is shown in blue.

attenuation of the dipole magnetic field. The assumption of a dipole field is only necessary for quantitatively estimating the strength. In general some form of radial attenuation can be envisioned in multipole fields as well.

A simple setup consisting of a slab, which is 1000 times as wide as high, was simulated in order to get a feeling for the behavior of CRSF reflection and the resulting cyclotron line shapes. The slab is positioned one slab height below a point source emitting photons isotropically, but only downwards onto the slab. Figure 6.13 illustrates this simple geometry, which is called slab 0-1 geometry following the naming conventions of the classical geometries.

This setup is expected to yield the same spectra as a slab 1-0 geometry for negative angles to the B-field axis. The resulting angular dependent spectra for such a setup are shown in Fig. 6.14 for two values of the optical depth parallel to the magnetic field axis. The number of escaping photons for several angles to the magnetic field axis are binned on the input energy grid (solid black line). The blue dashed line shows the correspondingly binned seed photons, which are injected downwards only (see Fig. 6.13). The angle to the magnetic field axis decreases from an almost anti-parallel orientation to the B-field axis in the top panel to an orientation parallel to the magnetic field axis at the bottom. The left side shows the case of a low optical depth of $10^{-4}\,\tau_\mathrm{T}$. An increase in line depth, or height in the case of reflected photons ($\mu > 0$), can be observed for a higher optical depth of $10^{-3}\,\tau_\mathrm{T}$ on the right hand side. Both simulations assume a magnetic field strength of $B = 0.0385\,B_\mathrm{crit}$ and an electron parallel temperature of $k_\mathrm{B}T = 7\,\mathrm{keV}$. Strong emission at the CRSF line wings can be observed in the case of reflected radiation, that is, for photons escaping at positive angles to the magnetic field axis. The absolute strength of these emission wings and their relative strength as compared to the cyclotron line center both depend on the viewing angle to the magnetic field axis. Under these conditions and with the assumptions made in this simulation, that is, the optical depth regime, the averaging over polarization, and the simple geometric setup, and the absorption of radiation at the neutron star surface,

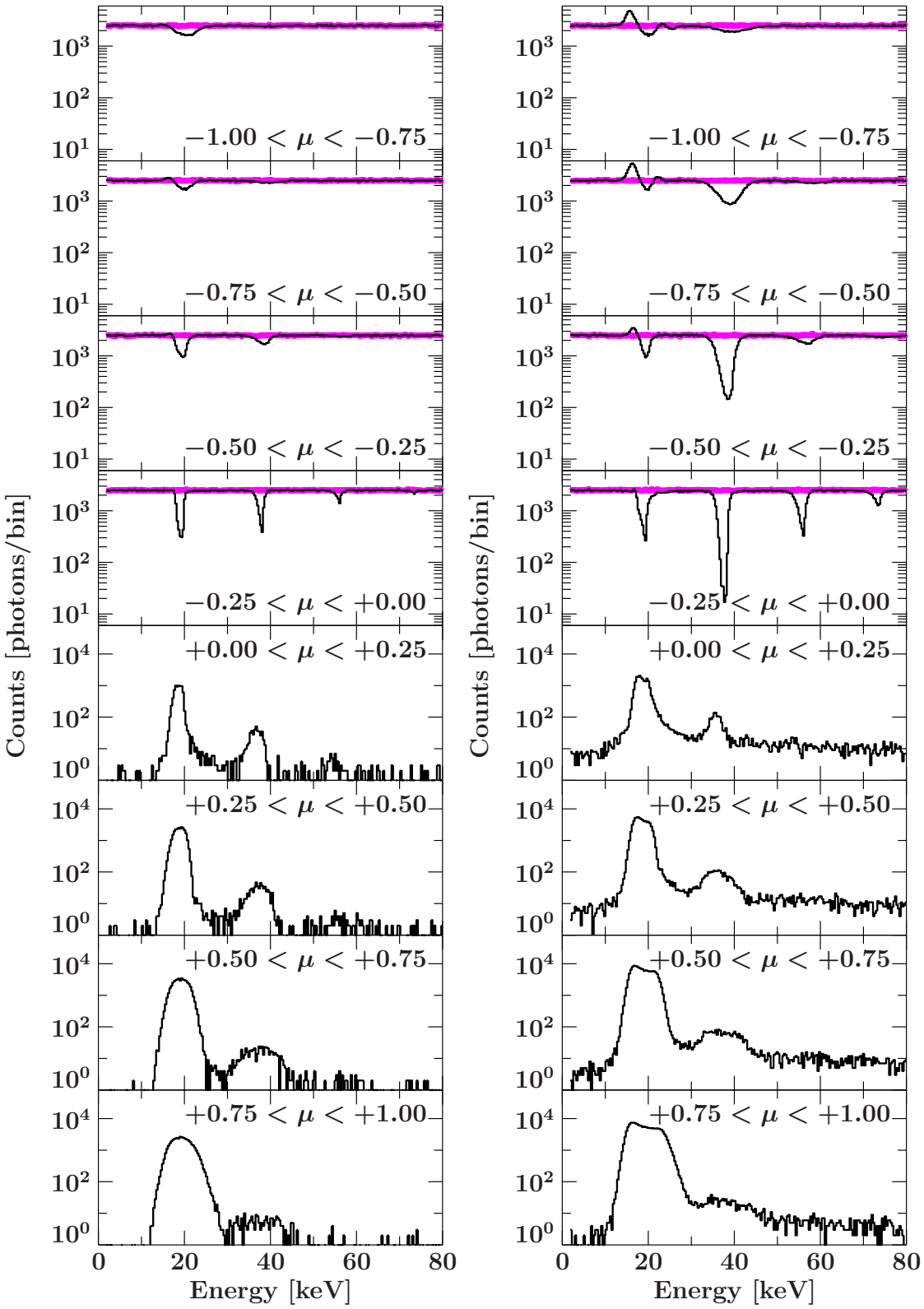

Figure 6.14.: Number of photons escaping from a simulated slab 0-1 geometry. See text for an explanation.

the formation of cyclotron features observed in absorption seems to be questionable[6].

A total of $N_{\rm cont} = 3940000$ photons were injected into the simulation semi-isotropically, equally distributed in 394 energy bins. Their individual energies within each energy bin have been sampled from a uniform probability distribution, which results in some statistical fluctuations, resulting in some jittering of the blue dashed line in Fig. 6.14, which is showing the input photons. The baseline of the transmitted ($\mu < 0$) photon spectra exactly underlies the continuum, which demonstrates that the majority of photons escape unaltered. Interactions take place only around the CRSF resonant energies. In the following the transmission and reflection coefficients, T and R, respectively, are calculated for these example simulation runs. It should be noted before, though, that this terminology is slightly misleading in that the $T + R = 1$ relation normally expected from such terms, is not fulfilled here since the number of photons is not conserved because of photon spawning. Therefore the "spawning" coefficient is calculated as well.

$$T_{\tau_\parallel=10^{-4}} = \frac{N_{\mu<0}}{N_{\rm cont}} = \frac{3855430}{3940000} \approx 0.9785 \tag{6.2}$$

$$R_{\tau_\parallel=10^{-4}} = \frac{N_{\mu>0}}{N_{\rm cont}} = \frac{130428}{3940000} \approx 0.0331 \tag{6.3}$$

$$S_{\tau_\parallel=10^{-4}} = T + R - 1 \approx 0.0116 \tag{6.4}$$

In the case of a ten times higher optical depth, the reflection coefficient increases by a factor of ∼3, and ∼5 times as many spawned photons are generated:

$$T_{\tau_\parallel=10^{-3}} = \frac{N_{\mu<0}}{N_{\rm cont}} = \frac{3759452}{3940000} \approx 0.9542 \tag{6.5}$$

$$R_{\tau_\parallel=10^{-3}} = \frac{N_{\mu>0}}{N_{\rm cont}} = \frac{418684}{3940000} \approx 0.1063 \tag{6.6}$$

$$S_{\tau_\parallel=10^{-3}} = T + R - 1 \approx 0.0604 \tag{6.7}$$

The transmitted radiation reaches the neutron star surface and is, depending on the model assumed, probably mostly absorbed. Turolla et al. (2004) calculated the absorption coefficient as a function of energy for $\sim 10^{12}$ G strong magnetic fields for different angles to the magnetic field and found that the monochromatic absorption coefficient approaches 80–100% for typical energy values of cyclotron lines energies (see their Figs. 2 and 3). In combination with the reflected radiation at the cyclotron line energies, cyclotron lines would most probably be observed in emission rather than in absorption if one assumes that they are formed at the neutron star surface. This result directly contradicts the scenario proposed by Poutanen et al. (2013).

[6] One can still argue that the continuum radiation is mixed with the CRSF emission and only a partial region of, e.g., the neutron star atmosphere is not illuminated leaving a gap in the spectra. But the measured luminosities give raise to the assumption that explaining CRSFs with this scenario is not possible as well.

7

SUMMARY & CONCLUSIONS

In this thesis I described the physical principles and the theory of cyclotron scattering (Chapter 3). Starting from scratch, a new software package has been developed for the simulation of synthetic cyclotron lines (Chapter 4). It includes an adaptive cross section table generation scheme, which makes the improved flexibility and accuracy compared to previous approaches computationally viable (Section 4.7.1). The simulation code itself is fully parallelized and includes the complete physics of cyclotron scattering in strong magnetic fields in the most accurate manner possible. The assumptions and approximations, such as numerical integration methods and necessary simplifications have been laid out in Section 3.1 of this thesis in order to allow for a detailed comparison to other approaches. The comparison to other works following similar approaches, such as works on the calculation of data products used in the simulation or competing simulations, has been performed in this thesis, as well (see, e.g., Sections 3.3–3.5 and 4.6). The agreement in both cases fortifies the acceptance of this software as the proper tool for the simulation of cyclotron lines. Furthermore, it has been proven to be applicable to real data by providing, for the first time, a working fit model based on a Monte Carlo simulation fully incorporating the correct thermally averaged scattering cross sections. The development of this software on physical grounds alone has been a tremendous task due to the complexity of the involved interactions and their often analytically intangible nature. In addition to the software development, multiple applications have been performed in order to reap physical insight from the newly developed tools. Thus the influences of the most relevant parameters for cyclotron line formation have been discussed in Chapter 5 and the

discovered trends will help observers to make physical decisions during the procedure of fitting the data of accreting neutron star binaries. Further applications of this new model include the calculation of cyclotron lines for different physical input continua, that is, a combination with physical accretion column continuum emission models (Section 6.3), as well as, a study of the phase lags observed at the cyclotron energies in the spectra of accreting neutron star binaries (Section 6.4), which result from the strong angular dependence of the angular CRSF emission patterns. And, of course, the cyclotron line model has been fitted to real data observed with the X-ray satellite *NuSTAR* (Sections 6.1–6.2), whose remarkable energy resolution allows, for the first time, studies of the shape of observed cyclotron lines. A new theory for the location of the line forming region was tested quantitatively, for the first time, in Section 6.5 by making use of the flexibility of the new simulation code. The results suggest that the formation of cyclotron lines via reflection on the neutron star surface is possible, but the CRSFs would then occur in emission rather than absorption. However, such a scenerio is quite unrealistic because observations lack evidence for emission features.

Finally, the thermally averaged scattering cross section tables and the XSPEC model with a set of Green's function tables, covering the typical parameter ranges of neutron star binaries for different geometries, have been made publicly available (see Schwarm et al., 2017a,b, and Sections 4.7.1 and 4.9). Their newly gained availability furthermore turned out to serve as a catalyst for the pooling of physical models of diverse domains with the ultimate aim of improving the understanding of a neutron star accretion column's last mile.

This work will now close with an outlook on possible future studies since the applications of the newly developed simulation and the corresponding XSPEC model could not be maxed out at all in the course of just one thesis. One late-breaking development lays in the experimental measurements of polarization, which are becoming possible only now. Since the successful launch of the first promising mission of this kind, *X-Calibur*, the reliable measurement of X-ray polarization has become a reality. In Section 4.10 the extensibility of the `CycloSim` simulation suite with respect to the inclusion of polarization is discussed. Connecting such simulations with real data will further constrain the largely degenerated parameter range of accreting X-ray binaries.

The study of the impact of anisotropically distributed seed photons is another area in which the simulation may provide valuable insight. Araya-Góchez & Harding (2000) discussed some of its aspects. Such anisotropies are expected in the accretion columns of accreting neutron star binaries due to Lorentz boosting of photons generated in the moving bulk frame by processes such as blackbody or synchrotron radiation. Depending on where exactly the cyclotron line is expected to form, this introduces an additional boosting factor. As discussed in Chapter 6, the usage of realistic input continua — in contrast to, e.g., a constant input continuum or a powerlaw with a gentle slope but without a high-energy cut-off — results in the suppression of strong line wings around the fundamental cyclotron line. This is especially evident in the case of slab geometry. Section 6.3 shows that a magnetic field gradient might smear out the line wings in the case of cylinder geometry, meaning that the line wings contribute to the spectra over the whole energy range. Araya-Góchez & Harding (2000) found that, regardless of the usage of slab or cylinder geometry, the

line wings observed in simulations with isotropic input radiation are strongly suppressed if a suitable anisotropic seed photon source is assumed. The boosting of photons due to the bulk velocity is already fully integrated in the code and has been partly studied by Schwarm et al. (2012). The inclusion of completely different seed photon patterns — instead of isotropic but boosted emission patterns — into the code is an easy task because it only involves the addition of some lines of code in the function which is sampling the seed photon properties. Furthermore, such a study could be performed without any changes in the code by altering the input angle distribution such that only input photons for one angle are generated. Then, analogue to the case of mono-energetic photon injection, Green's functions can be calculated to sample the medium's response to photon injection into individual input angles. This would also allow for a general model for arbitrary seed photon distributions and facilitate the extrapolation to higher optical depths. Such an extrapolation scheme would successively propagate photons through an optically thin medium in order to calculate the output spectrum for an optically thick medium. This kind of extrapolation is already implemented in the `cyclofs` model (see Section 4.9) but without taking into account the angular redistribution due to cyclotron scattering.

The influence of a different magnetic field structures is another topic, which can be accessed using the `CycloSim` software. Nishimura (2005), for example, already discussed the influence of a non-dipole magnetic field for slab 1-0 and slab 1-1 geometries. However, the imaginable field configurations are endless. By building an accretion column from multiple slabs, stacked radially and on top of each other, each with its own magnetic field strength, such scenarios can be modeled with the code provided here.

Although it has been demonstrated in Section 6.3 that the combination with a height dependent version of the continuum model of Becker & Wolff (2007) is easily realizable with the `cyclofs` XSPEC model, the deployment of a corresponding production version is still to be made. Similar studies about the superposition of cyclotron lines from different line forming regions have been performed by Nishimura (2008) with the result of the creation of broad and shallow cyclotron line profiles.

Another domain where the code may be applicable, though only after careful considerations about the validity of some assumptions have been made, is the domain of magnetars. These systems exhibit even stronger magnetic fields and may give rise for the generation of proton cyclotron lines, which have been claimed for some soft gamma-ray repeaters (see, e.g., Ibrahim et al., 2002, 2003; Tiengo et al., 2013). By replacing the electron mass with the proton mass and implementing the corresponding cross sections for proton cyclotron interactions, the fully parallelized MC mechanism of `CycloSim` could be used in this regime, as well.

These are just some of an endless number of possible applications and it is probably desirable to start with the ones, which can be performed already without further programming work. These include the investigation of more complex geometries, magnetic field and velocity gradients, the continuation of the combination with physical continuum and light bending models, and, of course, further application of the XSPEC model to sources, to name just a few.

Bibliography

Adler S.L., 1971, Annals of Physics, 67, 599

Akiyama S., Wheeler J.C., Meier D.L., Lichtenstadt I., 2003, ApJ, 584, 954

Akmal A., Pandharipande V.R., Ravenhall D.G., 1998, Phys. Rev. C, 58, 1804

Alexander S.G., Meszaros P., 1991a, ApJ, 372, 565

Alexander S.G., Meszaros P., 1991b, ApJ, 372, 554

Alexander S.G., Meszaros P., Bussard R.W., 1989, ApJ, 342, 928

Alfvén H., 1963, Space Sci. Rev., 2, 862

Alfvén H., 1967, Icarus, 7, 387

Antoniadis J., Freire P.C.C., Wex N., et al., 2013, Science, 340, 448

Araya R.A., 1997, Ph.D. thesis, Johns Hopkins University, Baltimore

Araya R.A., Harding A.K., 1996, A&AS, 120, C183

Araya R.A., Harding A.K., 1999, ApJ, 517, 334

Araya-Góchez R.A., Harding A.K., 2000, ApJ, 544, 1067

Arnaud K.A., 1996, In: Jacoby G.H., Barnes J. (eds.) Astronomical Data Analysis Software and Systems V, ASP Conf. Ser., 101, Astron. Soc. Pacific, San Francisco, 17

Arons J., Klein R.I., Lea S.M., 1987, ApJ, 312, 666

Australia Telescope National Facility 2005, Webinterface, Version 1.54, `http://www.atnf.csiro.au/research/pulsar/psrcat/`

Baade W., Zwicky F., 1934a, Proc. NAS, 20, 259

Baade W., Zwicky F., 1934b, Proc. NAS, 20, 254

Bai T., 1981, ApJ, 243, 244

Baring M.G., Gonthier P.L., Harding A.K., 2005, ApJ, 630, 430

Basko M.M., Sunyaev R.A., 1975, A&A, 42, 311

Basko M.M., Sunyaev R.A., 1976, MNRAS, 175, 395

Bauswein A., Goriely S., Janka H.T., 2013, ApJ, 773, 78

Becker P.A., 1998, ApJ, 498, 790

Becker P.A., 2014, priv. comm.

Becker P.A., Klochkov D., Schönherr G., et al., 2012, A&A, 544, A123

Becker P.A., Wolff M.T., 2005a, ApJ, 621, L45

Becker P.A., Wolff M.T., 2005b, ApJ, 630, 465

Becker P.A., Wolff M.T., 2007, ApJ, 654, 435

Bell S.J., Hewish A., 1967, Nature, 213, 1214

Bildsten L., Chakrabarty D., Chiu J., et al., 1997, ApJS, 113, 367

Blair D.G., Candy B.N., 1985, MNRAS, 212, 219

Blandford R.D., 2005, In: Bulletin of the American Astronomical Society, 37, 1220

Blandford R.D., Applegate J.H., Hernquist L., 1983, MNRAS, 204, 1025

Bonazzola S., Heyvaerts J., Puget J.L., 1979, A&A, 78, 53

Bonnet-Bidaud J.M., Mouchet M., 1998, A&A, 332, L9

Börner G., Meszaros P., 1979, Plasma Physics, 21, 357

Bothe W., 1933, Naturwissenschaften, 21, 825

Bothe W., Becker H., 1930a, Zeitschrift fur Physik, 66, 307

Bothe W., Becker H., 1930b, Naturwissenschaften, 18, 705

Bothe W., Becker H., 1930c, Naturwissenschaften, 18, 894

Bothe W., Fränz H., 1927, Zeitschrift fur Physik, 43, 456

Bowyer S., Byram E.T., Chubb T.A., Friedman H., 1964, AJ, 69, 135

Breed M., Venter C., Harding A.K., 2016, In: Boettcher M., Buckley D., Colafrancesco S., Meintjes P., Razzaque S. (eds.) Proceedings of the 3rd Annual Conference on High Energy Astrophysics in Southern Africa
Breit G., 1938, Phys. Rev., 53, 153
Breit G., Wigner E., 1936, Phys. Rev., 49, 519
Brown G.E., 1995, ApJ, 440, 270
Bussard R.W., Alexander S.B., Meszaros P., 1986, Phys. Rev. D, 34, 440
Caballero I., Kraus U., Santangelo A., et al., 2011, A&A, 526, A131
Campbell C.G., (ed.) 1997, Magnetohydrodynamics in Binary Stars, Astrophysics and Space Science Library, 216
Canuto V., Chiu H.Y., Chiuderi C., 1970, Nature, 225, 47
Canuto V., Lodenquai J., Ruderman M., 1971, Phys. Rev. D, 3, 2303
Canuto V., Ventura J., 1977, Fund. Cosmic Phys., 2, 203
Casares J., Charles P., Kuulkers E., 1998, ApJ, 493, L39
Chadwick J., 1932, Nature, 129, 312
Chakrabarty D., Roche P., 1997, ApJ, 489, 254
Chakrabarty D., Tomsick J.A., Grefenstette B.W., et al., 2014, ApJ, 797, 92
Chandrasekhar S., 1931, ApJ, 74, 81
Chandrasekhar S., 1935a, MNRAS, 95, 226
Chandrasekhar S., 1935b, MNRAS, 95, 207
Coburn W., Heindl W.A., Rothschild R.E., et al., 2002, ApJ, 580, 394
Coburn W., Kretschmar P., Kreykenbohm I., et al., 2005, ATEL, 381
Coe M.J., Roche P., Everall C., et al., 1994, MNRAS, 270, L57
Condon J., 2016, Essential Radio Astronomy - Pulsars, http://www.cv.nrao.edu/course/astr534/Pulsars.html
Corbet R., 1985, Space Sci. Rev., 40, 409
Corbet R.H.D., 1984, A&A, 141, 91
Corbet R.H.D., 1986, MNRAS, 220, 1047
Cumming A., Arras P., Zweibel E., 2004, ApJ, 609, 999
Curie I., Joliot F., 1932, Nature, 130, 57
dal Fiume D., Orlandini M., Cusumano G., et al., 1998, A&A, 329, L41
Daugherty J.K., Harding A.K., 1983, ApJ, 273, 761
Daugherty J.K., Harding A.K., 1986, ApJ, 309, 362
Daugherty J.K., Ventura J., 1977, A&A, 61, 723
Daugherty J.K., Ventura J., 1978, Phys. Rev. D, 18, 1053
Davidson K., 1973, Nature Physical Science, 246, 1
Davidson K., Ostriker J.P., 1973, ApJ, 179, 585
Davis J.E., 2016, S-Lang Programmer's Library, http://www.jedsoft.org/slang/
De Luca A., Caraveo P.A., Mereghetti S., et al., 2005, ApJ, 623, 1051
Demorest P.B., Pennucci T., Ransom S.M., et al., 2010, Nature, 467, 1081
Drake F.D., 1968, Science, 160, 416
Drake F.D., Craft H.D., 1968a, Nature, 220, 231
Drake F.D., Craft, Jr. H.D., 1968b, Science, 160, 758
Drake F.D., Gundermann E.J., Jauncey D.L., et al., 1968, Science, 160, 503
Duncan R.C., Thompson C., 1992, ApJ, 392, L9
Dyson F.J., 1949, Phys. Rev., 75, 486
ECAP/Remeis observatory & MIT 2016, isisscripts, http://www.sternwarte.uni-erlangen.de/isis/
Enoto T., Makishima K., Terada Y., et al., 2008, PASJ, 60, S57
Enoto T., Sasano M., Yamada S., et al., 2014, ApJ, 786, 127
Falkner S., Dauser T., Falanga M., Wilms J., 2013, Acta Polytechnica, in press
Falkner S., Schwarm F.W., Schönherr G., et al., 2017, ApJ, in prep.
Farinelli R., Ceccobello C., Romano P., Titarchuk L., 2012, A&A, 538, A67
Farinelli R., Ferrigno C., Bozzo E., Becker P.A., 2016, A&A, 591, A29
Faucher-Giguère C.A., Kaspi V.M., 2006, ApJ, 643, 332
Fenimore E.E., Conner J.P., Epstein R.I., et al., 1988, ApJ, 335, L71
Fernández R., Thompson C., 2007, ApJ, 660, 615
Ferrario L., Wickramasinghe D., 2006, MNRAS, 367, 1323

Ferrario L., Wickramasinghe D., 2008, MNRAS, 389, L66
Ferrigno C., Becker P.A., Segreto A., et al., 2009, A&A, 498, 825
Ferrigno C., Falanga M., Bozzo E., et al., 2011, A&A, 532, A76
Feynman R.P., 1949, Phys. Rev., 76, 749
Ftaclas C., Kearney M.W., Pechenick K., 1986, ApJ, 300, 203
Fujioka S., Zhang Z., Ishihara K., et al., 2013, Scientific Reports, 3, 1170
Fürst F., Grefenstette B.W., Staubert R., et al., 2013, ApJ, 779, 69
Fürst F., Pottschmidt K., Miyasaka H., et al., 2015, ApJ, 806, L24
Fürst F., Pottschmidt K., Wilms J., et al., 2014, ApJ, 780, 133
Geppert U., Rheinhardt M., 2002, A&A, 392, 1015
Gerend D., Boynton P.E., 1976, ApJ, 209, 562
Ghosh P., Lamb F.K., 1979, ApJ, 234, 296
Ghosh P., Pethick C.J., Lamb F.K., 1977, ApJ, 217, 578
Giacconi R., Gursky H., Kellogg E., et al., 1971, ApJ, 167, L67
Giacconi R., Gursky H., Paolini F.R., Rossi B.B., 1962, Phys. Rev. Letters, 9, 439
Giacconi R., Gursky H., Waters J.R., 1964, Nature, 204, 981
Giacconi R., Gursky H., Waters J.R., 1965, Nature, 207, 572
Gnedin I.N., Sunyaev R.A., 1974, A&A, 36, 379
Gold T., 1968, Nature, 218, 731
Goldreich P., Reisenegger A., 1992, ApJ, 395, 250
Gonthier P.L., Baring M.G., Eiles M.T., et al., 2014, Phys. Rev. D, 90, 043014
Gonthier P.L., Harding A.K., Baring M.G., et al., 2000, ApJ, 540, 907
Graziani C., 1993, ApJ, 412, 351
Greenstein G., Hartke G.J., 1983, ApJ, 271, 283
Guilet J., Foglizzo T., Fromang S., 2011, ApJ, 729, 71
Gunn J.E., Ostriker J.P., 1970, ApJ, 160, 979
Guo Q., Garson A., Beilicke M., et al., 2011, ArXiv e-prints, 1101.0595
Haensel P., Urpin V.A., Iakovlev D.G., 1990, A&A, 229, 133
Hannahs S.T., Palm E.C., 2010, Journal of Low Temperature Physics, 159, 366
Harding A.K., Daugherty J.K., 1991, ApJ, 374, 687
Harding A.K., Lai D., 2006, Reports on Progress in Physics, 69, 2631
Harding A.K., Preece R.D., 1989, ApJ, 338, L21
Harrison F.A., Craig W.W., Christensen F.E., et al., 2013, ApJ, 770, 103
Heindl W.A., Coburn W., Gruber D.E., et al., 2000, In: McConnell M.L., Ryan J.M. (eds.) American Institute of Physics Conference Series, 510, 173
Heinke C.O., Ho W.C.G., 2010, ApJ, 719, L167
Hemphill P.B., 2016, priv. comm.
Hemphill P.B., Becker P.A., Fürst F., et al., 2017, MNRAS, in prep.
Herold H., 1979, Phys. Rev. D, 19, 2868
Herold H., Ruder H., Wunner G., 1982, A&A, 115, 90
Hertzsprung E., 1911, Publikationen des Astrophysikalischen Observatoriums zu Potsdam, 22, A1
Hewish A., Bell S.J., Pilkington J.D.H., et al., 1968, Nature, 217, 709
Hollerbach R., Rüdiger G., 2002, MNRAS, 337, 216
Hollerbach R., Rüdiger G., 2004, MNRAS, 347, 1273
Houck J.C., Denicola L.A., 2000, In: Manset N., Veillet C., Crabtree D. (eds.) Astronomical Data Analysis Software and Systems IX, ASP Conf. Ser., 216, Astron. Soc. Pacific, San Francisco, 591
Hoyle F., Narlikar J., 1968, Nature, 218, 123
Ibrahim A.I., Safi-Harb S., Swank J.H., et al., 2002, ApJ, 574, L51
Ibrahim A.I., Swank J.H., Parke W., 2003, ApJ, 584, L17
Isenberg M., Lamb D.Q., Wang J.C.L., 1998a, ApJ, 493, 154
Isenberg M., Lamb D.Q., Wang J.C.L., 1998b, ApJ, 505, 688
Istomin Y.N., Haensel P., 2013, Astronomy Reports, 57, 904
Jaisawal G.K., Naik S., 2015, MNRAS, 453, L21

Jaisawal G.K., Naik S., 2016, MNRAS, 461, L97
Johnson M.H., Lippmann B.A., 1949, Phys. Rev., 76, 828
Jones P.B., 1988, MNRAS, 233, 875
Katz J.I., 1973, Nature Physical Science, 246, 87
Kholtygin A.F., Igoshev A.P., Fabrika S.N., 2011, In: Romanyuk I.I., Kudryavtsev D.O. (eds.) Magnetic Stars, 303
Kirk J.G., 1980, Plasma Physics, 22, 639
Kirk J.G., Meszaros P., 1980, ApJ, 241, 1153
Klein O., Nishina T., 1929, Zeitschrift fur Physik, 52, 853
Klochkov D., Staubert R., Postnov K., et al., 2008, A&A, 482, 907
Kompaneets A.S., 1957, Sov. Phys. – JETP, 4, 730
Konar S., Bhattacharya D., 1997, MNRAS, 284, 311
Konar S., Bhattacharya D., 1999a, MNRAS, 303, 588
Konar S., Bhattacharya D., 1999b, MNRAS, 308, 795
Koyama K., Kawada M., Tawara Y., et al., 1991, ApJ, 366, L19
Kraus U., Blum S., Schulte J., et al., 1996, ApJ, 467, 794
Kraus U., Nollert H.P., Ruder H., Riffert H., 1995, ApJ, 450, 763
Krawczynski H., 2016, Successful Launch!, `https://sites.wustl.edu/xcalibur/2016/09/17/successful-launch/`
Kreykenbohm I., Kretschmar P., Wilms J., et al., 1999, A&A, 341, 141
Kreykenbohm I., Mowlavi N., Produit N., et al., 2005, A&A, 433, L45
Krimm H.A., Holland S.T., Corbet R.H.D., et al., 2013, ApJS, 209, 14
Krolik J.H., 1991, ApJ, 373, L69
Kühnel M., 2016, priv. comm.
Kühnel M., Müller S., Kreykenbohm I., et al., 2013, A&A, 555, A95
Lai D., 2001, Reviews of Modern Physics, 73
Lai D., Ho W.C., 2003a, Phys. Rev. Letters, 91, 071101
Lai D., Ho W.C.G., 2003b, ApJ, 588, 962
Lamb D.Q., Wang J.C.L., Wasserman I.M., 1990, ApJ, 363, 670
Lamb F.K., 1975, In: Bergman P.G., Fenyves E.J., Motz L. (eds.) Seventh Texas Symposium on Relativistic Astrophysics, Annals of the New York Academy of Sciences, 262, 331
Lamb F.K., Pethick C.J., Pines D., 1973, ApJ, 184, 271
Landau L., 1938, Nature, 141, 333
Landau L.D., 1932, Phys. Zs. Sowjet., 1, 285
Lander S.K., Jones D.I., 2011, MNRAS, 412, 1730
Langer S.H., 1981, Phys. Rev. D, 23, 328
Latal H.G., 1986, ApJ, 309, 372
Lattimer J.M., 2012, Annual Review of Nuclear and Particle Science, 62, 485
Lattimer J.M., Prakash M., 2004, Science, 304, 536
Leahy D.A., 2002, MNRAS, 334, 847
Levine A.M., Corbet R., 2006, ATEL, 940
Lutovinov A., Tsygankov S., 2009, ApJ, 35, 433
Lyness J.N., 1969, J. ACM, 16, 483
Madsen K.K., Harrison F.A., Markwardt C.B., et al., 2015, ApJS, 220, 8
Makino F., GINGA Team 1988a, IAU Circ., 4575
Makino F., GINGA Team 1988b, IAU Circ., 4577
Makishima K., Mihara T., 1992, In: Tanaka Y., Koyama K. (eds.) Frontiers Science Series, 23
Makishima K., Mihara T., Ishida M., et al., 1990, ApJ, 365, L59
Makishima K., Mihara T., Nagase F., Tanaka Y., 1999, ApJ, 525, 978
Mallick R., Schramm S., 2014, Phys. Rev. C, 89, 045805
Maloney P.R., Begelman M.C., Pringle J.E., 1996, ApJ, 472, 582
Manchester R.N., Hobbs G.B., Teoh A., Hobbs M., 2005, AJ, 129, 1993
Mandl F., Shaw G., 1984, Quantum Field Theory, John Wiley & Sons
Mason K.O., Murdin P.G., Parkes G.E., Visvanathan N., 1978, MNRAS, 184, 45P
Mastrano A., Lasky P.D., Melatos A., 2013, MNRAS, 434, 1658
Matsuda Y.H., Herlach F., Ikeda S., Miura N.,

2002, Review of Scientific Instruments, 73, 4288
Maxwell J.C., 1860a, Philosophical Magazine, 4th series, 19, 19
Maxwell J.C., 1860b, Philosophical Magazine, 4th series, 20, 21
McBride V.A., Wilms J., Kreykenbohm I., et al., 2007, A&A, 470, 1065
McKeeman W.M., 1962, Comm. ACM, 5, 604
Melrose D.B., Zhelezniakov V.V., 1981, A&A, 95, 86
Mészáros P., 1978, A&A, 63, L19
Mészáros P., 1992, High-energy radiation from magnetized neutron stars., University of Chicago Press, Chicago, IL
Meszaros P., Nagel W., 1985, ApJ, 298, 147
Meszaros P., Nagel W., Ventura J., 1980, ApJ, 238, 1066
Mészáros P., Riffert W., 1988, ApJ, 327, 712
Mészáros P., Ventura J., 1978, Phys. Rev. Letters, 41
Mészáros P., Ventura J., 1979, Phys. Rev. D, 19, 3565
Middleditch J., Nelson J., 1976, ApJ, 208, 567
Mihalas D., 1978, Stellar atmospheres - 2nd edition, W. H. Freeman and Co., San Francisco
Mihara T., 1995, Ph.D. thesis, Dept. of Physics, Univ. of Tokyo (M95)
Mihara T., Makishima K., Kamijo S., et al., 1991, ApJ, 379, L61
Mihara T., Makishima K., Nagase F., 2004, ApJ, 610, 390
MPI Forum 1994, MPI: A Message-Passing Interface Standard, Technical Report FUT-CS-94-230, University of Tennessee, Knoxville, TN
Mukherjee D., Bhattacharya D., 2012, MNRAS, 420, 720
Müller S., Ferrigno C., Kühnel M., et al., 2013, A&A, 551, A6
Mushtukov A.A., 2016a, priv. comm.
Mushtukov A.A., 2016b, priv. comm.
Mushtukov A.A., 2016c, priv. comm.
Mushtukov A.A., Nagirner D.I., Poutanen J., 2016, Phys. Rev. D, 93, 105003
Mushtukov A.A., Suleimanov V.F., Tsygankov S.S., Poutanen J., 2015, MNRAS, 447, 1847
Nagase F., 1989, PASJ, 41, 1
Nagel W., 1980, ApJ, 236, 904
Nagel W., 1981, ApJ, 251, 288
Nishimura O., 1994, PASJ, 46, 45
Nishimura O., 2005, PASJ, 57, 769
Nishimura O., 2008, ApJ, 672, 1127
Nobili L., Turolla R., Zane S., 2008a, MNRAS, 386, 1527
Nobili L., Turolla R., Zane S., 2008b, MNRAS, 389, 989
Noble M.S., 2008, Concurrency and Computation: Practice and Experience, 20, 1877
Novick R., Weisskopf M.C., Angel J.R.P., Sutherland P.G., 1977, ApJ, 215, L117
Oertel M., Providência C., Gulminelli F., Raduta A.R., 2015, Journal of Physics G Nuclear Physics, 42, 075202
Oppenheimer J.R., Snyder H., 1939, Phys. Rev., 56, 455
Oppenheimer J.R., Volkoff G.M., 1939, Phys. Rev., 55, 374
Ostriker J.P., Gunn J.E., 1969, ApJ, 157, 1395
Pacini F., 1967, Nature, 216, 567
Pacini F., Salpeter E.E., 1968, Nature, 218, 733
Page D., Geppert U., Weber F., 2006, Nuclear Physics A, 777, 497
Page D., Lattimer J.M., Prakash M., Steiner A.W., 2004, ApJS, 155, 623
Parkes G.E., Murdin P.G., Mason K.O., 1980, MNRAS, 190, 537
Pavlov G.G., Shibanov I.A., Iakovlev D.G., 1980, Ap&SS, 73, 33
Payne D.J.B., Melatos A., 2004, MNRAS, 351, 569
Payne D.J.B., Melatos A., 2007, MNRAS, 376, 609
Payne D.J.B., Vigelius M., Melatos A., 2008, In: Yuan Y.F., Li X.D., Lai D. (eds.) Astrophysics of Compact Objects, American Institute of Physics Conference Series, 968, 227
Pechenick K.R., Ftaclas C., Cohen J.M., 1983, ApJ, 274, 846
Peng Q.H., Tong H., 2007, MNRAS, 378, 159
Pethick C.J., 1992, Reviews of Modern Physics, 64, 1133
Pétri J., 2015, MNRAS, 450, 714
Petterson J.A., 1977a, ApJ, 218, 783

Petterson J.A., 1977b, ApJ, 214, 550
Petterson J.A., 1977c, ApJ, 216, 827
Pietsch W., Oegelman H., Kahabka P., et al., 1986, A&A, 163, 93
Pilkington J.D.H., Hewish A., Bell S.J., Cole T.W., 1968, Nature, 218, 126
Pons J.A., Geppert U., 2007, A&A, 470, 303
Postnov K.A., Gornostaev M.I., Klochkov D., et al., 2015a, MNRAS, 452, 1601
Postnov K.A., Mironov A.I., Lutovinov A.A., et al., 2015b, MNRAS, 446, 1013
Postnov K.A., Yungelson L.R., 2014, Living Reviews in Relativity, 17, 3
Potekhin A.Y., Lai D., Chabrier G., Ho W.C.G., 2004, ApJ, 612, 1034
Pottschmidt K., Kreykenbohm I., Wilms J., et al., 2005, ApJ, 634, L97
Poutanen J., Mushtukov A.A., Suleimanov V.F., et al., 2013, ApJ, 777, 115
Prakash M., Bombaci I., Prakash M., et al., 1997, Phys. Rep., 280, 1
Pravdo S.H., Bussard R.W., 1981, ApJ, 246, L115
Pravdo S.H., Bussard R.W., Becker R.H., et al., 1978, ApJ, 225, 988
Priedhorsky W.C., Terrell J., 1983, ApJ, 273, 709
Pringle J.E., 1981, ARA&A, 19, 137
Pringle J.E., 1996, MNRAS, 281, 357
Pringle J.E., Rees M.J., 1972, A&A, 21, 1
Reig P., Roche P., 1999, MNRAS, 306, 100
Reisenegger A., 2007, Astronomische Nachrichten, 328, 1173
Ridpath I., 2004, A Dictionary of Astronomy, Oxford University press, Oxford
Roche P., Green L., Hoenig M., 1997, IAU Circ., 6698
Rosenberg H., 1910, Astronomische Nachrichten, 186, 71
Ruderman M., 1991a, ApJ, 366, 261
Ruderman M., 1991b, ApJ, 382, 587
Ruderman R., 1991c, ApJ, 382, 576
Russell H.N., 1914, Popular Astronomy, 22, 275
Rybicki G.B., Lightman A.P., 1979, Radiative processes in astrophysics, Wiley-Interscience, New York
Sakurai S., Yamada S., Torii S., et al., 2012, PASJ, 64, 72
Sang Y., Chanmugam G., 1987, ApJ, 323, L61
Sasaki M., Müller D., Kraus U., et al., 2012, A&A, 540, A35
Savonije G.J., 1979, A&A, 71, 352
Schönherr G., 2007, Ph.D. thesis, Eberhard-Karls-Universität Tübingen, Tübingen
Schönherr G., Schwarm F.W., Falkner S., et al., 2014, A&A, 564, L8
Schönherr G., Wilms J., Kretschmar P., et al., 2007a, In: The Obscured Universe. Proceedings of the VI INTEGRAL Workshop, ESA Special Publication, 622, 457
Schönherr G., Wilms J., Kretschmar P., et al., 2007b, A&A, 472, 353
Schreier E., Levinson R., Gursky H., et al., 1972, ApJ, 172, L79
Schubert C., 2000a, Nuclear Physics B, 585, 407
Schubert C., 2000b, Nuclear Physics B, 585, 429
Schwarm F., Schönherr G., Wilms J., Kretschmar P., 2012, In: PoS INTEGRAL 2012, 153
Schwarm F.W., 2010, Diploma thesis, Dr. Karl Remeis-Sternwarte, Astronomisches Institut der Universität Erlangen-Nürnberg & ECAP
Schwarm F.W., 2016, Remeis-C-Library, `http://www.sternwarte.uni-erlangen.de/~schwarm/rcl`
Schwarm F.W., Ballhausen R., Falkner S., et al., 2017a, A&A, 601, A99
Schwarm F.W., Schönherr G., Becker P.A., et al., 2013, In: AAS/High Energy Astrophysics Division, 13, 126.31
Schwarm F.W., Schönherr G., Falkner S., et al., 2017b, A&A, 597, A3
Schwarm F.W., Schönherr G., Kühnel M., Wilms J., 2014, In: European Physical Journal Web of Conferences, 64, 02007
Scott D.M., Leahy D.A., Wilson R.B., 2000, ApJ, 539, 392
Shabad A.E., 1975, Annals of Physics, 90, 166
Shakura N.I., Prokhorov M.E., Postnov K.A., Ketsaris N.A., 1999, A&A, 348, 917
Shternin P.S., Yakovlev D.G., Heinke C.O., et al., 2011, MNRAS, 412, L108
Sina R., 1996, Ph.D. thesis, University of Maryland, College Park, MD

Snyder J.P., 1987, Map projections: A working manual, USGS Numbered Series 1395, U.S. Government Printing Office, Washington, D.C.
Soffel M., Herold H., Ruder H., Ventura J., 1985, A&A, 144, 485
Soffel M., Ventura J., Herold H., et al., 1983, A&A, 126, 251
Sokolov A.A., Ternov I.M., Bagrov V.G., et al., 1968, Soviet Physics, 11, 4
Staubert R., 1997, In: Bulletin of the American Astronomical Society, 29, 793
Staubert R., Klochkov D., Postnov K., et al., 2009, A&A, 494, 1025
Staubert R., Klochkov D., Vasco D., et al., 2013, A&A, 550, A110
Staubert R., Klochkov D., Wilms J., et al., 2014, A&A, 572, A119
Staubert R., Schandl S., Klochkov D., et al., 2006, In: D'Amico F., Braga J., Rothschild R.E. (eds.) The Transient Milky Way: A Perspective for MIRAX, American Institute of Physics Conference Series, 840, 65
Staubert R., Schandl S., Wilms J., 2000, In: McConnell M.L., Ryan J.M. (eds.) The Fifth Compton Symposium, American Institute of Physics Conference Series, 510, 153
Staubert R., Shakura N.J., Postnov K.A., et al., 2007, In: The Obscured Universe. Proceedings of the VI INTEGRAL Workshop, ESA Special Publication, 622, 465
Steiner A.W., Lattimer J.M., Brown E.F., 2013, ApJ, 765, L5
Stella L., White N.E., Davelaar J., et al., 1985, ApJ, 288, L45
Sturner S.J., Dermer C.D., 1994, A&A, 284, 161
Sturrock P.A., 1971, ApJ, 164, 529
Suchy S., Pottschmidt K., Wilms J., et al., 2008, ApJ, 675, 1487
Taam R.E., van den Heuvel E.P.J., 1986, ApJ, 305, 235
Takeyama S., Sawabe H., Kojima E., 2010, Journal of Low Temperature Physics, 159, 328
Tanaka Y., 1986, In: Mihalas D., Winkler K.H.A. (eds.) IAU Colloq. 89: Radiation Hydrodynamics in Stars and Compact Objects, Lecture Notes in Physics, 255, Springer Verlag, Berlin, 198
Tananbaum H., Gursky H., Kellogg E.M., et al., 1972, ApJ, 174, L143
Taylor J.H., Manchester R.N., Lyne A.G., 1993, ApJS, 88, 529
Thompson C., 2008, ApJ, 688, 499
Thompson C., Duncan R.C., 1993, ApJ, 408, 194
Thompson C., Lyutikov M., Kulkarni S.R., 2002, ApJ, 574, 332
Thorne K.S., Ipser J.R., 1968a, ApJ, 153, L215
Thorne K.S., Ipser J.R., 1968b, ApJ, 152, L71
Thorsett S.E., Chakrabarty D., 1999, ApJ, 512, 288
Tiengo A., Esposito P., Mereghetti S., et al., 2013, Nature, 500, 312
Townsend L.J., Coe M.J., Corbet R.H.D., Hill A.B., 2011, MNRAS, 416, 1556
Truemper J., Kahabka P., Oegelman H., et al., 1986, ApJ, 300, L63
Truemper J., Pietsch W., Reppin C., et al., 1978, ApJ, 219, L105
Truran J.W., Cameron A.G.W., 1971, Ap&SS, 14, 179
Tsygankov S.S., Lutovinov A.A., Churazov E.M., Sunyaev R.A., 2007, Astronomy Letters, 33, 368
Turolla R., Zane S., Drake J.J., 2004, ApJ, 603, 265
Ulmer M.P., Baity W.A., Wheaton W.A., Peterson L.E., 1973, ApJ, 184, L117
Urpin V.A., Muslimov A.G., 1992, MNRAS, 256, 261
van den Heuvel E.P.J., Bitzaraki O., 1995, A&A, 297, L41
van der Klis M., 2000, ARA&A, 38, 717
Vasco D., Staubert R., Klochkov D., et al., 2013, A&A, 550, A111
Ventura J., 1979, Phys. Rev. D, 19, 1684
Ventura J., Nagel W., Meszaros P., 1979, ApJ, 233, L125
Verner D.A., Ferland G.J., Korista K.T., Yakovlev D.G., 1996, ApJ, 465, 487
Voges W., Pietsch W., Reppin C., et al., 1982, ApJ, 263, 803
Wang J.C.L., Lamb D.Q., Loredo T.J., et al., 1989, Phys. Rev. Letters, 63, 1550

Wang J.C.L., Wasserman I., Lamb D.Q., 1993, ApJ, 414, 815
Wang J.C.L., Wasserman I.M., Salpeter E.E., 1988, ApJS, 68, 735
Wasserman I., Salpeter E., 1980, ApJ, 241, 1107
Wheeler J.A., 1966, ARA&A, 4, 393
White N.E., Swank J.H., Holt S.S., 1983, ApJ, 270, 711
Whitlock L., 1989, ApJ, 344, 371
Wick G.C., 1950, Phys. Rev., 80, 268
Wigner E.P., 1946, Phys. Rev., 70, 15
Wijers R.A.M.J., Pringle J.E., 1999, MNRAS, 308, 207
Wilms J., Allen A., McCray R., 2000, ApJ, 542, 914
Wolff M.T., Becker P.A., Gottlieb A.M., et al., 2016, ApJ, 831, 194
Woods P.M., Thompson C., 2006, In: Lewin W.H.G., van der Klis M. (eds.) Compact stellar X-ray sources, Cambridge Astrophysics Series, 39, Cambridge University Press, Cambridge, UK, 547
Worley A., Krastev P.G., Li B.A., 2008, ApJ, 685, 390
Wunner G., 1979, Phys. Rev. Letters, 42, 79
Yahel R.Z., 1979, ApJ, 229, L73
Yahel R.Z., 1980, A&A, 90, 26
Yakovlev D.G., Haensel P., Baym G., Pethick C., 2013, Physics Uspekhi, 56, 289
Yakovlev D.G., Pethick C.J., 2004, ARA&A, 42, 169
Yamada M., Kulsrud R., Ji H., 2010, Reviews of Modern Physics, 82, 603
Yusifov I., Küçük I., 2004a, In: Uyaniker B., Reich W., Wielebinski R. (eds.) The Magnetized Interstellar Medium, Copernicus GmbH, Katlenburg-Lindau, 159
Yusifov I., Küçük I., 2004b, A&A, 422, 545
Zhelezniakov V.V., 1981, Ap&SS, 77, 279
Zheleznyakov V.V., Litvinchuk A.A., 1986, In: Guyenne T.D., Zeleny L.M. (eds.) Plasma Astrophysics, ESA Special Publication, 251, 375

A MULTIMEDIA CONTENT

This thesis comes with additional multimedia content (AMC) available on the attached compact disc or online at the following address:

`www.sternwarte.uni-erlangen.de/~schwarm/thesis`

Note that the online content is updated and extended continuously in order to provide other scientists with the latest version of the content. The compact disc contains the static version at the time of thesis submission.

A.1. Electronic Version

The electronic version of this thesis is named **2017-Schwarm-Thesis.pdf**. It provides an electronically readable version of and coincides to the minutest detail with the paper version.

A.2. Trace

The MC simulation described in Section 4 normally stores only photons escaping the geometric shape of the simulated setup for the sake of reduced file size and disk writing

operations. It does provide the option to store the photons and electrons at each step, though. A movie of the simulation process, showing the path of all photons, can be generated by interpolating the photon positions from this data at equally spaced time frames. An example of a so generated movie is contained (**trace.mov**), showing a randomly sampled fraction, of 1–10%, of all photons to enhance the lucidity. The seed photons are injected from a point source at the bottom of a slab-like medium (slab 1-0 geometry). Photons with energies above and below the resonance energy can escape immediately, while the photons close to fulfilling the resonance condition (yellowish) are scattering until their energy and/or angle with respect to the magnetic field axis are changed sufficiently by their interactions with the electrons. Escaping photons are collected in four different angular bins producing synthetic cyclotron line spectra for four different viewing angles with respect to the B-field axis.

B

THE REMEIS-C-LIBRARY (RCL)

Most of the code written in the course of this thesis has been put into the Remeis-C-library (Schwarm, 2016, RCL). Not only does it contains helper functions for everyday scientific life, such as methods for file I/O or mathematical functions beyond the standard math library, but also functions for explicitly calculating the cyclotron scattering cross sections using the method described in Section 3.5. Methods for interpolating from the Green's function tables described by Schwarm et al. (2017a) are contained, as well as functions for calculating the decay rates for cyclotron emission and cross sections for cyclotron absorption and scattering. The RCL has been developed for the main purpose of code modularization, accessibility, and for reducing code duplication. It originates from the code development of `CycloSim`, but has been programmed with usage in other applications in mind. A general wrapping scheme has been developed in order to provide most functionality in `S-Lang/ISIS`, as well.

The documentation and instructions for installation can be found online (Schwarm, 2016):

`http://www.sternwarte.uni-erlangen.de/~schwarm/rcl`

The code is organized in terms of several modules, each providing specific functionality. The following list provides a short overview. Some of them, which are providing functions directly related to the scientific content of this thesis, are described in more detail and linked to the corresponding sections.

arg Handling of and testing for command line arguments.

cdf Implementation of the cumulative distribution functions used in several integration methods.

cgi Server side web functionality.

config Unification of several configuration file formats, such as .cfg/nginx/JSON with a consolidated interface. This module is based on the Universal Configuration Library Parser (libucl) and the Configuration File Library (libconfig).

const Physical and mathematical constants and an interface for accessing them.

cyclo Functions dealing with electrons in strong magnetic fields, such as, methods for the calculation of the decay rates and cross sections from Sections 3.4, 3.3, and 3.5 and utility functions for calculating important parameters such as the resonance energies of cyclotron lines and the energy of an electron in a strong magnetic field.

debug Configurable printing of debugging messages.

dll Interface for calling arbitrary functions from Dynamically Linked Libraries.

file Functions for file I/O, testing, and filename operations.

fork Ancillary functions for forking child processes.

geo Geometric functions and collision testing. This module is still in the alpha testing phase.

grid Functions for manipulating grids, i.e., arrays of double numbers, which are mostly assumed to be monotonically increasing.

input User interaction with the keyboard or mice (currently keyboard only).

integr Several numerical integration methods with a united interface.

interp Interpolation and extrapolation methods.

list An C implementation for linked lists.

log Logfile message logging.

macro Ancillary macro library.

math Mathematical functions.

mem Methods for memory allocation and handling.

mpi High level auxiliary functions for the Message Passing Interface (MPI Forum, 1994, MPI). Includes a generalized way of distributing work amongst multiple processes using a load balancing master-client work sharing scheme.

net Network communication over sockets.

omp OpenMP parallelization ancillary functions.

par Parameter file handling using the Parameter Interface Library (PIL).

physics Several physical distributions and helper functions.

print Generalized interface for printing (warning/error) messages to the screen.

random Random number generation and random number server for serving random numbers from the same seed to multiple clients via sockets or MPI.

slang C embedded S-Lang interpreter for loading, modifying, and executing S-Lang code.

spec Handling of spectra, i.e., a combination of a grid with a double array of values.

string String manipulation and auxiliary functions.

table Implementation for storing numbers, spectra, or even arbitrary data in FITS binary tables for all parameter combinations of an arbitrary number of input parameters. The only limitation so far is that each input parameter grid must be the same for all other parameters or at least generatable from a template grid by a function and a specific parameter combination. The `cyclofs` model uses this module for the creation and interpolation from Green's function tables necessary to programmatically disentangle the time consuming MC simulation process from the choice of input continuum (see Sections 4.3, 4.8, and 6.1–6.4).

time Methods for measuring time.

tool Template macros for developing RCL tools. This is used by the RCL itself for the implementation of a command line interface to RCL functions.

unit Simple unit conversion.

ut Unit testing frame work for C code.

vector Linear algebra vector math.

C

THE CycloSim SOFTWARE

In the following the basic usage of `CycloSim` is laid out in order to provide information about how adaptive mean free path tables, Monte Carlo simulation results, and Green's function tables can be generated. Due to the enormous flexibility of the code and the different data products generated by it, its direct invocation has become somewhat unhandy and gave rise to the provision of additional helper scripts, which can be used to obtain data products quickly using default settings. Three of these *Meta-Scripts* are available for the three types of data products yielded by the `CycloSim` software:

Mean Free Path interpolation tables (MFPs) FITS files storing the thermally averaged scattering cross sections as described by Schwarm et al. (2017b). These files are used by the simulation code to interpolate mean free paths and sample the interacting electron's initial spin and its initial momentum parallel to the magnetic field axis.

PHOton files storing escaped photons (PHOs) Tables storing the seed photons injected into, and the processed photons escaping from, the Monte Carlo simulation. The FITS files contain the simulated setup, that is, the configured slabs and sources, as well. They can be used to study the distribution of the escaping photons directly, as, for example, done by Schönherr et al. (2014) or Schwarm et al. (2017b), or, if configured accordingly, for calculating the simulated medium's response to monoenergetic photon injections. This is done by configuring the source(s) to have the source type *GREENS*.

Green's function tables for the XSPEC model The results from simulation runs

with *GREENS* type sources can be binned to Green's function tables, which are used by the `cyclofs`, `cyclocol`, and `cyclocap` XSPEC local models to imprint synthetic cyclotron lines on arbitrary input continua. The filenames of the generated tables should provide a good idea for the simulated geometry and the usage of slab-like geometry tables together with the column model `cyclocol` is strongly discouraged just like the combination of cylinder-like geometries with the `cyclocap` model for obvious reasons.

In the following a listing of the directory structure of the `CycloSim` software suite is given:

```
cyclosim ..................................................Root directory
├─bin ....................................................Compiled binaries
│ └─cyclosim ..................................CycloSim executable
├─cyclo ..............................Low level routines for CRSF physics
│ └─sina .....................Modified cross section code from Sina (1996)
├─cyclo-init.csh ..................................csh initialization file
├─cyclo-init.sh ..................................bash initialization file
├─cyclomc ..............  Original cross section code from Sina (1996),
│                        Simulation code from Araya & Harding (1999), and
│                                        IDL scripts from Schönherr (2007)
│ └─...
├─include ..........................Header dependencies for CycloSim
├─lib ..............................Library dependencies for CycloSim
├─Makefile ....................................Main CycloSim Makefile
├─pil ....................................Parameter Interface Library (PIL)
├─rcl ..........................................Remeis C-Library (RCL)
├─run ..................................................Execution directory
│ ├─bin .....................Meta-Scripts for calculation of data products
│ │ ├─setup_mfp.sh ..............................Script for MFP jobs
│ │ ├─setup_pho.sh ..............................Script for PHO jobs
│ │ └─setup_greens.sh .........Script for Green's function table creation
│ ├─default ..................................Example configuration files
│ └─etc ....................... Configuration files used by the Meta-Scripts
├─sim ..................................................Simulation code
└─tools ..................................... Scripts for plotting and testing
```

The *Meta-Scripts* are contained in the `run/bin` subdirectory of `CycloSim`'s root directory. They make use of the configuration files in the configuration directory `run/etc`. Their usage is described individually in the following in the order as they would be called to go the whole way from the MFP table creation to the fitting model. Note that before running any of these scripts or running the `cyclosim` binary, the environment must be initialized by sourcing the initialization files from the `CycloSim` root directory, that is, assuming the current directory is the root directory,

```
source cyclo-init.sh
```

for Bash shell and

```
source cyclo-init.csh
```

for tcsh.

1.) setup_mfp.sh <MFP directory>

This script is using the following files from the configuration directory (files in parenthesis are optional):

(cyclosim.par) is an PIL parameter file. It is copied to the MFP directory.

(mfp.setup) is an additional setup file, which is copied to the MFP directory as well.

B.grid contains the magnetic field values for which MFP tables should be calculated.

T.grid contains the temperatures for which MFP tables should be calculated.

EB.grid contains the energy start grid, which will be refined adaptively during MFP table calculation.

muabs.grid contains the angle start grid, which is also refined adaptively during MFP table calculation.

The MFP directory will be created and inside it the basic directory structure of MFP and PHO calculations:

```
MFP/PHO directory
├─ config ..............................Configuration files
├─ grid ................................Grid files
├─ job .................................Torque job scripts
├─ log .................................Log files
└─ submit_all.sh ....Ancillary script for submitting all jobs
```

The MFP calculations can be started individually by submitting the desired job scripts or all jobs can be submitted to the queue by running the `submit_all.sh` script. The jobs can be run manually by replacing `mpiexec` inside the job script by `mpirun -n <number of CPUs>` if a resource management system is unavailable. Please note that depending on the settings in the *Meta-Script* and the additional configuration files, these calculations take a very long time (see Schwarm et al., 2017b, for details).

2.) setup_pho.sh <PHO directory>

Apart from the `cyclosim.par` parameter file from the root directory, this script is using the following files from the configuration directory:

B.grid contains the magnetic field values for which PHO files should be calculated.

T.grid contains the temperatures for which PHO files should be calculated.

Ein.grid contains the energies used as input energies if not superseded in the configuration file.

EB.grid contains the output grid, depending on the setup this file might be used instead of `Ein.grid`.

***.grid** represent all grid files in the configuration directory.

***.conf** represent all config files in the configuration directory.

Additional optional command line parameters are listed if the script is called without arguments. Currently this includes overrides for simulated parameter combinations and energy grid files and only plays a role for the integration with the experimental web interface. The script generates a data product directory structure, basically identically to the one listed above for the case of the MFP table creation. Jobfiles are generated for all combinations of magnetic fields and temperatures for all configurations of the CRSF medium (i.e., `.conf` files) found in the configuration directory. The MFP table directory is set at the top of the **setup_pho.sh** *Meta-Script*. The jobs may be submitted all at once by executing the generated `submit_all.sh` script. The simulation times strongly depend on the configured setup (see Schwarm et al., 2017a, for some examples).

3.) setup_greens.sh <greenstable> <pho1> [<pho2>[<pho3>[...]]]

This script is using the following files from the configuration directory:

mu.grid Angular binning.

Ein.grid Energy binning.

It produces a Green's function table, <greenstable> by binning all PHO files provided as additional command line arguments according to the angular and energy grids in the configuration directory. The calculation time for the binning of the PHOs is negligible compared to the time needed for their simulation. It is advised to use the script on the machine storing the PHOs in order to avoid unnecessary network bandwidth usage.

Acknowledgments

I am very grateful for my time at the Remeis observatory, the pleasant work atmosphere at which is first and foremost owed to the superior trinity Horst Drechsel, Uli Heber, and my adviser Joern Wilms. As much as I missed the presence of Horst, talking with whom I always enjoyed, from the first day of his retirement, I am pleased to see that the line of both proficient and kind superiors is pursued with the appointment of Manami Sasaki. It is this cordiality that I first recognized as I was a student of the astronomical lab course myself and taking the exam for my intermediate diploma with Uli. Special thanks go, of course to Joern, not only for advising my thesis but also for giving me responsibility right from the beginning of our collaboration. I very much appreciate the possibilities and trust you gave me to balance my theoretical work by living out my inner engineer with projects like the maintenance of (and fun projects with) the observatory's radio telescopes and the construction of the ∼100 TB storage array for project "Datengrab". One of the most influential persons for this work has been Gabriele Schönherr, who introduced me to the matter of cyclotron lines at the very beginning. Thank you very much, Gabi, for the satisfying discussions about the physics and for being as adventurous as you are. I really enjoyed sharing a campsite with you as a conference accommodation and I am keeping up the hope that our "CampCon" will become reality one day. Thank you, Katja Pottschmidt, for the huge amount of comments you gave me, which have been an essential source of improvements for this work and related publications. I am very thankful to Peter Becker and Mike Wolff for providing height dependent spectra of, and advise on, their physical continuum model. Mike, I treasured the discussion about the height dependence of the BW07 model while having a "Shawarma" for lunch at the HEAD meeting in Monterey. Pete, you showed great interest in my work from the very beginning, I appreciate that very much. In this phase at the beginning, but also later on, Prof. Dr. Rüdiger Staubert, Carlo Ferrigno, and Dima Klochkov always provided many valuable hints and comments that I would have overlooked. The same applies to Peter Kretschmar who gave me the opportunity to come to ESAC right after graduation. The stimulating discussions with Ekatharina Sokolova-Lapa about the matter of polarization and its different implementations provided me with important insights and culminated in a separate section of this thesis. Thank you, Katya, for the foundation of the "CRSF post" and also for the recreational jam session. I want to thank Alexander Mushtukov for the correspondence about and the deep comparison of our scattering cross sections and the short but valuable discussion we had about polarization at the Physics at the Magnetospheric Boundary conference in Geneva. Much credit goes to Ramin Sina for his code for the calculation of the CRSF scattering cross sections and to Rafael Araya for his simulation code. Without having these codes this work would have gotten much less far. I thank Osamu Nishimura-san for comparing his scattering cross section profiles to mine in the very early stage of this thesis. I consulted his impressive works on cyclotron lines consistently. Diana Marcu-Cheatham and Paul Hemphill, I enjoyed working together with you in the MAGNET collaboration, our conversations at conferences, and your stay at the observatory very much! And thank you, Paul, for performing the first beta-testing of the physical CRSF model. The importance of letting an independent person performing tests with such a new model can not be emphasized enough. Also I want to thank all the members of the MAGNET collaboration for the valuable meetings and telecons from which I learned a lot and the International Space Science Institute in Bern for inspiring team meetings. Many thanks to John E. Davis for developing an interpreted programming language with the C-like syntax that I love so much, namely `S-Lang` (Davis, 2016), and for its `slxfig` package, with which most figures in this thesis have been produced. I also want to thank Michael S. Nobel for the development of the `S-Lang Interface Package` (Noble, 2008, SLIRP), which made it possible to wrap all the code from the `RCL` (Schwarm, 2016) library automatically into an S-Lang package and therefore allowed for providing its functionality to `ISIS/S-Lang` users. The developers of the Interactive Spectral Interpretation System (Houck & Denicola, 2000, ISIS), John C. Houck and L. A. Denicola deserve credit too. ISIS is a powerful tool for data analysis of all kinds and I am happy to got to know it well. This research has made use of a collection of ISIS functions (`isisscripts`) provided by the ECAP/Remeis observatory & MIT (2016), the developers of which earn some acknowledgment as well for sharing their work with the scientific community. This seems to be the just the right point to express my gratitude to Manfred Hanke. Not only did he introduce me into the beauty of the S-Lang programming language, developed many of the extensively used functions in the `isisscripts`, provided me the opportunity to present my engineering work on project "Datengrab"

at the TNG OpenTech day, and shared his experience with test driven software development with the Remeis people even after leaving the observatory, but also did he introduce me to my, at that time newly gained, responsibilities as a system administrator and repeatedly told me the administrative password for the LDAP interface without making fun of me, even after I had tumbled it up for the third time on the same day because I refused to write it down. And of course I want to thank the whole Remeis gang for being good colleagues: My first office mate, Alfred Tillich, for facilitating my entrance to office work. My second office mate, Cornellia Müller, for the very productive and comfortable working atmosphere. Tobias Beuchert and Simon Kreuzer for fun at the office, Natalie Hell for social interaction at late working hours, and Sebastian Falkner for many discussions about neutron star geometries and relativistic light bending. I thank the students from the RISE and other exchange programs who spend a summer at the observatory and enriched the institute with a variety of both social and professional nature, especially Aisha Mahmoud, Luke Schiefelbein, and Kunal Deoskar, thank you for the diverting evenings. And thank you, Paula Izquierdo for your delicious cooking! Furthermore I want to thank you, Laura, and Ana, Barragan, for the heartily reception in Madrid. Thorsten Brand for valuable discussions about electronics and other interesting conversations. Michael Wille for being a good programmer and good conversations. Macarena Sagredo for good conversations as well, and for improving my English skills and proof reading papers. Markus Schindewolf for the chocolate. My system administrator colleagues, Ingo Kreykenbohm, Thomas Dauser, and Matthias Kühnel, for efficient task sharing and shared suffering from demanding users. Ralf Ballhausen for introducing me to *NuSTAR* data extraction and analysis, and for answering mails at late hours on weekends. Felix Fürst, thank you for the insight on some of the specific quirks of *NuSTAR* and for the most awesome conference experience at the COSPAR in Moscow. Matthias “now Bissinger”, for being motivatable for activities nobody else was fond of doing, such as playing the guitar together, evil electronic projects, and the workouts. Mirjam for our mutual motivation to work out as well. Victoria Grinberg (and Flo!) for the great conversations and for providing guidance. Keira and my beloved Kurt for keeping the office clean and for enliven me when humans failed to do so. Anne Baczko for bringing Keira and for your steady friendliness. Andreas Irrgang for precious advise on how to write a thesis. Wiebke Eikmann for pushing me forward and for so many other things that I can not even start to enumerate here! Eva Ziegerer, for the office gossip, for inviting me to my first basketball game to see you and your “Devils”, and for just being a good person. And, of course, Eugenia Litzinger (now Fink), I am grateful to you for many things like the organization of numerous Christmas parties, for supplying the observatory with coffee, for buying a pool for the garden when summer threatened to melt us, and for providing me with your different point of view, but mostly for having my back when I needed it. Also, I am in debt of Edith Day, without whom I would have been lost in bureaucracy more than once. I thank the cleaning ladies for their toleration of the chaos that I called my place of work. And some more in loose order that I can not leave unmentioned: Isabella Caballero, Prof. Dr. Joachim Trümper, the trainees at ESAC, Elise Egron, Maria Hirsch, Christoph Grossberger, Marilyn Latour, Arash Bodaghee, Prof. Irmela Bues, Moritz Böck, Matthias Kadler, Norbert Jansen, Heinz Edelmann, Rene Hudec, Dr. Karl Remeis, and all the people that I forgot.

Last but not least I want to thank some of the people who supported me personally. First of all, thank you, Antonia Cramm for your warmth, your understanding, and for always having an open ear for me. I appreciate your patience during the past months, your care, your knowledge, and our discussions more than I am capable of expressing!

Isabel, Isi, Chrissi, Petzi, Lisa (and family), Eike, and the Annas, thank you for a social life outside the observatory, Michelle for your support and the good conversations, and David for consistently dropping in on me despite your full time table. Thank you, Thorsten, for our philosophical, physical, technical, and mathematical discussions and Jens for our intensive hikes and that I can share my thoughts with you.

Most of all I want to thank my mother, Margit Schwarm. Thank you for always supporting me, for my happy childhood, your patience, and for sharing your worldly wisdom with me whenever I need it!

Am allermeisten möchte ich meiner Mutter, Margit Schwarm, danken. Danke, dass Du mich immer unterstützt hast, für meine glückliche Kindheit, Deine Geduld, und dafür, dass Du Deine Lebensweisheiten mit mir teilst, wann immer ich sie benötige!